Title
Revealing Design Principles of Biological Networks through Optimization and Dynamical System Approaches

Author
Chang, Shyr-Shea

Publication Date
2019

Peer reviewed|Thesis/dissertation

UNIVERSITY OF CALIFORNIA

Los Angeles

Revealing Design Principles of Biological Networks through Optimization and Dynamical System Approaches

A dissertation submitted in partial satisfaction
of the requirements for the degree
Doctor of Philosophy in Mathematics

by

Shyr-Shea Chang

2019

ABSTRACT OF THE DISSERTATION

Revealing Design Principles of Biological Networks
through Optimization and Dynamical System Approaches

by

Shyr-Shea Chang
Doctor of Philosophy in Mathematics
University of California, Los Angeles, 2019
Professor Marcus L. Roper, Chair

Biological networks, such as vascular networks and neural circuits, are ubiquitous in nature. An understanding of these networks can help us understand their response to damages, which could lead to novel treatments. They can also inspire the design of man-made networks, as evolution has millions of years to figure out optimal designs. The advancement in imaging techniques has created high-dimensional data streams, which is difficult to analyze by conventional approaches. On the other hand, quantitative tools are naturally suited for processing large data sets, and they become more and more important in improving our knowledge on biological networks. Among existing tools ranging from network science to stochastic analysis, here we focus on optimization and dynamical system approach. Optimization links biological functions to corresponding network structures, which can give predictions to be compared with the data. The dynamical system approach is suited for analyzing time series data and complex interaction between the vertices, which is often exploited in biological systems for intricate signalings and regulations.

This thesis is devoted to the study of biological networks with optimization and dynamical system, focused on two specific biological systems: microvascular network and bipolar disorder. For microvascular networks, we first study a specific example of embryonic zebrafish trunk network, and reveal the significance of flow uniformity in this network. Then we derive analytical structures of networks with optimal transport efficiency, which is widely

regarded as the organizing principle of vascular networks, especially for large vessels such as aorta. To compare the morphologies of transport efficient and uniform flow networks, we develop algorithm that is capable of finding optimal networks with general target functions and constraints, and show that the principle of uniform flow creates more realistic microvascular networks under many different topologies. Finally, we propose an vessel adaptation mechanism based on stress sensing dynamic to explain how microvascular networks stay resilient to noise, and how they grow into uniform flow networks. For bipolar disorder, we mathematically analyze a dynamical model based on the interaction of mood and expectation. We show that bipolar disorder can be viewed as a bifurcation in the direction from normal to cyclic personality. We also consider the case where positive and negative events are sensed differently, and describe the bifurcation in this case. Finally we apply commonly used medicine on the model, and recover clinically observed phenomena on bipolar disorder patients.

The dissertation of Shyr-Shea Chang is approved.

Alexander J. Levine

Mason A. Porter

Tom Chou

Marcus L. Roper, Committee Chair

University of California, Los Angeles

2019

To my parents and my wife

TABLE OF CONTENTS

LIST OF FIGURES

LIST OF TABLES

ACKNOWLEDGMENTS

First, I would like to thank my advisor Marcus Roper for his guidance and unfailing support. From him I learned the joy of science, and the courage to take on difficult problems. I would like to thank my committee members, Tom Chou, Mason Porter, and Alex Levine. I would like to thank Andrea Bertozzi and Inwon Kim for their advice on academic career. I would like to thank my collaborators, Ruby Tu, Yunxuan Li, and Shirlyn Wang for their effort on our work, Samantha Dundon, Kahye Song, Hyejeong Kim, Kyung In Baek, Chih-Chiang Chang, Andrew Pietersen, Dimitri Bikos, Yu-Hsiu Liu, and Cynthia Chen for their help and effort on the experiments, Tatyana Gavrilchenko for her help on the theory and simulation. Sheng-Ping Hwang, Amy Gladfelter, Sang Joon Lee, Thomas Mason, and Tzung Hsiai for their experimental expertise, Van Savage, Eleni Katifori, and Karen Alim for their theoretical expertise and helpful discussions. I would like to thank Martha, Maida, and Jacquie for their help on the administrative affairs.

I would also like to thank my friends from UCLA, Michael, Zach and Kaity, Eric, Melanie, Dave, Jeremy, Stephanie, Alex, Sam, Will, Bon-Soon, Yacoub, Jean-Michelle, Thomas, Minh, Dustan, Paul and Emi, Kyung, Bohyun, Zane, Angela, Gyu Eun, Redmond, Blaine, Björn, Fei, Hans, and Ivy for being with me through the years in graduate school. I would like to thank our neighbors, Sandy and Jack, Amber and David, Teresa and Liyang, and Annie and Alvin for their emotional support. I would like to thank my high school classmates, Jyun-Yu, Jiun-Ting, Yang-Ting, and Chen-Yu for their company. I would like to thank Kaitlyn for being my elder academic sibling and her many helpful advice. I would like to thank my family and friends over in Taiwan. Finally, I would like to thank my beloved wife Chichi for everything she did for me.

This work is funded by UCLA Alumni Society Fellowship, System and Integrative Biology Training Grant (NIH T32-GM008185), Dissertation Year Fellowship, and Fellowship for Abroad Study from Taiwan Department of Education.

VITA

2013 B.S. in Mathematics, National Taiwan University, Taipei, Taiwan

2016 M.A. in Mathematics, UCLA

PUBLICATIONS

Shyr-Shea Chang and Marcus Roper. "Microvascular networks with uniform flow." *Journal of Theoretical Biology*, 462, 48–64, 2019.

Shyr-Shea Chang and Tom Chou. "A dynamical bifurcation model of bipolar disorder based on learned expectation and asymmetry in mood sensitivity." *Computational Psychiatry*, 2, 205–222, 2018.

Shyr-Shea Chang and Marcus Roper. "Minimal transport networks with general boundary conditions." *SIAM Journal on Applied Mathematics*, 78(3), 1511–1535, 2018.

Shyr-Shea Chang, Shenyinying Tu, Kyung In Baek, Andrew Pietersen, Yu-Hsiu Liu, Van M Savage, Sheng-Ping L Hwang, Tzung K Hsiai, and Marcus Roper. "Optimal occlusion uniformly partitions red blood cells fluxes within a microvascular network." *PLoS Computational Biology*, 13(12), e1005892, 2017.

Kahye Song, Shyr-Shea Chang, and Sang Joon Lee. "How the pine seeds attach to/detach from the pine cone scale?." *Frontiers in Life Science*, 10(1), 38–47, 2017.

Kahye Song, Shyr-Shea Chang, Marcus Roper, Hyejeong Kim, and Sang Joon Lee. "A biologically-inspired symmetric bidirectional switch." *PloS One*, 12(1), e0169856, 2017.

Samantha E Dundon, Shyr-Shea Chang, Abhishek Kumar, Patricia Occhipinti, Hari Shroff, Marcus Roper, and Amy S Gladfelter. "Clustered nuclei maintain autonomy and nucleocytoplasmic ratio control in a syncytium." *Molecular Biology of the Cell*, 27(13), 2000–2007, 2016.

CHAPTER 1

Introduction

Biological networks are networks applied to biology, with either vertices and edges representing biological entities, or a theoretical interpretation of the system under study. A biological network can be a physical representation of a biological system, such as vascular networks in animals and plants [BTK13, MSA03] and hypha networks in fungi [RSH13], with edges being vessels and vertices being junctions, and the neural networks in brain [BB06], with vertices being neurons and the edges being synaptic connections. It can also be a higher-level representation of a biological process, such as the relation between emotion and memory [SS88], that serves as an abstraction of an otherwise overly complicated network that potentially involves billions of neurons. An understanding biological networks can help us predict their response in pathological situations, such as acute damage like stroke and trauma, and chronic condition such as dementia, which could lead to novel treatment for the diseases. For example, after removal of coronary occlusion, the perfusion in the heart is often not restored, blocked by endothelial protrusions and cell rouleaux [RK06]. Knowing the mechanism of capillary responses may lead to new medicine that help preventing this pathology. The study on these networks could also guide the construction man-made networks and improve their performance. For example, the slime mold network connects to food sources placed on major japanese cities around Tokyo with comparable efficiency and robustness as the Tokyo rail system in several days, and the rail system took tens of years to build [TTS10]. While man-made networks such as highways suffer from congestion, the transport speed of nuclei in fungal networks increases with the number of nuclei in the group [HDF16].

Gaining insight into biological networks requires quantitative tools, as a network can have thousands of vertices and edges, often coupled with complex dynamics. For example, the

capillary network in mouse brain cortex contains tens of thousands of vessels in a millimeter cube [BTK13]. The blood flows are in the Stokes regime [Ach90], and changes in the radius of a vessel can lead to global redistribution of flow. The advancement of technology has enabled production of large data sets. Time series data of gene expression can be obtained for thousands of genes [HEB05], and the neuronal connectivity in mouse brain can be established by the fMRI techniques [AST12]. Despite our ability to generate high-resolution data on biological networks, there is much space for theoretical development that links these data to the underlying structure of the networks, which will point to new experiments that help us understand these networks.

One mathematical tool that gives insight to biological networks is optimization. The organisms are under the constant force of evolution over millions of years, and the hypothesis is that the networks with better performance on their functions, which may vary from network to network, tend to persist and be seen in present days. Mathematically speaking, this means that the observed network structure can be predicted by optimizing the hypothesized function of the network. Indeed this has been the case for vascular networks in animals and plants. In 1926 Murray proposed a law for vascular networks, now named after him, derived from the optimal transport efficiency [Mur26b]. The Murray's law, which states the blood flow is proportional to the cubic power of the vessel radius, has been verified in both animals and plants [She81, MSA03]. Recent studies continued his philosophy of transport efficient networks [BM07], but also turned to other biological functions, such as robustness and fluctuation, to explain vascular networks with morphologies not explainable by transport efficiency [KSM10, Cor10].

Another powerful tool to dissect biological networks is through dynamical system approaches. Many biological processes are not well-characterized by their current states, but can only be intrinsically described by the trajectories of the variables. One example is the bipolar disorder, which is characterized by an emotional state oscillating between manic and depressive episodes. At any given time point, a bipolar emotional state will be mistaken with mania, depression, or even euphoria state, and the dynamic of the oscillations is intrinsic to the pathology. The dynamic also provides a mechanism to form the observed network

structure revealed by optimization, as it is unlikely the organism construct its network by carefully following a genetic blueprint that specifies every single detail, such as the positions of all the cells. In vascular networks, the adaptation of the vessel to the endothelial shear stress exerted by its blood flow is shown to create transport efficient network [HC13], and the pruning by this adaptation has been observed [CJL12]. On the other hand, it has been argued that this shear stress adaptation along cannot generate all the observed vascular networks, as no loops can be preserved by this process [HVS96].

In this dissertation, we will explore biological networks with the afore mentioned quantitative tools. We aim to discover the design principles of these networks – what functions they perform, what structures correspond to these functions, and how the networks grow into these structures. We will focus on vascular networks at the capillary network, and the dynamical system of bipolar disorder models. In the dissertation, we create new mathematical tools that provide quantitative predictions, and we compare them to biological data from our own experiments.

The rest of the dissertation is organized into five parts and a concluding chapter:

Chapter 2: We study the trunk vascular network in zebrafish embryos. We show that the occlusions of the red blood cell in the capillaries are finely tuned to create uniform blood flow. We also reveal the trade-off between flow uniformity and transport efficiency, and that zebrafish trunk vasculature achieves uniform flow at the cost of transport efficiency.

Chapter 3: We study the analytical structure of transport efficient networks under both Neumann and Dirichlet boundary conditions. Previous work has shown that these networks are trees under Neumann boundary conditions. However this is not true for general boundary conditions, as we show by a counter-example. We prove that transport efficient networks globally satisfy Murray's law, and derive conditions under which transport efficient networks are trees.

Chapter 4: We propose a gradient descent algorithm that can find optimal networks with general target functions and constraints. Previous works focus on finding transport efficient networks with a fixed amount of building material. However we saw that flow uni-

formity is prioritized in certain biological systems, and there are likely to be other biologically relevant target functions and constraints. We use our algorithm to compare transport efficient and uniform flow networks under different network topologies, such as branching tree and square grids. We also impose transport cost as a constraint, and reveal a bifurcation in zebrafish trunk vasculature when the relative cost of transport exceeds a threshold.

Chapter 5: We study the adaptation of capillary networks. Previously we showed that zebrafish trunk vascularture are uniform flow networks. However it is unclear how the network grows into its final form, and how the network resists noise perturbation, as tiny change in vessel radius can largely alter its conductance by perturbing the lubrication layer. We propose an adaptation mechanism based on the distinct shear stress signal created by the red blood cells. We show that this mechanism can create large loopy networks, unlike the previous mechanisms based on average shear stress signaling, and zebrafish trunk vasculature can be generated by this mechanism. Under growth or genetic perturbation, the red blood cell concentration is perturbed, which can destabilize this mechanism. We show that this instability is observed in experimental data, and our model quantitatively predict the changes.

Chapter 6: We study a dynamical model for bipolar disorder based on the interaction of mood and expectation. By a close analysis on a variant of a previously proposed model, we show that bipolar disorder naturally occurs when the mood sensitivity exceeds a threshold, in the direction from normal to cyclic personality. We derive an asymptotic expression for the magnitude of mood oscillation, and we analyze the quantitative behavior of the threshold when positive and negative events are perceived differently. Finally we apply commonly used medicine on the model, and explain clinically observed phenomena, such as the early manic episodes introduced by antidepressants.

CHAPTER 2

Optimal occlusion uniformly partitions red blood cells fluxes within a microvascular network

This chapter was based on: Shyr-Shea Chang, Shenyinying Tu, Kyung In Baek, Andrew Pietersen, Yu-Hsiu Liu, Van M Savage, Sheng-Ping L Hwang, Tzung K Hsiai, and Marcus Roper. "Optimal occlusion uniformly partitions red blood cells fluxes within a microvascular network." *PLoS Computational Biology*, 13(12), e1005892, 2017.

2.1 Introduction

Vascular networks transport oxygen, carbon dioxide and sugars within animals. Exchange of both nutrients and gases occurs primarily in narrow vessels (e.g. capillaries) that are typically organized into reticulated networks. The narrowest vessels are comparable in diameter to red blood cells, forcing cells to squeeze through the vessels. Accordingly, hereditary disorders or diseases affecting the elasticity of cells and preventing them from contorting through narrow vessels can disrupt microvascular circulation [Tom14]. The cost of blood flow transport in the cardiovascular system is thought to dominate the metabolic burden on animals [WBE97]. The rate at which energy must be expended to maintain a constant flow of blood through a vessel is inversely proportional to the 4th power of the vessel radius. Red blood cells occlude the vessels that they pass through, further increasing the resistance of those vessels [SBM16]. Accordingly capillaries and arterioles account for half of the total pressure drop within the network, and thus half of its total dissipation [Hal15]. Experiments in which cells are deformed using optical tweezers, or by being pushed through synthetic micro-channels have shown that the extreme deformability of mammalian red blood cells requires continous

ATP powered-remodeling of the connections between membrane and cytoskeleton. ATP released by deformed cells may induce vasodilation facilitating passage of cells through the narrowest vessels [WRS08]. Thus, chemical as well as hydraulic power inputs are needed to maintain flows through microvessels [BLJ09, PBA10].

Why do micro-vessels need to be so narrow? A textbook answer to this question is that smaller, more numerous capillaries allow for more uniform vascularization of tissues – ensuring that "no cell is ever very far from a capillary" [Hal15]. If smaller vessels are favored physiologically and red blood cell diameter acts as a lower bound on capillary diameters, then networks in which capillary diameters match those of red blood cells may be selected for. However, red blood cell sizes do not seem to be stiffly constrained – for example measured red blood cell volumes vary over almost an order of magnitude (19 to 160 femto-liters) between different mammals [HBG91]. Since for a fixed capillary diameter, a small decrease in red blood cell diameter would greatly reduce rates of energy dissipation for red blood cells traveling through capillary beds [SH96], the evolutionary forces maintaining red blood cells and capillary diameters remain unclear.

There is a natural analogy between occlusion of vessels by red blood cells, and the congestion that occurs in data or road networks [CJ89, YH98]. Efforts to construct efficient transport networks often focus on reducing congestion [CJ89], yet although cardiovascular networks are thought to be organized to minimize transport costs (i.e. the viscous dissipation occuring within the network) [Mur26b, She81]; the presence of congestion at the finest scales seems at odds with minimizing these costs. Could the extreme deformation of cells passing through capillaries be an adaptive feature of the cardiovascular network? By directly stretching cells using optical tweezers Rao et al. [RBC09] showed that deforming red blood cells releases oxygen. But it remains an untested hypothesis that squeezing cells so that they may pass through capillaries accelerates oxygen release, and therefore contributes to the function of the network. Indeed, earlier models suggest that alterations in the shape of the red blood cell surface decrease rates of oxygen exchange [WP93].

In this work we use mathematical modeling to reveal a previously unreported contribution of occlusive dynamics to the efficient functioning of the cardiovascular network. Moreover we

link occlusive dynamics to a different open mystery of cardiovascular function. Specifically given that microvessels are distributed throughout the body and at very different distances from the heart, there is surprising consistency among measured flow rates in different capillaries [KMH98, COA03, SUP03] (with some exceptions [PSG95]). Indeed consistency in flow rates may be biophysically necessary: if flow rate in a capillary is too low, the cells surrounding the capillary may not receive enough oxygen, but if the flow rate is too high, then red blood cells may leave the capillary bed before surrendering their oxygen to the surrounding cells. If the cardiovascular system is treated as an idealized symmetric branching network (such as in [WBE97]) then flows are automatically uniformly partitioned at each level of the network, including among capillaries. But real cardiovascular networks have complex topologies, and it is not clear how the uniform flow can be achieved among billions of capillaries whose distances from the heart can range over several orders of magnitude.

In this work we show that in the embryonic zebrafish, a model system for studying cardiovascular development [CIC08], answers to these two questions may be closed linked. Tuned occlusion – i.e. small differences in the resistance that vessels present to cells – ensures that red blood cells are uniformly partitioned between the finest vessels within the zebrafish trunk. Although zebrafish red blood cells have quite different morphologies from mammalian red blood cells, the matching in sizes of red blood cell and narrow vessel means that occlusive dynamics occur in the zebrafish network. Our experimental observations confirm previous measurements that red blood cells are uniformly partitioned between fine vessels [SUP03], yet in the absence of tuned occlusion, we demonstrate that the vessels closest to the zebrafish heart would receive 11-fold higher rates of flow that vessels furthest from the heart. In other words these vessels would act as hydraulic short-circuits. In further support of the hypothesis that occlusion is an adaptive feature of the network we calculate optimal occlusive dynamics – i.e. the distribution of occlusive feedbacks (the negative feedbacks each cell exerts on cells trying to enter the same vessel) that leads to the most uniform partitioning of red blood cells between the smallest vessels. The occlusive feedbacks within the real zebrafish conform very closely to this optimal distribution.

Microvascular networks have been postulated to be organized to minimize the cost of

transport (i.e. the total viscous dissipation associated with blood flow) [BCF00, BM07, Mur26b, KSM10]. Certainly in larger vessels within both the arterial and venous vascular network, vessel radii appear to be organized to minimize dissipation [She81, ZSW92]. Yet, our results suggest that rather than eliminating cellular congestion, fine vessels make use of it. As a direct demonstration of the tradeoff between minimizing the cost of transport and tuning occlusion to route red blood cells uniformly, we show that the optimal distribution of occlusive feedbacks that uniformizes red blood cell partitioning increases hydraulic dissipation in the network 11 fold compared with a network in which the smallest measured occlusive feedbacks occur within each vessel. Thus, taken together, our results advance a potential new optimization principle – uniform routing of red blood cells – that may underlie the organization of microvascular networks generally.

2.2 Materials and methods

2.2.1 Ethics statement

All animal experiments performed at Academia Sinica were approved by the Animal Use and Care Committee of Academia Sinica (protocol # 12-12-482). Zebrafish were bred and maintained at the UCLA Core Facility. Zebrafish experiments were performed in compliance with the Institutional Animal Care and Use Committees (IACUC) at the University of California, Los Angeles (UCLA) (under animal welfare assurance number A3196-01)

2.2.2 Imaging zebrafish trunk vessels and red blood cell movements

To measure the red blood cell fluxes in zebrafish trunk vascular network we cultured double transgenic Tg(fli1:GFP; gata1:ds-red) zebrafish embryos, in standard E3 medium supplemented with 0.05% methylene blue solution at 28.5 °C. In this transgenic fish line, fli1, a transcription factor associated with blood vessel morphogenesis is tagged with green fluorescent protein, causing the endothelial cells surrounding blood vessels to fluoresce green. Additionally, GATA-1, a transcription factor associated with erythrogenesis is tagged with red

fluorescent protein, so that the red blood cells traveling through the GFP-labelled network fluoresce red. Zebrafish larvae were sedated with neutralized 0.02% tricaine solution(Sigma, MO) and mounted in 1–2% low melting agarose (Sigma-Aldrich, MO) for imaging. Erythrocytes were imaged at 4 day post fertilization (dpf) under a fluorescent microscope (Zeiss, Germany) with 50 ms exposure time. To measure detailed geometry and occlusive feedback of zebrafish trunk network we re-imaged a single 4 dpf zebrafish. We measured vessel lengths and radii from GFP-images taken under 10× magnification using a Zyla sCMOS camera on a Zeiss Axio Imager A2 fluorescent microscope. To measure the flow velocity, the same scope was used to take images in the DsRed channel at time intervals of 0.078–0.107 sec. Red blood cells were manually tracked in image sequences using ImageJ [SAF12].

2.2.3 Mathematical modeling of occlusion and parameter estimation

Flow is laminar within each zebrafish microvessel[HKF03, JNE06]. The Womersley number [Ped03] that characterizes the importance of unsteadiness effects in time-dependent flow, which for a vessel of diameter d, carrying blood with kinematic viscosity ν, and with heart rate f, is given by $Wo = \sqrt{\frac{2\pi f d^2}{\nu}}$. Within the largest trunk vessels $d \approx 12\,\mu$m, the viscosity of whole blood is $\nu \approx 5 \times 10^{-6}$ m^2/s [WBP03], and the heart-rate is approximately $f = 2$ s^{-1}, so $Wo = 1.9 \times 10^{-2} \ll 1$, meaning that we may neglect pulsatile effects. Flow is uniform along each vessel, except within an entry region whose length is $\ell \ll Ud^2/\nu$ for a vessel of diameter d, through which blood travels at a speed U [Lig75]. Maximum blood velocities are on the order of 0.3 cm/s [MSS07], so using the diameter of the largest trunk vessels we obtain: $\ell \ll 0.3\,\mu$m. Since the entry region is much smaller than the typical vessel length, we treat the flow in each vessel as being uniform along its length. Putting these ingredients together, we find that the flow through each vessel is inversely proportional to the resistance of the vessel, and the resistance may be calculated using Stokes' equations (i.e. the equations for slow-creeping flows [Lig75]) from the geometry of the vessel and from the number of red blood cells that it contains. Mechanistic models to predict the motions of red blood cells through micro-vessels or through microfluidic channels with comparable diameters have been developed in previous works [SBM16, WTD07, PS05]. Throughout this

work we adopt a simple model for red blood cell occlusion in which the resistance of each vessel increases linearly with the number of red blood cells present. That is, if the number of red blood cells in a narrow vessel is given by n, then its resistance is given by an equation:

$$R(n) = R_0 + n\alpha_c \ . \tag{2.1}$$

where R_0 is the resistance of the vessel in the absence of red blood cells, i.e. is given by the Hagen–Poiseuille law relating the pressure drop and flow rate in a tube carrying viscous fluid, so that for a vessel of length ℓ and radius r: $R_0 = \frac{8\mu_{pl}\ell}{\pi r^4}$, where $\mu_{pl} \approx 1cP$ is the viscosity of the non-red blood cell component of the flood. Here the parameter α_c, which we call the occlusion strength in this chapter, gives the increase in vessel resistance per red blood cell. Equation (2.1) represents a form of non-Newtonian rheology, the deviation of resistance from simple viscous fluid. In particular, the apparent viscosity of blood, i.e. $R(n)\pi r^4/8\mu_{pl}\ell$, increases with hematocrit, i.e. with the concentration of red blood cells. Equation (2.1) can be derived from the micromechanical model of [SHP98]. Indeed any model in which the pressure drop across the red blood cell is proportional to the velocity of the cell will produce a relationship like Equation (2.1), and so identical equations are also used to model the traffic of droplets or particles through microfluidic channels [SA08, FO85]. In all of these models, α_c, which we may think of as the intrinsic resistance of a single cell [SA08, SHP98, SSO86, Poz05], depends on the specific details of how the movements of cells, droplets or particles along the walls of the capillary or channel are lubricated. α_c therefore depends on parameters that we can not measure experimentally, including the thickness and porosity of the glyocalyx that coats the endothelial wall of the capillary, as well as being sensitive to changes in vessel radius [PS05, SHP98] that are too small to be detected in light microscopy. It also depends upon the elastohydrodynamic deformation of both the cells and the capillary wall [WTD07]. Accordingly we treat α_c as a phenomenological constant, to be measured directly by fitting Equation (2.1) to real flow data. Specifically for each micro-vessel, we can measure both the velocity of flow within the vessel and the number of red blood cells that it contains. We note that due to the Fahraeus effect [FO85, AGP79] the velocity of red blood cells is in general larger than the flow velocity. However in human

vessels whose diameters are comparable relative to human red blood cells to the diameter of the zebrafish vessel relative to the zebrafish's red blood cells, the ratio of red blood cell velocity to whole blood velocity is less than 1.09 [AGP79]. Hence we approximate the flow velocity by the velocity of the red blood cell in this measurement. The pressure difference across each vessel varies in time due to the variable pressure within the aorta, and also, less predictably because, since the resistance of all vessels changes from moment to moment, there are pressure feedbacks across the entire network. But we assume that there is an overall average pressure drop across each vessel that is constant in time but changes from vessel to vessel. Under conditions of time-independent pressure drop, the velocity of cell movement, v, in each vessel will be inversely proportional to the vessel resistance $R(n)$. Thus Equation (2.1) predicts that a plot of $1/v$ against n will give a straight line, the slope of which can be used to calculate α_c. Here we used the modeled flows in the fine vessels where no red blood cell is present to determine the intercepts, which can be calculated by using Hagen–Poiseuille formula (see Section 2.3.2). By regressing $1/v$ against n for each micro-vessel we calculate the variation of occlusive effects through the network (see Appendix A for more details of the regression).

2.2.4 Incorporating occlusion into transport models

To study how varying occlusive effects between different microvessels may affect distribution of red blood cells, we incorporated Equation (2.1) into both continuum and discrete models of transport through the network.

For continuum level modeling, we assumed that the concentration of red blood cells was a constant, ρ, in each vessel. *Phase separation* of red blood cells can occur when flows divide at vessel junctions – that is red blood cells may split in different proportions than whole blood [PLC89] – but separation was not seen in our data (i.e. all Se vessels had the same average red blood cell concentration of number per volume), and cannot account for the uniformity of red blood cell flows, as we discuss in the Results section. Thus if the constant concentration (number/volume) of red blood cells is ρ, then a vessel of volume V is expected to contain

$n = \rho V$ cells. Once each vessel in the network has been assigned a resistance, then we can solve for the flows in the entire network, by applying Kirchoff's first law (conservation of flux) to calculate the pressure at each branching and fusion point, and then using the pressure difference across each vessel to calculate flows [Mur26b, Kro22, ZL77]. We discuss the geometry of the network and boundary conditions in the Results section.

Since each micro-vessel is so small, typically each vessel contains no more than one or two cells at a time (but occasionally 3–5 cells were present in a vessel, see Appendix A). For this reason we expected Poisson noise effects (i.e. fluctuations in the number of cells contained within each vessel) to influence red blood cell fluxes. We therefore built a discrete model, in which the trajectories of every single red blood cell traveling through the trunk network were directly simulated. Our discrete model is based on the droplet traffic model of [SA08]. Initially 990 cells are distributed uniformly through aorta according to measured zebrafish red blood cell concentrations [MQK03]. At each step we calculate the resistance for each capillary by Equation (2.1), and then use the hydraulic resistor network model to calculate the whole blood flow rates within each vessel. We then let cells travel according to the predicted whole blood velocity in their vessel. Again we assume that the velocity of cell matches with flow velocity in Se vessels. The diameter of the dorsal aorta (DA) is larger and this mismatch may be significant in the DA. Since the cell velocity depends linearly on the flow velocity we expect this effect to increase the cell fluxes in all Se vessels equally and to therefore influence the partitioning of cells only weakly. While for precise prediction of cell fluxes the inclusion of this velocity mismatch will be necessary, here we are developing a minimal model that singles out the effect of occlusive feedbacks, and hence we assume that the cell velocity is the same as flow velocity in all vessels. When a cell arrives at a node of the network; i.e. at a point where a vessel branches into two, which vessel it enters is determined randomly by a Bernoulli process; that is the probability of cell entering a vessel is determined by the flow rate ratio of the two vessels. We therefore suppress the Zweifach-Fung effect [Fun73]. The Zweifach–Fung effect characterizes the uneven distribution of red blood cells at a branching point, depending, amongst other factors, on stream lines at the branching point, and exibility of the cell [BAR08, SCK16, CHJ16]. Here we use a minimal model that neglects the Zweifach–Fung

effect because we see that only occlusive feedbacks can account for uniform partitioning of cells. Indeed, we found no difference between the red blood cell concentration concentration (number / unit volume) of vessels in the rostral Se artery ($2.88 \times 10^{-4} \pm 2.19 \times 10^{-4}$ $1/\mu\text{m}^3$) and in the caudal Se artery ($2.18 \times 10^{-4} \pm 2.72 \times 10^{-4}$ $1/\mu\text{m}^3$). Flows are then recomputed for the new distribution of cells. Cells that leave the network, i.e. reach the end of one of the vessels within the simulated part of the network are immediately reintroduced into the network via the aorta. For each combination of parameters, we simulated 1000 s of red blood cell movement, with a time step of 0.1 s. Using fluorescence microscopy to track red blood cells meant that our measurement frame rate was too low to directly measure cell velocities within the aorta. So we fit total inflow into the trunk via the aorta to match the mean flux across all fine vessels to the experimentally measured mean flux.

2.3 Results

2.3.1 Geometry of the zebrafish trunk microvasculature

The 4 day post fertilization zebrafish trunk vasculature is topologically simple. Oxygenated red blood cells (henceforth RBCs) flow into the zebrafish trunk via the dorsal aorta (DA) and return the heart via the posterior cardinal vein (PCV). The microvasculature consists of a series of parallel intersegmental vessels (Se) that, if the vasculature were laid flat, would span between the aorta and cardinal vein like the rungs of a ladder (Fig. 2.1A). Se are divided into intersegmental arteries (SeA) that connect to the aorta, and intersegmental veins (SeV) that connect to the posterior cardinal vein. SeA and SeV connect via another vessel called the Dorsal Longitudinal Anastomotic Vessel (DLAV), and in different parts of the DLAV, red blood cells flow toward the tail of the fish or toward its head. Red blood cells can enter the PCV by flowing along one of the SeA, through a section of the DLAV, and then along one of the SeV. Significantly, however, they can also flow directly from the DA into the PCV, since the two connect at the far end of both vessels in the tail of the fish.

The positions of SeAs and SeVs vary from embryo to embryo [IHW01]. In particular, SeVs

and SeAs do not strictly alternate their connections with the DLAV. To form a model that does not depend on any specific A-V pattern we choose to connect SeAs and SeVs directly in a pairwise manner (Fig. 2.1B), reducing the model to a bilaterally symmetric network in which no flow occurs in the DLAV (which can therefore be suppressed). Then we assign the same conductances for directly connected SeAs and SeVs and the same conductances for sections of DA as for the symmetric matching segments of PCV. Under these symmetry assumptions the pressures at the intersection of SeA and SeV is the same for each SeA/SeV pair, and we can shift this pressure to zero without affecting the calculations. Solving flows in this network reduces to solving flows in the lower half of Fig. 2.1B with fixed inflow in the beginning of the aorta and zero pressures at the intersections between SeAs and SeVs, and between DA and PCV at the tail.

2.3.2 Absence of occlusion produces uneven fluxes within the SeA

As a first step we calculated the RBC flux in intersegmental arteries (SeA) with no occlusion or untuned occlusive effects and compared to experimental measurements. That is we approximated the resistance of each vessel using (2.1) with $\alpha_c = 0$ and treating the blood as a continuous phase, so that μ_{pl} replaced by μ_{wb}, the viscosity of whole blood ($\mu_{wb} \approx 5$ cP in zebrafish [WBP03]). This reduced model serves as a motivation and readers interested in the full model may skip to Section 2.3.4. We measured the lengths of each vessel directly from fli1a-EGFP images. SeAs were all assigned the same radius (2.9 μm), while because the DA tapers from the head to the tail, we independently measured DA radii between each SeA (see Appendix A). Although ultimately tuned variation in SeA radii will be one way to explain changes in occlusive feedbacks, these variations strongly affect the parameter α_c in Equation (2.1) but have little effect on R_0. To model flows without feedbacks we can therefore neglect SeA radius variations. We focus on the arterial half of the network made up of SeA and DA vessels. We identify the vertices in this network, i.e. the points at which vessel branch or fuse, as points $i = 1, 2, \ldots n$, with respective pressures p_i (Fig. 2.1B). The number of SeAs, n, increases as the fish grows: for the 4 dpf zebrafish in our experiments n ranges from 9 to 13. For definiteness in modeling, we assume $n = 12$. If vertices i and

j are connected by a vessel, with resistance R_{ij}, then the total flow of blood along this vessel will be $(p_i - p_j)/R_{ij}$. Solving for the flows in the network is equivalent to finding the pressures $\{p_i\}$. For the zebrafish cardiovascular network we labeled vertices along the DA as $i = 1, 2, \ldots, n$. A vertex, $i = n+1$, represents the end of the DA in the tail of the zebrafish, where it connects directly to the PCV, and we label the vertices where the SeA meet the DLAV as $i = n+2, n+3, \ldots 2n+1$. At vertices $i = n+1, \ldots 2n+1$, our symmetry boundary conditions require that $p_i = \text{const.}$, and we set arbitrarily the value of this constant to be 0. Thus only the pressures $\{p_i : i = 1, \ldots n\}$ need to be determined. We find these pressures by applying Kirchoff's First Law (conservation of flux), at each point where the pressure is determined, i.e. $\sum_{j \in n(i)} (p_i - p_j)/R_{ij} = 0$, except at $i = 1$ (the vertex closest to the heart). At this vertex, $\sum_{j \in n(1)} (p_1 - p_j)/R_{1j} = F$, where F is the total supply of blood to the trunk which is fit to real data (see Section 2.2). All summations are taken over the neighbor set, $n(i)$, i.e. over all vertices that are linked to i.

The model of the zebrafish trunk microvasculature as an hydraulic resistor network (neglecting occlusive effects) follows many previous capillary network models (see e.g. [Mur26b, Kro22, ZL77]). The equations are formally identical to those for an electrical resistor network, with pressures replacing voltages, and flow rates replacing currents. Just as placing a wire across the terminals of a battery in an electrical resistor network will short circuit the network (i.e. divert current from higher resistance paths), the first SeA is predicted to receive a larger-than-even share of the blood flow from the zebrafish trunk, with flow rates decreasing exponentially rapidly with distance from the heart. In total there is a predicted 11-fold difference between the flows through the first and last SeA (Fig. 2.1C).

A simplified resistor network model that treats each SeA as having the same resistance, and assigns same resistances to each segment of DA between SeAs (i.e. ignores DA taper) quantitatively reproduces the exponential decay. To build the simplified model we assume that each segment of the DA has the same hydraulic resistance, and that each SeA has the same resistance. Using the measured mean radii and lengths, each DA has the same conductance, written as: $\kappa_1 = 1/R_1 = 9.4 \times 10^5$ μm^{4}s/g, while all Se vessels have the same conductance, written as: $\kappa_2 = 1/R_2 = 3.9 \times 10^4$ μm^{4}s/g. Then conservation of flow at vertex

$i = 2, \ldots, n$ gives:

$$-\kappa_1 p_{i-1} + (2\kappa_1 + \kappa_2)p_i - \kappa_1 p_{i+1} = 0 \ , \tag{2.2}$$

This is a second order recurrence equation with constant coefficients. Its general solution is:

$$p_i = C_+ \xi_+^i + C_- \xi_-^i, \tag{2.3}$$

where $\xi_\pm$ are the roots of the auxiliary polynomial $\xi^2 - (2 + \lambda)\xi + 1 = 0$, in which there is a single dimensionless parameter: $\lambda = \frac{\kappa_2}{\kappa_1} = 0.04$. This equation has two roots, with $\xi_+ > 1$ and $\xi_- < 1$. In general C_+ and C_- must both be non-zero to satisfy our boundary conditions (namely $p_{n+1} = 0$ and $F = \kappa_2 p_1 + \kappa_1(p_1 - p_2)$). However the two components give rise to exponentially growing and decaying pressures respectively. Typically the first term will negligible, except potentially in a small boundary layer region consisting of the vertices in the tail. Therefore over most vertices $p_i \sim C_- \xi_-^i$, i.e. the pressure decays exponentially with distance from the heart, causing flows in the SeAs to decay exponentially as a result. For the real zebrafish network: $\xi_- = 0.81$. Despite the simplification in geometry, the analytic formula agrees quite well with the solution to the full system of linear equations (compare gray and black curves in Fig. 2.1C). Additionally, we note that for any $\lambda > 0$, it is impossible to organize an auxiliary polynomial without having one root $\xi_- < 1$, so exponential decay in fluxes is an inescapable feature of the ladder-like geometry of the trunk vasculature.

Although embryonic tissues receive oxygen primarily by diffusion through the skin [PB96, RD09], vascular transport of oxygen becomes essential to embryo development after 2.5 weeks[WSD95]. So we expect that a zebrafish with the large predicted difference in fluxes between trunk vessels would be disadvantaged. But because oxygen can diffuse through the zebrafish tissues, we first verified that the differences in fluxes predicted by the model lacking occlusive feedbacks would actually lead to differences in oxygenation in the trunk tissues. To do this, we modeled oxygen diffusion through the trunk by a reaction-diffusion equation, using the formulation and oxygen consumption coefficients derived by [KBL03], and treating the vessels as oxygen sources (Fig. 2.1D, and see Appendix A for details of the model). Note that our model includes only the contribution of oxygen perfusion from the blood to trunk oxygenation. For a real zebrafish at 4 dpf, these uneven oxygen levels would be compensated

for by diffusion through the skin. However, our model shows that diffusion of oxygen within the zebrafish trunk can not compensate even at 4 dpf for uneven flows within the Se vessels.

2.3.3 Red blood cell flows are uniform among trunk vessels

In contrast with the resistor network model, which predicts that the first Se vessel short circuits the network, measured RBC fluxes are nearly uniform between Se-vessels in living zebrafish. We tracked fluorescently tagged red blood cells moving through each of the 9–13 SeAs within 6 living, sedated, zebrafish (see Section 2.2), over a total time interval of 26s per SeA. Fluxes in individual vessels varied greatly in time, due to the rapid change of blood pressures within the DA over the zebrafish cardiac cycle [MSS07] and likely also due to non-linear dynamics of the cells themselves within vessels [FYS12], so the variability of flow rates was large for each vessel. However, mean fluxes varied little from vessel to vessel (Fig. 2.2A). Each embryo exhibited variable RBC fluxes throughout the trunk. However the envelope of the lines of best fit for all six fish showed no consistent differences in RBC fluxes between first and last Se. Specifically from the six sets of zebrafish data we used bootstrapping method (generating replicate measurements for each Se vessel from the measured mean and standard deviation over all six fish) to estimate regression statistics. The gray envelope in Fig. 2.2A shows the 95% confidence interval on all regressions thereby generated. We found that over all regressions $m = 0.012 \pm 0.032$ (mean $\pm$ standard deviation), showing no statistically changes in RBC flux from vessel to vessel.

2.3.4 Occlusive feedbacks with variable strengths determine red blood cell fluxes

There are two major ingredients missing from the hydraulic resistor network model that could explain the anomalies between the predictions of that model and the real zebrafish flow rate data: phase separation of red blood cells and occlusive feedbacks effects [PSG90, PLC89]. Separation occurs because red blood cells do not divide in the same ratios as whole blood when blood vessels branch: When a red blood cell passes through a junction at which a vessel branches into two daughter vessels of different sizes, it is more likely to

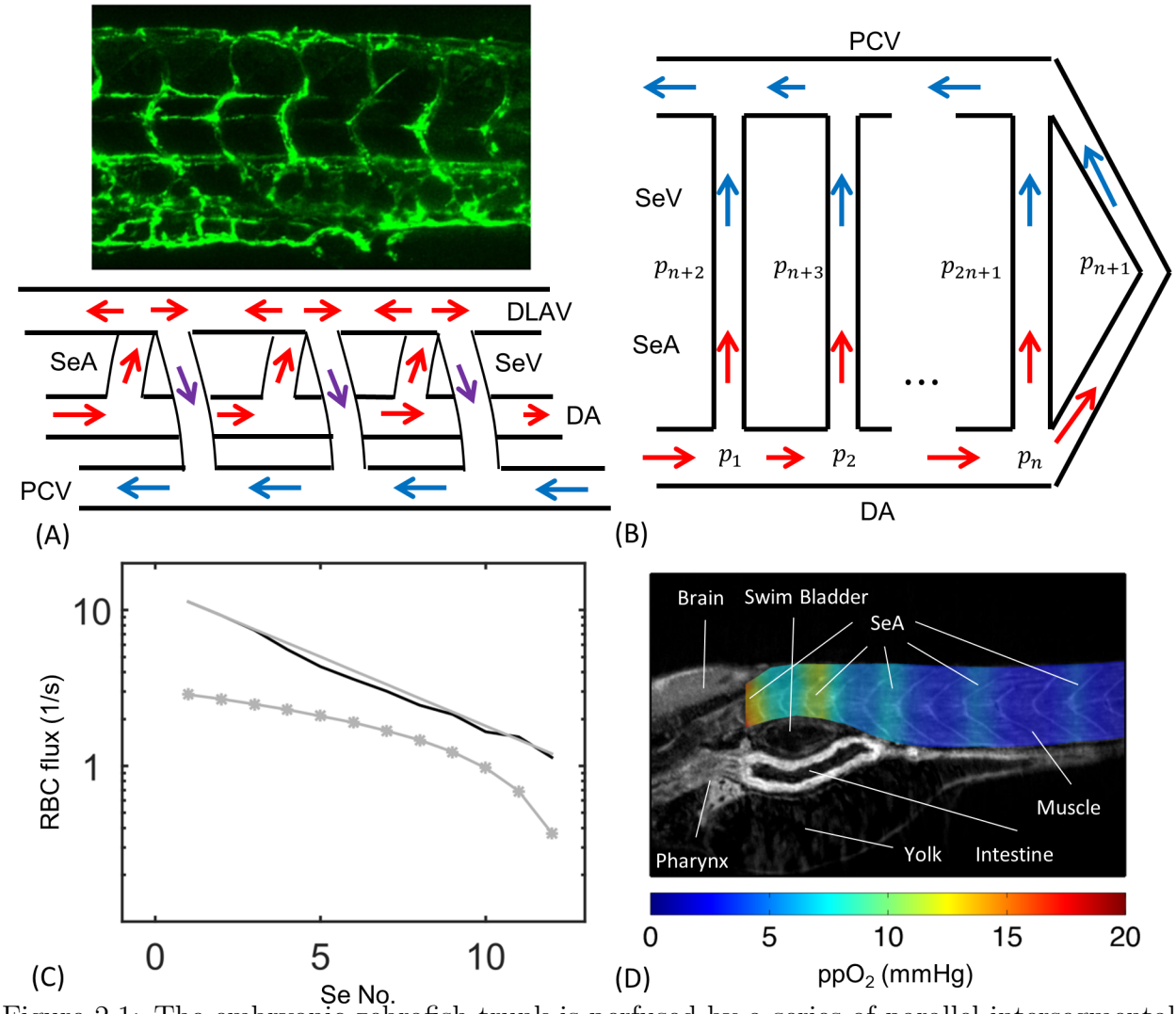

Figure 2.1: The embryonic zebrafish trunk is perfused by a series of parallel intersegmental arteries (SeAs). Hydraulic models for the network predict that the first of these SeA will short circuit flow through the trunk. (A) 4 day post-fertilization zebrafish embryo trunk network and wiring diagram showing PCV, DA and Se vessels in which SeA connect directly to SeV. (B) Representation of the same network as a set of hydraulic resistors. (C) A resistor network model predicts that cell fluxes decrease exponentially with distance from the heart (Black curve: numerical solution using real geometric parameters, Gray line: asymptotic model. For these two curves flow rates are multiplied by the concentration of red blood cell $\rho = 0.003\ \mu m^{-3}$ measured in [MQK03]). By contrast an occlusive feedback model incorporating uniform occlusion strength $\alpha_c = 1.01 \times 10^{-6} g/\mu m^4 s$ did not lead to more uniform distribution of red blood cell fluxes between vessels (Gray stars). Se vessels with smaller numberings are closer to the heart. (D) Anisotropic fluxes produce uneven oxygen perfusion within the trunk. Simulation results are superimposed on a zebrafish CT image reproduced from [SMC12], which was permitted under CC BY license by the authors.

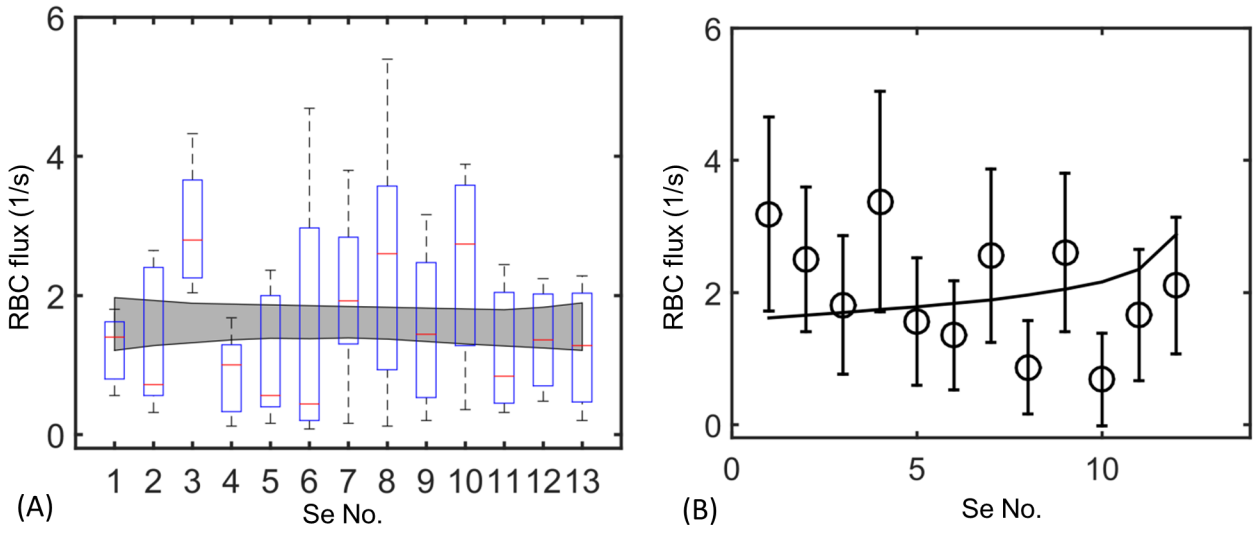

Figure 2.2: Measured cell fluxes in real zebrafish embryos are almost uniform across all microvessels. (A) Measured fluxes in 6 4dpf zebrafish. Box-and-whisker plots show the mean measured fluxes for all 6 zebrafish, while the gray region is the envelope produced by bootstrapped regressions of flux against Se No., which is a numbering of Se vessels starting from the rostral trunk. (B) A model incorporating tuned occlusion strength (black curve) agrees well with the data from a single 4dpf zebrafish (black circles), see Section 2.3. Bars: standard deviation of flux.

enter the larger daughter vessel than would be expected based on the ratio of fluxes in the two daughter vessels. Phase separation cannot explain the uniform distribution of red blood cells seen across real zebrafish microvessels: to correct for an 11-fold difference in flow rates between first and last Se vessels, there would need to be an 11-fold increase in hematocrit between these vessels, in the absence of occlusive effects (since then hematocrit must increase exponentially to compensate for exponentially decreasing flow rates). This was not observed in our experiments. Indeed Pries et al. [PS05] explicitly fit measurements of red blood cell fluxes at the branch points of blood vessels, and parameterized the amount of phase separation that occurred. When we applied their model to the zebrafish microvasculature, only minute variations in hematocrit were predicted between different SeAs (see Appendix A).

By contrast, we observed large feedback effects within the SeA, i.e. the presence of a red blood cell reduces the flow in the vessel and hence the entering probability of the next cell. We individually tracked red blood cells in a single 4dpf zebrafish, and plotted the inter-entry intervals, i.e. the times between consecutive red blood cells entering each vessel, condensing data from all SeAs since all vessels have the same approximate rate of blood cell entry (see Fig. 2.3). In the absence of feedbacks, we would expect the inter-entry times to be distributed randomly, i.e. as an exponential random variable. Our red blood cell tracking shows that a single red blood cell passes through an SeA in a mean time of 0.3s. Inter-cell entry intervals larger than 0.3s (i.e. cell entries into unoccupied SeAs) were distributed exponentially (see the inset to Fig. 2.3). However, inter-entry intervals less than 0.3s were not exponentially distributed, and we saw far fewer cells entering vessels less than 0.3s apart (i.e. while the vessels were already occupied by other cells) than would be expected based on the exponential distribution (Fig. 2.3, main panel). In fact we found that inter-entry intervals less than 0.3s were approximately uniformly distributed. These observations are suggestive of a negative feedback mechanism, whereby entry of a red blood cell into an SeA reduces for some time afterward the probability of another red blood cell entering the same SeA.

We tested for statistical support for the presence of negative feedback by two methods.

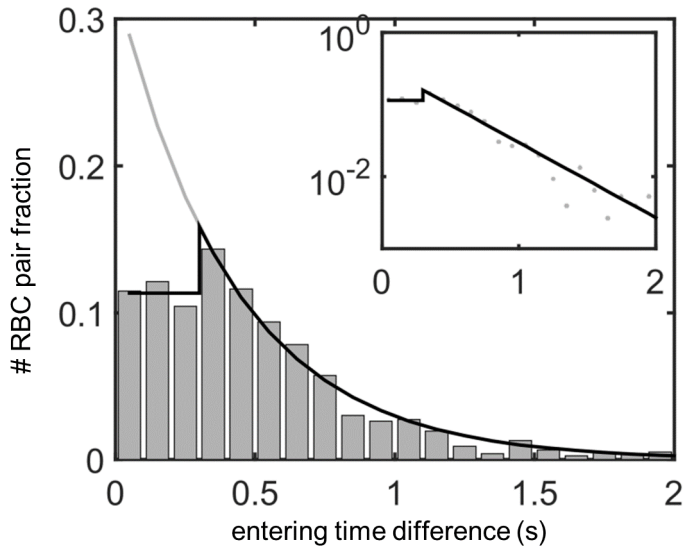

Figure 2.3: Red flood cell flows in the real intersegmental artery network are affected by feedbacks, as shown by a significantly lower fraction of red blood cells entering the same vessel within 0.3s of each other. Shown: Distribution of inter-entry times for cells entering all 12 SeAs. In the absence of feedbacks, inter-entry times will be exponentially distributed (black curve), while real inter-entry times follow an exponential distribution only when cells enter the vessel more than 0.3s apart, and have uniform distribution when cells enter the vessel within 0.3s of each other (black star curve). Inset: The semi-log plot of the linear-exponential distribution (black curve) fits well to the data (gray dots) above 0.3s, showing the exponential distribution when the inter-entry time is long enough for the first cell to leave the vessel. We bin the inter-entry time intervals into $0.1s$ bins which is the typical time resolution of our videos.

First, we extrapolated the exponential fit for time intervals greater than 0.3s to estimate the number of cells that should enter the SeA between 0 and 0.3s, if cell entries into SeA were independent events. For the zebrafish trunk data this amounted to 533 cell entries, compared to the 261 actually observed, and the difference in statistically significant by the Fisher's exact test ($p = 3.9 \times 10^{-22}$ against independence). Secondly, we fit the distribution of cell entry times directly, to compare an independent model with an exponential probability density function (pdf), with a model in which the feedbacks were modeled by a composite pdf, with uniform probabilities for inter-cell entry intervals less than 0.3s, and an exponential pdf for cell entry intervals greater than 0.3s. The Akaike Information Criterion score corrected for small samples (AICc) [HST98] for the composite pdf was 4.02×10^3, whereas the AICc for the pdf assuming independence was 4.07×10^3, supporting the inclusion of feedback effects.

In mammals red blood cells must squeeze through narrow capillaries. Passage through these narrow vessels is facilitated by specific cellular adaptations – cells are un-nucleated, and have a biconcave shape, assisting cell deformation. By contrast zebrafish red blood cells are almost spherical and are nucleated. However, since the diameters of SeAs are closely comparable to red blood cell diameters (both 6 μm), we speculated that zebrafish red blood cells may also fit tightly within the SeAs. We directly measured these dynamics by measuring the dependence of the velocity within a SeA upon the number of red blood cells contained in the vessel (see Section 2.2). Velocities within each SeA are affected by the phase of the cardiac cycle as well as by nonlinear cell-cell and cell-wall dynamics [SHP01, SUS80], so there is large variability in these velocities, and pressures are also affected by changes in conductances throughout the network (Fig. 2.4A). However, in each vessel we found that $1/v$ increased linearly with the number of cells, n, consistent with the model for occlusion in Equation (2.1). In physical terms, when a cell travels through a vessel, it almost blocks the vessel. Because a large pressure difference must be maintained over the cell to push it forward through the SeA, flow within the vessel slows, so that fewer red blood cells enter a vessel once it contains a cell.

We measured the occlusive effect within each SeA, i.e. the parameter α_c in Equation (2.1) by fitting the slope of the graph of $1/v$ against n (see Fig. 2.4A). The intercept of the

graph is given by the speed within the SeA when it contains no red blood cells. We get that speed from the model of flow without occlusive feedbacks, described above, so there is only one free parameter to be estimated for each SeA. Equation (2.1) represents a form of non-Newtonian rheology, since it gives that the resistance of each vessel increases as hematocrit (i.e. n) increases. The parameter α_c represents the intrinsic resistance per cell [SA08, SHP98, SSO86, Poz05], and it depends on the relative size of the cell and SeA (i.e. how tightly the red blood cell must be squeezed to travel along the vessel), cellular deformation due to elastohydrodynamic effects [WTD07], as well as upon the surface chemistry of both. In particular, [SHP98] built a physically informed model of cells moving through a narrow vessel, including both cell deformation, and interactions between the cell and the vessel glycocalyx: a polymer brush that covers and lubricates the endothelial lining of the vessel. They found that α_c is highly sensitive to biophysical parameters: the thickness of the glycocalyx layer as well as its porosity (i.e. to the concentration of polymer), as well as to small changes in vessel radius.

To assay the potential for controllability for the occlusive effect, α_c, we measured α_c independently in each of the twelve SeAs, in all cases by fitting the data for the dependence of $1/v$ upon n (see Appendix A for more details of the fit). The experimentally measured occlusion strength decreased from first to last SeA (Fig. 2.4B), over a range of $\alpha_c = 3.0 \times 10^{-7}$–$2.8 \times 10^{-5}$ $g/\mu m^4 s$. In physical terms, red blood cells occlude closer vessels to the heart more than distal vessels. These values are consistent with the range given in Secomb et al.'s model [SHP98] in which α_c could range from $\alpha_c = 1.8 \times 10^{-7}$ to 1.6×10^{-5} $g/\mu m^4 s$. Our measurement of α_c also agrees with an earlier theoretical model of Secomb et al.'s which did not consider glycocalyx ($\alpha_c = 4.7 \times 10^{-7}$–$3.8 \times 10^{-6}$ $g/\mu m^4 s$ [SSO86]), a numerical model of Pozrikidis' which simulated the time course of cell deformation ($\alpha_c = 2.4 \times 10^{-7}$–$1.1 \times 10^{-6}$ $g/\mu m^4 s$ [Poz05], as well as an experimental fit to earlier data ($\alpha_c = 1.4 \times 10^{-7}$ $g/\mu m^4 s$ [FO85])). Note however, that the micromechanical and numerical models of [SHP98, SSO86, Poz05] was created for mammalian red blood cells in capillaries and must be applied with caution here; indeed glycocalyx parameters have not been measured in zebrafish. Although the differences between zebrafish and mammalian RBCs mean that we must allow that the

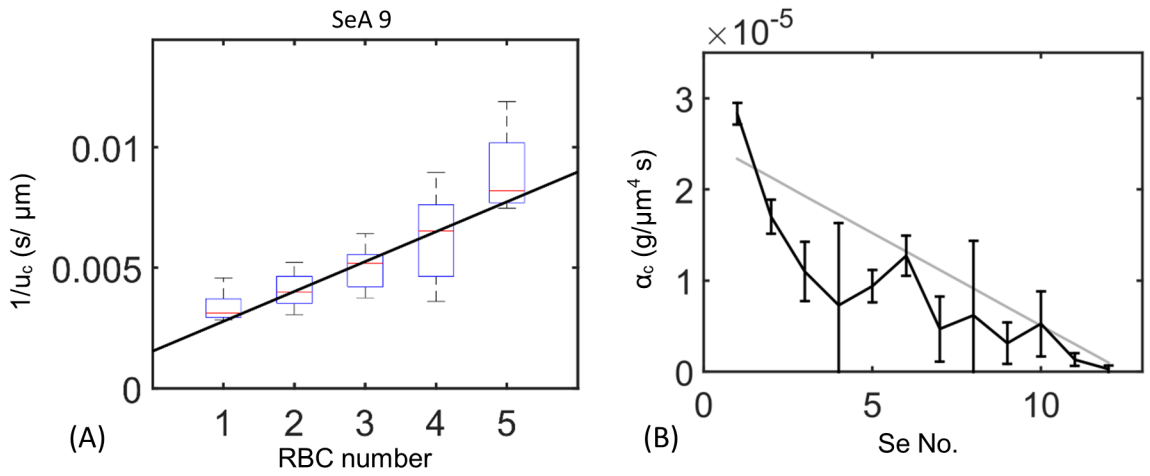

Figure 2.4: Occlusion of SeAs by cells feeds back onto the flow through the SeA. (A) Equation 2.1 predicts that the reciprocal of cell velocity increases linearly with the number of cells in each Se vessel. Displayed: data from the 9th Se artery (Boxplot) and regression to determine feedback per cell, α_c (curve). The y-intercept is determined from the theoretical plasma velocity in a network with no cells. For data from other Se arteries see Appendix A. (B) Measured α_c values decrease from first to last Se artery. Gray line: linear regression of α_c against Se vessel index. Bars: 95% confidence intervals calculated by those of linear regressions. Se vessels with smaller numberings are closer to the heart.

parameters controlling occlusive feedback α_c may be different in zebrafish than in mammalian vessels, the mammalian data generally support the possibility of tuning feedbacks over a large range of values. The intrinsic resistance α_c depends on many factors, including cell velocity, thickness of glycocalyx layer, and the deformation of the cell. Here we focus on the effect of α_c on the partitioning of the cells rather than the detailed mechanism that causes the variation.

2.3.5 Tuning occlusive effects between different micro-vessels uniformly partitions red blood cells

We simulated around 17 min of red blood cell flow through the zebrafish vascular network, assuming the same occlusive effect for every microvessel, using a discrete model in which

every red blood cell trajectory was tracked and in which vessel resistances were modeled using Equation (2.1) (see Section 2.2) using the same occlusive feedback parameter ($\alpha_c = 1.01 \times 10^{-6} g/\mu m^4 s$) for each vessel. The model continued to predict that red blood cell fluxes within vessels decrease exponentially with distance from the heart (Fig. 2.1C). This can be rationalized as follows: If α_c is identical between intersegmental vessels, and phase separation is assumed to be negligible, then the model predicts that the resistance of each vessel will increase on average from the value given by the Hagen–Poiseuille law by $\alpha_c \cdot \mathrm{Hct} \cdot V/V_c$, where V is the volume of the vessel, V_c is the volume of a single cell and Hct is the hematocrit. The approximate model derived in Section 2.3.2 demonstrates that variation in SeA length from head to tail of the zebrafish contribute very little to partitioning of red blood cell fluxes between SeAs, so changing the resistance of each vessel by an amount simply proportional to its length, will similarly not prevent exponential decay of red blood cell fluxes.

The potential effect size of including occlusive feedbacks is much larger than the effect of phase separation: predicted red blood cell flux decreased by a factor of more than 7 in the phase separation model (see Appendix A). We therefore hypothesized that varying occlusive effects between different SeAs may uniformly distribute red blood cells through the network. To probe how variations in occlusive feedback could be used to control the distribution of red blood cells, we studied a reduced model of the vascular network (readers who are mainly interested in simulation results may skip this analysis by going straight to Section 2.3.6). Specifically, we built a mean-field model for the flows in a model network including only the first and last SeAs, as well as the direct connection between the DA and PCVs (the labeling of vessels and branching points is shown in Fig. 2.5A). In each vessel the cells were assumed to be well-mixed and cell fluxes are divided in proportion to flow rates at all nodes. Then the hematocrit will be the same in all vessels. For simplicity we express our equations in terms of the concentration of red blood cells (number / volume), ρ, rather than the hematocrit. ρ and hematocrit (Hct) are simply related by $\rho = \mathrm{Hct}/V_c$ where V_c is the volume of a cell. Let R_i be the modified resistance of the ith vessel according to Equation (2.1). Then by applying Kirchoff's first law at the branching points at which first and second Se vessel branch off

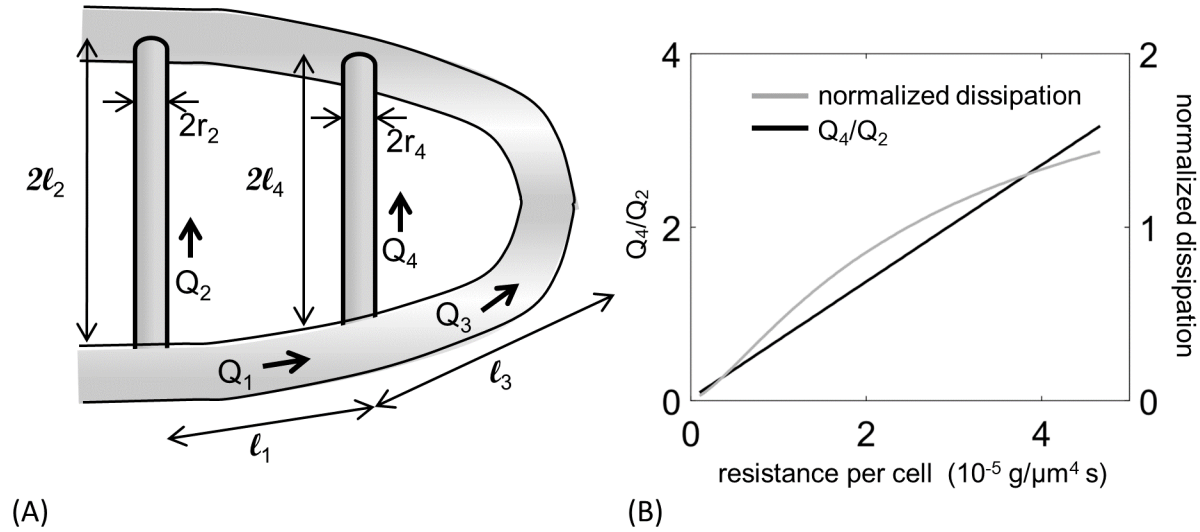

Figure 2.5: A reduced vascular network model shows that occlusive effects need to be varied between SeAs, and exposes trade-offs between flow uniformity and transport efficiency. (A) Diagram of the reduced model of the network showing vessel lengths l_i, fluxes Q_i, and radii r_i. (B) Increasing the occlusion strength α_2 increases flux uniformity, measured by the ratio of fluxes in the last and the first Se (black curve), but also increases dissipation (gray curve), if the total flux through both Se vessels is maintained.

from the aorta, we obtain the pressures at these points, i.e. p_1 and p_2:

$$F = \frac{p_1 - p_2}{R_1} + \frac{p_1}{R_2}, \frac{p_1 - p_2}{R_1} = \frac{p_2}{R_3} + \frac{p_2}{R_4}, \tag{2.4}$$

Here F is the total flux of blood into the network, and we can solve Equations (2.4) by linear algebra (see Appendix A). Of particular interest is is the ratio of fluxes in the two Se, which measures how uniformly the different vessels are kept supplied with cells:

$$\frac{Q_4}{Q_2} = \frac{R_{2_0} + V_2\rho\alpha_2}{R_{4_0} + V_4\rho\alpha_4}\left(1 + \frac{R_1}{R_3} + \frac{R_1}{R_4 + V_4\rho\alpha_4}\right)^{-1} \tag{2.5}$$

Here α_2, α_4 are respectively the values of α_c in the first and last SeA, R_{2_0}, R_{4_0} are the resistances of the two SeAs in the absence of red blood cell occlusion, and V_i is the volume of vessel i. Most of the parameters in Equation (2.5) are tightly constrained: the dimensions of the two Se vessels are similar (in fact $R_{2_0} \approx 2R_{4_0}$ and $V_2 \approx 2V_4$), moreover, since the vessel network extends during development and supplies the tail fin in adult zebrafish[PEM09,

BBW06], the aorta must maintain approximately the same radius along its length, leading to $R_1 \approx 11R_3$. Thus the second factor of Equation (2.5) $\left(1 + \frac{R_1}{R_3} + \frac{R_1}{R_4+V_4\rho\alpha_4}\right)^{-1}$ has an upper bound $\frac{1}{12}$. Therefore the only parameters that can be used to increase Q_4/Q_2 (i.e. eliminate short-circuiting of the network by the first SeA) are the relative sizes of α_2 and α_4. Q_4/Q_2 is largest if $\alpha_2 \gg \alpha_4$, i.e. if occlusion effects are stronger in the first SeA. Thus uniform flow requires stronger occlusion in vessels close to the heart, consistent with experimental observations in real zebrafish (Fig. 2.4B).

However our reduced model also shows that varying occlusion strengths between vessels creates trade-offs between uniformity and the transport efficiency, measured by the dissipation:

$$\begin{aligned} D_{\text{network}} = \; & \tfrac{8\mu_{wb}}{\pi r_a^4}(\ell_1 Q_1^2 + \ell_3 Q_3^2) + \tfrac{8\mu_{pl}}{\pi r_c^4}(\ell_2 Q_2^2 + \ell_4 Q_4^2) \\ & + \rho(Q_2^2 V_2 \alpha_2 + Q_4^2 V_4 \alpha_4). \end{aligned} \tag{2.6}$$

(See Appendix A for derivation). Here ℓ_i is the length of the ith vessel, r_a is the radius of the DA, and r_c is the radius of the Se vessels. To compare equivalent networks as we vary α_2 we also vary F, the total flow into the trunk, to keep the total flux through the pair of Se vessels $(Q_2 + Q_4)$ constant. Dissipation in the thin layers of fluid surrounding each RBC dominates D_{network}, so as α_2 increases D_{network} increases. The highest ratios of Q_4/Q_2 are therefore also the most dissipative networks (Fig. 2.5B).

2.3.6 Observed variation in occlusive effects optimizes uniform distribution of red blood cells

We modified our simulation from Section 2.3.5 to incorporate the observed variations in occlusive effects; i.e. using the different measured values of α_c in each vessel. We used the regressed data (gray line in Fig. 2.4B) to capture the decreasing trend of α_c from head to tail. When vessels were assigned the experimentally measured values of α_c, red blood cells became uniformly distributed between SeAs, and matched closely to the real flow observations (see Fig. 2.2A, B).

Are the measured variations in occlusive effects really evidence of adaptive tuning of

the zebrafish cardiovascular network, or could they arise from incidental changes caused for example by the different ages of vessels at different distances along the trunk? New SeAs are progressively added to the trunk at the tail of the zebrafish as the trunk elongates, and we wanted to evaluate the alternate hypothesis that the younger vessels farther from the heart had lower occlusive effects simply because they have a thinner glycocalyx coating, or else because structural adaptation of vessels to the flows through them may tend to reduce vessel radii over time [PSG98]. Although neither alternate explanation can be totally ruled out, we were able to test how close the observed distribution of occlusive effects is to one that optimizes the uniform partitioning of red blood cell flows between vessels. Specifically, we ran discrete cell simulations of flow within the network for different distributions of occlusive effects: that is, we varied $\Delta\alpha_c$, defined to be the difference in α_c between the first and last SeAs, assuming a linear variation of α_c in the intermediate vessels. For each model network, we calculated the coefficient of variation (CV) in the red blood cell flux, i.e. the standard deviation in red blood cell flow rate over all vessels, normalized by the mean flow rate. Smaller values of CV correspond to a more uniform distribution of red blood cell flows. Using discrete cell simulations, i.e. tracking every cell trajectory, produces more accurate estimates of red blood cell fluxes in principle than the continuum modeling from Section 2.3.5, because cell number fluctuations within each SeA are comparable to the mean number of cells. Since the change in resistance of a vessel depends on the number of cells in the vessel according to Equation (2.1), the distribution of red blood cell flows for a given distribution of occlusive effects depends on hematocrit. Accordingly, we varied both hematocrit and occlusive effect distributions independently in our simulations. We found for any fixed hematocrit, near uniform flux (CV close to 0) can be achieved only over a narrow range of $\Delta\alpha_c$ (Fig. 2.6A). Too little difference in intrinsic resistance between first and last SeAs, and the first SeA short-circuits the network, as discussed in Section 2.3.2. But too large a difference in occlusive effects can have the opposite effect, leading to the vessels furthest from the heart receiving more flow than vessels closest to the heart. The optimal distribution the occlusive effects is realized along a single curve in $(\Delta\alpha_c, \rho)$ space. We found that the observed occlusion effect distribution is close to the optimal value for the

real zebrafish hematocrit [MQK03] (Fig. 2.6A).

2.4 Acknowledgments

We thank the Taiwan Zebrafish Core Facilities at Academia Sinica (TZCAS) and at NHRI (TZCF) for providing Tg(gata1:dsRed; fli1a:EGFP) transgenic fish, and Jérémy Lévéque for performing early calculations for Figure 1C.

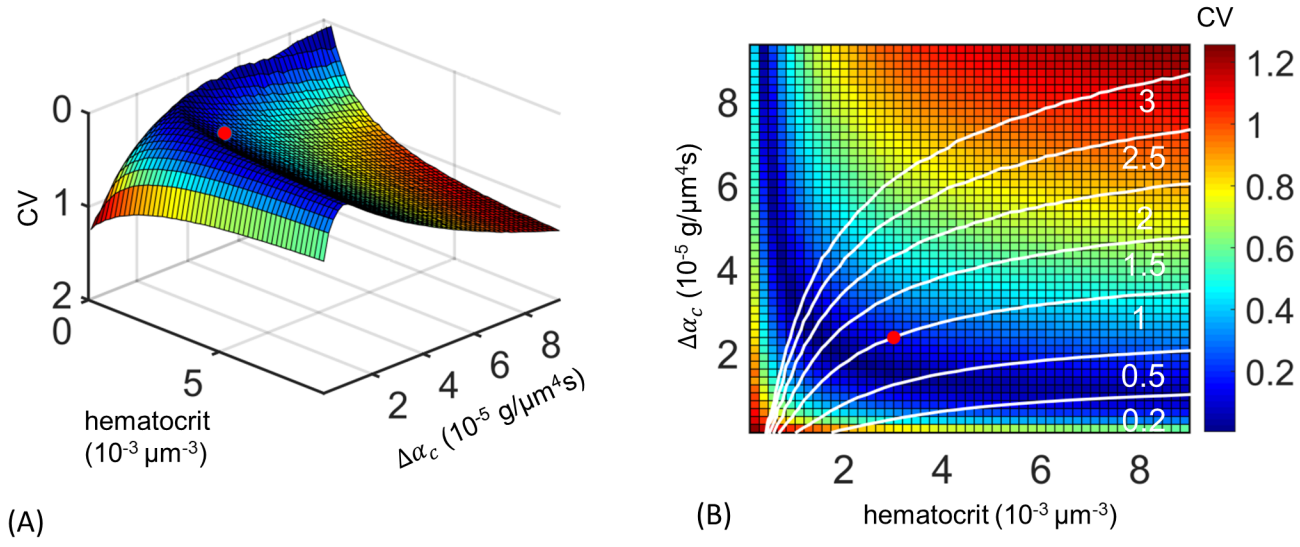

Figure 2.6: Tuned occlusion strengths uniformly distribute flow across different Se vessels. (A) Dependence of flux uniformity upon controllable parameters is explored by allowing blood cell concentration, ρ, and difference in occlusive effects between first and last Se vessel, $\Delta\alpha_c$, to vary independently and computing the coefficient of variation (CV) for flow through all Se vessels. Flux uniformity is achieved only within a narrow manifold of values of blood cell concentrations and occlusive effect differences. The empirical values (red dot) lie close to this optimal manifold. (B) Higher uniformity can be achieved if blood cell concentration is decreased (moving leftward from the red dot) but at the cost of increasing dissipation. Transport costs are reduced if $\Delta\alpha_c$ is decreased (moving downward), and can be reduced by 11-fold if there is no difference occlusive effect between different Se arteries but at the cost of reducing uniformity of RBC fluxes. Colors show CV values from (A) and white curves show level sets of dissipation; the dissipation is normalized by its value in the real zebrafish.

CHAPTER 3

Minimal transport networks with general boundary conditions

This chapter was based on: Shyr-Shea Chang and Marcus Roper. "Minimal transport networks with general boundary conditions." *SIAM Journal on Applied Mathematics*, 78(3), 1511–1535, 2018.

3.1 Introduction

Organisms across the kingdoms of life; including plants, animals, fungi, and water molds rely on vascular networks to transport fluids, nutrients or cellular materials [RUM11]. In vertebrate animals, a cardiovascular network transports oxygenated blood from the heart to tissues throughout the body, and returns waste gases to the heart and lungs. Distruption of this network even at the level of finest vessels, including the systemic microvessel degradation associated with diabetes mellitus, or acute damage associated with traumatic brain injury, has long term irreparable health consequences. Accordingly parallel experimental efforts have targeted the same goal of complete mapping of microvascular networks [BTK13, WHY14, KBS15]. Yet interpreting these data streams is held back by lack of information on the organizing principles underlying the mapped networks.

One principle that has been used to dissect these networks is Murray's law (Murray, 1926 [Mur26b]). Murray's law states that if a network made up of hydraulic conduits minimizes a total cost made up of the sum of the total dissipation and of the material used to build the network, then the radius of each conduit within the network is proportional to the cube root of the flow that it carries. Murray's law has been verified by studies on plant

and mammalian vascular networks ([She81, MSA03, TNQ01], but also see [She81] for a discussion of networks that do not apparently obey Murray's law). This result draws upon several assumptions that we will systematically analyze in this chapter, so we present a brief derivation in Section 3.2.1. A key part of this derivation is that changing the radius of the vessel does not affect the flows passing through it. In other words, flows and radii can be treated as independent variables. However the flows within a network generally depend on the conductances within the network – so changing radii of vessels within the network may alter the flows. Accordingly it is not obvious that when the feedback between vessel radius and flow is considered, i.e. when conduits are considered assembled within a network, Murray's law will continue to hold, or that a dissipation minimizing network configuration actually exists.

Durand [Dur07] studied optimization of dissipation on networks in which multiple sources were linked to multiple edges with arbitrarily complex network of edges and vertices. A prior set of edges can be assigned (potentially including straightline paths between every pair of sources and or sinks), and one searches for the network that uses some, but not necessarily all, of the prior edges, and that minimizes the total dissipation for a prescribed material cost. This approach, in which material is prescribed as a holonomic constraint and a minimally dissipative network is sought consistent with this constraint, is not obviously equivalent, in the sense of producing the same family of optimal networks, as Murray's approach, which we may view as a penalty function method for optimizing dissipation under material cost. But it has been adopted in many recent works on optimal networks [Dur07, BM07, KSM10]. Durand showed that any network that solves this optimization problem must be simply connected, i.e. given any two vertices in the network there is at most one path connecting them, so the network is either a tree or a forest. However the proof given in [Dur07] only addresses networks in which flow rates (i.e. Neumann boundary conditions) are imposed at the vertices of the network, and leaves open networks where pressures can be imposed (i.e. both Neumann and Dirichlet boundary conditions). We can quickly see that for some combinations of boundary conditions the minimally dissipative network is not simply connected, and we give an example in Section 3.2.2. This example shows that

minimizing dissipation on a network with multiple pressure boundary conditions produces a multiply connected, i.e. non-tree network. The relevance of the example network shown in Figure 3.1 to real biological transport network design may seem unconvincing; however even quite simple networks commonly used as models for biological transport can exhibit non-equivalent optima under the different formulations for material costs. To see how substantial the difference can be in Section 3.2.3 we give an example of a network and target function for which: the constraint formulation results in a different network from the penalty function formulation.Moreover, when using the constraint formulation to optimize this network, key qualitative features of the optimal network depend on the total material allocated to the network, a fact that has apparently not received scrutiny.

In this chapter we will discuss the consequences of boundary conditions on optimal networks, as well as the effect of different formulations of material cost. We will focus on networks minimizing transport costs, since these have recieved the most attention to date [BM07, KSM10, BCF00]. We show that under the most general boundary conditions pathologies associated with minimizing dissipation are overcome if one instead minimizes a complementary dissipation that includes work done by pressure vertices [FTC17, Lov13, Ach90]. A network with minimal complementary dissipation is simply connected for all boundary conditions, a property previously only proven for minimally dissipative networks with Neumann boundary conditions. Networks optimizing complementary energy resolve pathological networks like the one in Fig. 3.1 by disconnecting pressure vertices with the same pressure. The complementary energy reduces to dissipation when all the pressure vertices have the same pressure, so previous theoretical results for optimal networks are recovered. If at least one vertex with Neumann boundary condition is present minimally dissipative networks will disconnect all the Dirichlet vertices from each other, so ultimately our results provide a formal proof that minimally dissipative networks satisfy Murray's law, are simply connected, and disconnect pressure vertices under this narrower set of boundary conditions.

Throughout we model material costs via holonomic constraints, rather than using Murray's original approach of using penalty functions. The final leg of our argument is to elucidate the conditions under which the two formulations are equivalent; that is, they produce

the same family of optimal networks as the cost or penalty parameters are varied. In particular we show that the two formulations are equivalent if the network flows are not affected by uniform rescaling of conductances, a property held by any network in which all pressure vertices have identical pressures, including any network that minimizes the complementary energy.

Taken together, our results comprehensively expose the effect of boundary conditions, especially vertices with specified pressures, and of formulations of material cost on minimally dissipative networks. It also suggests an energy function that incorporates the work done by pressure vertices that may be a more suitable target function for optimization than dissipation.

3.2 Background

3.2.1 Derivation of Murray's Law

Consider a cylindrical tube with radius r and length ℓ with a flow f going through. By flow we mean that a volume f of fluid (e.g. blood) passes through each cross-section of the network in unit time. In appropriate units, the energy cost of maintaining the vessel can be written as

$$E = D + ar^2\ell = f^2R + ar^2\ell \tag{3.1}$$

where $D = f^2R$ is the dissipation, R is the hydraulic resistance, and a is the energy cost for maintaining unit volume of blood vessel. Under Hagen–Poiseuille's law $R = \frac{8\mu\ell}{\pi r^4}$ where μ is the viscosity of the blood. Suppose r is tuned such that the energy cost is minimized under fixed amount of inflow f. Then the derivative of E over r should vanish, i.e.

$$\frac{dE}{dr} = 0 \Rightarrow -\frac{32f^2\mu\ell}{\pi r^5} + 2ar\ell = 0 \Rightarrow f = \sqrt{\frac{a\pi}{16\mu}}r^3 \tag{3.2}$$

and hence, as claimed, $r \propto f^{\frac{1}{3}}$. Note however, that this calculation assumes that we can treat f as an independent variable – that is, changing the tube radius r does not affect the

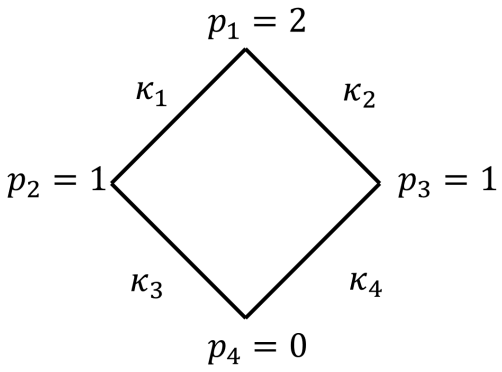

Figure 3.1: A non-tree minimal dissipation network.

flow through the vessel.

3.2.2 An example of a minimal dissipative network with loops

Consider a square network made of 4 edges and 4 vertices, all of which have pressure specified. Vertices and edges are numbered as shown in Figure 3.1. In this network flows can be determined locally, i.e. the flow on one link does not depend on flows on others. Specifically

$$Q_1 = \kappa_1, Q_2 = \kappa_2, Q_3 = \kappa_3, Q_4 = \kappa_4. \tag{3.3}$$

The total dissipation within the network is

$$D = \sum_{i=1}^{4} \kappa_i. \tag{3.4}$$

We follow Durand [Dur07] by specifying the total material available to build the network. Since all edges have the same length this constraint takes the form $\sum_i r_i^2 = \text{const}$, where r_i is the radius of edge i. Now since by the Hagen–Poiseuille law $\kappa_i \propto r_i^4$, we may equivalently write the constraint in the form:

$$K^{\frac{1}{2}} = \sum_{i=1}^{4} \kappa_i^{\frac{1}{2}}, \tag{3.5}$$

for some $K > 0$. To minimize dissipation under the material constraint we write the dissipation in the network and add a Lagrange multiplier to enforce the material constraint:

$$\Theta = \sum_{i=1}^{4} \kappa_i + \lambda(\sum_{i=1}^{4} \kappa_i^{\frac{1}{2}} - K^{\frac{1}{2}}). \tag{3.6}$$

We find the optimal conductances within the network by setting equal to 0 each of the partial derivatives of Θ with respect to the variables $\{\kappa_i\}$ in the form:

$$0 = \frac{\partial \Theta}{\partial \kappa_i} = 1 + \frac{\lambda}{2}\kappa_i^{-\frac{1}{2}} \Rightarrow \kappa_i = \frac{\lambda^2}{4} \qquad \forall 1 \leq i \leq 4. \tag{3.7}$$

The Lagrange multiplier λ can be determined from the material constraint:

$$K^{\frac{1}{2}} = \sum_{i=1}^{4} \kappa_i^{\frac{1}{2}} = 2\lambda \Rightarrow \lambda = \frac{K^{\frac{1}{2}}}{2}. \tag{3.8}$$

We have therefore identified a candidate local extremum with $\kappa_i > 0 \; \forall 1 \leq i \leq 4$. but this local extremum might not be the global minimizer. The set on which we need to minimize the dissipation, i.e. $\{(\kappa_1, \kappa_2, \kappa_3, \kappa_4) | \sum_{i=1}^{4} \kappa_i^{\frac{1}{2}} = K^{\frac{1}{2}}\}$, is compact, so the global minimum must be attained either at the local extremum, or on one of the set boundaries $\kappa_i = 0$ for some $1 \leq i \leq 4$. To analyze the dissipation on domain boundaries we can simply assume that $n \leq 4$ conductances are positive and recalculate λ in the same fashion:

$$K^{\frac{1}{2}} = \sum_{i=1}^{4} \kappa_i^{\frac{1}{2}} = \frac{n}{2}\lambda \Rightarrow \lambda = \frac{2K^{\frac{1}{2}}}{n}. \tag{3.9}$$

Now we can calculate the dissipation and see which n gives the lowest dissipation (let $\mathcal{K} \subseteq 1, 2, 3, 4$ be the set of positive conductances so $|\mathcal{K}| = n$):

$$D = \sum_{i \in \mathcal{K}} \frac{1}{4}\lambda^2 = \sum_{i \in \mathcal{K}} \frac{K}{n^2} = \frac{K}{n} \tag{3.10}$$

so $n = 4$ indeed results in minimal dissipation network; consisting of a single loop through all four vertices. Note additionally that, on this prior network, treating material costs as holonomic constraint or penalty function does not produce equivalent results. Indeed the

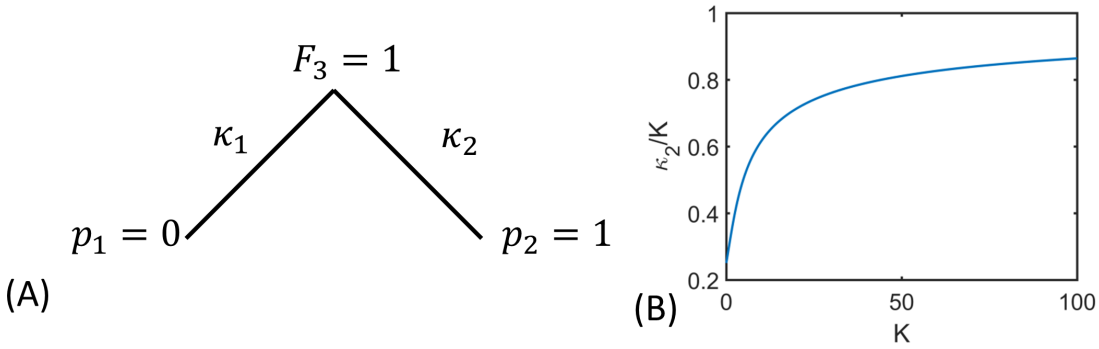

Figure 3.2: The different formulations of imposing material as constraint or penalty function affect the optimal network for the same target function. (A) A network in which a vertex with prescribed inflow, $F_3 = 1$, is connected to two vertices on which pressures are prescribed. (B) The asymmetry of the network increases as the total prescribed material K increases, as predicted by the asymptotic analysis in Section 3.1.

sum of dissipation and material costs is trivially minimized in a network in which all edges have been eliminated.

3.2.3 Formulation of material costs affects the existence of an optimal network

We demonstrate that the formulation of material costs affects the existence of an optimal network, by studying an example network. Consider a simple network comprising two edges (Fig. 3.2A) and minimizing

$$f = \sum_{i=1}^{2} \left(Q_i - \frac{1}{2} \right)^2 . \tag{3.11}$$

This target function is inspired by our own studies of flow in microvascular networks, which have shown that uniform partitioning of flows in microvessels is prioritized over transport costs [CTB17]. By minimizing f we are uniformizing the flows going through the edges to the pressure vertices. We compare the solutions from following either of our optimization approaches. First we treat the material cost as a penalty function, i.e. follow Murray's formulation, and minimize

$$\Theta = \sum_{i=1}^{2}(Q_i - \frac{1}{2})^2 + a\sum_{i=1}^{2}\kappa_i^{\frac{1}{2}}. \tag{3.12}$$

The pressure at the flow vertex is determined by Kirchhoff's first law, which states that the flows along the two edges must sum to the inflow at vertex 3, i.e.:

$$p_3\kappa_1 + (p_3 - 1)\kappa_2 = 1 \Rightarrow p_3 = \frac{1 + \kappa_2}{\kappa_1 + \kappa_2}. \tag{3.13}$$

The total cost function Θ can be rewritten, after p_3 is solved for by Equation 3.13, as

$$\Theta = \left(\frac{(1 + \kappa_2)\kappa_1}{\kappa_1 + \kappa_2} - \frac{1}{2}\right)^2 + \left(\frac{(1 - \kappa_1)\kappa_2}{\kappa_1 + \kappa_2} - \frac{1}{2}\right)^2 + a(\kappa_1^{\frac{1}{2}} + \kappa_2^{\frac{1}{2}}). \tag{3.14}$$

We will show that Θ does not have a minimizer. First notice $(\kappa_1, \kappa_2) = (0, 0)$ is not allowed since p_3 cannot be determined in this case. The minimum value of Θ is zero, and $(\kappa_1, \kappa_2) = (0, 0)$ is the only configuration of the network that might achieve this value since otherwise $\kappa_1^{\frac{1}{2}} + \kappa_2^{\frac{1}{2}} > 0$. It suffices to show that we can find networks with $\Theta > 0$ arbitrarily close to zero. If we let $\kappa_1 = \kappa_2 = \epsilon > 0$ then

$$\Theta = \frac{\epsilon^2}{2} + 2a\epsilon^{\frac{1}{2}} \to 0 \qquad \text{as } \epsilon \to 0 \tag{3.15}$$

and we showed that Θ does not have a minimizer. On the other hand if we impose the total material as a constraint we have

$$\Theta = (\frac{(1 + \kappa_2)\kappa_1}{\kappa_1 + \kappa_2} - \frac{1}{2})^2 + (\frac{(1 - \kappa_1)\kappa_2}{\kappa_1 + \kappa_2} - \frac{1}{2})^2 \tag{3.16}$$

where

$$\kappa_1^{\frac{1}{2}} + \kappa_2^{\frac{1}{2}} = K^{\frac{1}{2}} \tag{3.17}$$

with a predetermined total material K. A minimum will happen if $Q_1 = Q_2 = \frac{1}{2}$ with the material constraint satisfied, so we can search for the global minimum by setting

$$\frac{\kappa_1 + \kappa_1\kappa_2}{\kappa_1 + \kappa_2} = \frac{1}{2} \Rightarrow \kappa_1 = \frac{\kappa_2}{1 + 2\kappa_2} \tag{3.18}$$

(the other equation is redundant since $Q_1 + Q_2 = 1$). The material constraint then reads

$$[1 + (1 + 2\kappa_2)^{\frac{1}{2}}]\frac{\kappa_2^{\frac{1}{2}}}{(1 + 2\kappa_2)^{\frac{1}{2}}} = K^{\frac{1}{2}}. \tag{3.19}$$

This equation does not admit an analytical solution, but since the left hand side is monotonically increasing with κ_2 and can take any value between 0 and ∞, it can be solved for any finite $K > 0$. In particular asymptotic solutions can be obtained as $K \to 0^+$ and as $K \to \infty$. When $K \ll 1$ we have $\kappa_2 \leq K \ll 1$ so

$$K^{\frac{1}{2}} = [1 + (1 + 2\kappa_2)^{\frac{1}{2}}]\frac{\kappa_2^{\frac{1}{2}}}{(1 + 2\kappa_2)^{\frac{1}{2}}} \sim 2\kappa_2^{\frac{1}{2}} \Rightarrow \kappa_1 = \kappa_2 = \frac{K}{4}. \tag{3.20}$$

In the case of $K \gg 1$ if we assume $\kappa_2 \gg 1$ we can obtain

$$K^{\frac{1}{2}} = [1 + (1 + 2\kappa_2)^{\frac{1}{2}}]\frac{\kappa_2^{\frac{1}{2}}}{(1 + 2\kappa_2)^{\frac{1}{2}}} \sim \kappa_2^{\frac{1}{2}} \Rightarrow \kappa_2 \sim K. \tag{3.21}$$

Therefore the increase in total material K increases the network asymmetry $\frac{\kappa_2}{\kappa_1}$, as also suggested by numerical results (Fig. 3.2B).

3.3 Notation

In this work we consider a set of vertices $k = 1, ..., V$ that connect to each other by vessels or edges. We indicate that vertices are neighbors in the network by writing $\langle k, l\rangle = 1$ if vertices k, l are linked by an edge and $\langle k, l\rangle = 0$ otherwise. This relation between vertices is symmetric, in the sense that $\langle k, l\rangle = \langle l, k\rangle$. If $\langle k, l\rangle = 1$ a non-negative conductance κ_{kl} and a flow Q_{kl} are associated with the edge, with $\kappa_{kl} = \kappa_{lk}$ and $Q_{kl} = -Q_{lk}$. We model flows within hydraulic networks by assuming that a pressure p_k can be assigned to each vertex k and there is a linear relation between flow and pressure difference, i.e. $Q_{kl} = (p_k - p_l)\kappa_{kl}$. We divide the vertices of the network into two classes with the definitions as follows: Neumann vertices where flow into the network is known, i.e. $\sum_{l\,:\,\langle k,l\rangle=1} Q_{kl} = q_k$, where q_k is the flow into the network at vertex k, and Dirichlet vertices at which pressure is prescribed. Vertices that are not connected to external fluid sources, sinks or reservoirs are typically of Neumann

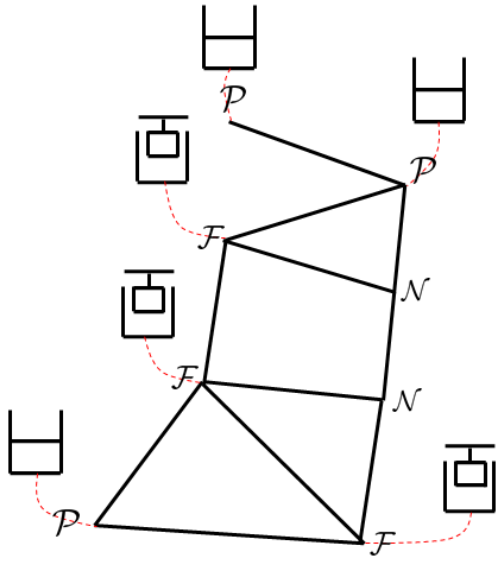

Figure 3.3: A network diagram showing Dirichlet (pressure) vertices $\mathcal{P}$ and Neumann (flow) vertices $\mathcal{F}$, along with vertices $\mathcal{N}$ where no boundary condition is imposed. In Chapter 4 we define $\mathcal{V}_N = \mathcal{N} \cup \mathcal{F}$ and $\mathcal{V}_D = \mathcal{P}$.

type, with inflow $q_k = 0$ (Fig. 3.3). Let $\mathcal{P}$ denote the set of pressure (or Dirichlet) vertices and $\mathcal{F}$ the set of flow (or Neumann) vertices with nonzero inflow (we require $\mathcal{P} \cap \mathcal{F} = \phi$ since when combined with the compatibility conditions discussed below this condition is sufficient for the flows to be unique. In the case $\mathcal{P} \cap \mathcal{F} \neq \phi$ neither existence nor uniqueness of flows can be guaranteed). For definiteness we say $k \notin \mathcal{P} \cup \mathcal{F}$ if no boundary condition is imposed, i.e. $\sum_{l\,:\,\langle k,l\rangle=1} Q_{kl} = 0$. A Kirchhoff flow is defined as the flow $Q_{kl} = (p_k - p_l)\kappa_{kl}\ \forall \langle k, l\rangle = 1$, where the pressures satisfy

$$\begin{cases} \sum_{l\,:\,\langle k,l\rangle=1}(p_k - p_l)\kappa_{kl} = 0\,, & k \notin \mathcal{P} \cup \mathcal{F} \\ p_k = \bar{p_k}\,, & k \in \mathcal{P} \\ \sum_{l\,:\,\langle k,l\rangle=1}(p_k - p_l)\kappa_{kl} - q_k = 0\,, & k \in \mathcal{F}, q_k \neq 0 \end{cases} . \tag{3.22}$$

It is well-known that connected networks with $\mathcal{P} \neq \phi$ have uniquely determined pressures and therefore they have unique Kirchhoff flows [LP16] (Connected networks are networks where $\forall 1 \leq k, l \leq V$ we can devise a path from k to l; that is: $\exists k_1, k_2, ..., k_n$ s.t. $\langle k, k_1\rangle =$

$\langle k_i, k_{i+1}\rangle = \langle k_n, l\rangle = 1\ \forall 1 \le i \le n-1$ and $\kappa_{kk_1}, \kappa_{k_i k_{i+1}}, \kappa_{k_n l} > 0\ \forall 1 \le i \le n-1$). In case $\mathcal{P} = \phi$ the Kirchhoff flow is uniquely determined so long as $\sum_{k\in\mathcal{F}} q_k = 0$, and pressures are determined up to an additive constant. If the condition on total inflow is violated there is no solution for p_k's and the pressures are ill-defined. This result is quite important for developing intuition about the role of Dirichlet vertices in networks so we give a proof in Appendix B. On the other hand if the network is not connected then it consists of finitely many connected components, and each component would have to satisfy the condition for the Kirchhoff flow to be uniquely determined. We define a *physical network* to be a network whose conductances κ_{kl} and pressure conditions admit a unique Kirchhoff flow solution.

3.4 Results

In this section we state the main results of this chapter, and describe several properties of physical networks that globally minimize the dissipation and the complementary dissipation, a concept analogous to the notion of complementary energy for externally loaded elastic body. These results will be proven in Sections 3.5−3.10.

Definition 3.4.1. The dissipation function given flows Q_{kl} and conductances κ_{kl} for $\langle k, l\rangle = 1$ is defined by

$$D = \sum_{k>l, \langle k,l\rangle = 1} \frac{Q_{kl}^2}{\kappa_{kl}} \tag{3.23}$$

Definition 3.4.2. The complementary dissipation of a network given flows Q_{kl} and conductances κ_{kl} for $\langle k, l\rangle = 1$ is defined by

$$f = \sum_{k>l, \langle k,l\rangle = 1} \frac{Q_{kl}^2}{\kappa_{kl}} - 2\sum_{k\in\mathcal{P}} p_k \sum_{l\,:\,\langle k,l\rangle = 1} Q_{kl} \tag{3.24}$$

We call f the complementary dissipation because it resembles the complimentary energy defined in linear elasticity which allows the displacement field within an externally loaded elastic body to be calculated via minimization of a function [FTC17, Lov13, Ach90]. Notably

this function, the complementary energy, is defined to be equal to the stored internal elastic energy minus the work done by any external traction, which is similar to our expression (rate of dissipation minus twice the rate of working of external tractions). We introduce the material constraint as

$$K = \sum_{k>l,\langle k,l\rangle=1} \kappa_{kl}^{\frac{1}{2}} d_{kl}. \tag{3.25}$$

Here $d_{kl} = \ell_{kl}^{\frac{3}{2}}$, where ℓ_{kl} is the length of link kl in the hydraulic network. The d_{kl} can be any set of positive weights for generality. A fundamental question is whether a global minimizer of dissipation (4.15) or complementary dissipation (3.24) exists under material constraint or penalty:

Proposition 3.4.1. *Suppose the network topology and boundary conditions are physical, i.e.* $\kappa_{kl} > 0 \ \forall \langle k,l\rangle = 1$ *results in a physical network. Then there exists a physical network that globally minimizes dissipation (4.15) or complementary dissipation (3.24) under material constraint (3.25). In addition there exists a physical network that minimizes dissipation (4.15) under material penalty, i.e. minimizes*

$$\Theta = \sum_{k>l,\langle k,l\rangle=1} \frac{Q_{kl}^2}{\kappa_{kl}} + a \sum_{k>l,\langle k,l\rangle=1} \kappa_{kl}^{\frac{1}{2}} d_{kl} \tag{3.26}$$

under no constraint.

Observe that the complementary dissipation (3.24) with material penalty might not have a global minimizer. Consider a simple network made up of two pressure vertices with prescribed pressures $p = 1, 0$ connected by an edge with conductance κ. Then the complementary dissipation with material penalty is $-\kappa + a\kappa^{\frac{1}{2}} d_{12}$, which goes to $-\infty$ as $\kappa \to \infty$. Thus a global minimizer does not exist in this example. Now we define Murray's law:

Definition 3.4.3. A physical network is said to satisfy Murray's law if there is a constant $a > 0$ such that the following relation between Kirchhoff flow Q_{kl} and conductance κ_{kl} holds $\forall \langle k,l\rangle = 1$:

$$\kappa_{kl} = a\frac{|Q_{kl}|^{\frac{4}{3}}}{d_{kl}^{\frac{2}{3}}}. \tag{3.27}$$

If flows obey the Hagen–Poiseuille law (so that $\kappa_{kl} \propto r_{kl}^4$ where r_{kl} is the radius of edge kl), then Equation 3.27) implies that $|Q_{kl}| \propto r_{kl}^3$. Our first result reframes Murray's law with respect to global minimizers.

Theorem 3.4.1. *A physical network that globally minimizes the complementary dissipation (3.24) under material constraint (3.25) satisfies the Murray's law.*

Our second and third results establish properties previously attributed to minimal dissipative networks [Dur07] but now allowing for both Neumann and Dirichlet boundary conditions. Let a path between vertices k, l be a set of vertices $k = k_1, k_2, ..., k_n = l$ such that no vertex is listed more than once and $\langle k_i, k_{i+1}\rangle = 1, \kappa_{k_i k_{i+1}} > 0 \; \forall 1 \leq i \leq n-1$.

Theorem 3.4.2. *In a physical network that globally minimizes the complementary dissipation (3.24) under material constraint (3.25) there is exactly one path between any pair of points, except the case this network has no flow in it, i.e.* $Q_{kl} = 0 \; \forall \langle k, l\rangle = 1$.

Theorem 3.4.3. *A physical network that globally minimizes the complementary dissipation (3.24) under material constraint (3.25) has no path connecting 2 pressure vertices with the same prescribed pressure, except the case that the network has no flow in it.*

From these results we can rederive properties of minimal dissipative networks for boundary conditions considered by Durand [Dur07].

Corollary 3.4.1. *A physical network that globally minimizes dissipation (4.15) under the material constraint (3.25) satisfies Murray's law, has no loops, and has no paths connecting two pressure vertices if all the pressure vertices have the same specified pressure*

Proof. It suffices to show that the complementary dissipation (3.24) reduces to dissipation (4.15). Since Kirchhoff flow remains the same up to an additive constant on all pressures we can without loss of generality let $p_0 = 0$. Then $f = D$ and the results carry through. □

While it is possible that two pressure vertices with different prescribed pressures connect in networks with minimal complementary dissipation, it does not happen for minimal dissipative networks that have at least one vertex with flow boundary condition.

Proposition 3.4.2. *In a physical network that globally minimizes the dissipation (4.15) under material constraint (3.25) with $\mathcal{F} \neq \phi$, no pair of pressure vertices are connected by a path.*

This along with Corollary 3.4.1 establishes a general result on minimally dissipative networks

Corollary 3.4.2. *A physical network that globally minimizes the dissipation (4.15) under material constraint (3.25) with $\mathcal{F} \neq \phi$ satisfies Murray's law (3.27), has no loops in the sense of Theorem 3.4.2, and has no paths connecting two pressure vertices in the sense of Proposition 3.4.2.*

Proof. Suppose we have a physical network that globally minimizes dissipation (4.15) with $|\mathcal{P}| = n$ and the connected components (where two vertices can be connected only by links with positive conductance) of the network are labeled $G_1, G_2, ..., G_m$. From Proposition 3.4.2 we know that two pressure vertices cannot connect, so $m \geq n$ and each subgraph includes at most one pressure vertex, i.e. $|G_i \cap \mathcal{P}| \leq 1 \; \forall 1 \leq i \leq m$. Now we look at a specific subnetwork G_i. The subnetwork satisfies the assumptions of Corollary 3.4.1, so it has to satisfy Murray's law (3.27) and also contain no loops; or else there is no flow in G_i. Since this argument holds for all subnetworks the whole network satisfies Murray's law and contains no loops. □

Throughout this work we follow recent work [BM07, KSM10] by imposing material cost as a constraint rather than following Murray's approach of imposing it as a penalty function. Here we discuss the conditions under which these different formulations are equivalent for minimally dissipative networks.

Proposition 3.4.3. *Suppose the flows in each minimally dissipative network under material constraint (3.25) are invariant when conductances are uniformly rescaled, i.e. the network with $\kappa'_{kl} = \beta\kappa_{kl}, \beta > 0$ has the same flows as that in the original network. Then there is*

a bijection $K(a)$ from $(0,\infty)$ to $(0,\infty)$ such that every minimally dissipative network with material constraint K is a minimally dissipative network with material penalty under some coefficient a (3.26) and vice versa.

For networks with at least one flow boundary condition we know from Cor. 3.4.2 that all the pressure vertices disconnect and hence the flows in minimally dissipative networks under material constraint are invariant when conductances are uniformly rescaled. Thus

Corollary 3.4.3. *If the network has at least one flow vertex, i.e. $\mathcal{F} \neq \phi$, then the minimal dissipation problem under material constraint (3.25) and material penalty (3.26) are equivalent in the sense of Proposition 3.4.3.*

3.5 Proof of Proposition 3.4.1

Proof. To begin consider the dissipation function (4.15) under material constraint (3.25). Suppose there are E edges then the intersection of $\{\kappa_i \geq 0\}$ and the material constraint surfaces forms a compact set A in $\mathbb{R}^E$. For each physical network the flow is obtained by inverting an invertible matrix with components continuously dependent on the conductances so the dissipation is continuous in the conductances. Dissipation is finite at each physical network since $\kappa_{kl} = 0 \Rightarrow Q_{kl} = 0$. However not all the networks in this set are physical, specifically when a subnetwork with unbalanced flow boundary conditions is separated out, and we need to exclude non-physical networks but keep the set compact. By assumption $\kappa_{kl} > 0 \ \forall \langle k,l \rangle = 1$ results in a physical network, so a non-physical network must have a set of edges $k_i l_i$ with $\kappa_{k_i l_i} = 0$ for $i = 1, 2, ..., n$. It suffices to show that physical networks with $\kappa_{k_1 l_1}, ..., \kappa_{k_n l_n} < \epsilon$ have dissipation uniformly converging to infinity as $\epsilon \to 0^+$, so we can exclude this set without excluding a possible global minimum. If $\kappa_{k_1 l_1}, ..., \kappa_{k_n l_n} = 0$ gives a non-physical network there will be a connected component C connected by $kl \notin \{k_1 l_1, ..., k_n l_n\}$ and with $\sum_{i \in C \cap \mathcal{F}} q_i \neq 0$ but $\mathcal{P} \cap C = \phi$. Without loss of generality let $q_{tot} = \sum_{i \in C \cap \mathcal{F}} q_i > 0$ and assume $k_1 l_1, ..., k_m l_m$ with $m \leq n$ connect C with the rest of the network, i.e. $k_i \in C$ and $l_i \notin C \ \forall 1 \leq i \leq m$. Then the unbalanced flow in C must flow out through $k_1 l_1, ..., k_m l_m$ so

$$\sum_{i=1}^{m} Q_{k_i l_i} = q_{tot} \Rightarrow \exists 1 \leq j \leq m \; s.t. \; Q_{k_j l_j} \geq \frac{q_{tot}}{m}. \tag{3.28}$$

Then

$$D = \sum_{k<l,\langle k,l\rangle=1} \frac{Q_{kl}^2}{\kappa_{kl}} \geq \frac{Q_{k_j l_j}^2}{\kappa_{k_j l_j}} \geq \frac{q_{tot}^2}{m^2 \epsilon} \geq \frac{q_{tot}^2}{n^2 \epsilon}. \tag{3.29}$$

Since q_{tot} is independent of $\epsilon > 0$ the dissipation of physical networks in the set $\{\kappa_{k_i l_i} < \epsilon | 1 \leq i \leq n\}$ goes to infinity uniformly as $\epsilon \to 0^+$. Now for each non-physical network we can identify all the edges with zero conductance and create this set, with $\epsilon > 0$ chosen such that $\epsilon < \frac{K^2}{(\sum_{k>l,\langle k,l\rangle=1} d_{kl})^2}$, where K is the prescribed material cost, and all the physical networks within this set have dissipation greater than that of the uniform conductance network, i.e. $\kappa_i = \frac{K^2}{(\sum_{k>l,\langle k,l\rangle=1} d_{kl})^2} \; \forall 1 \leq i \leq E$. Then if we exclude this set of networks from A we will obtain a non-empty set (since the uniform conductance network is in the set) and we will not exclude the global minimum (since the uniform conductance network has lower dissipation than all the physical networks in the excluded set). Now we repeat this procedure for all $k_1 l_1, ..., k_n l_n$ if zero conductance on these edges produces a non-physical network. Since there are only finitely many edge subsets and each operation produces a compact set we know the remaining set is still compact. Then a globally minimally dissipative network exists since a continuous function always achieves its global minimum on compact sets. The proof for dissipation with material penalty (3.26) follows along the same lines except that now A is defined by $\{\sum_{k<l,\langle k,l\rangle=1} \kappa_{kl}^{\frac{1}{2}} d_{kl} \leq M | \kappa_i \geq 0\}$ and M chosen to be larger than the dissipation with material penalty (3.26) of the uniform conductance network.

Finally we consider the complementary dissipation (3.24) with material constraint (3.25). The proof is similar except that now we need to establish a uniform upper bound of $|\sum_{k\in\mathcal{P}} p_k \sum_{l \,:\, \langle k,l\rangle=1} Q_{kl}|$ for all physical networks in A. Then since the pressure work term is continuous with the conductance and we can exclude non-physical networks once we have this bound we can prove the existence of global minimizer as above. Since the flows depend linearly on the boundary conditions we can write $Q_{kl} = Q_{kl}^{(f)} + Q_{kl}^{(p)}$, where $\{Q_{kl}^{(f)}\}$ is obtained by setting all pressure vertices to have zero pressure and keeping all the flow boundary con-

ditions and $\{Q_{kl}^{(p)}\}$ by setting all the flow vertices to have zero flow (i.e. remove the flow boundary condition on all flow vertices) and keeping all the pressure boundary conditions. It suffices to bound the pressure work term in these flows separately. In the network with $Q_{kl}^{(p)}$ notice that the maximum principle applies, i.e. if we let $\bar{p} = \max_{p_i, i\in\mathcal{P}}, \underline{p} = \min_{p_i, i\in\mathcal{P}}$ we have

$$\underline{p} \leq p_i \leq \bar{p} \tag{3.30}$$

for all vertices, i, that are connected to a pressure vertex (let the set of $i \notin \mathcal{P}$ and i connected to a pressure vertex be C). This is obvious if $i \in \mathcal{P}$. If $i \in C$ Kirchhoff's first law at vertex i may be rewritten as:

$$p_i = \frac{\sum_{j\,:\,\langle i,j\rangle=1} p_j \kappa_{ij}}{\sum_{j\,:\,\langle i,j\rangle=1} \kappa_{ij}} \tag{3.31}$$

($\sum_{j\,:\,\langle i,j\rangle=1} \kappa_{ij} > 0$ since i connects to a pressure vertex and hence must connect to at least one adjacent vertex). Suppose for contradiction that $\exists p_{i_0} < \underline{p}$ with $i_0 \in C$. Then we can without loss of generality have $p_{i_0} \leq p_j\ \forall j \in C$, and for Equation (3.31) to hold we must have $p_j = p_{i_0}\ \forall \kappa_{ji_0} > 0$. By assumption i_0 connects to a pressure vertex $k \in \mathcal{P}$ so $p_k = p_{i_0} < \underline{p}$, a contradiction. Similarly we can prove that $p_i \leq \bar{p},\ \forall i \in C$. Thus if we let the maximum degree of all the vertices be d we have

$$|\sum_{k\in\mathcal{P}} p_k \sum_{l\,:\,\langle k,l\rangle=1} Q_{kl}^{(p)}| \leq |\mathcal{P}| \max\{|\bar{p}|, |\underline{p}|\}(\bar{p} - \underline{p}) d \frac{K^2}{\min\{d_{kl}\}^2} \tag{3.32}$$

which is a uniform bound for all the physical networks satisfying the material constraint (3.25). Now we consider the pressure work term with $Q_{kl}^{(f)}$. Without loss of generality we can assume $|\mathcal{F}| = 1$ since we can split any flow boundary condition into the sum of boundary $\{Q_{kl}^{(f,1)}\}, ..., \{Q_{kl}^{(f,|\mathcal{F}|)}\}$, where $\{Q_{kl}^{(f,i)}\}$ is the flow in which only the i_{th} flow boundary condition is applied, and for concreteness we let $q_{i_f} < 0$ where i_f denotes the only flow vertex in the network. Now we focus on a specific $\{Q_{kl}^{(f,i)}\}$ and abbreviate it as $\{Q_{kl}\}$. We claim that $0 \leq \sum_{l\,:\,\langle k,l\rangle=1} Q_{kl} \leq -q_{i_f}\ \forall k \in \mathcal{P}$. Suppose for contradiction that $\sum_{l\,:\,\langle k_0,l\rangle=1} Q_{k_0 l} < 0$ for a $k_0 \in \mathcal{P}$. Then $\exists k_1$ such that $\langle k_1, k_0\rangle = 1$ and $p_{k_1} > p_{k_0}$ by the assumption. If

$k_1 \in \mathcal{P}$ we have a contradiction since $p_{k_1} = p_{k_0} = 0$, so $k_1 \notin \mathcal{P} \cup \mathcal{F}$ or $k_1 \in \mathcal{F}$. In either case we have $\sum_{l \neq k_0 \,:\, \langle k_1, l\rangle = 1} Q_{k_1 l} = q_{k_1} - Q_{k_1 k_0}$, where $q_{k_1} = q_{i_f}$ if $k_1 \in \mathcal{F}$ and is zero otherwise. Thus the left hand side sums to a non-positive number so we can find k_2 such that $\langle k_2, k_1\rangle = 1$ and $p_{k_2} > p_{k_1}$. Following this procedure we can find distinct $k_0, k_1, ..., k_n$ such that $p_{k_i} > p_{k_{i-1}}$ $\forall 1 \leq i \leq n$ (if any two of the vertices are the same they would have the same pressure). Since $n > 0$ is arbitrary we can let $n = V$, the number of vertices, so one of k_i must belong to $\mathcal{P}$, a contradiction. The statement $\sum_{l \,:\, \langle k,l\rangle = 1} Q_{kl} \leq -q_{i_f}$ comes from the fact

$$\sum_{k \in \mathcal{P}} \left(\sum_{l \,:\, \langle k,l\rangle = 1} Q_{kl} \right) = -q_{i_f} \tag{3.33}$$

so if $\exists k_0 \in \mathcal{P}$ such that $\sum_{l \,:\, \langle k_0,l\rangle = 1} Q_{k_0 l} > -q_{i_f}$ there must be a $k_0' \in \mathcal{P}$ such that $\sum_{l \,:\, \langle k_0',l\rangle = 1} Q_{k_0' l} < 0$, a contradiction. Similar estimates for $q_{i_f} > 0$ can be obtained in the same manner. With the estimates on the inflow into pressure vertices we have

$$|\sum_{k \in \mathcal{P}} p_k \sum_{l \,:\, \langle k,l\rangle = 1} Q_{kl}^{(f)}| \leq |\mathcal{P}| \max\{|\bar{p}|, |\underline{p}|\} |q_{i_f}|. \tag{3.34}$$

With these estimates we established an upper bound for the pressure work term and hence the global minimizer for the complementary dissipation (3.24) under material constraint (3.25). □

3.6 Proof of Theorem 3.4.1

Proof. Consider a physical network that does not satisfy Murray's law, and we will show that this is not a global minimizer of complementary dissipation (3.24) under material constraint (3.25). Suppose our network has flows and conductances $\tilde{Q}_{kl}, \tilde{\kappa}_{kl}$, and assume for now that $\tilde{Q}_{kl} \neq 0$ $\forall \langle k, l\rangle = 1$. Now define κ_{kl} to be the conductances that satisfy Murray's law (3.27) and the material constraint (3.25) based on the fluxes in our original network, i.e.

$$\kappa_{kl} = a\frac{|\tilde{Q}_{kl}|^{\frac{4}{3}}}{d_{kl}^{\frac{2}{3}}} \quad \forall\langle k,l\rangle = 1, \quad K = \sum_{k>l,\langle k,l\rangle=1} \kappa_{kl}^{\frac{1}{2}} d_{kl} \tag{3.35}$$

where $a > 0$ is uniquely determined by the material constraint. We show that this comparative network has strictly smaller complementary dissipation (3.24), i.e.

$$\sum_{k>l,\langle k,l\rangle=1} \frac{\tilde{Q}_{kl}^2}{\kappa_{kl}} - 2\sum_{k\in\mathcal{P}} p_k \sum_{l\,:\,\langle k,l\rangle=1} \tilde{Q}_{kl} < \sum_{k>l,\langle k,l\rangle=1} \frac{\tilde{Q}_{kl}^2}{\tilde{\kappa}_{kl}} - 2\sum_{k\in\mathcal{P}} p_k \sum_{l\,:\,\langle k,l\rangle=1} \tilde{Q}_{kl}. \tag{3.36}$$

We show this inequality by proving that the conductances satisfying Murray's law is the global minimizer of complementary dissipation (3.24) when flows $\tilde{Q}_{kl}$ are held constant and the material constraint (3.25) is imposed. Consider the dissipation with a Lagrange multiplier imposing material constraint (since the pressure work term does not change when $\tilde{Q}_{kl}$ are held fixed)

$$\Theta = \sum_{k>l,\langle k,l\rangle=1} \frac{\tilde{Q}_{kl}^2}{\kappa_{kl}} + \lambda\Big(\sum_{k>l,\langle k,l\rangle=1} \kappa_{kl}^{\frac{1}{2}} d_{kl} - K\Big). \tag{3.37}$$

First we find the stationary points:

$$0 = \frac{\partial\Theta}{\partial\kappa_{kl}} = -\frac{\tilde{Q}_{kl}^2}{\kappa_{kl}^2} + \frac{\lambda}{2}\kappa_{kl}^{-\frac{1}{2}} d_{kl} \Rightarrow \kappa_{kl} = 2^{\frac{2}{3}}\frac{|\tilde{Q}_{kl}|^{\frac{4}{3}}}{(\lambda d_{kl})^{\frac{2}{3}}} \quad \forall\langle k,l\rangle = 1 \tag{3.38}$$

which is Murray's law when Hagen–Poiseuille's law is applied. Now λ can be solved for by plugging Equation (3.38) back into the material constraint (3.25). Since the material constraint (3.25) along with $\kappa_{kl} \geq 0\ \forall\langle k,l\rangle = 1$ forms a compact set this is the unique global minimum so long as no minima occur on the boundaries, i.e. there is no local minimum for which $\exists\langle k,l\rangle = 1$ s.t. $\kappa_{kl} = 0$. However since $\tilde{Q}_{kl} \neq 0\ \forall\langle k,l\rangle = 1$ any $\kappa_{kl} = 0$ will result in $f = \infty$ and thus global minimizers cannot happen on boundaries. Since the set of conductances that satisfy Murray's law on the material constraint surface is the only stationary point in the interior, and we have dispensed with global minima on the boundary it must be the unique global minimizer, and the inequality (3.36) holds. Now to finalize our proof we remove the assumption that $\tilde{Q}_{kl} \neq 0\ \forall\langle k,l\rangle = 1$. Then we need

to show that the new conductances κ_{kl} along with original boundary conditions yield a physical network under the assumption that $\tilde{\kappa}_{kl}$ with boundary conditions gives a physical network, and that the conductances κ_{kl} that satisfy Murray's law is still the unique global minimizer. The first aspect is trivial in the case $\tilde{Q}_{kl} \neq 0 \ \forall \langle k,l \rangle = 1$ since this condition implies that $\tilde{\kappa}_{kl}, \kappa_{kl} > 0 \ \forall \langle k,l \rangle = 1$. However $\tilde{Q}_{kl} = 0$ does not imply $\tilde{\kappa}_{kl} = 0$ while κ_{kl} will be zero, and the concern is that applying Equation (3.35) will produce a set of disconnected networks that are not physical networks. Consider a connected subnetwork of $\{\tilde{\kappa}_{kl}\}$ containing some edges with zero flows $\tilde{Q}_{k_1 l_1} = \tilde{Q}_{k_2 l_2} = \cdots = \tilde{Q}_{k_n l_n} = 0$ (the statement that a network is a physical network is equivalent to all its connected subnetworks being physical networks). Assume for contradiction that a connected component of this subnetwork G_s is not a physical network with conductances κ_{kl}. By the non-physical network assumption we have $G_s \cap \mathcal{P} = \phi$ and $\sum_{k \in G_s \cap \mathcal{F}} q_k \neq 0$. However since $\tilde{Q}_{k_i l_i} = 0 \ \forall 1 \leq i \leq n$ we have $\sum_{k \in G_s} \sum_{l \,:\, \langle k,l \rangle = 1, l \in G_s} \tilde{Q}_{kl} = \sum_{k \in G_s} \sum_{l \,:\, \langle k,l \rangle = 1} \tilde{Q}_{kl} = \sum_{k \in G_s \cap \mathcal{F}} q_k \neq 0$, contradicting the fact that there is a well-defined pressure $\tilde{p}_k$ on G_s since $\sum_{k \in G_s} \sum_{l \,:\, \langle k,l \rangle = 1, l \in G_s} \tilde{Q}_{kl} = \sum_{k \in G_s} \sum_{l \,:\, \langle k,l \rangle = 1, l \in G_s} (\tilde{p}_k - \tilde{p}_l) \tilde{\kappa}_{kl} = \sum_{k,l \in G_s, k > l, \langle k,l \rangle = 1} (\tilde{p}_k - \tilde{p}_l) \tilde{\kappa}_{kl} + (\tilde{p}_l - \tilde{p}_k) \tilde{\kappa}_{kl} = 0$.

Now we address the second aspect; namely that the set of conductances κ_{kl} that satisfy Murray's law is still the unique global minimizer of dissipation under fixed flow $\tilde{Q}_{kl}$. Let us enumerate all the links with zero flows by $k_1 l_1, ..., k_n l_n$. We have $n < E$ where E is the number of edges since if all the flows are zero the network will already satisfy the Murray's law (3.27) with $a = 0$. It suffices to show that any network with $\kappa_{k_i l_i} > 0$ for some $i \in \{1, ..., n\}$ cannot be a global minimizer. Then we can restrict ourselves on the surface $\kappa_{k_1 l_1} = \cdots = \kappa_{k_n l_n} = 0$ and do the same calculation (when $\tilde{Q}_{kl} = 0 \ \forall \langle k,l \rangle = 1$ the network already satisfies the Murray's law with the constant $a = 0$, so this case can be excluded). However the result is immediate in this case because if we set $\kappa_{k_i l_i} = 0 \ \forall i \in I$ and scale the rest of the conductances up by a multiplicative constant we will strictly reduce the dissipation, so it cannot be a global minimizer.

Now we fix the conductances κ_{kl} and change the flows in order to satisfy Kirchhoff's laws. We claim that among all the flows that satisfy conservation of mass and flow boundary conditions, i.e. $\sum_{l, \langle k,l \rangle = 1} Q_{kl} = 0$ if $k \notin \mathcal{P} \cup \mathcal{F}$ and $\sum_{l, \langle k,l \rangle = 1} Q_{kl} - q_k = 0$ if $k \in \mathcal{F}$ the

Kirchhoff flow minimizes the function (3.24) with κ_{kl} fixed. Then since the original flow $\tilde{Q}_{kl}$ lies in this category we can show

$$\sum_{k>l,\langle k,l\rangle=1} \frac{Q_{kl}^2}{\kappa_{kl}} - 2\sum_{k\in\mathcal{P}} p_k \sum_{l\,:\,\langle k,l\rangle=1} Q_{kl} \leq \sum_{k>l,\langle k,l\rangle=1} \frac{\tilde{Q}_{kl}^2}{\kappa_{kl}} - 2\sum_{k\in\mathcal{P}} p_k \sum_{l\,:\,\langle k,l\rangle=1} \tilde{Q}_{kl} \tag{3.39}$$

which finishes the proof. To see this we can impose the Lagrange multipliers for conservation of mass and flow boundary conditions on function (3.24):

$$\Theta = \sum_{k>l,\langle k,l\rangle=1} \frac{Q_{kl}^2}{\kappa_{kl}} - 2\sum_{k\in\mathcal{P}} p_k \sum_{l,\langle k,l\rangle=1} Q_{kl} - \sum_{k\notin\mathcal{P}} \lambda_k \left(\sum_{l,\langle k,l\rangle=1} Q_{kl} - q_k \right) \tag{3.40}$$

where λ_k are Lagrange multipliers (for convenience we set $q_k = 0$ if $k \notin \mathcal{P}\cup\mathcal{F}$). To minimize this function we take derivatives and set them to zero:

$$0 = \frac{\partial\Theta}{\partial Q_{kl}} = \frac{2Q_{kl}}{\kappa_{kl}} - (\lambda_k - \lambda_l) \tag{3.41}$$

and we define $\lambda_k = 2p_k$ if $k \in \mathcal{P}$. If we apply conservation of flux and flow boundary condition on $k \notin \mathcal{P}$ in terms of λ_k's, i.e. substituting Q_{kl}'s by λ_k's using Equation (3.41), and impose $\lambda_k = 2p_k$ for $k \in \mathcal{P}$, then λ_k's satisfy the exact same equations as the pressure under Kirchhoff's laws. We know from Section 3.3 that if $\mathcal{P} \neq \phi$ then the pressure has a unique solution; otherwise the pressure is determined up to an additive constant, which has no effect on the flows. Therefore the flows Q_{kl}'s always have a unique solution. To show that Kirchhoff flow is a global minimum of the complementary dissipation (3.24) notice that now the conservation of mass and flow boundary condition constraints might not give us a compact set, so there is no boundary. However f has quadratic growth in flow through any link, so we can find $M > 0$ s.t. $f > 2b$ whenever $|Q_{kl}| > M$ for any $\langle k,l\rangle = 1$, where b is the value of the complementary dissipation f for Kirchhoff flow. Then since f has a global minimum in the compact set $|Q_{kl}| \leq M$ $\langle k,l\rangle = 1$ and it cannot be on the boundary it will have to be the Kirchhoff flow, which establishes that the Kirchhoff flow is the unique global minimizer of the complementary dissipation (3.24) given fixed conductances κ_{kl}, which finishes the proof. □

3.7 Proof of Theorem 3.4.2

Proof. Consider a physical network that contains a loop, e, with at least 3 points, i.e. $k_1, ..., k_n$ with $\langle k_i, k_{i+1}\rangle = 1, \kappa_{k_i k_{i+1}} > 0 \ \forall 1 \leq i \leq n$ (we set $k_{n+1} = k_1$) and $n \geq 3$, and let $C = \{(k_1, k_2), ... , (k_{n-1}, k_n), (k_n, k_1)\}$ be the set of ordered pairs denoting all the edges in the loop. Without loss of generality we can assume that the loop does not intersect itself, i.e. $|\{k_1, ..., k_n\}| = n$; otherwise we can choose a non-selfintersecting subloop from it and proceed with the subloop. First we assume that $Q_{k_1 k_2}, ..., Q_{k_n k_1}$ are not all the same. We know from Section 3.6 that adjusting conductances according to Murray's law under material constraint will decrease the dissipation without changing the pressure work term in the complementary dissipation function (3.24) and that the resulting network will remain physical, so we can decrease the complementary dissipation by adjusting the conductances on the loop according to Murray's law with the material on the loop fixed. Therefore without loss of generality we can assume that $\exists a > 0$ s.t. $\tilde{\kappa}_{k_i k_{i+1}} = a\frac{|\tilde{Q}_{k_i k_{i+1}}|^{\frac{4}{3}}}{d_{kl}^{\frac{2}{3}}} \ \forall 1 \leq i \leq n$. Now we consider adding in a loop current Q, that is we add the same current Q to each edge in the loop, and adjust the conductances by Murray's law under material constraint, i.e. set

$$Q_{kl} = \tilde{Q}_{kl} + Q \quad \text{and} \quad \kappa_{kl} = \mu\frac{Q_{kl}^{\frac{4}{3}}}{d_{kl}^{\frac{2}{3}}} \qquad \forall (k,l) \in C \tag{3.42}$$

where

$$\mu = \frac{K_{\text{loop}}^2}{(\sum_{(k,l)\in C} Q_{kl}^{\frac{2}{3}} d_{kl}^{\frac{2}{3}})^2}, \quad K_{\text{loop}} \doteq \sum_{(k,l)\in C} \tilde{\kappa}_{kl}^{\frac{1}{2}} d_{kl} \tag{3.43}$$

(we say $(k,l) \in C$ if the ordered pair $(k,l) = (k_i k_{i+1})$ for some $1 \leq i \leq n$). Notice that for any $Q \in \mathbb{R}$ the new flows $Q_{kl}, (k,l) \in C$ along with the original flows outside of the loop $\tilde{Q}_{kl}, \langle k,l\rangle = 1, (k,l), (l,k) \notin C$ still satisfy conservation of mass and flow boundary conditions since the addition of Q does not change the total flow into any of the vertices. If $\{k_1, ..., k_n\} \cap \mathcal{P} = 0$ then changing the flow will only change the dissipation on the loop, and we only need to consider

$$D_{\text{loop}} \doteq \sum_{(k,l)\in C} \frac{Q_{kl}^2}{\kappa_{kl}}. \tag{3.44}$$

If this is not the case suppose that our network contains a certain number of pressure vertices: $k_{n_1}, ..., k_{n_m} \in \mathcal{P}$ with $m \leq n$. For any k_{n_j} if we restrict the sum $\sum_{l\,:\,\langle k_{n_j}, l\rangle} Q_{k_{n_j} l}$ to edges in the loop, then it can be written as $Q_{k_{n_j}, k_{n_j}+1} + Q_{k_{n_j}, k_{n_j}-1}$ (recall that we assumed the loop has no self-interception). Since $Q_{kl} = \tilde{Q}_{kl} + Q$ we will have $Q_{k_{n_j}, k_{n_j}+1} + Q_{k_{n_j}, k_{n_j}-1} = \tilde{Q}_{k_{n_j}, k_{n_j}+1} + \tilde{Q}_{k_{n_j}, k_{n_j}-1}$ $\forall Q \in \mathbb{R}$ and the pressure work term does not change. Thus in either case if we find flows and conductances on the loop that decrease the dissipation on the loop (3.44) they will decrease the complementary dissipation (3.24) as well. Therefore if we show that D_{loop} strictly decreases after adding a loop current (3.42), then the Kirchhoff flow on the new network will have lower complementary dissipation by the argument in Section 3.6, a contradiction.

To show this first we calculate

$$D_{\text{loop}} = \sum_{(k,l)\in C} \frac{Q_{kl}^2}{\kappa_{kl}} = \sum_{(k,l)\in C} \frac{Q_{kl}^{\frac{2}{3}} d_{kl}^{\frac{2}{3}}}{\mu} = \frac{(\sum_{(k,l)\in C} Q_{kl}^{\frac{2}{3}} d_{kl}^{\frac{2}{3}})^3}{K_{\text{loop}}^2}. \tag{3.45}$$

The derivative with respect to Q is (we let $A = \sum_{(k,l)\in C} Q_{kl}^{\frac{2}{3}} d_{kl}^{\frac{2}{3}}$ for simplicity of notations)

$$\frac{dD_{\text{loop}}}{dQ} = \frac{2A^2}{K_{\text{loop}}^2} \sum_{(k,l)\in C} Q_{kl}^{-\frac{1}{3}} d_{kl}^{\frac{2}{3}}. \tag{3.46}$$

Since Q_{kl} are not all the same for $(k,l) \in C$ we have $A > 0$ (and $K_{\text{loop}} > 0$ by definition) and the factor $\frac{2A^2}{K_{\text{loop}}^2}$ is always positive, so the sign of derivative depends only on $\sum_{(k,l)\in C} Q_{kl}^{-\frac{1}{3}} d_{kl}^{\frac{2}{3}}$ in this case (we will discuss the case $A = 0$ later). Now we show that $Q_{kl} = 0$ for some $(k,l) \in C$ is always a local minimum. Suppose $Q_{kl} = \epsilon$ where $\epsilon \to 0^+$. Then $Q_{kl}^{-\frac{1}{3}} \to \infty$ and we will have $\frac{dD_{\text{loop}}}{dQ} > 0$. The same argument applies to $Q_{kl} = -\epsilon$ so $Q_{kl} = 0$ is indeed a local minimum. To show that global minima can only happen when $Q_{kl} = 0$ for some $(k,l) \in C$ notice that there exists at least one global minimum since $D_{\text{loop}} \to \infty$ as $Q \to \pm\infty$ and D_{loop} is a continuous function of Q. This global minimum may be attained only where $\frac{dD_{\text{loop}}}{dQ} = 0$

or if the derivative is not defined. For the derivative to be not defined we will have at least one $Q_{kl} = 0$, which corresponds to a local minimum with a cusp in D_{loop} as discussed. Now suppose $\frac{dD_{\text{loop}}}{dQ} = 0$ so $B \doteq \sum_{(k,l)\in C} Q_{kl}^{-\frac{1}{3}} d_{kl}^{\frac{2}{3}} = 0$ and $Q_{kl} \neq 0 \; \forall (k,l) \in C$. Then we can take the second derivative:

$$\frac{d^2 D_{\text{loop}}}{dQ^2} = \frac{8AB^2}{3K_{\text{loop}}^2} - \frac{2A^2}{3K_{\text{loop}}^2} \sum_{(k,l)\in C} Q_{kl}^{-\frac{4}{3}} d_{kl}^{\frac{2}{3}} < 0 \tag{3.47}$$

since by assumption $Q_{kl} \neq 0 \; \forall (k,l) \in C$. Thus the local extrema with $Q_{kl} \neq 0 \; \forall (k,l) \in C$ are all local maxima, and a global minimum will happen only if $\exists (k,l) \in C$ s.t. $Q_{kl} = 0$. Now we fix the conductances $\kappa_{kl} \; \forall (k,l) \in C$ and the original conductances outside the loop $\tilde{\kappa}_{kl} \; \forall (k,l), (l,k) \notin C$ and change the flow to Kirchhoff flow. If this is a physical network then as we have seen in Section 3.6 this process strictly decreases the complementary dissipation if the flow is not already the Kirchhoff flow, and the proof finishes since the step of adding a loop current Q strictly decreases the dissipation on the loop and thus the complementary dissipation since a loop cannot be a global minimizer.

It remains to show that the resulting network is a physical network. Suppose for contradiction that after adding a loop current Q we can produce a non-physical connected subnetwork G_s of $\{\kappa_{kl}\}$ by deleting the zero flux edges (when $(k,l) \notin C$ let $\kappa_{kl} = \tilde{\kappa}_{kl}$ be the original conductance since the procedure (3.42) does not change conductances outside of the loop). Similar to the proof in Section 3.6 it suffices to show that the original flow $\{\tilde{Q}_{kl}\}$ satisfies $\sum_{k\in G_s} \sum_{l \,:\, \langle k,l\rangle = 1} \tilde{Q}_{kl} = \sum_{k\in G_s} \sum_{l \,:\, \langle k,l\rangle = 1, l\in G_s} \tilde{Q}_{kl}$ since the non-physical network assumption implies $\sum_{k\in G_s} \sum_{l \,:\, \langle k,l\rangle = 1} \tilde{Q}_{kl} = \sum_{k\in \mathcal{F}\cap G_s} q_k \neq 0$, contradicting that $\sum_{k\in G_s} \sum_{l \,:\, \langle k,l\rangle = 1, l\in G_s} \tilde{Q}_{kl} = 0$. To establish the equality we split the sum into the parts $k \in G_s \backslash e$ and $k \in G_s \cap e$ where $e = \{k_1, ..., k_n\}$ is the set of vertices in the loop. The equality $\sum_{k\in G_s\backslash e} \sum_{l \,:\, \langle k,l\rangle = 1} \tilde{Q}_{kl} = \sum_{k\in G_s\backslash e} \sum_{l \,:\, \langle k,l\rangle = 1, l\in G_s} \tilde{Q}_{kl}$ holds because for $k \in G_s \backslash e$ any edge connecting it does not lie in C, so $\langle k,l\rangle = 1, l \notin G_s$ implies $0 = \kappa_{kl} = \tilde{\kappa}_{kl}$ and $\tilde{Q}_{kl} = 0$. When $k \in G_s \cap e$ we will have to consider connected components of $G_s \cap e$ of $\{\kappa_{kl}\}$ restricted in the loop C. Let $G_1, ..., G_m, m \leq n$ be those connected components, i.e. if $k \in G_i, l \in G_j, i \neq j$ then there is no path $k = l_1, ..., l_h = l$ with (l_i, l_{i+1}) or

$(l_{i+1}, l_i) \in C, \kappa_{l_i l_{i+1}} > 0 \ \forall 1 \leq i \leq h-1$. Now consider a specific G_i and let $k_1^{(i)}, k_2^{(i)}$ be its two end vertices (the only two vertices that are connected to only one vertex in G_i by edges in C), with $l_1^{(i)}, l_2^{(i)}$ be the neighboring vertices in the loop that are not in G_i, i.e. $(k_1^{(i)}, l_1^{(i)}), (l_2^{(i)}, k_2^{(i)}) \in C, l_j^{(i)} \notin G_i, j = 1, 2$ (the order switching comes from the orientation of the edges). Then $\sum_{k \in G_i} \sum_{l \,:\, \langle k,l \rangle = 1} \tilde{Q}_{kl} = \sum_{k \in G_i} \sum_{l \,:\, \langle k,l \rangle = 1, l \in G_s} \tilde{Q}_{kl} + \sum_{j=1,2} \tilde{Q}_{k_j^{(i)} l_j^{(i)}}$ since again we do not have to consider flows on edges that are not in the loop. Now the sum $\sum_{j=1,2} \tilde{Q}_{k_j^{(i)} l_j^{(i)}} = 0$ because $\kappa_{k_j^{(i)} l_j^{(i)}} = 0, j = 1, 2$ indicates that $\tilde{Q}_{k_1^{(i)} l_1^{(i)}} = -\tilde{Q}_{k_2^{(i)} l_2^{(i)}}$ since this is the only circumstance that an addition of a loop current eliminates both edges (the minus sign again comes from the orientation of the edges). Therefore $\sum_{k \in G_s \cap e} \sum_{l \,:\, \langle k,l \rangle = 1, l \in G_s} \tilde{Q}_{kl} = \sum_{i=1}^{m} \sum_{k \in G_i} \sum_{l \,:\, \langle k,l \rangle = 1, l \in G_s} \tilde{Q}_{kl} = \sum_{i=1}^{m} \sum_{k \in G_i} \sum_{l \,:\, \langle k,l \rangle = 1} \tilde{Q}_{kl} = \sum_{k \in G_s \cap e} \sum_{l \,:\, \langle k,l \rangle = 1} \tilde{Q}_{kl}$ and the non-physical network hypothesis leads to a contradiction.

Now we discuss the remaining case $\tilde{Q}_{kl} = Q_0 \in \mathbb{R} \ \forall (k,l) \in C$. In this case we must have $Q_0 = 0$ since otherwise when $Q_0 > 0$ we will have $p_{k_1} > p_{k_2} > \cdots > p_{k_m} > p_{k_1}$, a contradiction, and similarly for $Q_0 < 0$. By assumption the network has at least one edge that has flow in it and does not comprise the loop, i.e. there is an edge kl such that $(k,l), (l,k) \notin C$ and $Q_{kl} \neq 0$. Since the loop carries no flow we can set $\kappa_{kl} = 0 \ \forall (k,l) \in C$ without changing the complementary dissipation. To show that adding these materials back to edges with flows in them strictly decreases the complementary dissipation we prove a generalized Rayleigh's principle that allows for Dirichlet boundary conditions.

Lemma 3.7.1 (Rayleigh's Principle)**.** *The complementary dissipation (3.24) monotonically decreases with the conductance of each edge, i.e. if we let $\{\tilde{\kappa}_{kl}\}, \{\tilde{Q}_{kl}\}$ be the sets of conductances and flows that satisfy all boundary conditions and $\{\kappa_{kl}\}, \{Q_{kl}\}$ be another sets of conductances with Q_{kl} being the Kirchhoff flows, and they are on the same network with the same boundary conditions, then*

$$\kappa_{kl} \geq \tilde{\kappa}_{kl} \quad \forall \langle k,l \rangle = 1 \Rightarrow \sum_{k>l, \langle k,l \rangle = 1} \frac{Q_{kl}^2}{\kappa_{kl}} - 2 \sum_{k \in \mathcal{P}} p_k \sum_{l \,:\, \langle k,l \rangle = 1} Q_{kl} \leq \sum_{k>l, \langle k,l \rangle = 1} \frac{\tilde{Q}_{kl}^2}{\tilde{\kappa}_{kl}} - 2 \sum_{k \in \mathcal{P}} p_k \sum_{l \,:\, \langle k,l \rangle = 1} \tilde{Q}_{kl}. \tag{3.48}$$

Moreover, if $\kappa_{kl} > \tilde{\kappa}_{kl}$ on an edge with $\tilde{Q}_{kl} \neq 0$, then the inequality holds.

Proof. To show the inequality we change the conductances and flows in two steps (we can without loss of generality change $\tilde{Q}_{kl}$ to the Kirchhoff flows corresponding to $\tilde{\kappa}_{kl}$ since from Section 3.6 we know doing so reduces the complementary dissipation). First we change the set of conductances from $\{\tilde{\kappa}_{kl}\}$ to $\{\kappa_{kl}\}$ and show that the complementary dissipation with the non-Kirchhoff flows $\tilde{Q}_{kl}$ decreases. Then we relax the flows to Kirchhoff flows Q_{kl}, which we know decreases the complementary dissipation from Section 3.6. In the first step we can ignore the pressure work term $\sum_{k\in\mathcal{P}} p_k \sum_{l\,:\,\langle k,l\rangle=1} \tilde{Q}_{kl}$ since the flows remain unchanged and the pressures are prescribed. Then the fact $\kappa_{kl} \geq \tilde{\kappa}_{kl}$ implies that $\sum_{k>l,\langle k,l\rangle=1} \frac{\tilde{Q}_{kl}^2}{\kappa_{kl}} \leq \sum_{k>l,\langle k,l\rangle=1} \frac{\tilde{Q}_{kl}^2}{\tilde{\kappa}_{kl}}$, which finishes the proof. The strict inequality comes from that $\frac{\tilde{Q}_{kl}^2}{\kappa_{kl}} < \frac{\tilde{Q}_{kl}^2}{\tilde{\kappa}_{kl}}$ if $\tilde{Q}_{kl} \neq 0$ and $\kappa_{kl} > \tilde{\kappa}_{kl}$. □

If we let $\{\tilde{\kappa}_{kl}\}$ to be the set of original conductances but with $\tilde{\kappa}_{kl} = 0\ \forall (k,l) \in C$, and $\{\tilde{Q}_{kl}\}$ be the set of the original flows, since $\sum_{k>l,\langle k,l\rangle=1} \tilde{\kappa}_{kl}^{\frac{1}{2}} d_{kl} < K$ we can find a new set of conductances $\{\kappa_{kl}\}$ with $\kappa_{kl} \geq \tilde{\kappa}_{kl}, \sum_{k>l,\langle k,l\rangle=1} \kappa_{kl}^{\frac{1}{2}} d_{kl} = K, \kappa_{kl} = 0\ \forall (k,l) \in C$, and $\exists \langle k,l\rangle = 1$ such that $\kappa_{kl} > \tilde{\kappa}_{kl}, \tilde{Q}_{kl} \neq 0$, then by Rayleigh's principle the complementary dissipation of $\{\kappa_{kl}\}, \{Q_{kl}\}$ will be strictly less than that of $\{\tilde{\kappa}_{kl}\}, \{\tilde{Q}_{kl}\}$ and the proof follows. □

3.8 Proof of Theorem 3.4.3

Proof. To prove that there is no path connecting 2 pressure vertices with the same pressure suppose there is a path $k_1, ..., k_n$ with $\langle k_i k_{i+1}\rangle = 1, \kappa_{k_i k_{i+1}} > 0\ \forall i = 1, ..., n-1$, $n \geq 2$, and $k_1, k_n \in \mathcal{P}$ with $p_{k_1} = p_{k_n}$. As in Section 3.7 we can redistribute the conductances in the path to satisfy Murray's law with the material in this path held constant without increasing the complementary dissipation (3.24). Without loss of generality We may assume that this path does not self-intersect because we can otherwise extract a subpath that does not self-intersect. Since we will only adjust flow and conductances on the path we can again restrict our attention to contribution of this path to the complementary dissipation:

$$f_{\text{path}} = \sum_{(k,l)\in C} \frac{Q_{kl}^2}{\kappa_{kl}} - 2 \sum_{k\in C_p} p_k \sum_{l\,:\,\langle k,l\rangle=1, l\in C_n} Q_{kl}. \tag{3.49}$$

Here as before we let C be the set of ordered pairs of edges in the path, i.e. $C = \{(k_1, k_2), ..., (k_{n-1}, k_n)\}$, and C_p be the set of all the pressure vertices in the path, and $C_n = \{k_1, ..., k_n\}$. Now we add in a path current Q that resembles the loop current in Section 3.7, i.e.

$$Q_{kl} = \tilde{Q}_{kl} + Q, \quad \kappa_{kl} = \mu \frac{Q_{kl}^{\frac{4}{3}}}{d_{kl}^{\frac{2}{3}}} \qquad \forall (k,l) \in C \tag{3.50}$$

where

$$\mu = \frac{K_{\text{path}}^2}{(\sum_{(k,l)\in C} Q_{kl}^{\frac{2}{3}} d_{kl}^{\frac{2}{3}})^2}, \quad K_{\text{path}} \doteq \sum_{(k,l)\in C} \tilde{\kappa}_{kl}^{\frac{1}{2}} d_{kl} \tag{3.51}$$

and $\tilde{Q}_{kl}, \tilde{\kappa}_{kl}$ denote the original flow and conductance, which according to Theorem 3.4.1, are related via Murray's law. We can see that if $k \in C_p$ but $k \neq k_1, k_n$ then $\sum_{l\,:\,\langle k,l\rangle = 1, l \in C_n} Q_{kl}$ consists of 2 terms in which the path current Q cancels, so adding path current does not affect the pressure work terms for these vertices. Similarly the original flows are constants in the pressure work term and can be ignored if we only wish to tease out the dependence of f_{path}. Thus up to an additive constant:

$$f_{\text{path}} = \sum_{(k,l)\in C} \frac{Q_{kl}^2}{\kappa_{kl}} - 2(p_{k_1} - p_{k_n})Q = \sum_{(k,l)\in C} \frac{Q_{kl}^2}{\kappa_{kl}} = D_{\text{path}} \tag{3.52}$$

where the sign comes from our convention that the path current flows out of k_1 but flows into k_n. Thus the complementary dissipation reduces to dissipation on the path in this case. Also notice that adding a path current will not affect the conservation of mass and flow boundary conditions since it adds no flow to $k_2, ..., k_{n-1}$ and k_1, k_n are pressure vertices and do not have prescribed inflow, so if the procedure (3.50) strictly reduces the dissipation on the loop f_{path} we can relax the flows to Kirchhoff flows without increasing the complementary dissipation, which leads to a contradiction. Since D_{path} has the same form as D_{loop} in Section 3.7 we can prove in the same way that if Q_{kl} are not all the same for $(k,l) \in C$ the global minimum only happens when $Q_{kl} = 0$ for some $(k,l) \in C$, which leads to a contradiction, and if $Q_{kl} = Q_0\ \forall (k,l) \in C$ we must have $Q_0 = 0$ or we will have $p_{k_1} \neq p_{k_n}$, a contradiction. In this case by assumption we have an edge kl with $(k,l), (l,k) \notin C$ and

$Q_{kl} \neq 0$. Then similarly to Section 3.7 we can remove the materials on the path C and apply Rayleigh's principle to decrease the complementary dissipation, which finishes the argument. One last issue needed to be addressed is whether cutting this path will result in a non-physical network. As in Section 3.7 we can define connected segments in the path after the path is cut and suppose for contradiction that there is a subnetwork connected to multiple connected segments. If this segment contains k_1 or k_n then there is at least one pressure vertex and this subnetwork is physical. Otherwise this subnetwork connects to only connected segments in the middle which have the same original flows into and out of them, and we have $0 = \sum_{k\in G_s} \sum_{l\,:\,\langle k,l\rangle=1, l\in G_s} \tilde{Q}_{kl} = \sum_{k\in G_s} \sum_{l\,:\,\langle k,l\rangle=1} \tilde{Q}_{kl} \neq 0$ where G_s is the non-physical subnetwork after cutting the path, a contradiction. □

3.9 Proof of Proposition 3.4.2

Proof. Suppose we start with a physical network that globally minimizes the dissipation (4.15) under the material constraint (3.25) with $n \doteq |\mathcal{P}| \geq 2$ (otherwise there is nothing to prove). Since the number of paths connecting two different pressure vertices is finite we can assume that there is a finite number of paths linking pressure vertices. On any path we can decrease the dissipation restricted on the path by adding a path current and adjust the conductances according to Murray's law as in Section 3.8 in the case that not all the flows (with sign determined by the path direction) are the same, and by simply reducing all the flows to zero if they all agree and eliminating the whole path while scaling up the rest of the network by a multiplicative constant to meet the material constraint (3.25), given that this path does not comprise all the network. This procedure strictly reduces the dissipation since in the case not all the flows on the path are the same we will cut a proper set of them as in Section 3.8, which strictly decreases the dissipation. In case where all the flows are the same on the path, because $|\mathcal{F}| \neq \phi$, a flow vertex cannot lie on this path (otherwise the flows will not all be the same), so there will always be an edge not in this path with nonzero flow. Thus we can eliminate each path one at a time, strictly decreasing the dissipation while still satisfying the conservation of mass and flow boundary conditions and also the network

remaining physical so long as we are not taking out the last path, in which case we have to worry about this path comprising the whole network.

Up to now we do not solve for the flows according to Kirchhoff's laws since this might not decrease dissipation (it is only guaranteed to decrease the complementary dissipation). Notice that while we might take out multiple paths at a time in case of several paths sharing common links, the number of paths will never increase since no new edge with positive conductance can be created in this process. If we never reach the situation where we need to take out the last path, which is possible because eliminating one path may also disconnect others, then we do not have to worry about the path we are taking out might comprise the whole network (since there are other distinct paths), and we reach a network with connected components $G_1, ..., G_m$ with $m \geq n$ since each component can contain at most one pressure vertex. Then the complementary dissipation function becomes

$$f = \sum_{k>l, \langle k,l \rangle = 1} \frac{Q_{kl}^2}{\kappa_{kl}} - 2 \sum_{k=1}^{n} p_k \sum_{l \,:\, \langle k,l \rangle = 1} Q_{kl} \tag{3.53}$$

if we without loss of generality let $k = 1, ..., n$ be the pressure vertices in $G_1, ..., G_n$ respectively. Since $Q_{kl} = 0$ when $k \in G_i, l \in G_j$ when $i \neq j$ we can isolate the contribution of a component G_i to the complementary dissipation, starting from:

$$\begin{aligned} 0 &= \sum_{k,l \in G_i, \langle k,l \rangle = 1} (p_k - p_l)\kappa_{kl} = \sum_{k \in G_i} \left(\sum_{l \in G_i \,:\, \langle k,l \rangle = 1} Q_{kl} \right) \\ &= \sum_{k \in G_i} \left(\sum_{l \,:\, \langle k,l \rangle = 1} Q_{kl} \right) = \sum_{l \,:\, \langle i,l \rangle = 1} Q_{il} + \sum_{k \in G_i \cap \mathcal{F}} q_k. \end{aligned} \tag{3.54}$$

Thus

$$f = \sum_{k>l, \langle k,l \rangle = 1} \frac{Q_{kl}^2}{\kappa_{kl}} + 2 \sum_{i=1}^{n} p_i \sum_{k \in G_i \cap \mathcal{F}} q_k = D + C \tag{3.55}$$

where C is constant for any flow field Q_{kl} that satisfies conservation of mass, the prescribed flow boundary condition, and $Q_{kl} = 0$ whenever $\kappa_{kl} = 0$, which is necessary for $f < \infty$

thus necessary for Q_{kl} being a global minimizer of f when κ_{kl}'s are fixed. So, if Q_{kl} is not already the Kirchhoff flow and we change the current Q_{kl}'s to the Kirchhoff flow (the network is physical according to the same argument in Section 3.8) then we will decrease the complementary dissipation, which is now equivalent to decreasing dissipation. Thus flow adjusting gives us a network with strictly smaller smaller dissipation, contradicting our assumption that we were starting with a global minimizer.

To complete our proof we must consider the case that we do need to disconnect the last path and this last path has constant flow on it. This path cannot comprise the whole network because if it were to comprise the entire network from the assumption $\mathcal{F} \neq \phi$ we must have $k_i \in \mathcal{F}$ for $1 < i < N$ where N denotes the number of vertices in this path (that is all the path vertices between $i = 1$ and $i = N$, exclusively, are flow vertices) and there is at least one such interior vertex, or there is an isolated $k \in \mathcal{F}$ that does not connect to any other vertex, which cannot be true for a physical network. Then $\sum_{l\,:\,\langle k_i,l\rangle=1} Q_{k_i l} = 0$, a contradiction to the fact that k_i is a flow vertex. Thus we can disconnect the last path in any case and the argument goes through as before to a contradiction.

□

3.10 Proof of Proposition 3.4.3

Proof. The material-invariance property of minimally dissipative network under material constraint (3.25) means that all the global minimizers will have the same dissipation if their materials are scaled to be the same. To see this suppose $\{\kappa_{kl}\}, \{\kappa'_{kl}\}$ are minimally dissipative networks with material K, K'. Consider the network $\{\beta\kappa_{kl}\}$ with $\beta = (\frac{K'}{K})^2$, so that $\{\beta\kappa_{kl}\}$ has material K'. Then since $\{\kappa'_{kl}\}$ is a minimally dissipative network with material K' we have

$$\frac{D}{\beta} \doteq \sum_{k>l,\langle k,l\rangle=1} \frac{Q_{kl}^2}{\beta\kappa_{kl}} \geq \sum_{k>l,\langle k,l\rangle=1} \frac{Q_{kl}'^2}{\kappa'_{kl}} = D'. \tag{3.56}$$

Similarly if we define $\beta' = (\frac{K}{K'})^2 = \frac{1}{\beta}$ we have

$$\frac{D'}{\beta'} \geq D \Rightarrow D' = \frac{D}{\beta} \tag{3.57}$$

and the networks $\{\kappa_{kl}\}, \{\kappa'_{kl}\}$ have the same dissipation if their materials are scaled to be the same. This implies that if $\{\hat{\kappa}_{kl}\}$ is a minimally dissipative network with material $K = 1$, then $\{\beta\hat{\kappa}_{kl}\}$ is a minimally dissipative network of any $K > 0$ with $\beta = K^2$. While $\{\hat{\kappa}_{kl}\}$ is not unique since all the minimally dissipative networks with $K = 1$ have the same dissipation it does not matter which network we use. Now consider a minimally dissipative network $\{\kappa_{kl}\}$ with material penalty under coefficient a (3.26). Suppose this network has material K. The network must be a minimally dissipative network with material constraint K. If it were not also the minimally dissipative network, then the minimally dissipative network would have a smaller value of Θ in Equation (3.26). Thus we can assume $\kappa_{kl} = \beta\hat{\kappa}_{kl}$ where $\beta = K^2$. A concern is that global minimizers of (3.26) under the same coefficient a may have different amounts of material. However since they all have the form $\{\beta\hat{\kappa}_{kl}\}$ for some unit network $\{\hat{\kappa}_{kl}\}$ we can calculate

$$\Theta = \sum_{k>l,\langle k,l\rangle=1} \frac{\hat{Q}_{kl}^2}{\beta\hat{\kappa}_{kl}} + a \sum_{k>l,\langle k,l\rangle=1} \beta^{\frac{1}{2}}\hat{\kappa}_{kl}^{\frac{1}{2}} d_{kl} = \frac{\hat{D}}{\beta} + a\beta^{\frac{1}{2}}. \tag{3.58}$$

If $\{\beta\hat{\kappa}_{kl}\}$ is truly a global minimizer the derivative must vanish since $\Theta \to \infty$ as $\beta \to 0^+, \infty$, i.e.

$$0 = \frac{d\Theta}{d\beta} = -\frac{\hat{D}}{\beta^2} + \frac{a}{2}\beta^{-\frac{1}{2}} \Rightarrow \beta = (\frac{2\hat{D}}{a})^{\frac{2}{3}}. \tag{3.59}$$

Since $\beta = K^2$ where K is the material of the network $\{\beta\hat{\kappa}_{kl}\}$ we have

$$K = (\frac{2\hat{D}}{a})^{\frac{1}{3}} \tag{3.60}$$

and in particular, all networks must have the same value of K. This bijection $K(a)$ between material constraint and coefficient of material penalty shows that the two different formulations are equivalent for minimally dissipative network under the material-invariance assumption. □

3.11 Acknowledgments

This research was funded by grants from the NSF (under grant number DMS-1351860 to MR). SSC was also supported by the National Institutes of Health, under a Ruth L. Kirschstein National Research Service Award (T32-GM008185). The contents of this chapter are solely the responsibility of the authors and do not necessarily represent the official views of the NIH. MR also thanks Eleni Katifori and Karen Alim for useful discussions, and the American Institute of Mathematics for hosting him during one part of the development of this chapter.

CHAPTER 4

Microvascular Networks with Uniform Flow

This chapter was based on: Shyr-Shea Chang and Marcus Roper. "Microvascular networks with uniform flow." *Journal of Theoretical Biology*, 462, 48–64, 2019.

4.1 Introduction

The large vessels within animal ardiovascular networks are widely believed to be shaped primarily by the necessity of minimizing the cost of transport. This minimization leads to Murray's law for the relationship between a vessel's radius and the flow of blood through it, which has been verified in dog intestine microvasculature and plant bundle network [She81, MSA03]. The idea that networks should be organized to optimize transport costs for given amount of material investment provides a powerful tool for understanding the organization of networks, and underpins use of CFD models to optimize vascular geometries in cardiac surgery [MBR09], as well as studies explaining the scaling of metabolic needs with organism size [WBE97, GBW01]

Work on cardiovascular network optimization has focused primarily on the largest vessels in the network. Do the same optimization principles and constraints apply for finer vessels – arterioles and capillaries? Indeed if we divide the cardiovascular network into levels, we can estimate the total dissipation within each level as the product of the pressure drop between the level and the next and the total volume of blood passing through all vessels in that level per unit time. Now since we expect the same volume blood to be cleared through every level of the network in its passage from the heart to the finest vessels of the network, pressure drops alone become a proxy for the relative dissipations occurring at different levels. In the

pressure measurements summarized in Guyton and Hall [Hal15], we find the pressure drop from the arteriole level to the capillary level (~ 60 mmHg) accounts for half of the total drop from the heart to the capillary level (~ 120 mmHg).

Mathematical modeling of microvascular networks has illuminated how networks with statistically predictable properties may emerge from the growth of vessels following rules for oxygen taxis and self avoidance [LPS01, HCR12], the disconnection and reconnection of capillaries [NEL06], and the remodeling of small vessels in response to the blood flows they carry [CJL12]. However, despite the success of these mechanistic models for network formation, there are, to our knowledge, no works that have identified physical principles that may explain microvascular network organization and vessel geometries in the same way that Murray's law describes the largest vessels within the network. For example, while Hu and Cai [HC13] have hypothesized that capillary networks minimize transport costs, we are aware of no data that shows that principles of dissipation minimization extend to these vessels. Indeed microvascular networks typically contain abundant loops [COA03, WHY14, BTK13, SRB15] (also see Fig. 4.1), but minimally dissipative networks, when subject to constant loads, can be proven to never contain loops [Dur07, CR18], at least when supplying steady flows of blood. Hence, the minimization of dissipation alone can not explain organization in microvascular networks [HVS96, PHL10]. Our study of zebrafish trunk vasculature suggests that blood flows are uniformly distributed among fine vessels at the cost of transport efficiency, that is red blood cells are delivered at identical rates to the finest vessels of the trunk (i.e. the intersegmental vessels) [CTB17]. Maintaining uniform flows across each vessel requires precise tuning of vessel radii. To show that tuning is needed we compare the real zebrafish trunk flow with flows in a ensemble of theoretical zebrafish trunk vasculatures. These theoretical vasculatures are created by simply permuting the radii measured in the real zebrafish trunk vessels. In all of $10,000$ theoretical trunk vasculatures, we found that the partitioning of blood flows between finest vessels, measured by the coefficient of variation (CV) of flow was less uniform than in the real zebrafish trunk (Fig. 4.2). The same analysis reveals a trade-off between transport efficiency and flow uniformity: All of the simulated networks had lower dissipation than the real network, and in general dissipation decreased as CV of flows in-

creased. Thus, uniform flow is bought at the cost of decreased transport efficiency. Why might microvascular networks, like the zebrafish trunk, be adapted for uniform flow? Blood flow may serve as a proxy for oxygen perfusion; since red blood cells carry oxygen that then diffuses from the vessel into the tissue that surrounds it, uniform delivery of red blood cells to vessels may be an important precondition for uniform perfusion (but see Discussion). Indeed when we simulated oxygen perfusion in a model zebrafish trunk in which every fine vessel was assigned the same radius, we found that oxygen entering the trunk from the blood was strongly concentrated around the fine vessels closest to the fish's heart [CTB17]. The evolutionary adaptation to vessels to create oxygen perfusion [MM07] may result in microvascular networks with optimally uniform blood flow, but a detailed comparison between networks with uniform blood flow with real microvascular networks is lacking. To determine whether optimization for uniform flow can explain the structure of real microvascular networks, we develop in this chapter an algorithm for generating networks that optimize arbitrary functions of flow, going beyond previous works (summarized in Table 4.1) that have computed networks that optimize transport costs (and in the case of [KSM10] resistance to damage).

To find the uniform flow networks we devise a gradient descent algorithm with Lagrange multipliers to tune the hydraulic conductances of vessels and derive uniform flow networks under fixed network topologies. At each step gradient descent algorithms calculate the optimal direction to perturb the variables in a system to optimize a target function, and approach the optimum after several small steps [CZ13]. Lagrange multipliers are used widely to solve constrained optimization problems [NR18]. In our algorithm they are implemented to impose the laws of flow conservation in the network and to constrain the cost of maintaining the network. We use the algorithm to study uniform flow networks (1) on a model capillary bed consisting of a rectangular grid with single inflow (arteriole) and outflow (venule) (Fig. 4.1A), and (2) on a model of the zebrafish trunk that includes both main trunk vessel (dorsal aorta) and the fine (intersegmental) vessels that branch off from it (Fig. 4.1B).

In particular, we compare the morphologies of minimally dissipative and uniform flow networks. We find that uniform flow capillary beds contain loops that are not present in minimally dissipative networks. We are able to analytically show that, in a class of networks we

call stackable, the blood flows in uniform flow networks agree with those in uniform conductance networks (See Section 4.3.2), hence they provably contain loops. Stackable networks include other popular models for capillary beds branching trees and honeycomb grids, as well as square grids. We show that, in zebrafish trunk topology, the real conductances of vessels are in almost exact accordance with the conductances required to create uniform flow. These results suggest that principle of uniform flow explains the zebrafish trunk network geometry. By contrast, minimization of dissipation produces networks with unrealistic morphologies. Our algorithm will then allow the uniform flow to be evaluated as an optimization principle for general microvascular networks.

To explore how uniform flow networks may yet be constrained by transport costs, we calculate networks in the zebrafish trunk while constraining both the total cost of the vessel material and the blood flow dissipation. When the relative importance of transport cost is gradually increased, we observed an abrupt change in both the flow uniformity and network morphology, resembling a phase transition: in particular, up until dissipation reaches a critical point, the optimal network is apparently unconstrained by dissipation. Thus even when a network is actually subject to multiple constraints, it may apparently be organized to ignore all but a subset of these constraints. Thus optimizing a single target function (e.g. dissipation) may be endowed with surprising power to predict shapes of real networks that are, in reality, targeting multiple functions [Mur26b].

The rest of this chapter is organized as follows: In Section 4.2.1 we introduce the mathematical notations for describing microvascular networks. In Section 4.2.2 we describe a gradient descent algorithm to find general optimal networks. In Sections 4.2.3 – 4.2.7 we write down the detailed formulation of the algorithm when finding minimally dissipative and uniform flow networks under different topologies and constraints. In Section 4.3.1 we use the algorithm to calculate minimally dissipative networks and show that they agree with previous work. In Section 4.3.2 we compare minimally dissipative and uniform flow networks on the capillary bed model (a square grid). In Section 4.3.3 we extend our results to uniform flow zebrafish trunk networks, and show that the principle of uniform flow produces networks that match experimental data. In Section 4.3.4 we impose both material cost and dissipa-

tion as constraints on uniform flow networks, and describe a phase transition in network morphology that occurs as the relative weight of the two constraints is varied.

Target functional	Constraint	Method
$\sum \frac{Q_{kl}^2}{\kappa_{kl}}$	$\sum \kappa_{kl}^\gamma$	local topological optimization [Dur06], global optimization [BM07], structural adaptation [HC13], growth and structural adaptation [RK16], Section 4.3.1
$\sum \frac{Q_{kl}^2}{\kappa_{kl}}$ with damage and flow fluctuations	$\sum \kappa_{kl}^\gamma$	global optimization [KSM10], fluctuating source [Cor10]
$\sum \frac{1}{2} Q_{kl}^2$	$\sum \kappa_{kl}^\gamma$	Section 4.3.2
$\sum \frac{1}{2}(Q_{kl} - \bar{Q})^2$	$\sum \kappa_{kl}^\gamma$	Section 4.3.3
$\sum \frac{1}{2} Q_{kl}^2$	$\sum \left(\kappa_{kl}^\gamma + a\frac{Q_{kl}^2}{\kappa_{kl}}\right)$	Section 4.3.4
$\sum \frac{1}{2}(Q_{kl} - \bar{Q})^2$	$\sum \left(\kappa_{kl}^\gamma + a\frac{Q_{kl}^2}{\kappa_{kl}}\right)$	Section 4.3.4

Table 4.1: Comparison between previous works on optimal transport networks and the results presented in this work. Previous works focus on optimizing dissipation either alone or in combinations with damage resistance or flow fluctuations (first two rows). They constrain the network by imposing a fixed material cost of vessels. Our work agrees with previous work on the morphologies of minimally dissipative networks under material constraint (first row), but extends the classes of the target functions and constraints. Specifically we study uniform flow networks, under both material constraint and a Murray constraint that includes dissipation (last four rows).

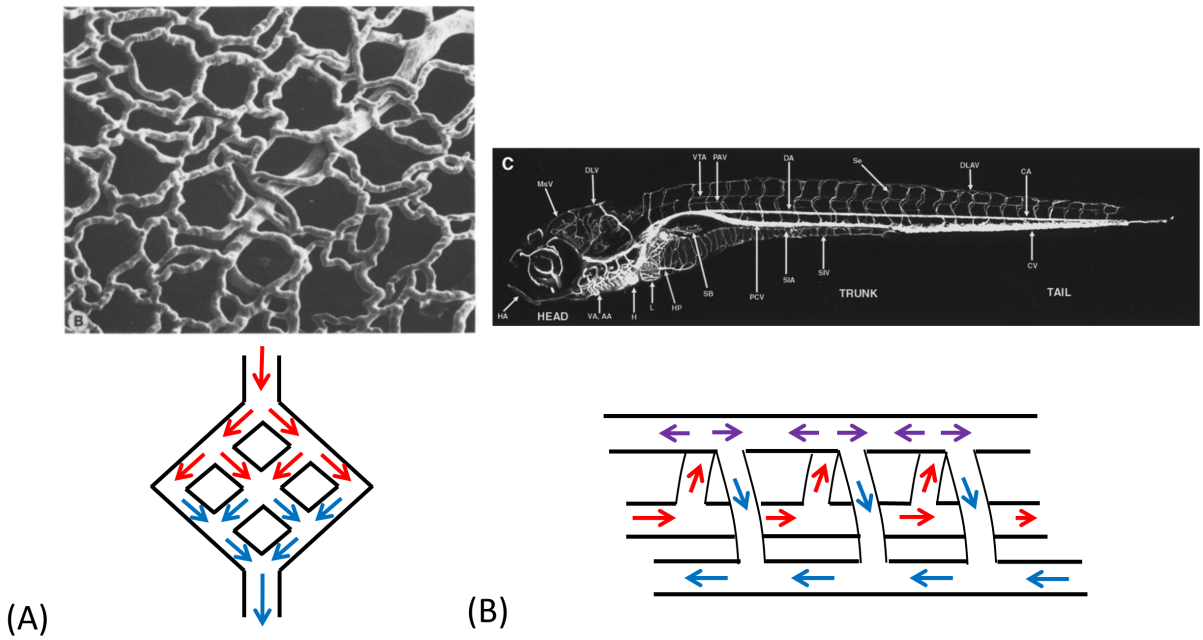

Figure 4.1: Examples of complex microvascular networks and the corresponding model networks. (A) Capillary bed in salamander skin [MJ79]. (B) Microvascular network of zebrafish 7.5 days post fertilization (dpf) embryo [IHW01, CTB17].

4.2 Methods

4.2.1 Physical modeling and notation

First we mathematically frame the problem of finding optimal networks for general network topology. Consider an undirected graph $(\mathcal{V}, \mathcal{E})$ with V vertices $k = 1, \ldots, V$. For any given 2 vertices k, l we write $\langle k, l \rangle = 1$ if there is a edge linking k and l and $\langle k, l \rangle = 0$ if k and l are not linked. Each edge in the network is assigned a conductance κ_{kl}; the flow Q_{kl} in the edge is then determined by $Q_{kl} = (p_k - p_l)\kappa_{kl}$, where p_k and p_l are respectively the pressures at the vertices k and l. In typical microvascular networks vessel diameters are on the order of 10 μm, and blood flow velocities are on the order of 1 mm/s, so the Reynolds number, which represents the relative importance of inertia to viscous stresses, is $Re = UL/\nu \approx 4 \times 10^{-3}$, using the viscosity of whole blood $\nu \approx 2.74$ mm^2/s. Since $Re \ll 1$ inertial effects may be neglected, and the conductances of individual vessels will be obtained by Hagen–Poiseuille's

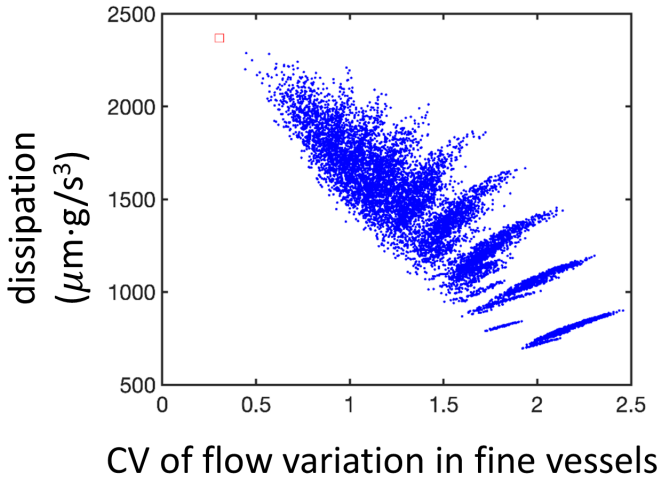

Figure 4.2: Zebrafish trunk microvascular network (red square) optimizes uniform flow in fine vessels at a high transport cost, compared to untuned networks (blue dots). The untuned networks are obtained by randomly permuting the conductances of fine vessels in a real zebrafish trunk network [CTB17]. The transport cost is characterized by dissipation [BM07, Ach90], and the flow variation is quantified by the coefficient of variation of flows in the fine vessels.

law [Ach90]:

$$\kappa = \frac{\pi r^4}{8\mu\ell} \tag{4.1}$$

where κ is the conductance, μ is the blood viscosity, ℓ is the vessel length, and r is the vessel radius. In ascribing a well-defined pressure to each vertex within the graph, and applying the Hagen–Poiseuille law to compute edge flows from pressures, we assume that there are unidirectional flows within each vessel, ignoring the entrance and exit effects that occur when vessels branch or merge [CTB17]. In capillary networks hydraulic conductances might change with concentration of red blood cells, a physiological effect known as Fahraeus–Lindqvist effect [PS05], which can change our expression here. Although our method can be generalized to include this effect (see Discussion), we will use our default model (4.1) throughout this work.

The networks we consider consist of vertices and predescribed edges where conductance

may be positive (or zero if required by the algorithm, in which case the vessel is pruned) along with two kinds of boundary conditions on vertices (Fig. 3.3). At any vertex in the network we can either impose Kirchoff's first law (conservation of flux)

$$\sum_{l\,:\,\langle k,l\rangle=1} Q_{kl} = \sum_{l\,:\,\langle k,l\rangle=1} \kappa_{kl}(p_k - p_l) = q_k \qquad \forall 1 \le k \le V \ , \tag{4.2}$$

where q_k is the total flow of blood entering the network (or leaving it if $q_k < 0$) at vertex k, or we impose $p_k = \bar{p}_k$ (i.e. pressure is specified). We say a vertex is in $\mathcal{V}_D = \mathcal{P}$ (or is Dirichlet) if pressure is specified, or in $\mathcal{V}_N = \mathcal{F} \cup \mathcal{N}$ (is Neumann) if Kirchhoff's first law is imposed (possibly with inflow or outflow). This system of V linear equations forms a discretized Poisson equation with Neumann and Dirichlet boundary conditions imposed on selected vertices, and the flow is uniquely solvable if and only if each connected component of the network (connected by edges with positive conductances) either has at least one Dirichlet vertex or $\sum_{k\in\mathcal{V}_N} q_k = 0$ with sum restricted to the component [LP16, CR18]. The uniform flow network has the flows on all edges being as uniform as possible, that is the flows $\kappa_{kl}(p_k - p_l)$ on some subset of the edges are close to being identical (See Section 4.2.4 for a detailed discussion). However, to understand the tradeoffs between perfusion and other network objectives, we may also add e.g. total viscous dissipation as an additional cost. We therefore have the general goal of how to tune the conductances within the network to minimize arbitrary predetermined objective function $f(\{p_k\}, \{\kappa_{kl}\})$, where $\{p_k\}$ means the set of all p_k's and $\{\kappa_{kl}\}$ denotes the set of all κ_{kl}'s. Previous works (see Table 4.1) have shown how to generate networks that minimize the total viscous dissipation occurring within the network: $f(\{p_k\}, \{\kappa_{kl}\}) = \sum_{k>l,\langle k,l\rangle=1} \kappa_{kl}(p_k - p_l)^2$.

This optimization is complicated by the coupling of the pressures $\{p_k\}$ and conductances $\{\kappa_{kl}\}$ through Equations (4.2). Since the relationship between $\{p_k\}$ and $\{\kappa_{kl}\}$ is holonomic, we may incorporate it into a functional via Lagrange multipliers. Lagrange multipliers are a widely used method to solve optimization problems when the variables are subject to holonomic constraints (i.e. must solve some differentiable equation). They allow us to treat the variables as if they were independent for the purpose of calculating partial derivatives, at the cost of introducing new auxiliary variables – one for each constraint [CZ13]. The

functional that we want to minimize in this chapter will take the form:

$$\Theta = f(\{p_k\}, \{\kappa_{kl}\}) + \lambda \left[\sum_{k>l, \langle k,l \rangle = 1} \left(a\kappa_{kl}(p_k - p_l)^2 + \kappa_{kl}^{\gamma} d_{kl}^{1+\gamma} \right) - K \right] - \sum_k \mu_k \left(\sum_{l, \langle k,l \rangle = 1} \kappa_{kl}(p_k - p_l) - q_k \right). \tag{4.3}$$

which has $V_N + 1$ Lagrange multipliers: a set $\{\mu_k | k \in \mathcal{V}_N\}$ enforcing Kirchoff's first law on Neumann vertices (the set $\mathcal{V}_N$ with $|\mathcal{V}_N| = V_N$), and a single multiplier λ that constrains the amount of energy that the organism can invest in pushing blood through the network and in maintaining the vessels that make up the network. The transport constraint is made up of two terms: $\sum \kappa_{kl}(p_k - p_l)^2$ represents the total viscous dissipation within the network, while $\sum \kappa_{kl}^{\gamma} d_{kl}^{\gamma+1}$ represents the total cost of maintaining the network (the *material constraint*) [Mur26b, BM07, KSM10], with d_{kl} being the vessel length. K is the total amount of material and dissipation to which the network should adhere. The exponent γ can be altered to embody different models for the cost of maintaining a network. In our default model (Equation (4.1)) conductance of an edge is proportional to the fourth power of its radius, so if the cost of maintaining a particular vessel is proportional to its surface area (and thus to its radius), then we expect $\gamma = 1/4$, while if the cost is proportional to volume then $\gamma = 1/2$. In general we need $\gamma < 1$ to produce well posed optimization problems (otherwise, the cost of building a vessel can be indefinitely reduced by subdividing the vessel into finer parallel vessels). We initially adopt the same material cost function definition as was used in previous work, i.e. $a = 0$ [KSM10, BM07], but in the latter part of the chapter we will incorporate a parameter $a > 0$ that represents the relative importance of network maintenance and dissipation to the cost of maintaining the network. When presenting optimal networks, we will discuss the effect of varying a (as well as asymptotic limits in which $a \to 0$) upon the network geometry. Since Murray's work on dissipation-minimizing networks [Mur26b, Mur26a] is equivalent to minimizing the constraint function [CR18], we will adopt the shorthand of calling the network cost term the *Murray constraint*.

Table 4.1 gives a systematic description of previous work on minimizing functionals across networks, as well as outlining the new results that will be presented here on the optimization

of (4.3).

4.2.2 A gradient descent method with extended Lagrange multipliers

At any local minimum of Θ, each of the partial derivatives of (4.3) must vanish. In order to locate such points, we adopt a gradient descent approach, in which κ_{kl} are treated as adiabatically changing variables. That is: $\frac{\partial\Theta}{\partial\kappa_{kl}}$ is calculated, and an optimal perturbation of the form $\delta\kappa_{kl} = -\alpha\frac{\partial\Theta}{\partial\kappa_{kl}}$ is applied to ensure Θ decreases each time the conductances in the network are updated. At the same time, the other variables in the system, namely $\{p_k, \mu_k, \lambda\}$, are assumed to vary much more rapidly, to remain at a local equilibrium, so that:

$$\frac{\partial\Theta}{\partial p_k} = \frac{\partial\Theta}{\partial\mu_k} = \frac{\partial\Theta}{\partial\lambda} = 0 \ . \tag{4.4}$$

Our ability to perform gradient descent therefore hinges on our ability to solve the system of $2V_N + 1$ equations (4.4) for each set of conductances $\{\kappa_{kl}\}$ that the network passes through on its way to the local minimum. Fortunately it turns out that for general target functions f only one nonlinear equation in a single unknown variable needs to be solved for to solve all of the conditions (4.4); the other equations are linear and can be solved with relatively low computational cost.

Because we will consider multiple variants of the Murray constraint, in what follows we will write the summand that enforces the Murray constraint in the general form: $\lambda g(\{p_k\}, \{\kappa_{kl}\})$. Then the condition that $\frac{\partial\Theta}{\partial\mu_k} = 0$, $k \in \mathcal{V}_N$, merely enforces the system of mass conservation statements at each Neumann-vertex in the network (4.2). These equations represent a discretized form of the Poisson equation and can be solved by inverting a sparse $V_N \times V_N$ matrix with $O(E, V_N)$ entries [LP16]. That is, we write:

$$Dp = f \tag{4.5}$$

where $f_k = q_k$ is the prescribed inflow at Neumann vertices and $f_k = \bar{p}_k$, the prescribed

pressure at Dirichlet vertices. $-D$ is a form of graph Laplacian:

$$D_{kl} \doteq \begin{cases} \sum_{l,\langle k,l\rangle=1} \kappa_{kl}\,, & k = l, k \notin \mathcal{V}_D \\ -\kappa_{kl}, & \langle k,l\rangle = 1\,, k \notin \mathcal{V}_D \\ \kappa^{(1)}, & k = l\,, k \in \mathcal{V}_D \\ 0\,, & \text{otherwise} \end{cases} \tag{4.6}$$

where $\kappa^{(1)} = 1$. (For any $\kappa^{(1)} \neq 0$, D is full rank; we will make use of other positive constant values for $\kappa^{(1)}$ later.)

To solve for $\{\mu_k\}$, we consider the system of equations $\frac{\partial \Theta}{\partial p_k} = 0$, $k \in \mathcal{V}_N$:

$$0 = \left(\frac{\partial f}{\partial p_k} + \lambda \frac{\partial g}{\partial p_k}\right) - \sum_{l,\langle k,l\rangle=1} (\mu_k - \mu_l)\kappa_{kl}. \tag{4.7}$$

If λ, $\{p_k\}$ and $\{\kappa_{kl}\}$ are all known then these equations again take the form of a discrete Poisson equation, however, just as with the solution of the pressure equation, these equations themselves do not admit unique solutions unless a reference value of μ_k is established. If $\mathcal{V}_D \neq \phi$, i.e. if pressure is specified at least one vertex within $(\mathcal{V}, E)$, then $\mu_k = 0\ \forall k \in \mathcal{V}_D$ and Eqns. (4.7) admit a unique solution; otherwise the μ_k's are determined up to a constant (see Appendix C). For some forms of target function f and constraint function g, we will show that μ_k's for the minimizer are directly related to the pressures, with no need to solve the Poisson equation by a separate matrix inversion.

However, to use Equation (4.7) to solve for μ_k it is still necessary to know the Lagrange multiplier that enforces the Murray constraint (i.e. λ). The simplest way to derive λ is to dictate that the variational of the constraint function should vanish when κ_{kl} is updated, since the constraint function should remain constant under changes in conductances, i.e.:

$$0 = \sum_{k \notin \mathcal{V}_D} \frac{\partial g}{\partial p_k} \delta p_k + \sum_{k>l,\langle k,l\rangle=1} \frac{\partial g}{\partial \kappa_{kl}} \delta \kappa_{kl} \tag{4.8}$$

(we set $\delta p_k = 0$ if $k \in \mathcal{V}_D$) where

$$\delta \kappa_{kl} = -\alpha \frac{\partial \Theta}{\partial \kappa_{kl}} = -\alpha \left(\frac{\partial f}{\partial \kappa_{kl}} + \lambda \frac{\partial g}{\partial \kappa_{kl}} - \kappa_{kl}(\mu_k - \mu_l)(p_k - p_l)\right). \tag{4.9}$$

At this point in our calculation $\{\delta p_k\}$ and $\{\mu_k\}$ are undetermined. The Lagrange multipliers $\{\mu_k\}$ can be solved in terms of the still unknown λ from (4.7) (see Appendix C). The $\{\mu_k\}$

are linear functions of λ since (4.7) is a linear system. To obtain δp_k for each $k \in \mathcal{V}_N$ we calculate the variational in Kirchhoff's first law:

$$\sum_{l,\langle l,k\rangle=1} \delta\kappa_{kl}(p_k - p_l) + \kappa_{kl}(\delta p_k - \delta p_l) = 0. \tag{4.10}$$

When written in matrix form, the matrix multiplying $\{\delta p_k\}$ is again the negative of the graph Laplacian, $-D$. Thus $\{\delta p_k\}$ can be solved in terms of λ so long as the original matrix system is solvable for $\{p_k\}$. Since $\{\mu_k\}$ are linear in λ, $\{\delta p_k\}$ are also linear in λ, which implies that the right hand side of Equation (4.8) is linear in λ. Therefore λ can be solved in closed form from Equation (4.8), and the optimal variation $\delta\kappa_{kl}$ can be determined from equation (4.9).

With $\{p_k\}$, $\{\mu_k\}$, and λ solvable given $\{\kappa_{kl}\}$ we can perform gradient descent using Equation (4.9) and numerically approach a minimizer. However our descent method has the following limitations: 1. For finite step sizes α, conductances may drop below 0 when perturbed according to Equation (4.9). 2. The method only conserves the Murray function up to terms of $O(\delta\kappa)$.

To avoid negative conductances we truncate at a small positive value ϵ at each step, i.e. set:

$$\kappa_{kl}^{(n+\frac{1}{2})} = \max\{\kappa_{kl}^{(n)} - \alpha\frac{\partial\Theta}{\partial\kappa_{kl}}, \epsilon\}. \tag{4.11}$$

To ensure that the constraint is exactly obeyed we then project the conductances $\{\kappa_{kl}^{(n+\frac{1}{2})}\}$ onto the constraint manifold $g(\{p_k\}, \{\kappa_{kl}\}) = 0$, via a projection function:

$$\kappa_{kl}^{(n+1)} = h(\kappa_{kl}^{(n+\frac{1}{2})}) \quad \forall\langle k,l\rangle = 1, k > l. \tag{4.12}$$

Throughout this work we consider three possible projection functions: One choice is to project according to the normal of the constraint surface:

$$\kappa_{kl}^{(n+1)} = \kappa_{kl}^{(n+\frac{1}{2})} - \beta\frac{\partial g}{\partial\kappa_{kl}}(\{p_k^{(n+\frac{1}{2})}\}, \{\kappa_{kl}^{(n+\frac{1}{2})}\}), \quad \forall\langle k,l\rangle = 1, k > l \tag{4.13}$$

The value of β must be chosen numerically to ensure that $g(\{p_k^{(n+1)}\}, \{\kappa_{kl}^{(n+1)}\}) = 0$ exactly. This entails recomputing the pressure distribution $\{p_k^{(n+1)}\}$ for each β value, and secant search on β to obtain the root. Another approach we have followed is varying the parameter

λ. This method has comparable complexity to projection on $\{\kappa_{kl}^{(n+\frac{1}{2})}\}$; since the $\{\mu_k\}$ depend linearly on λ via Equation (4.7), $\{\kappa_{kl}^{(n+1)}\}$ depends linearly on the parameter λ. However, just as with the projection method, we must still recompute the $\{p_k^{(n+1)}\}$ for each trial set of $\{\kappa_{kl}^{(n+1)}\}$. Moreover, for some target functions f or constraint functions g, it is difficult to derive closed-form expressions for λ (i.e. to calculate the partial derivatives $\frac{\partial f}{\partial p_k}$ and $\frac{\partial g}{\partial p_k}$). In this case λ may only be computed numerically, by solving $g(\{p_k^{(n+1)}(\lambda)\}, \{\kappa_{kl}^{(n+1)}(\lambda)\}) = 0$. A third approach that we have adopted is to simply scale the conductances:

$$\kappa_{kl}^{(n+1)} = \beta \kappa_{kl}^{(n+\frac{1}{2})}, \quad \forall \langle k, l \rangle = 1, k > l \tag{4.14}$$

where β is chosen to satisfy the Murray constraint. This method produces theoretically suboptimal corrections on the conductances, but it is typically easy to compute a value of β that satisfies the Murray constraint. In particular, under certain boundary conditions, e.g. $p_k = \bar{p}, \ \forall k \in \mathcal{V}_D$ within each connected component of the network (meaning that all pressure vertices within a single connected component have the same imposed pressures, which is trivially true if there is only one Dirichlet vertex in each connected subcomponent of the graph), a rescaling of the conductances throughout the network leaves the fluxes on each edge unaffected. For a uniform flow network, this rescaling affects the constraint function g, but not the target function f.

4.2.3 Calculating minimally dissipative networks

To calculate minimally dissipative networks we set the target function to be the dissipation $\sum_{\langle k,l \rangle = 1, k>l} \kappa_{kl}(p_k - p_l)^2$ and the constraint to be the total amount of material. Thus the function to minimize becomes:

$$\Theta = \sum_{\langle k,l \rangle = 1, k>l} \kappa_{kl}(p_k - p_l)^2 + \lambda \Big(\sum_{\langle k,l \rangle = 1, k>l} \kappa_{kl}^{\gamma} - K^{\gamma} \Big) - \sum_{k \notin \mathcal{V}_D} \mu_k \Big(\sum_{l, \langle k,l \rangle = 1} \kappa_{kl}(p_k - p_l) - q_k \Big). \tag{4.15}$$

Here we ignore d_{kl} since we assume all the vessels have the same length which may be scaled to 1 by choice of units, but different vessel lengths can be readily incorporated by adding d_{kl} back in the following equations. The equations for adiabatic variation of p_k and μ_k are

derived from

$$\frac{\partial \Theta}{\partial p_k} = \sum_{l,\langle k,l\rangle=1} 2\kappa_{kl}(p_k - p_l) - \sum_{l,\langle k,l\rangle=1} \kappa_{kl}(\mu_k - \mu_l), \qquad k \notin \mathcal{V}_D \tag{4.16}$$

and the fixed pressure boundary condition on pressure vertices allows us to specify that:

$$\mu_i = 0 \qquad \forall i \in \mathcal{V}_D \tag{4.17}$$

The μ_k are therefore solving a variant of the Kirchhoff flux conservation equations:

$$D\mu = 2Dp \tag{4.18}$$

with D as defined in Equation 4.6.

This system can be solved for μ_k under the same conditions as the pressure equations being solvable (see Appendix C). In particular if, as in the network topologies we study in this work, the only pressure boundary conditions imposed at vertices in $\mathcal{V}_D$ are of the form $p = 0$, then $\mu_k = 2p_k, \forall k \in \mathcal{V}$, i.e. μ_k's represent the pressures. Now we calculate the derivatives of Θ with respect to the conductances:

$$\frac{\partial \Theta}{\partial \kappa_{kl}} = (p_k - p_l)^2 + \lambda\gamma\kappa_{kl}^{\gamma-1} - (\mu_k - \mu_l)(p_k - p_l) = \lambda\gamma\kappa_{kl}^{\gamma-1} - (p_k - p_l)^2. \tag{4.19}$$

In general we determine λ from Equations (4.8,4.9,4.10). However the constraint function g is independent of $\{p_k\}$ in this case, so Equation (4.8) becomes

$$0 = \sum_{k>l,\langle k,l\rangle=1} \frac{\partial g}{\partial \kappa_{kl}} \delta\kappa_{kl} \tag{4.20}$$

and we can solve λ directly in terms of $\{p_k\}, \{\kappa_{kl}\}$:

$$\lambda = \frac{\sum_{\langle k,l\rangle=1,k>l} \kappa_{kl}^{\gamma-1}(p_k - p_l)^2}{\sum_{\langle k,l\rangle=1,k>l} \gamma\kappa_{kl}^{2\gamma-2}} \tag{4.21}$$

As described in Section 4.2.2 we project $\{\kappa_{kl}\}$ along $\frac{\partial g}{\partial \kappa_{kl}} = \gamma\kappa_{kl}^{\gamma-1}$ after each step of the algorithm. At each step of the algorithm, we solve for the pressures p_k from the conductances $\{\kappa_{kl}\}$, then the μ_k, and then descend according to Eqn. (4.19). Analyzing minimal dissipation on networks allows us to compare the performance of the algorithm described in this chapter with previous work [BM07, KSM10] (See Section 4.3.1).

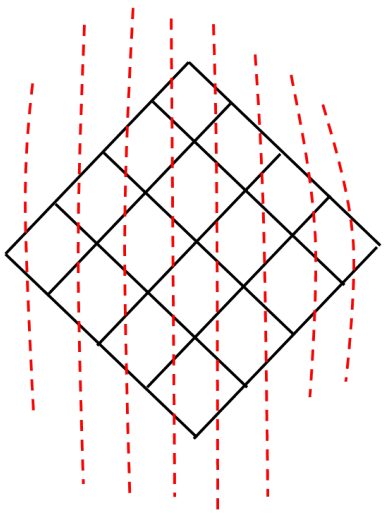

Figure 4.3: A quadrilateral grid (black) can be divided using a set of non-intersecting control surfaces (red dashed lines) such that each edge in the grid is intersected by exactly one control surface.

4.2.4 Calculating microvascular networks with uniform flow

We now turn to other target functions that have not been extensively studied. At the level of micro-vessels it is likely that uniform flow rather than transport efficiency is the dominant principle underlying network organization, as shown in the comparison between the zebrafish trunk network with its untuned counterparts (Fig. 4.2). We frame this question more generally, i.e. ask what organization of vessels achieves a given amount of flow $\bar{Q}$ on all edges or equivalently, how the flow variation

$$f(\{p_k\},\{\kappa_{kl}\}) = \sum_{\langle k,l\rangle=1, k>l} \frac{1}{2}(Q_{kl}-\bar{Q})^2 \tag{4.22}$$

may be minimized by optimal choice of conductances κ_{kl}.

To simplify the target function we expand the function f and abandon the constant term:

$$f(\{p_k\},\{\kappa_{kl}\}) = \sum_{k>l,\langle k,l\rangle=1} \left(\frac{1}{2}Q_{kl}^2 - \bar{Q}Q_{kl}\right). \tag{4.23}$$

Under the assumption that the total flow on all edges is conserved, i.e.:

$$\sum_{\langle k,l\rangle=1,k>l} Q_{kl} = C \tag{4.24}$$

the function f can be reduced to

$$f(\{p_k\},\{\kappa_{kl}\}) = \sum_{\langle k,l\rangle=1,k>l} \frac{1}{2} Q_{kl}^2 \tag{4.25}$$

by ignoring constants. The assumption (4.24) is valid in networks provided that the network may be divided into levels: that is, a series of control surfaces may be constructed between source (inflow to the network) and sink (outflow from the network), with each edge intersected by exactly one control surface and each path from source to sink intersecting all control surfaces (Fig. 4.3). We call networks with this property stackable. The stackability of a network depends both on its geometry and the positions of sources and sinks: a honeycomb grid is also stackable when source and sink are arranged across the diameter of the network, but the square-grid network is not stackable if the sink were on the bottom instead of the right corner. Then since the total flow across each control surface is the same, the total flow over all network edges is $\sum_{k>l,\langle k,l\rangle=1} Q_{kl} = SF$ where F is the total sink strength and S is the number of control surfaces. Both symmetric branching trees and quadrilateral grids (such as the one shown in Fig. 4.3) are examples of stackable networks, and both can be used as simplified models of microvascular transport networks [HCR12].

For the model capillary bed network we have only one pressure vertex, which means that a multiplicative scaling in all the conductances does not affect the flow. Therefore solving unconstrained optimal networks is equivalent to solving those with material constraints. Without any constraint the function to be optimized can now be written as

$$\Theta = \sum_{\langle k,l\rangle=1,k>l} \frac{1}{2}(p_k - p_l)^2 \kappa_{kl}^2 - \sum_{k\in\mathcal{V}_N} \mu_k \left(\sum_{l,\langle k,l\rangle=1} \kappa_{kl}(p_k - p_l) - q_k \right). \tag{4.26}$$

To do the gradient descent we calculate

$$\frac{\partial\Theta}{\partial p_k} = \sum_{l,\langle k,l\rangle=1} \kappa_{kl}^2 (p_k - p_l) - \sum_{l,\langle k,l\rangle=1} (\mu_k - \mu_l)\kappa_{kl}, \qquad k \notin \mathcal{V}_D \tag{4.27}$$

$$\frac{\partial \Theta}{\partial \kappa_{kl}} = \kappa_{kl}(p_k - p_l)^2 - (\mu_k - \mu_l)(p_k - p_l). \tag{4.28}$$

At each step we can solve for μ_k by setting $\frac{\partial \Theta}{\partial p_k} = 0$ in Eqn. (4.27), along with $\mu_k = 0, k \in \mathcal{V}_D$, and we can calculate the gradient from Eqn. (4.28). Note that here we have neither Murray nor material constraint, so a numerical projection is not required to ensure that the constraint is being exactly met, and the network can be obtained by repeating the procedure until convergence (See Section 4.3.2).

4.2.5 Calculating embryonic zebrafish trunk vasculatures with uniform flow

To compare putative network optimization principles on the zebrafish trunk vasculature, we start by identifying our model for the trunk network. Blood flows into the trunk of the zebrafish from the heart through the dorsal aorta and then passes into minute vessels called intersegmental (Se) vessels. Blood then returns to the heart via the cardinal vein. These vessels are arranged just like rungs (Se) and parallels (cardinal vein and dorsal aorta) of a ladder (Fig. 4.7A). Most gas exchange in the network is assumed to occur in the Se vessels. As the zebrafish develops further minute vessels form between the Se vessels, converting the trunk into a dense reticulated network [IHW01]. We focus on the mechanisms underlying flow distribution in the main fine vessels. Since the zebrafish trunk network is symmetric, we can consider only half of the network consisting of the aorta and intersegmental arteries, designated by vertices $v_1, ..., v_{2n+1}$ and edges $e_1, ..., e_{2n}$ with n being the number of Se vessels. Since this topology does not satisfy the assumption (4.24) we have to consider the full uniform flow target function:

$$f(\{p_k\}, \{\kappa_{kl}\}) = \sum_{i=1}^{n} \frac{1}{2}(Q_{2i} - \bar{Q})^2, \tag{4.29}$$

where $\bar{Q}$ is a predetermined flow for all the capillaries (in the following arguments edge-defined quantities such as Q_i are indexed with the edges, and vertex-defined quantities such as p_i are indexed with the vertices). Using this indexing scheme, the function to be optimized

becomes:

$$\Theta = \sum_{i=1}^{n} \frac{1}{2}\kappa_{2i}^2 p_i^2 - \sum_{i=1}^{n} \bar{Q}\kappa_{2i} p_i - \sum_{i=2}^{n-1} \mu_i[\kappa_{2i-3}(p_i - p_{i-1}) + \kappa_{2i-1}(p_i - p_{i+1}) + p_i\kappa_{2i}]$$
$$- \mu_1[\kappa_1(p_1 - p_2) + p_1\kappa_2 - F] - \mu_n[\kappa_{2n-3}(p_n - p_{n-1}) + p_n\kappa_{2n-1} + \kappa_{2n}p_n]. \quad (4.30)$$

Just as in Section 4.2.4 we do not need to introduce a Lagrange multiplier enforcing the material constraint because the target function only depends on flows, and we can scale all conductances to realize any material constraint without affecting the target function. For performing gradient descent method on this function we calculate the partial derivatives of Θ:

$$\frac{\partial\Theta}{\partial p_i} = \begin{cases} \kappa_{2i}^2 p_i - \bar{Q}\kappa_{2i} - (\kappa_{2i-1} + \kappa_{2i-3} + \kappa_{2i})\mu_i + \kappa_{2i-1}\mu_{i+1} + \kappa_{2i-3}\mu_{i-1}\,, & i \neq 1, n \\ \kappa_2^2 p_1 - \bar{Q}\kappa_2 - (\kappa_1 + \kappa_2)\mu_1 + \mu_2\kappa_1\,, & i = 1 \\ \kappa_{2n}^2 p_n - \bar{Q}\kappa_{2n} - (\kappa_{2n-3} + \kappa_{2n-1} + \kappa_{2n})\mu_n + \kappa_{2n-3}\mu_{n-1}\,, & i = n \end{cases} . \quad (4.31)$$

$$\frac{\partial\Theta}{\partial \kappa_i} = \begin{cases} \kappa_i p_{i/2}^2 - \bar{Q}p_{i/2} - \mu_{i/2}p_{i/2}\,, & i|2 = 0 \\ -(\mu_{\frac{i+1}{2}} - \mu_{\frac{i+3}{2}})(p_{\frac{i+1}{2}} - p_{\frac{i+3}{2}})\,, & i|2 = 1, i \neq 2n-1 \\ -\mu_n p_n\,, & i = 2n-1 \end{cases} . \quad (4.32)$$

Then we impose the physical boundary conditions, i.e. fixed inflow into the network and zero pressure on the ends of the main aorta and the capillaries, and perform gradient descent to find the optimal network (See Section 4.3.3).

Since no constraint is imposed on the uniform flow zebrafish trunk network the explicit relation between vessel radius and conductance does not need to be specified (see Section 4.2.1). Therefore when we compare the uniform flow network to experimental data in Section 4.3.3 we can assume that, instead of the default model (4.1), the occlusive effect of red blood cells contribute to the effective vessel conductance [CTB17].

4.2.6 Calculating uniform flow network on capillary beds under Murray's constraint

So far we have followed previous work [BM07, KSM10] by calculating all of our optimal networks under constraints on the total material (or without constraints if the target function

does not involve conductances). However both material investment and transport costs (i.e. dissipation) may contribute to the total cost of a particular network. We modify our cost function, g, to include both costs. In this case $g(\{p_k\},\{\kappa_{kl}\}) = \sum(a\kappa_{kl}(p_k - p_l)^2 + \kappa_{kl}^\gamma) - K$ depends on both pressure and conductance, and the full mechanism for keeping g constant during the gradient descent needs to be used. Specifically now we are minimizing the function

$$\Theta = \sum_{\langle k,l\rangle=1,k>l} \frac{1}{2}Q_{kl}^2 + \lambda\left(\sum_{\langle k,l\rangle=1,k>l}(a\kappa_{kl}(p_k-p_l)^2+\kappa_{kl}^\gamma) - K\right) - \sum_{k\in\mathcal{V}_N}\mu_k\left(\sum_{l,\langle k,l\rangle=1}\kappa_{kl}(p_k-p_l) - q_k\right) \tag{4.33}$$

with $\gamma = \frac{1}{2}$ and $a > 0$. To calculate the optimal network by this method we need an explicit formula for λ. We introduce several notations to be used later. Suppose $\{b_{ij}\}$ is a set of quantities defined on the edges of the network. For any real constant c we define the matrix for the graph Laplacian with specified boundary conditions as

$$M_b^{(c)} = \begin{cases} \sum_{l,\langle k,l\rangle=1} b_{kl}\,, & k = l, k \notin \mathcal{V}_D \\ -b_{kl}\,, & \langle k,l\rangle = 1 \\ c\,, & k = l, k \in \mathcal{V}_D \\ 0\,, & otherwise \end{cases}. \tag{4.34}$$

We also abbreviate $M_b = M_b^{(1)}$. In the notation of Equation (4.6) $D = M_\kappa$. We define $D^{(n)} = M_{\kappa^n}$ for notational convenience. For a quantity v that is defined on the vertices of the network (such as pressure) we define the graph difference vector $\nabla v \in \mathbb{R}^E$ as

$$\nabla v_{kl} = v_k - v_l \qquad (k,l) \in \mathcal{E}, \tag{4.35}$$

where $\mathcal{E}$ denotes the set of ordered pairs of edges so that each edge only appears once in $\mathcal{E}$. Now we can derive explicit formulas for λ and $\delta\kappa$. From $\frac{\partial\Theta}{\partial p_k} = 0$ we obtain $\mu = D^{-1}D^{(2)}p + 2\lambda a p$ (recall here we have $f = \sum_{k>l,\langle k,l\rangle=1}\frac{1}{2}\kappa_{kl}^2(p_k-p_l)^2, g = \sum_{k>l,\langle k,l\rangle=1} a\kappa_{kl}(p_k - p_l)^2 + \kappa_{kl}^\gamma - K^\gamma$), and so:

$$\frac{\partial\Theta}{\partial\kappa_{kl}} = \lambda[\gamma\kappa_{kl}^{\gamma-1} - a(\nabla p_{kl})^2] + \kappa_{kl}(\nabla p_{kl})^2 - \nabla(D^{-1}D^{(2)}p)_{kl}\nabla p_{kl}. \tag{4.36}$$

We determine λ from the variational:

$$\begin{aligned} 0 = dg &= \sum_{k>l,\langle k,l\rangle=1} \gamma\kappa_{kl}^{\gamma-1}\delta\kappa_{kl} + a\delta\kappa_{kl}\nabla p_{kl}^2 + 2a\kappa_{kl}\nabla\delta p_{kl}\nabla p_{kl} \\ &= \sum_{k>l,\langle k,l\rangle=1} -\alpha(\gamma\kappa_{kl}^{\gamma-1} + a\nabla p_{kl}^2)\Big\{\lambda[\gamma\kappa_{kl}^{\gamma-1} - a\nabla p_{kl}^2] \\ &\quad + \kappa_{kl}\nabla p_{kl}^2 - \nabla(D^{-1}D^{(2)}p)_{kl}\nabla p_{kl}\Big\} + 2a\kappa_{kl}\nabla\delta p_{kl}\nabla p_{kl}. \end{aligned} \tag{4.37}$$

This formula depends on δp; the change in p produced by the change $\kappa \mapsto \kappa + \delta\kappa$. If we assume $p_i = 0\ \forall i \in \mathcal{V}_D$ we can write Equation (4.10) in matrix form as

$$M_{\delta\kappa}p + D\delta p = 0 \tag{4.38}$$

so

$$\delta p = -D^{-1}M_{\delta\kappa}p. \tag{4.39}$$

(Equation (4.38)) can be modified by adding a non-zero vector on the right hand side, if inhomogeneous pressure boundary conditions are applied.) Thus if we define auxiliary variables: $\beta \doteq \gamma\kappa^{\gamma-1} - a\nabla p^2, \chi \doteq \kappa\nabla p^2 - \nabla(D^{-1}D^{(2)}p)\nabla p$, so that $\delta\kappa = -\alpha(\lambda\beta + \chi)$, then:

$$\begin{aligned} 0 &= -\alpha\Big\{\lambda \sum_{k>l,\langle k,l\rangle=1} (\gamma\kappa_{kl}^{\gamma-1} + a\nabla p_{kl}^2)\beta_{kl} + \sum_{k>l,\langle k,l\rangle=1} (\gamma\kappa_{kl}^{\gamma-1} + a\nabla p_{kl}^2)\chi_{kl}\Big\} \\ &\quad - 2a \sum_{k>l,\langle k,l\rangle=1} \kappa_{kl}\nabla p_{kl}\nabla(D^{-1}M_{-\alpha\{\lambda\beta+\chi\}}p)_{kl}, \\ 0 &= \lambda \sum_{k>l,\langle k,l\rangle=1} \gamma^2\kappa_{kl}^{2\gamma-2} - a^2\nabla p_{kl}^4 - 2a\kappa_{kl}\nabla p_{kl}\nabla(D^{-1}M_{\beta}^{(0)}p)_{kl} \\ &\quad + \sum_{k>l,\langle k,l\rangle=1} (\gamma\kappa_{kl}^{\gamma-1} + a\nabla p_{kl}^2)\chi_{kl} - 2a\kappa_{kl}\nabla p_{kl}\nabla(D^{-1}M_{\chi}^{(-\frac{1}{\alpha})}p)_{kl}. \end{aligned} \tag{4.40}$$

Finally we can write down the formula for λ as

$$\lambda = \frac{-\sum_{k>l,\langle k,l\rangle=1}(\gamma\kappa_{kl}^{\gamma-1} + a\nabla p_{kl}^2)\chi_{kl} - 2a\kappa_{kl}\nabla p_{kl}\nabla(D^{-1}M_{\chi}^{(-\frac{1}{\alpha})}p)_{kl}}{\sum_{k>l,\langle k,l\rangle=1} \gamma^2\kappa_{kl}^{2\gamma-2} - a^2\nabla p_{kl}^4 - 2a\kappa_{kl}\nabla p_{kl}\nabla(D^{-1}M_{\beta}^{(0)}p)_{kl}}. \tag{4.41}$$

The value of λ in Eqn. (4.41) ensures that g remains constant up to $O(\delta\kappa_{kl})$ terms. However, we must also adjust $\{\kappa_{kl}\}$ at each step to exactly maintain the constraint following the method given in Section 4.2.2. In previous applications since g was a function of κ alone this

additional projection step did not require perturbation of pressures. Now both the change in κ_{kl} and the change in flow must be considered when adjusting conductances. We calculate here the additional terms created by the pressure variation. To project along the constraint surface normal we need to calculate the normal vector:

$$\begin{aligned} n_{kl} &= \frac{\partial}{\partial \kappa_{kl}} \Big\{ \sum_{i>j,\langle i,j\rangle} \left(\kappa_{ij}^{\gamma} + a\kappa_{ij}(p_i - p_j)^2\right) - K^{\gamma} \Big\} \\ &= \gamma \kappa_{kl}^{\gamma-1} + a(p_k - p_l)^2 + \sum_{\langle i,j\rangle, i>j} 2a\kappa_{ij}\left(\frac{\partial p_i}{\partial \kappa_{kl}} - \frac{\partial p_j}{\partial \kappa_{kl}}\right)(p_i - p_j). \end{aligned} \tag{4.42}$$

To obtain $\frac{\partial p_i}{\partial \kappa_{kl}}$ we differentiate Kirchhoff's first law with respect to κ_{kl}:

$$\sum_j \kappa_{ij}\left(\frac{\partial p_i}{\partial \kappa_{kl}} - \frac{\partial p_j}{\partial \kappa_{kl}}\right) + (\delta_{ik}\delta_{jl} - \delta_{il}\delta_{jk})(p_i - p_j) = 0 \tag{4.43}$$

or:

$$\sum_j \kappa_{ij}\left(\frac{\partial p_i}{\partial \kappa_{kl}} - \frac{\partial p_j}{\partial \kappa_{kl}}\right) = -(p_k - p_l)(\delta_{il} + \delta_{ik}). \tag{4.44}$$

Notice that $\frac{\partial p_i}{\partial \kappa_{kl}} = 0 \ \forall i \in \mathcal{V}_D$ since these p_i are fixed by the boundary conditions. Then we can solve for $\frac{\partial p_i}{\partial \kappa_{kl}}, 1 \le i \le V$ by solving the linear system (solvability was discussed in Appendix C) and calculate the normal vector.

4.2.7 Calculating uniform flow zebrafish microvascular network under Murray's constraint

The gradient descent method with Murray constraint closely follows Section 4.2.6 with the target function

$$\begin{aligned} \Theta = \sum_{(k,l)\in\mathcal{E}} \frac{1}{2}(\kappa_{kl}(p_k - p_l) - \bar{Q})^2 I_{kl} + \lambda \left(\sum_{\langle k,l\rangle = 1, k>l} (a\kappa_{kl}(p_k - p_l)^2 + \kappa_{kl}^{\gamma}) - K \right) \\ - \sum_{k\in\mathcal{V}_N} \mu_k \left(\sum_{l,\langle k,l\rangle = 1} \kappa_{kl}(p_k - p_l) - q_k \right) \end{aligned} \tag{4.45}$$

where $\mathcal{E} = \{(k,l) : \langle k,l\rangle = 1, k < l\}$ and the index convention here follows Fig. 4.7A. Here $I_{kl} = 1$ if and only if the edge kl is an intersegmental vessel. To carry out the gradient

descent we calculate

$$\frac{\partial \Theta}{\partial \kappa_{kl}} = (\kappa_{kl}(p_k - p_l) - \bar{Q})(p_k - p_l)I_{kl} - a\lambda(\nabla p^2)_{kl}$$

$$+\lambda\gamma\kappa_{kl}^{\gamma-1} - \nabla(D^{-1}\zeta)_{kl}\nabla p_{kl} \doteq \lambda\beta_{kl} + \chi_{kl} \qquad \forall (k,l) \in \mathcal{E} \tag{4.46}$$

Now given $\{\kappa_{kl}\}, \{p_k\}$ we need to solve for $\{\mu_k\}, \lambda$ for the algorithm. Again from $\frac{\partial \Theta}{\partial p_k} = 0$ we get

$$\mu = 2a\lambda p + D^{-1}\zeta \tag{4.47}$$

where

$$\zeta_k \doteq \begin{cases} \sum_{l,\langle k,l\rangle=1}(\kappa_{kl}(p_k - p_l) - \bar{Q})I_{kl}\kappa_{kl}\,, & k \notin \mathcal{V}_D \\ 0\,, & k \in \mathcal{V}_D \end{cases}. \tag{4.48}$$

To solve for lambda we can use Eqn. (4.41) if we calculate β, χ in Eqn. (4.46). Since the target function here is the same as that in Section 4.2.6 we have $\beta_{kl} = \gamma\kappa_{kl}^{\gamma-1}$. The χ can be calculated as

$$\chi_{kl} = (\kappa_{kl}(p_k - p_l) - \bar{Q})(p_k - p_l)I_{kl} - \nabla(D^{-1}\zeta)_{kl}\nabla p_{kl} \qquad (k,l) \in \mathcal{E} \tag{4.49}$$

With these expressions we can solve for λ by Eqn. (4.41) and obtain the expression for $\{\mu_k\}$ by Eqn. (4.47). Then we can carry out the gradient descent by Eqn. (4.46). Notice that if we set $\bar{Q} = 0, I_{kl} = 1\ \forall \langle k,l\rangle = 1$ then f is the same as in Section 4.2.6 and the expression of χ agrees with the auxiliary variable defined in that section.

4.3 Results

4.3.1 The algorithm finds known minimally dissipative networks

To evaluate the ability of our algorithm to find optimal networks we start with minimally dissipative networks that have been thoroughly studied. It has been proven that, when the exponent in material constraint γ is less than one, as is the case for vascular networks, the minimally dissipative networks with flow (Neumann) boundary conditions contain no loops

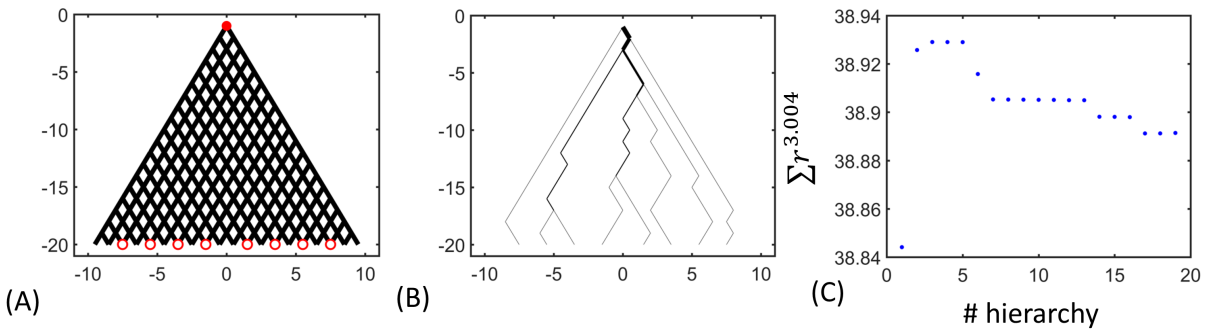

Figure 4.4: Minimally dissipative networks agree with previous work [BM07, Dur07] (with target function $\sum \kappa_{kl}(p_k - p_l)^2$ and material constraint $\sum \kappa_{kl}^{\gamma} - K^{\gamma}$ with $\gamma = \frac{1}{2}$). (A) We use a branching grid as our basic topology. There are $N = 20$ layers of vertices and a total of 380 edges, connecting a single source (red filled circle) with 8 sinks (red open circles). (B) A minimal dissipative network calculated by gradient descent method exhibits tree structure as predicted in [Dur07]. We imposed a fixed zero pressure on the top vertex and 8 evenly distributed outflows on the bottom. Each edge is initially assigned a positive uniformly random conductance to impose no prior knowledge on the algorithm. (C) Murray's law [Mur26b] is obeyed by the minimal dissipative network, indicated by the nearly constant sum of radius to an exponent 3.004 among different hierarchies in network shown in (B).

[Dur07] (this result was generalized to both flow and pressure (Dirichlet) boundary conditions in [CR18]). Those networks are also known to satisfy Murray's law [Mur26b, She81], which states that the sum of third power of vessel radii in the same hierarchy is a constant. Although the original derivation by Murray in 1926 was based on local optimization in a network in which flows are unaffected by changes in conductances, Murray's law is also necessary for a network to be a global minimizer [CR18]. To see whether our algorithm recovers these theoretical properties we consider a model for the branching vasculature in animals [WBE97] (Fig. 4.4A). We impose distributed sinks on the bottom and a single source on top (with pressure imposed to ensure solvability [LP16]). We apply the algorithm described in Section

4.2.3 starting from a network with no prior knowledge, i.e. all edges have the same uniformly random distribution of conductances. All 20 networks we simulated are trees (Fig. 4.4B), agreeing with previous theoretical work. To further validate our algorithm we calculate the Murray exponent by minimizing the coefficient of variation (CV) of sums of vessel radii in the same hierarchy to the exponent (Fig. 4.4C). The Murray exponents cluster tightly around 3 (3.01 ± 0.03, mean $\pm$ sd, 20 networks), which is the exponent in Murray's law [Mur26b]. So our algorithm recovers both properties of minimally dissipative networks [BM07].

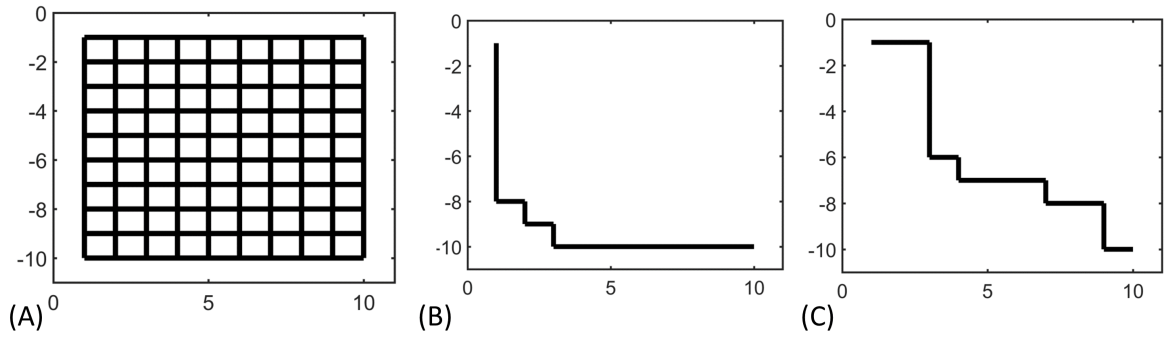

Figure 4.5: Minimally dissipative networks consist of a single conduit on capillary bed topology (with target function $\sum \kappa_{kl}(p_k - p_l)^2$ and material constraint $\sum \kappa_{kl}^{\gamma} = K^{\gamma}$ with $\gamma = \frac{1}{2}$ on a 10×10 square grid). (A) We represent the capillary bed network by a square grid where a single source and a single sink locate at upper-left and lower-right corners respectively. (B, C) Different initial conductances produce different optimal networks, but all optimal networks are made of a single wide conduit. Here we use a constant step size throughout the process, and at each step we project by surface normal to maintain the material constraint. Each edge is initially assigned a positive uniformly random conductance to impose no prior knowledge on the algorithm.

4.3.2 Uniform flow qualitatively explains network structure of capillary beds

Here we compare these organizing principles on the topology of capillary beds [TH03, MJ79] (Fig. 4.5A). We follow Section 4.2.3 to calculate minimally dissipative networks, and Section 4.2.4 to calculate uniform flow networks. We assume that the capillary bed is supplied by a single arteriole and blood leaves from a single venule. Networks formed according to the minimal dissipation principle consist of a single pipe following a geodesic route (Fig. 4.5B, C), which can be shown theoretically to be the optimal solution. Specifically, since the network cannot contain loops, and connects a single source to a single sink, there can only be one pipe in the network. Longer pipes have less material in each segment but the same flows as shorter pipes, so have higher total dissipation. Finally uneven material distribution has been ruled out by [Dur06]. This morphology contrasts sharply with empirically observed capillary structure [TH03, MD09, MJ79], suggesting that minimizing dissipation is not the dominant factor for capillary systems.

Uniform flow networks, on the other hand, might explain capillary bed morphology. Starting from a uniformly random configuration, our algorithm finds a network with an apparently random distribution of materials (Fig. 4.6A). The conductances have a smaller variance compared to the initial configuration, but do not have a clear pattern otherwise (Fig. 4.6B). While the uniform flow networks more closely resembles a capillary bed than a minimally dissipative network, it is not clear what quantitative characters can be used to compare the networks. As discussed in Section 4.2.4, the uniform flow target function simplifies to $\frac{1}{2}\sum Q^2$ on capillary bed topology, which allows us to analytically derive properties of uniform flow networks.

Theorem 4.3.1. *Any critical point of the target function (4.26) in which $p_k = 0\ \forall k \in \mathcal{V}_D$ has the same set of flows as a uniform conductance network with the same support on edges. That is, suppose we let κ_{kl}, Q_{kl} be the conductances and flows on the stationary network, and κ'_{kl}, Q'_{kl} be those on the uniform conductance network, i.e.*

$$\kappa'_{kl} = \begin{cases} 1\,, & \text{if } \langle k,l\rangle = 1 \text{ with } \kappa_{kl} > 0 \\ 0\,, & \text{if } \langle k,l\rangle = 1 \text{ with } \kappa_{kl} = 0 \end{cases}. \tag{4.50}$$

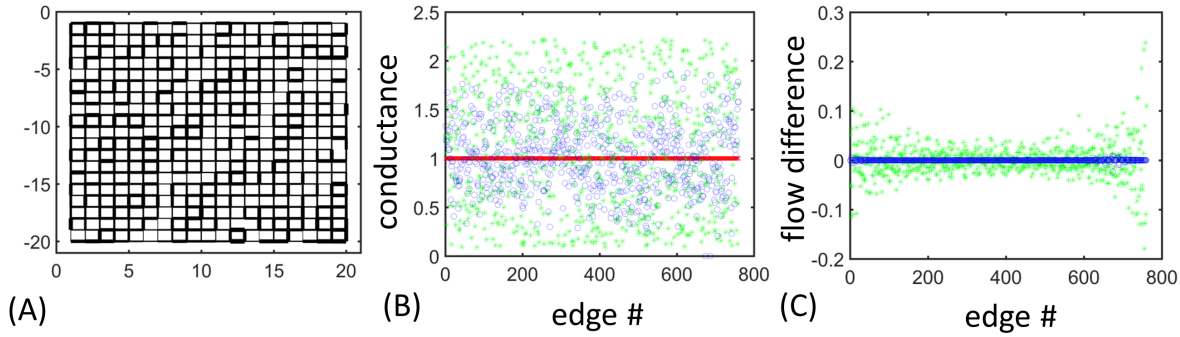

Figure 4.6: Uniform flow networks have a seemingly random morphology, but can be shown to have the same flows as a uniform conductance network (Here we show a 20×20 square grid network with 400 vertices). (A) An optimal network has an apparently random distribution of conductances. The edge widths are proportional to the conductances. (B) A closer view reveals that the conductances of the optimal network (blue circle) are quite different from uniform (red cross), and do not seem qualitatively different from initial conductances drawn from a uniform random distribution (green star). The conductances are normalized such that $\sum \kappa^{\frac{1}{2}}$ are the same. Each edge is initially assigned a positive uniformly random conductance to impose no prior knowledge on the algorithm. (C) The differences of flows from those in a uniform conductance network (blue circles) are uniformly zero, while the differences of initial flows from those in a uniform conductance network (green stars) are not.

Then

$$Q_{kl} = Q'_{kl} \qquad \forall \langle k, l \rangle = 1. \tag{4.51}$$

(The proof will be presented in the end of this subsection.) The theorem states that a uniform flow network, i.e. a local minimum of target function (4.26), will have the same flow as the network where all the edges with positive conductances are assigned unit conductance. In order to evenly distribute the flows, networks with all allowed edges present will have higher uniformity than networks in which some subset of edges have been cut (in-

deed among 100 uniform flow networks those with all edges present have an average value for the target function of 1.9465, compared to 1.9470 for networks with at least one edge cut). Therefore the uniform conductance network can predict the flows in all uniform flow (Fig. 4.6C). While the flows in uniform flow networks are tightly constrained, many possible configurations can achieve the same uniformity, and there is no visible pattern in the distribution of conductances for those networks, unlike minimally dissipative networks.

Proof of Theorem 4.3.1. The assumption that all pressure vertices have pressure zero is really an assumption that all pressure vertices have the same pressure: In the latter case since a constant shift in all pressures does not change the flows. To find the critical points of Θ we recall the derivatives in Eqns. (4.27, 4.28), along with $\mu_i = 0 \ \forall i \in \mathcal{V}_D$ by assumption. First we show that a uniform distribution of conductances would result in a critical point $(\{p_k\}, \{\mu_k\}, \{\kappa_{kl}\})$, by rewriting the equation $\frac{\partial \Theta}{\partial p_k} = 0$ (4.27) into the matrix form:

$$D\mu = D^{(2)}p. \tag{4.52}$$

Here D_{kl} is in Equation (4.6) and $-D^{(2)}$ is another graph Laplacian:

$$D^{(2)}_{kl} \doteq \begin{cases} \sum_{l,\langle k,l\rangle=1} \kappa^2_{kl}\,, & k = l, k \notin \mathcal{V}_D \\ -\kappa^2_{kl}\,, & \langle k,l\rangle = 1, k \notin \mathcal{V}_D \\ \kappa^{(2)}\,, & k = l, k \in \mathcal{V}_D \\ 0\,, & otherwise \end{cases} \tag{4.53}$$

in which the matrix is made full-rank if $\kappa^{(2)} > 0$ (similarly to the $\kappa^{(1)}$ constant in D). The $\kappa^{(1)}$ entries in D_{kl} enforce $\mu_k = 0$ at each $k \in \mathcal{V}_D$. The entries in $D^{(2)}$ are not needed since $p_k = 0$ at each $k \in \mathcal{V}_D$, but we add values here to emphasize the symmetry between $\{\mu_k\}$ and $\{p_k\}$. Now consider uniform conductances, i.e. $\kappa_{kl} = a > 0 \ \forall \langle k,l\rangle = 1$. We can set $\kappa^{(1)} = a$ and $\kappa^{(2)} = a^2$. Then we have $D = aD^{(2)}$ and since D is invertible (see Appendix C)

$$\mu = D^{-1}D^{(2)}p = ap. \tag{4.54}$$

Now this set of μ_k's and p_k's then also satisfies $\frac{\partial \Theta}{\partial \kappa_{kl}} = 0$ because

$$\frac{\partial \Theta}{\partial \kappa_{kl}} = a(p_k - p_l)^2 - a(p_k - p_l)^2 = 0. \tag{4.55}$$

Thus the network with uniform conductances along with pressures solved from the Kirchhoff's first law is indeed a critical point.

Now we show that any interior critical point, i.e. satisfying $\kappa_{kl} > 0 \; \forall \langle k, l \rangle = 1$, has the same flows as the uniform conductance network. We will see that for any such network the μ_k's represent the pressures of the uniform conductance network. Since all the conductances are positive we have $\frac{\partial \Theta}{\partial \kappa_{kl}} = 0 \; \forall \langle k, l \rangle = 1$. Assume for now $p_k - p_l \neq 0 \; \forall \langle k, l \rangle = 1$. Then from Equation (4.28) we obtain that the $\{\mu_k\}$ obey a system of equations

$$\kappa_{kl}(p_k - p_l) - (\mu_k - \mu_l) = 0, \qquad \forall \langle k, l \rangle = 1 \tag{4.56}$$

which may be rewritten as

$$\mu_k - \mu_l = \kappa_{kl}(p_k - p_l) = Q_{kl}, \qquad \forall \langle k, l \rangle = 1. \tag{4.57}$$

Kirchhoff's first law in terms of μ_k's then reads

$$\sum_{l, \langle k,l \rangle = 1} (\mu_k - \mu_l) = q_k \qquad \forall k \in \mathcal{V}_N, \qquad \mu_k = 0 \qquad \forall k \in \mathcal{V}_D. \tag{4.58}$$

In matrix form the equations can be written as

$$D\mu = F \tag{4.59}$$

where $F_k = q_k$ if $k \in \mathcal{V}_N$ and is zero otherwise, and D is defined as for network made up of unit conductances:

$$D_{kl} \doteq \begin{cases} \sum_{l,\langle k,l\rangle=1} 1\,, & k = l, k \notin \mathcal{V}_D \\ -1\,, & \langle k,l\rangle = 1, k \notin \mathcal{V}_D \\ 1\,, & k = l, k \in \mathcal{V}_D \\ 0\,, & \text{otherwise} \end{cases} \tag{4.60}$$

Because D is invertible we can solve for μ_k's from Eqn. (4.59). The $\{\mu_k\}$'s represent the pressures that would occur at each vertex if all conductances in the network were set equal to 1, creating uniform conductance network. Since the flows $Q_{kl} = \mu_k - \mu_l$ are determined by μ_k's we conclude that the locally optimal networks would have flows the same as in the network of uniform conductances.

To derive (4.56) from (4.28) we had to assume that $p_k \neq p_l$ whenever $\langle k,l\rangle = 1$. Consider the case where in the optimal network $p_k - p_l = 0$ for some $\langle k,l\rangle = 1$. For these (k,l)'s Eqn. (4.56) no longer holds and we have to set $\frac{\partial\Theta}{\partial p_k} = 0$ in Eqn. (4.27) to obtain extra information. We claim that $\mu_k = \mu_l$ if $p_k - p_l = 0$. This can be seen from a loop current argument similar to that used in Appendix C to prove existence and uniqueness of the $\{\mu_k\}$. Specifically, suppose for contradiction that $\mu_{k_1} \neq \mu_{k_2}$ for some pair of vertices with $p_{k_1} - p_{k_2} = 0$ and without loss of generosity let $\mu_{k_1} > \mu_{k_2}$. If k_1 and $k_2 \in \mathcal{V}_D$ then $\mu_{k_1} = \mu_{k_2} = 0$; so at least one of the two vertices does not lie in $\mathcal{V}_D$. If $k_2 \notin \mathcal{V}_D$ then $\frac{\partial\Theta}{\partial p_{k_2}} = 0$ implies:

$$\sum_{l,\langle k_2,l\rangle=1} \kappa_{k_2 l}^2 (p_{k_2} - p_l) = \sum_{l,\langle k_2,l\rangle=1} \kappa_{k_2 l}(\mu_{k_2} - \mu_l). \tag{4.61}$$

Since Eqn. (4.56) holds when $p_k - p_l \neq 0$ we have

$$0 = \sum_{l,\langle k_2,l\rangle=1, p_l = p_{k_2}} \kappa_{k_2 l}^2 (p_{k_2} - p_l) = \sum_{l,\langle k_2,l\rangle=1, p_{k_2} = p_l} \kappa_{k_2 l}(\mu_{k_2} - \mu_l). \tag{4.62}$$

Since $\kappa_{kl} > 0\ \forall \langle k,l\rangle = 1$ and the sum includes the negative summand $\kappa_{k_2 k_1}(\mu_{k_2} - \mu_{k_1})$ we can find l for which $\mu_l < \mu_{k_2}$ and $p_l = p_{k_2}$. We let $k_3 = l$ and repeat the process to find a neighbor of k_3 such that $p_l = p_{k_3}$ but $\mu_l < \mu_{k_3}$. We then can keep repeating this process until we reach a vertex $k_N \in \mathcal{V}_D$ (no vertex may be visited more than once). We have imposed $\mu_{k_N} = 0$. Now we trace through increasing μ_k's starting from k_2 and k_1 and we get $k'_1, ..., k'_{N'}$ such

that $\mu_{k'_n} < \mu_{k'_{n+1}}$ $\forall n = 1, ..., N' - 1$ and $\mu_{k'_1} > \mu_{k_1}$. By the same reasoning we have $k_{N'} \in \mathcal{V}_D$ and we reach a contradiction since $0 = \mu_{k'_{N'}} > \mu_{k'_{N'-1}} > \cdots > \mu_{k'_1} > \mu_{k_1} > \cdots > \mu_{k_N} = 0$. Therefore $\mu_k = \mu_l$ when $p_k = p_l$ and Eqn. (4.56) actually holds for all $\langle k, l \rangle = 1$. Again we conclude that the flows of a locally optimal network with non-zero conductances are the same as the flows in the uniform conductance network.

Finally we discuss the boundary case where $\kappa_{kl} = 0$ for some $\langle k, l \rangle = 1$, and we denote this set of edges by I. To avoid ill-posedness of pressures we require that that the matrix D is invertible. In this case we do not have Eqn. (4.56) for $\kappa_{kl} = 0$ because $\frac{\partial \Theta}{\partial \kappa_{kl}}$ need not be zero on these edges. However since there is no flow through edges with $\kappa_{kl} = 0$ we can write down Kirchhoff's first law as

$$D\mu = 0, \tag{4.63}$$

where $-D$ is again the graph Laplacian, but with zero conductance edges removed and other edges with conductance 1:

$$D_{kl} = \begin{cases} \sum_{l, \langle k,l \rangle = 1, (k,l) \notin I} 1\,, & k = l, k \notin \mathcal{V}_D \\ -1\,, & \langle k, l \rangle = 1, (k, l) \notin I \\ 1\,, & k = l, k \in \mathcal{V}_D \\ 0\,, & \text{otherwise} \end{cases} . \tag{4.64}$$

We can safely remove the zero conductance edges from the network because the difference $\mu_k - \mu_l$ no longer represents the flow Q_{kl}, and that we know $Q_{kl} = 0$ for these edges. By assumption we can solve for μ from Eqn. (4.63) so $\{\mu_k\}$ represent the pressures within the uniform conductance network, but with edges $\kappa_{kl} = 0$ removed from the network. □

4.3.3 Optimal zebrafish microvasculature

Comparison of the different organizing principles on our model capillary bed network suggests that uniform flow is prioritized more than transport efficiency for these networks. The comparison remains qualitative because although capillary beds in e.g. salamander skin do

resemble square grids [MJ79] (and Fig. 4.1A), this resemblance is only approximate, so it is difficult to test our theoretical predictions. The embryonic zebrafish trunk vasculature, on the other hand, can be completely mapped, down to the finest vessels. Moreover, the blood flows can be measured by tracking the motion of red blood cells ([SUP03, MSS07], as well as our previous work [CTB17]), thereby directly testing the flows predicted in optimal networks.

First we show how far the embryonic zebrafish network is from minimizing dissipation. The optimal morphology of the network depends on the boundary conditions we impose, and there are two conceivable ways to assign boundary conditions. One way is to assume a fixed inflow from the heart into the trunk from v_1. If one thinks of the venous part of the trunk as symmetric to the arterial part then the pressures in the middle of fine vessels need to be the same, and we can set $p_{n+1} = p_{n+2} = \cdots = p_{2n+1} = 0$ (since a constant shift in the pressure does not change the flow). Under this boundary condition we can find the minimally dissipative network by methods described in Secion 4.2.3. The minimally dissipative network eliminates all the edges but e_2, on which all the allowed material is used (Fig. 4.7B). This agrees with prior theoretical predictions since minimally dissipative networks cannot have loops, nor can they connect vertices with the same assigned pressure [CR18]. Therefore there are only $n + 1$ possibilities: the flow returns through one of the fine vessels $e_2, ..., e_{2n}$ or the tail e_{2n-1}. Since the shortest route would be going through the first fine vessel e_2, the minimally dissipative network concentrates all the material on e_2.

Instead of imposing a fixed pressure in the middle of the fine vessels, one can also impose a fixed flow [BM07, KSM10, Dur06] through each vessel. This boundary condition interprets into a uniform flow at each of the vertices $v_{n+2}, ..., v_{2n+1}$, and we can find a distribution of conductances that minimizes dissipation from Section 4.2.3. Now equal amount of flow passes through each fine vessels, leading to a decaying flow in the aorta from head to tail. Therefore the material is concentrated on the rostral part of the aorta, with all the fine vessels having equal amount of material (Fig. 4.7C). The imposed fixed flow then requires a decrease of pressure in the middle of fine vessels from head to tail, to compensate for the pressure drop in the aorta (Fig. 4.7D). Under symmetry of arterial and venous parts, this

pressure distribution then creates an unrealistic blood flow in the vein toward the tail, i.e. away from the heart.

Since the principle of minimal dissipation is unable to generate networks that resemble the observed zebrafish trunk microvasculature, we look at uniform flow networks and see if they match the observed vasculature. To avoid back flow in the vein we impose fixed pressure in the middle of fine vessels, and a fixed flow into the trunk from v_1. The zebrafish trunk vasculature is not stackable, so we use the square error target function (4.29) instead of (4.25), and we use methods described in Section 4.2.5 to find the uniform flow network. Instead of concentrating all the materials on the first capillary or tapering the aorta, the uniform flow network has constant conductance along the aorta and conductances on the fine vessels that increase exponentially with the distance from the heart (Fig. 4.8A). If vessels obeyed the Hagen–Poiseuille law (Eqn. (4.1)) a 20-fold change in conductance would require a 2-fold change in radii of fine vessels, which is not observed in the real zebrafish trunk [IHW01]. However, these fine vessels have radii that match the size of red blood cells; thus red blood cells almost totally occlude the vessels they pass through, adding a large increment to the vessel's hydraulic resistance [SBM16]. This increment depends sensitively on the gap distance between the cell and the endothelial wall, which is typically on the scale of 10–300 nm, and is smaller than the optical resolution for fluorescence microscopy [SHL10]. In our previous work, we proposed an indirect method that measures this increment based on the correlation between the flow speed and the number of cells in each fine vessel [CTB17]. When we compare the measured hydraulic resistance with the resistances of fine vessels in the uniform flow network, we see an excellent agreement between the predicted and measured resistances (Fig. 4.8B). Our results show that the principle of uniform flow quantitatively reproduces the zebrafish trunk geometry.

4.3.4 Murray constraint on optimal networks

So far we show that capillary networks prioritize uniform flow over minimizing dissipation, but biological networks may be subject to more than one constraint at a time. In capillary

networks the total dissipation will be higher when the density of capillaries increases, which in turn requires more energy input. As we noted in the introduction, fine vessels account for half of the cost of blood transport in the human body [Hal15], suggesting that capillaries will be constrained not only in respect to materials but also by dissipation. In this case the function to be optimized takes the full form of (4.4) with a constant $a > 0$, representing the relative importance of dissipation compared to material cost. Following Section 4.2.6 we can calculate uniform flow networks with the model capillary bed geometry under the Murray constraint (Fig. 4.9A). The uneven distribution of conductances resembles that in Section 4.3.2, and indeed for 20 networks with a ranges from 0 to 50, the function $\frac{1}{2}\sum Q^2$ clusters closely at the optimal value ($1.9461 \pm 9.25 \times 10^{-6}$, mean $\pm$ sd, 20 networks), i.e. that of uniform conductance network. This result is counter-intuitive since we would expect that constraining dissipation would prevent the network from achieving the non-constrained optimal uniformity in flows. However, on the capillary bed topology we can reason by a scaling argument. Suppose we find an optimal network under the material constraint. We calculate the total material cost K of this network. Then we calculate the optimal network in which Murray's constraint is imposed with allowed total energy K including both material costs and dissipation. Denote by κ_{kl} the conductances in the network under Murray constraint, and by κ'_{kl} the conductances in the optimal network under material constraint. If a is sufficiently close to zero then the target function of Murray network will be lower or equal to that of material network. The reasoning is that although $\sum \kappa'^{\gamma}_{kl} + a\frac{Q^2_{kl}}{\kappa'_{kl}} = K$ does not hold, we can try to solve for a multiplicative scaling $\beta > 0$ that satisfies $\sum(\beta\kappa'_{kl})^{\gamma} + a\frac{Q^2_{kl}}{\beta\kappa'_{kl}} = K$. Notice that Q_{kl} does not change under the scaling for this class of networks, so the value of target function is unaffected by scaling conductances. Now if $a > 0$ is small enough we expect to be able to find a solution β and $\{\beta\kappa'_{kl}\}$ is an admissible network in the sense that it obeys the Murray constraint. Thus the optimal network under the Murray constraint must have equal or smaller target function value than the optimal network obeying only the material constraint. By reversing this argument we can see that the optimal networks for small enough $a > 0$ actually agree with those with $a = 0$. The question is how large a has to be so that the Murray network is truly constrained by the total energy cost, and the optimal

networks under the Murray constraint and under the material constraint diverge. From our numerical simulations we can see that large changes of a can be accommodated with changing the morphology of the uniform flow networks from its unconstrained counterpart. We observe that increasing a decreases material costs (Fig. 4.9B), which is unintuitive since increasing a adds weight to dissipation, and we might expect this to encourage the network to decrease its dissipation. If we study the curve of $\sum(\beta\kappa'_{kl})^\gamma + a\frac{Q_{kl}^2}{\beta\kappa'_{kl}}$ as a function of β, the function is U-shaped and diverges when $\beta \to 0$ or $\beta \to \infty$. When a increases the total energy increases, and the network has to adjust itself to a low energy state. If the network is on the left side of the U this means increasing β, which increases the material cost to realize the constraint. In contrast when the network is on the right side of the curve, decreasing β will be the only way to lower the total energy, which explains the trends depicted in Fig. 4.9B. The simulation suggests that, on the capillary bed topology, constraining dissipation seems to have little effect on the morphology of uniform flow network.

Would uniform flow models of the zebrafish trunk follow the same trend? Using methods described in Section 4.2.7, we can calculate uniform flow networks under Murray constraint, with different values in a. When a is close to zero, the constrained networks have optimal flow uniformity, and dissipation increases as in the case of capillary bed topology (Fig. 4.10A). However, at a critical value around $a_c = 33.3$, a phase change occurs; the flows become less uniform and dissipation starts dropping (Fig. 4.10A). The network morphology changes dramatically, in particular conductances of the fine vessels become non-monotonic, and the flows are concentrated toward the head side of zebrafish (Fig. 4.10B, C). Our results suggest that, when a biological network has multiple constraints to meet, the network morphology will conform only to the tightest constraint, and then if the relative weight of these constraints is changed, the network changes dramatically only when another constraint becomes dominant.

4.4 Acknowledgments

MR and SSC were funded by grants from the NSF (under grant DMS-1351860) and NIGMS (under R01 GM126556). SSC was also supported by the National Institutes of Health, under

a Ruth L. Kirschstein National Research Service Award (T32-GM008185). The contents of this chapter are solely the responsibility of the authors and do not necessarily represent the official views of the NIH. MR also thanks Eleni Katifori and Karen Alim for useful discussions, and the American Institute of Mathematics for hosting him during part of the development of this chapter.

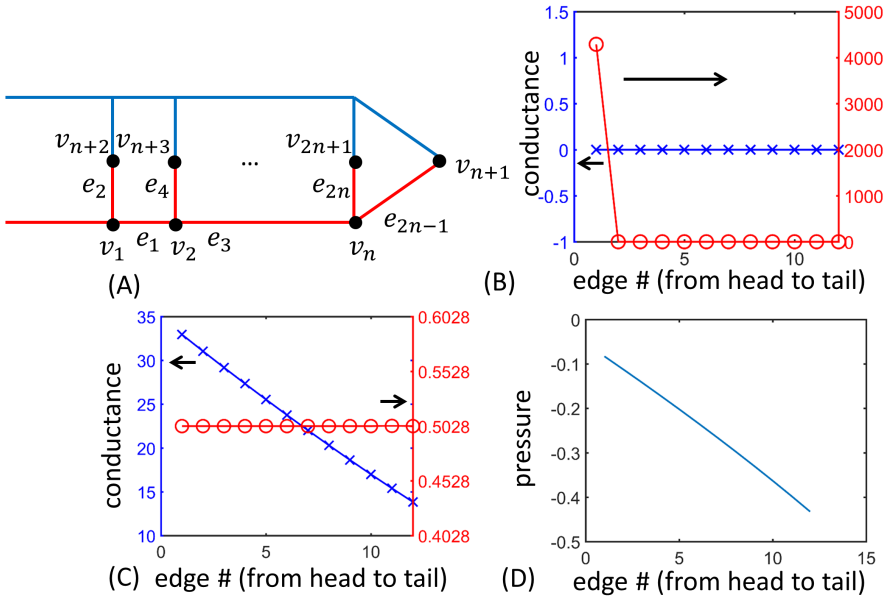

Figure 4.7: Minimal dissipative networks for zebrafish trunk vasculature do not explain observed morphology. (A) The zebrafish trunk vasculature can be simplified into a ladder network with arterial (red) and venous parts (blue). The edges $e_1, e_3, ..., e_{2n-1}$ are aorta segments and $e_2, e_4, ..., e_{2n}$ are capillaries. We use $n = 12$ in all the following calculations on zebrafish network. (B) The optimal dissipative network with $\gamma = \frac{1}{2}$ and fixed inflow does not correctly describe the zebrafish trunk network since all the conductances are concentrated on the first capillary (red circle), and the whole aorta is deleted (blue cross). In this calculation we imposed a fixed inflow on v_1 and fixed zero pressure on $v_{n+1}, ..., v_{2n+1}$. We started with $\kappa = 20$ for aorta segments and $\kappa = 1$ for capillaries to reflect the difference in radii in real zebrafish. This initial condition is used for all the following simulations. (C) The optimal dissipative network with $\gamma = \frac{1}{2}$ and fixed outflows has a tapering aorta (blue cross) and capillaries with the same conductances (red circle). We imposed zero pressure on v_1 and fixed outflows on $v_{n+1}, ..., v_{2n+1}$ with v_{n+1} taking half of the total outflow (i.e. $\frac{1}{2}F$) and $v_{n+2}, ..., v_{2n+1}$ evenly dividing the other half of F. (D) However the pressures on the ends of capillaries are decreasing to maintain uniform flows among capillaries, which is non-physical since this means that the blood flows toward the tail in the principal cardinal vein, due to the aorta-vein symmetry.

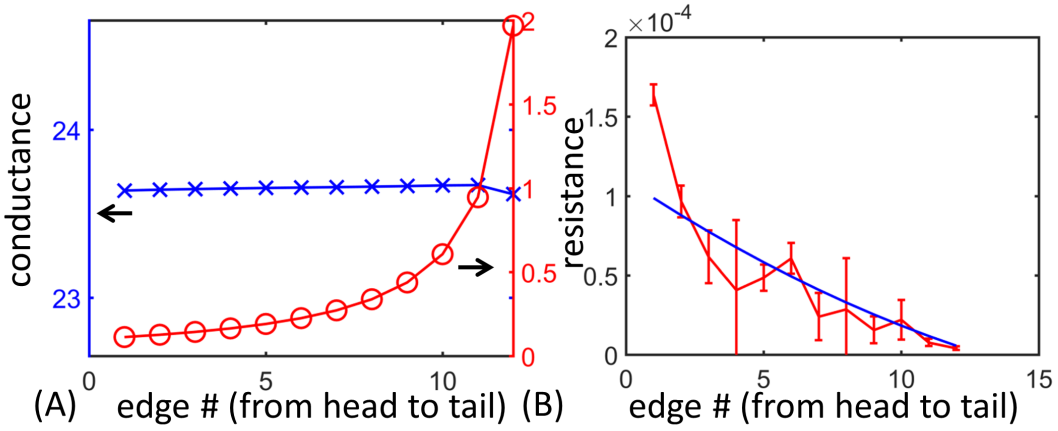

Figure 4.8: The uniform flow networks quantitatively explains the zebrafish trunk vascular network morphology. (A) The uniform flow network dictates a constant conductance on aorta segments (blue cross) but assigns conductances to Se vessels that increase exponentially from head to tail (red circle). We scale the conductances such that $\sum \kappa^{\frac{1}{2}}$ remains the same for comparison with minimal dissipative networks. We started with $\kappa = 20$ for aorta segments and $\kappa = 1$ for capillaries to reflect the difference in radii in real zebrafish. (B) The predicted hydraulic resistance (blue curve) agrees well with experimentally measured data (red curve, with 95% confidence intervals). The data is obtained from our previous work [CTB17] under the assumption that the volume fraction of the red blood cells is 0.45 [PS05]. Theoretical resistances are normalized by the mean since optimization only controls the relative resistances of vessels.

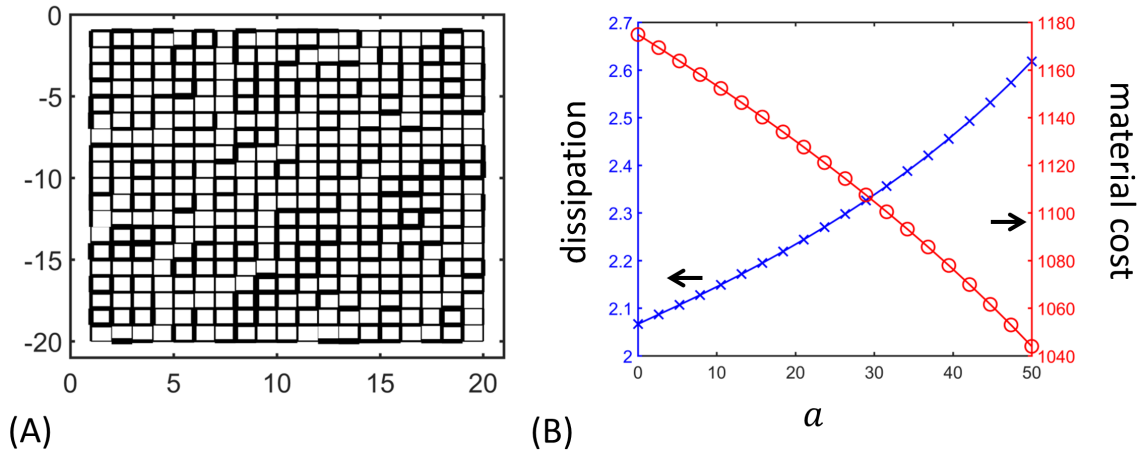

Figure 4.9: Uniform flow networks under Murray constraint have the same flows as the analytic solution in Sec 4.3.2, but exhibit tradeoff between dissipation and material cost as a increases. (A) For small a the uniform flow network with Murray constraint is equivalent to a network with material constraint. The network is constrained with $a = 36.8$, and the solution is selected from the best network visited during the gradient descent, with relative error in energy cost $< 10^{-4}$, as in the following simulations. Widths show the relative conductances. (B) When a is increased, the dissipation in the network increases (blue crosses), while the material cost decreases (red circles). The simulations were carried out in the manner of numerical continuation, i.e. the simulation for each a starts with the solution from previous a, and the simulation for $a = 0$ starts with a random conductance configuration. All the networks have the same fixed total energy cost $K = 1174.9$.

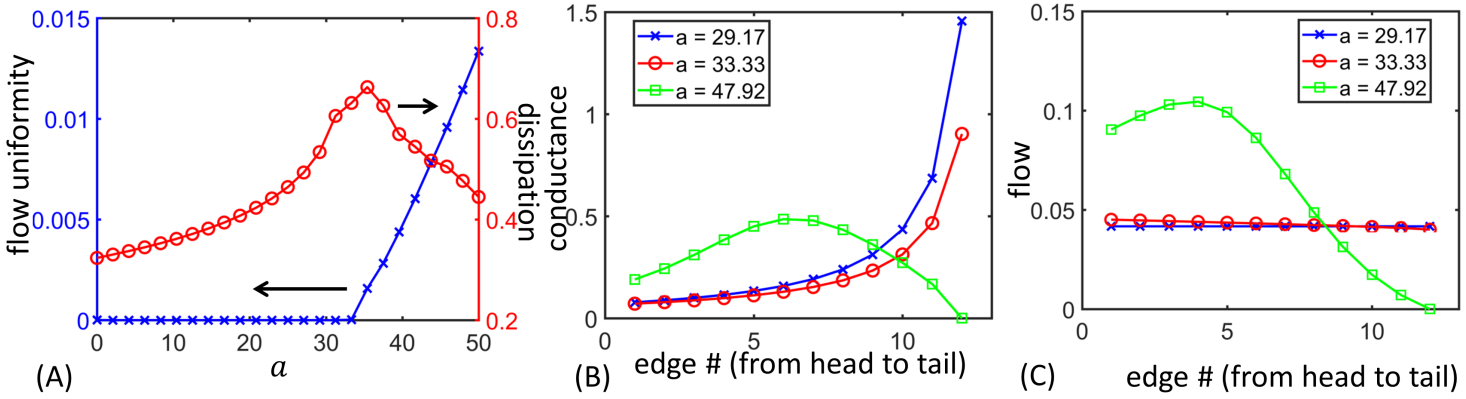

Figure 4.10: Uniform flow networks on zebrafish trunk topology exhibit a phase transition when a, the relative cost of dissipation to total material, is varied in the Murray constraint. (A) The target function remains zero for small a until $a_c = 33.3$ where a phase transition occurs and the value of target function suddenly increases (blue crosses). The dissipation (red circles) increases with a for $a < a_c$ just as for the capillary bed, but has a sharp decrease right after the critical value a_c. Here we adopted numerical continuation as in Fig. 4.9B, but when a local minimum around previous initial condition does not satisfy Murray constraint the initial configuration at $a = 0$ is reused for the initial conductances. The minimal value for the total energy cost upon scaling of conductances is used whenever the Murray constraint cannot be maintained. The Murray energy K is maintained to be 70.43 in all simulations by the projection method described in Section 4.2.6. The total energy cost is fixed to that of initial configuration (with uniform conductances in fine vessels being 1 and those in aorta being 20) when $a = 1$. The solution is selected from the best network visited during the gradient descent, with relative error in energy cost $< 10^{-4}$ (B) The conductances of capillaries change qualitatively after the phase transition. The morphology resembles the unconstrained network (Fig. 4.8A) before the phase transition (blue cross and red circle), but changes qualitatively afterwards (green square). (C) The flows are uniform before the phase transition (blue cross and red circle), but decrease from head to tail afterwards (green square).

CHAPTER 5

A stable shear stress adaptation mechanism for growth of microvascular networks

5.1 Introduction

Animal microvascular networks perfuse tissues with oxygen and sugars and remove waste. Since red blood cells almost fill the finest vessels, changes in vessel radius even at the order of tens of nanometers can potentially strongly alter the flows within the network [SBM16]. At the same time there are too many vessels for network growth to be fully determinate. Yet, although they may operate under many different constraints and objective functions, networks show remarkable levels of adaptation to create efficient or robust networks. For example, in the zebrafish trunk microvasculature a precise tapering of vessel radii from tail to head ensures that each vessel receives the same overall flow [CTB17]. Microvascular vessels are highly variable in radii, which can significantly change the conductances and the blood flow in the system. Penatrating arterioles and first capillaries in the mouse cortex, for example, vary more than 25% in diameter [CFJ18], and more than 10% variation in the diameters of arterioles in striated muscles is observed [KDG82]. To determine the precision with which vessel radii must be tuned to ensure uniform flow, we performed ensemble simulations in which vessel radii were perturbed from their real values, and counted the fraction of simulations in which the uniformity of flow, measured by the Coefficient of Variation (CV) of flow between all intersegmental (Se) vessels, was less than that in 4dpf zebrafish (Fig. 5.1A). Consistent with previous permutation based tests [CR19], including variation in vessel radii quickly led to decrease in uniformity, reflecting the fact that the true vessel radii are close to their optimal values for uniform flows. Once the radius permutation reaches 7%, fewer than

2.5% of the simulated networks had the same or more uniformity than the real networks (Fig. 5.1B). We interpret these results to mean that uniform flows constrain vessel radii to within 7% of an optimal set of values. To see whether Se vessels in zebrafish have similar constraints, we estimated the radii of first 6 SeAs in 6 zebrafish at 4 days post fertilization (dpf), using the measured red blood cell (RBC) fluxes in the SeAs and the relation between conductance and radius based on cell occlusion (Eqn. (5.2)). Even if the RBC fluxes in SeAs are flucuatory, with CVs ranging from 0.8 to 1.2, the radii of SeAs are tightly constrained, with the variation ranging from 0.03% to 0.3% (Fig. 5.1C). Indeed the conductance of Se vessels is proportioanl to the gap distance between the red blood cell and the endothelial wall. Since this distance is typically less than 10% of the capillalry radius [SBM16], small changes in the vessel radius can lead to significant changes in vessel conductances.

Accordingly it is generally thought that vessel radii are set by an adaptive process, changing in response to the blood flows passing through the vessel. Indeed endothelial cell growth is known to be highly responsive to flow, and many of the actors in the growth mechanotransduction pathways are known [KSK93, KT80, DH17, TG99, BLB17]. However, the precise physical form of this adaptation remains mostly unknown. Shear stress on the endothelium provides a natural read out of the flow in a vessel; Hu and Cai [HC13] showed that a network programmed to grow toward a state of uniform shear stress on each vessel realizes a minimally dissipative spanning tree on a given set of sources and sinks (the optimal transport network has uniform shear stress). However, real microvascular networks cannot be explained simply from the point of view of dissipation-minimization – e.g. they contain loops, which are not consistent with optimal transport only when additional constraints (fluctuating sources or sinks, resistance to damage) are added [Dur07, BM07, KSM10]. Moreover, when source and sink boundary conditions are replaced by fixed pressure conditions, then the same algorithm is unstable, and will disconnect all but two pressure nodes from the network [CR18]. [HCR12] sought to achieve stability to flow adaptation by incorporating variable network geometry – having vessels open and close within the network. However the limits on network size, or whether the need for coordinated vessel opening and closing may create tradeoffs with the other functioning of the network. Accordingly, recent models of network

structural adaptation have included chemical cues such as oxygen or glucose supply, along with shear stress, in order to remove vessel instabilities [PSG98]. However, we are not ware of any quantitative comparison between such models, and the trajectories of real networks. The developing zebrafish microvascular network, a widely used developmental model [IHW01], has already been used as a test system for models of vascular adaptation; in particular [CJL12] showed that flows decreased within vessels ~ 2.5 hours prior to the onset of decrease in vessel diameter, consistent with shear-responsive pruning of the network.

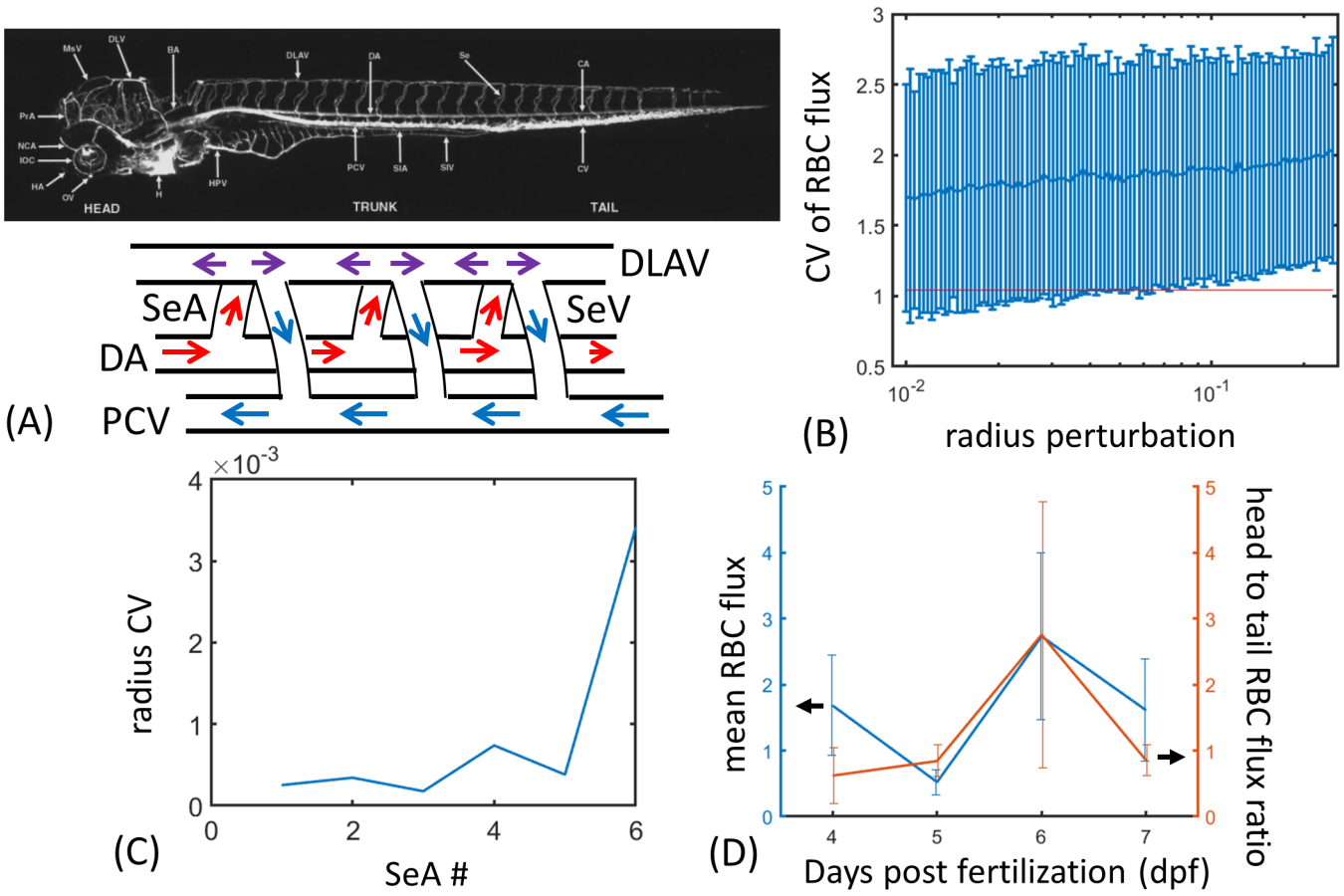

Figure 5.1: The radii of capillaries in embryonic zebrafish are tightly constrained. (A) A diagram for embryonic zebrafish trunk microvascular network. We focus on the microvascular network in the trunk and the tail (left: a 4dpf zebrafish), which has a topology like a ladder, with the dorsal aorta (DA) and the posterior cardinal vein (PCV) being the rails, and the intersegmental arteries (SeAs) and intersegmental veins (SeVs) being the rungs of the ladder (right) [IHW01]. (B) Zebrafish trunk networks can tolerate up to 7% of random perturbation in SeAs before the red blood cell flux becomes significantly less uniform than measured. We perturb the SeAs in the uniform flow zebrafish trunk network [CTB17] by independently normally distributed noises, with standard deviations ranging from 1% to 25% of the vessel radii. At about 7% perturbation of SeA radius, more than 97.5% of the simulated networks have higher Coefficient of Variation (CV) of red blood cell (RBC) fluxes than the mean value in 6 4dpf fish (red line), signified by that the measured CV is lower than the mean (blue curve) minus 2 standard deviations (blue error bars) of the simulated CV.

5.1 *(previous page)*: (C) The radii of capillaries in zebrafish networks are tightly constrained. We calculate the radii of first 6 SeAs by solving for the conductances according to the measured RBC fluxes in these vessels [CR19], and then recovering the SeA radii from conductances by Eqn. 5.2. The CV of SeA radii ranges from 0.03% to 0.3%, with the rostral SeAs more constrained than the caudal SeAs. SeAs with smaller numberings are closer to the heart. (D) The blood flow pattern is consistent in 4 to 7 dpf zebrafish. Both the mean RBC flux (blue, left axis) and the ratio of RBC fluxes in rostral and caudal trunk (orange, right axis), measured respectively by the sum of RBC fluxes in 4 SeAs closest and farthest from the heart, stay relatively constant throughout this developmental stage. Shown: mean $\pm$ s.d. from 2–3 samples each dpf.

Here we directly compare models for adaptation with measured blood flows in the embryonic zebrafish trunk. The zebrafish trunk is perfused by a single aorta connected to a single vein, via 20–30 intersegmental vessels resembling the rungs of a ladder [CTB17] (Fig. 5.1A). This simple topology allows simultaneous measurement of red blood cell fluxes in multiple fine vessels. We measured red blood cell flows in all of the intersegmental arteries (henceforth; SeAs), among fish ranging from 4 to 7 days post fertilization (dpf). We quantified the flow by two measures: the average flow per Se artery, and the heterogeneity of flow between rostral and distal vessels (namely the ratio of the average flow in the first 4 vessels closest to the heart, to the 4 SeAs furthest from the heart). During an imaging period from 4 to 7 dpf there is very little change in the mean flow through the Se arteries (Fig. 5.1. Additionally, and in line with our previous measurements in 4dpf embryos, although there is a high degree of variability among vessels [CTB17], there is no systematic bias of flow toward either tail or head (Fig. 5.1D). As mentioned above, uniform partitioning of flows between the two trunk regions requires fine tuning of vessel radii: all vessels had the same radius then those closest to the heart would shortcircuit the trunk, creating high flow eterogeneity. However the state in which all vessels receive the same flows is not a steady state of previous models of stress responsive growth. We used the model of Hu and Cai, in which the radius of vessel

adapts itself to the shear stress via $\frac{dr_i}{dt} = C(\tau_i - \bar{\tau}_i)r_i$, where r_i is the radius, τ_i is the shear stress, and $\bar{\tau}_i$ is the target shear stress of vessel i [HCR12]. Here vessels are assigned target stress values, $\bar{\tau}_i$, obtained from the desired steady state. However, although the uniform flow network is a steady state of this model, the growth model is unstable. The mechanism of instability is the same as for a simple parallel vessel network, which will be discussed shortly. Simulated networks eliminate all but one Se vessel, thereby producing minimal dissipation networks [CR19].

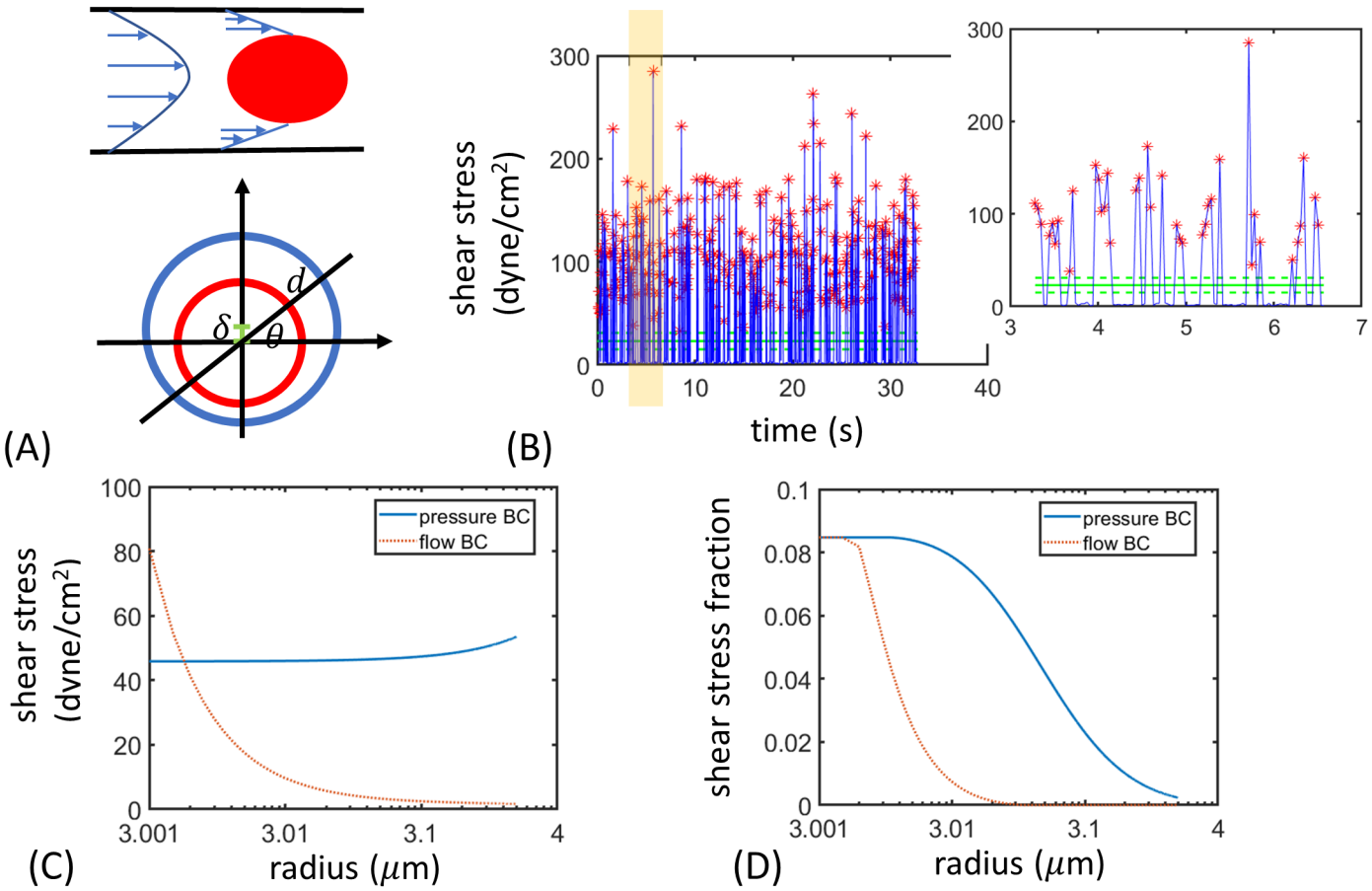

Figure 5.2: A shear stress activation model for vessel adaptation. (A) The small gap distance between the red blood cell and the endothelial wall creates large shear stress, compared to that generated by plasma flow only (up). The stress under the presence of a cell can be calculated by assuming a drift distance δ between the center of the cell from that of the vessel, and considering the gap distance d between the cell and the endothelial wall on a line that passes through the center of cell at an angle θ (down). (B) The shear stress experienced by an endothelial cell exceeds the empirical threshold for notch-1 activation when a cell is present. The stress shows strong fluctuations in a 33 second interval (blue line, left). When we look at a 4 second interval, we see that the shear stress created by red blood cells (red stars) is indeed much higher than that when the cell is absent. This difference crosses a threshold of 23 ± 8 dyne/cm^2 (green line and green dashed lines) previously measured to trigger notch-1 expression [BLB17].

5.2 *(previous page)*: Shown: shear stresses measured at the middle of a Se vessel in a 4dpf zebrafish. The velocities are measured by optical flow method [BFB92] and the cells are found by detecting the extrema of intensity. Then the shear stress is calculated by an integration similar to Eqn. 5.2, with $r = 3.02$ μm and $r_{RBC} = 3\mu$m. (C) One reason for the instability of the conventional shear stress adaptation model [HC13] is that the model only stabilizes a single vessel under the flow boundary condition (orange dotted) but not under the pressure boundary condition (blue line), as the stress increases as vessel dilates, which further increases the stress. We used a velocity of 130 μm/s for the flow and a pressure drop of 4300 dyne/cm^2 for the pressure boundary condition, which are on the same order with that experienced by a Se vessel in a 4dpf zebrafish. (D) The shear stress fraction from the stress activation model, on the other hand, stabilizes a single vessel under both boundary conditions, suggesting that it is more stable than the shear stress adaptation model. We used a threshold $\sigma_t = 380$ dyne/cm^2 and the same parameters as in (C).

In this work we propose a new shear stress adaptation mechanism in microvascular networks that takes into account that stresses in real vessels are highly unsteady. In Se vessels, just as in capillaries, cells travel in single file [SUP03]. The gap distance between the cell and the endothelial wall is typically ten to hundreds of nanometers [SBM16], so the shear stress on the portion of the endothelial wall around a red blood cell is much higher than the average shear stress (Fig. 5.2A). For comparison we show threshold stress values that are known to induce and to not induce expression of notch-1 [BLB17], which is implicated in vessel growth and repair. Our data show that shear stresses large enough to induce vessel remodelling are only attained during passage of a red blood cell. The endothelial cell experiences pulses of shear stress as red blood cells pass through (Fig. 5.2B). We therefore propose that the vessel radius change is driven by the time averaged fraction of endothelial cells that are activated by a shear stress higher than the target threshold.

5.2 Results

To calculate the fraction of activated endohelium for a given microvascular network we first calculate the blood flow in the network and then the shear stress on every point on the endothelial wall. The flow is laminar in microvascular vessels [Hov04, JNE06], so the hydraulic conductances of the vessels in the absence of red blood cells can be calculated by Hagen–Poiseuille law [Ach90]. Red blood cells temporarily occlude vessels they pass through. This occlusive effect has been modeled by adding a fixed increment to the vessel resistance per cell it contains [SHP01, SA08, CTB17]: $R = \bar{R} + n\alpha_c$, where R and $\bar{R}$ are the effective and Hagen–Poiseuille resistances of the vessel, n is the number of red blood cells in a vessel, and α_c is the occlusive strength per cell. The occlusive strength α_c depends on physiological properties of the vessel, such as radius and the protein coating on the endothelial wall [CTB17], but it singularly depends on the gap distance between the red blood cell and the endothelial wall [SBM16].

This gap thickness depends on the position of the cell within the vessel. Both interactions with the endothelium and the entropy of fluctuations in cell shape tend to push the cell away from the endothelial wall, and into the center of the vessel. We assume the center of the cell is normally distributed around the center of the vessel, with variance σ_n^2. Since normal distribution is isotropic we can instead consider a distribution on the drift distance δ between the centers of the cell and the vessel. Thus the distribution $p(\delta)$ of the drift distance δ is:

$$p(\delta) = \begin{cases} \frac{\frac{\delta}{\sigma_n} e^{-\frac{\delta^2}{2\sigma_n}}}{1-e^{-\frac{\delta_t^2}{2\sigma_n}}}, & \delta \leq \delta_t \\ \\ 0, & \text{otherwise} \end{cases} . \tag{5.1}$$

The cell is confined within the vessel so we need a truncation at $\delta_t < r - r_{RBC}$, where r_{RBC} is the radius of the cell. Here we choose $\sigma_n = \frac{r}{2}$ and $\delta_t = \frac{9}{10}(r - r_{RBC})$ through out the chapter. The gap distance d around the endothelium depends on the angle θ made with the point of closest separation (Fig. 5.2A). If $r - r_{RBC} \ll r_{RBC}$, we may use lubrication theory [Ach90] effectively approximating the flow at each angle as Couette flow. Then α_c can be

approximated as:

$$\alpha_c = \frac{\mu \ell_{RBC}}{\pi^2 r^3} \int_0^{\delta_t} p(\delta) \int_0^{2\pi} \frac{1}{d(\theta, \delta)} \, d\theta d\delta \tag{5.2}$$

if we approximate the coordinate system centered at the vessel by that centered at the cell. The gap distance d is $d = \frac{\delta \tan\theta + \sqrt{r^2 \sec^2\theta - \delta^2}}{\sec\theta} - r_{RBC}.$, where μ is the plasma viscosity, ℓ_{RBC} is the length of the cell, r is the radius of the vessel, and d is the gap distance between the cell and the wall. With the α_c and conductances of each vessel in the network calculated, the flows in the network can be solved for [CR19, MA18]. We can then calculate the fraction of activated endothelial cells. For fixed flow speed, the shear stress on the endothelial wall is inversely proportional to the gap distance. Therefore the shear stress increases from the top ($\theta = \frac{\pi}{2}$) to the bottom ($\theta = -\frac{\pi}{2}$) of the vessel. Cells are activated if their shear stress is higher than a threshold σ_t. For each drift distance δ a critical θ_t can be solved for such that the shear stress at the angle θ_t: $\sigma(\theta_t) = \mu \frac{u}{d(\theta_t, \delta)} = \sigma_t$, where u is the flow speed (we set $\theta_t = \frac{\pi}{2}$, if the whole circumference exceeds σ_t, and $-\frac{\pi}{2}$ if no part does). Typically the shear stress outside of the gap cannot exceed σ_t, so the fraction of activated cells is:

$$f = \frac{n \ell_{RBC}}{\ell} \frac{1}{\pi} \int_0^{\delta_t} p(\delta)(\theta_t(\delta) + \frac{\pi}{2}) d\delta. \tag{5.3}$$

The numerical value of $\theta_t(\delta)$ can be found quickly by bisection [BF10] since the shear stress is monotonic in θ. Then numerical integration is used to integrate in δ.

Single vessels remodel according to the rule

$$\frac{dr_i}{dt} = C_1(f_i - \bar{f})(r_i - r_{RBC}), \tag{5.4}$$

where r_i is the radius of the ith vessel, C_i is the rate of adaptation, and $\bar{f}$ is a target fraction of activated cells. To regularize the system we set a lower bound r_{RBC} on the vessel radius. During zebrafish trunk ontogeny, even if a Se vessel does not carry flow, it is not completely pruned [IHW01, SUP03]. We compare dynamics under this form of shear stress adaptation with a similarly modified form of the model in [HCR12]:

$$\frac{dr_i}{dt} = C_2(\tau_i - \bar{\tau})(r_i - r_{RBC}), \tag{5.5}$$

where τ_i is the average shear stress in vessel i, and $\bar{\tau}$ is the target shear stress. In both models [HCR12, HC13], we include the occlusive effect of the red blood cells upon their

resistance when calculating flows (5.2). Since red blood cells cannot enter vessels with small diameters, we assume that the linear hematocrit h (i.e. number of cells per length of Se vessel) is a constant when $r > r_{RBC} + \epsilon$, and zero otherwise. $\epsilon > 0$ is small enough to not have physical meaning, and our results do not depend on the precise value it is assigned. Our model represents a highly simplified version of the Zweifach–Fung effect [ZL77, BAR08, SCK16, CHJ16, Poz05], which ensures that by volume hematocrit is not necessarily constant through a network of blood vessels. We can evaluate the stability of either model of adaptation by plotting the signals, τ and f, against the vessel radius. The dependence of the signals on the vessel radius is plotted for both mechanisms (5.4, 5.5) when either the flow through the vessel or the pressure drop is fixed while its radius is changed, these being the two common boundary conditions imposed on a flow network [BM07, CR18]. Under a constant flow constraint, the shear stress decreases as the vessel radius increases, due both to increase in the gap between cells and the vessel walls, and smaller peak plasma velocities. Thus under model (5.5) the vessel radius converges globally to a value meeting the desired target shear stress. However, when constant pressure drop boundary conditions are imposed on the same vessel, then shear stress increases with vessel radius; since increases in radius increase the vessel's conductance, and hence blood velocity increases more rapidly than the cell gap does. Thus the radius of a vessel evolving according to model (5.5) will either decay to r_{RBC} or diverge. By contrast, the fraction of stress activated cells decreases monotonically with vessel radius, under both conditions of constrained flow or pressure drop. The effect of vessel radius for constrained flow vessels is the same as for the shear stress model. However, when pressure drop is conserved, a $O(r - r_{RBC})$ increase in vessel radius will strongly affect the cell-gap thickness, while only mildly affecting the velocity of cells. This is because, while the shear stress simply scales with the vessel radius under fixed pressure, the decrease of the shear stress fraction with the increased gap distance is stronger than its increase with the flow velocity.

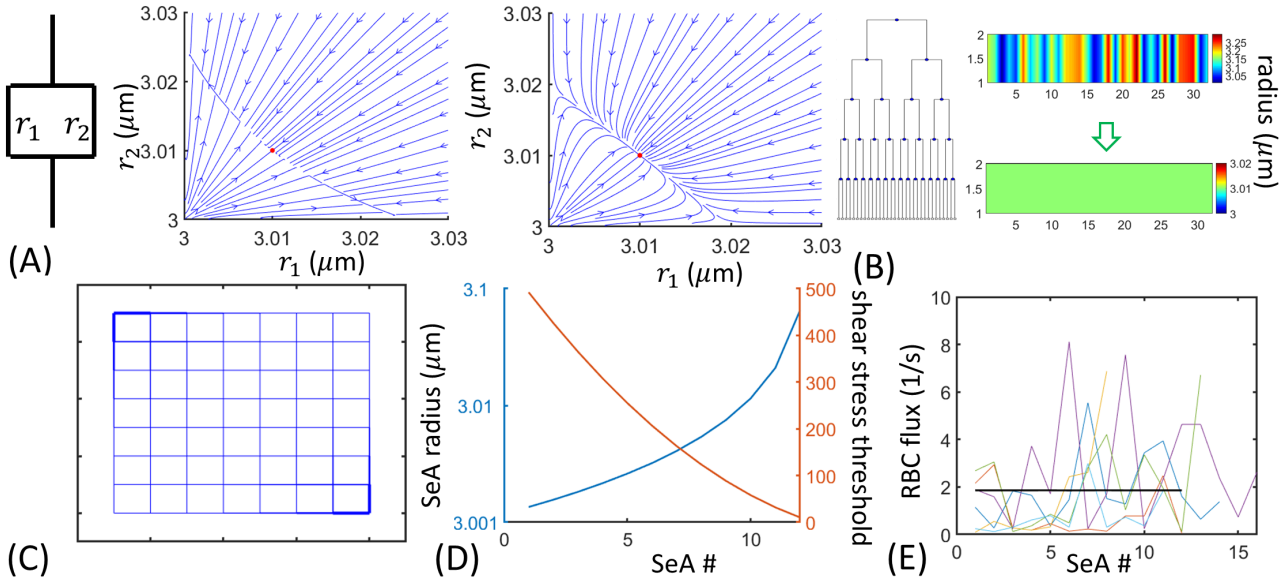

Figure 5.3: The stress activation (SA) model stabilizes network topologies commonly used to model microvascular networks, and creates realistic zebrafish trunk network. (A) The SA model stabilizes the parallel network with 2 vessels (left). The equilibrium is a saddle point in the previous shear stress model (middle) but a stable node in the activation model (right). The effect of red blood cells is included in both models (Eqn. (5.2)). We set the target shear stress and target stress fraction to be such that the state $(r_1, r_2) = (3.01, 3.01)\mu$m is stationary. We used a flow boundary condition with inflow $F = 1.5 \times 10^4$ μm^3/s. The stress threshold $\sigma_t = 380$ dyne/cm^2 is used in panels (A)-(C) and hematocrit 0.014 $1/\mu$m measured from a 4dpf fish is used in panels (A)-(D). (B) The SA model stabilizes hierarchical networks. We applied the model on hierarchical networks with 1–7 levels (left: a level 5 tree), with the lowest vessels following the dynamics (5.4) and the rest of vessel radii determined by Murray's law [Mur26b]. We start the vessels independently uniformly at random between radii 3.005–3.3 μm (up right), and all 70 networks (10 for each level) converge to networks with uniform capillary radius 3.01 μm, which we set to be the stationary state (bottom right). The ODEs are solved with a total time of 200 and $C = 40$.

5.3 *(previous page)*: (C) The SA model stabilizes square grid networks and produces uniform flow networks. We applied the model on 8×8 grids with 112 vessels, with a single inflow $F = 1.1 \times 10^5$ μm^3/s on the top left and outflow in the bottom right vertices. all vessels following the dynamics (5.4). The target stress fraction $\bar{f}$ is set uniformly to 0.025. All 10 networks converge to unpruned networks (shown), and the flows agree to those in the uniform conductance network (mean flow error: $9.1 \times 10^{-3} \pm 1.3 \times 10^{-3}$, mean $\pm$ SE), showing that these networks optimize flow uniformity [CR19]. The ODEs are solved with a total time of 400 and $C = 40$. (D) The SA model creates a realistic 4dpf zebrafish trunk network. We applied the model on the arterial part of the trunk network with 12 SeAs (Fig. 5.1A) [CTB17]. Due to asymmetry introduced by varied distances of SeAs from the heart, we set the stress thresholds σ_t according to a uniform flow zebrafish trunk network [CR19], but a constant stress fraction 0.085. The dynamics (5.4) on SeAs produced an unpruned network with radius increasing from head to tail. We start with a uniform SeA radius 3.6 μm, and the ODEs are solved with a total time of 80, an inflow $F = 3 \times 10^5$ μm^3/s, and $C = 50$. SeAs with smaller numberings are closer to the heart. (E) This SeA radius distribution creates a network with uniform red blood cell flux (black line). The measured RBC fluxes are more fluctuatory ($N = 6$, colored curves), but do not show systematic increase or decrease, which is captured by the uniform flow prediction.

The convergence of adaptation under both boundary conditions promises well for its stability in large networks, where each vessel experiences some hybrid of the two constraints. To quantitatively test the stability of the proposed mechanism we applied both models to a set of archetypal vascular networks. First we consider a simple parallel network with two vessels (Fig. 5.3A, left) with constant inflow into the network. We set the target signals $\bar{\tau}, \bar{f}$ to be the same in two vessels, so that there is one equilibrium with both vessels unpruned, i.e. $r_i > r_{RBC}$, with uniform vessel radius. As observed in [HCR12], the parallel network is unstable under model (5.5), and the only stable equilibrium points are the ones where one vessel is pruned (Fig. 5.3A, middle). In contrast, the proposed model (5.4) has a single

stable equilibrium point where both of the vessels have the same conductances and flows (Fig. 5.3A, right). The activation model also stabilizes large symmetric branching tree networks (Fig. 5.3B, left); we use the model to evolve radii of capillaries (the deepest vessels in the tree), and assume that all shallower branches have fixed radii determined by Murray's law [Mur26b]. Capillaries stably maintain the same radii in networks whose depth ranges from 2 to 7 vessels (i.e. 4 to 128 capillaries); over the same range of depths the most unstable eigenvalue increases from -0.56 to -0.21. Moreover, the equal capillary size constraint is robust even against finite perturbations: we simulated the adaptation of networks in which capillary initially varied from the equilibrium radius by $\sim 10\%$, and they still converged to networks in which all of the capillaries had the prescribed radius (Fig. 5.3B, right). Model (5.4) therefore allows stable adaptation of networks on a scale exceeding the vessel opening and closing model of [HCR12], which was shown to ensure stable adaptation of networks with depth 4.

We also applied the adaptation model to a square grid network, which has been used as a model for a capillary bed (Fig. 5.3C) [OWB10, CR19]. Although uniform activation of cell of the vessels does not physically require that each vessel receives the same flow, structural adaptation nonetheless produces a network with maximally uniform flow: it is impossible to creat any network on which flows in each vessel are the same, because of the number of vertices in which three vessels meet, but at which flow must nonetheless be conserved. However, the square grid is an example of a stackable network – it can be divided by surfaces that cut each vessel exactly once – so maximal uniformity occurs for a family of networks each of which has the same set of flows as one in which all vessels have the same conductance [CR19]. Under activation adaptation, the final, stable networks have an apparent hierarchy of vessel radii, thickest at the inlet and out let and along the mid-line of the grid, but matches the flows produced by a uniform conductance network to within 0.91%. Flow uniformity is tightly related to oxygen and metabolite exchange [MA18], and the proposed mechanism provides a theoretical guidance on creating microvascular networks with uniform flow.

Can activation adaptation produce the embryonic zebrafish trunk? Previous calculations [CTB17] have shown that the resistance of vessels must decrease from rostral to distal vessels

to ensure uniform flow. To achieve this we allow the shear stress threshold σ_t to vary between Se vessels, which may be determined by the pressure in the aorta before Se vessels form [IHW01]. Here we set the stress thresholds by the known structures of zebrafish trunk networks with uniform flow (computed in [CTB17, CR19]). The stress threshold is a simple function that monotonically decreases from head to tail (Fig. 5.3D). We evolved the zebrafish trunk network using model (5.4) starting with each Se vessel having a radius of $3.6\mu m$, initially therefore vanishing activation fraction of each Se vessel. From these initial conditions activation adaptation generates an unpruned network with vessel radii increasing from head to tail [CTB17, CR19]. The shear stress fractions match the target values, showing that the mechanism stabilizes the trunk network. The variation in vessel radius creates a blood flow pattern that agrees with the measured blood flow among $N = 6$ 4dpf zebrafish trunks (Fig. 5.3E): blood flow varies between Se vessels but does not systematically increase or decrease from head to tail.

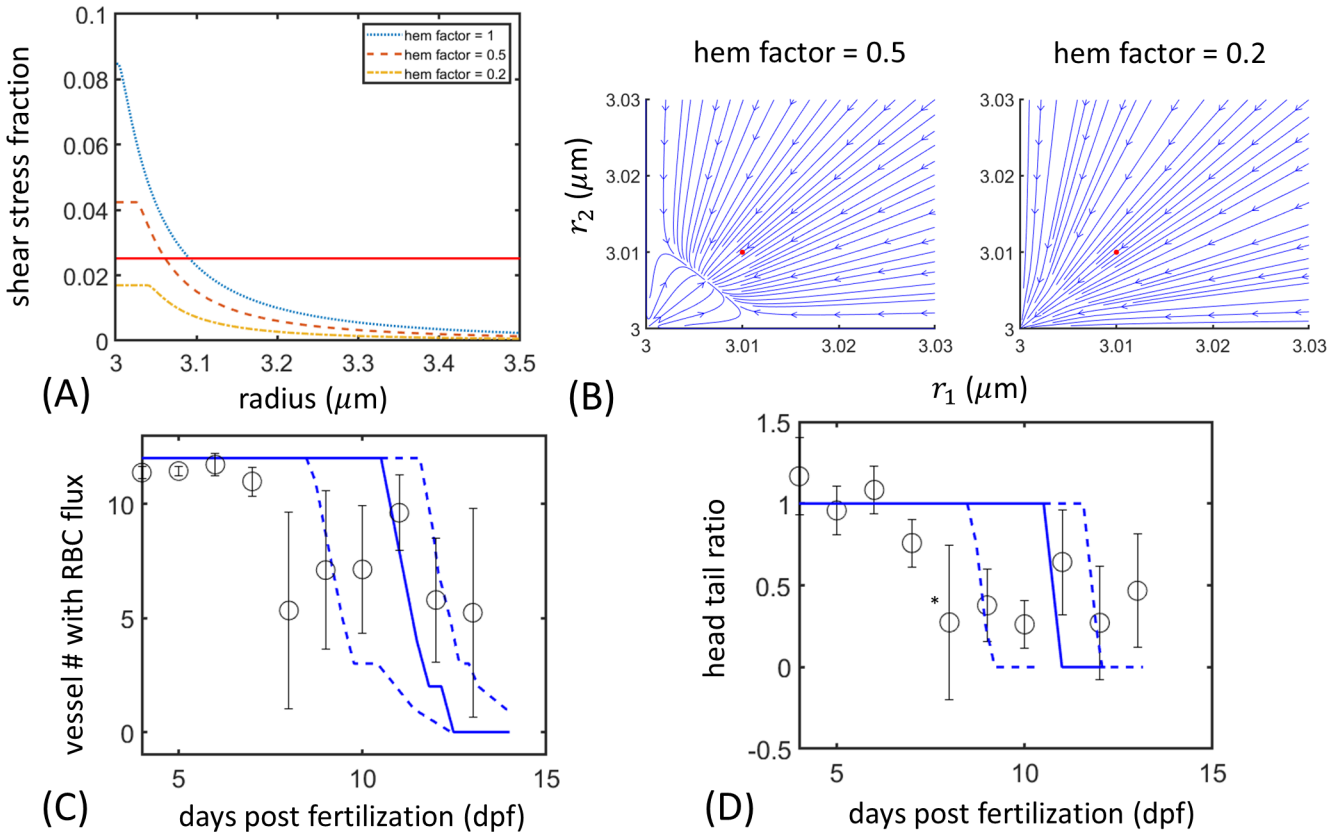

Figure 5.4: The stress activation (SA) model becomes unstable as hematocrit decreases, which predicts the pruning during zebrafish development from 4 to 13 dpf. (A) The stress fraction signal becomes weaker as the hematocrit decreases. At low hematocrit (0.2× normal hematocrit, yellow dash-dotted curve) the stress fraction at all vessel radii lies below a target stress fraction (red line), suggesting the occurrence of pruning. The parameters in panels (A), (B), (C) are the same as those in Fig. 5.2D (pressure boundary condition), Fig. 5.3A and D, respectively. (B) The hematocrit-induced pruning occurs in the parallel system with two vessels. When the hematocrit halves the normal value, the equilibrium is shifted toward smaller vessels (left, red dot: original equilibrium), and then at lower hematocrit an equilibrium with both vessel radii larger than the radius of the RBC ceases to exist (right). (C) The SA model with experimentally measured hematocrit predicts the pruning of Se vessels during zebrafish development.

5.4 *(previous page)*: We apply the dynamics (5.4) on zebrafish trunk topology with 12 SeAs, and change the hematocrit according to previous data [SUP03]. The model predicts a decrease in the number of vessels with RBC flow (blue curve), with a variation induced by uncertainties in hematocrit measurement (blue dashed curves: prediction from mean + SD hematocrit, and vice versa). This prediction matches our measurements of the fraction of Se vessels with RBC flow from 4 to 13 dpf (black dots, mean ± SD, 2–4 fish per dpf). A single parameter $C = 50$ was fitted to the data. The viscosity in the aorta is adjusted according to [GWS81]. (D) Additionally the SA model predicts the head tail asymmetry of RBC flow during zebrafish development. The model predicts a decrease in head tail ratio (blue solid and dashed curves), determined by the fraction of vessels with RBC flow in the rostral third of the trunk divided by that in the caudal third, that matches our measurements (black dots and error bars). The symbols have same meanings as in (C). Star: one data in 8 dpf with infinite ratio is ignored.

The fraction of stress-activated cells in a vessel depends on hematocrit. If the pressure difference across a single vessel is maintained, we plot the fraction of activated cells as a function of vessel radius for different hematocrits (Fig. 5.4A). The overall shape of the stress activation function remains the same, but the maximum fraction of activated endothelial cells decreases as the hematocrit decreases (Since hematocrit also affects the velocity of the cells changing hematocrit does not simply rescale the stress activation curve.). Hence, unless there is a compensatory decrease in the $\bar{f}$ or σ_t, the equilibrium radius of the vessel will decrease with hematocrit. At small enough hematocrit, $\bar{f}$ can no longer be attained at any radius, and the vessel will continue to shrink until red blood cells may no longer pass through it. When we reduce hematocrit in the same way in the two parallel vessels, equilibrium radius initially decreases in both vessels (Fig. 5.4B, left), and eventually vanishes with the whole network pruned (Fig. 5.4B, right).

Does the embryonic zebrafish network show the same structural evolution when hematocrit changes? During normal zebrafish development, there is a 3.5-fold decrease in hemat-

ocrit between 4dpf and 15dpf – i.e. immediately after the period of network stability assay in Fig. 5.1D [SUP03]. The reasons for this decrease are not known, but it may be part of the process of transition from short-lived primitive red blood cells to mature red blood cells [WSA96]. Accordingly the average hematocrit in Se vessels decreases in 4 to 14 dpf fish [SUP03]. Does the network adapt? We simulate the continuing development of zebrafish trunk vasculature by following model (5.4) using previous time series data of hematocrit [SUP03]. Our model predicts that reduced activation of endothelial cells causes vessels to shrink, and actually become unstable to carry red blood cells. The predicted increasing the number of Se vessels without red blood cell flux quantitatively agrees with real measurements of embryonic trunk flow (Fig. 5.4C). Additionally our model for structural adaptation predicts that the remaining RBC-carrying vessels will be primarily located in the tail of the zebrafish, partly since the tail vessels have the largest stable radius and partly because they maintain this radius by having the lowest threshold for shear stress activation, and will therefore be the slowest vessels to become too small to admit red blood cells. This, too, is supported by real zebrafish data. In Fig. 5.4D we show the fraction of the ratio of the vessels in the rostral third trunk that carry red blood cells to those in the caudal third trunk. The decrease of this head tail ratio over development, reflecting the skew of low toward the most distal of Se vessel, quantitatively matches the predictions of model (5.4).

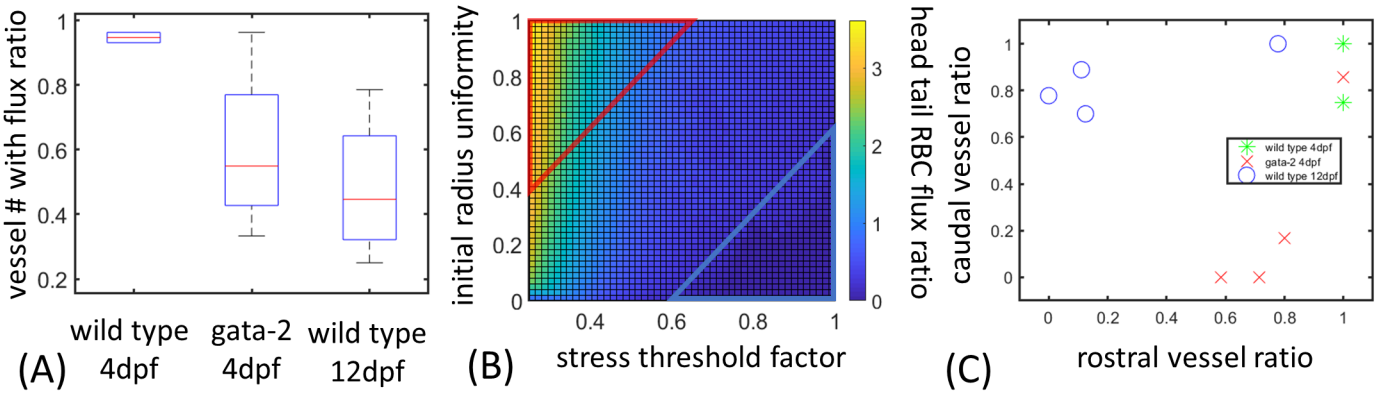

Figure 5.5: The stress activation (SA) model can explain the pruning pattern in gata-2 zebrafish where the number of red blood cells is reduced by half. (A) Gata-2 4dpf fish show a similar level of vessel pruning as wild type 12dpf fish, compared to wild type 4dpf fish (box plot), due to a reduced level of hematocrit. (B) Our simulations suggest that gata-2 4dpf fish can have a different pattern in RBC flow from wild type 12dpf fish, though they have a similar level in hematocrit. We simulate 2 days of development with different uniformity in initial radius (interpolated from a uniform radius of 3.065μm and the wild type 4dpf radius distribution shown in Fig. 5.3D) and scales in shear stress threshold, represented by a factor that multiplies the stress threshold distribution in wild type 4dpf fish shown in Fig. 5.3D. The parameters that model gata-2 4dpf fish produce focused RBC flow in the rostral trunk (red triangle), while those modeling wild type 12dpf fish reproduce focused RBC flow in the caudal trunk (blue triangle). (C) Our prediction of RBC flow pattern is verified by our measurements on gata-2 4dpf and wild type 12dpf fish. We plot the fractions of number of Se vessels with RBC flow in rostral and caudal thirds of the trunk. The vessels with RBC flow in gata-2 4dpf fish concentrate in the rostral trunk (red crosses), while those in wild type 12dpf fish focus in the caudal trunk (blue circles), compared to wild type 4dpf fish where most of the Se vessels have RBC flow (green stars).

To test whether the decrease in hematocrit drives changes in the geometry of the network, we performed additional experiments in which the GATA-2, a hematopoiesis transcription factor, was knocked down by injecting the fish with antisense morpholinos [VFL09]. Knock-

down fish had approximately half of the number of red blood cells seen in wild type fish [VFL09]. As our model predicts, structural adaptation of the network meant that only a small fraction of vessels (55% at 4 dpf) remained wide enough open to admit RBCs, which is close to that in wild type 12 dpf fish (45%) that has a similar hematocrit (Fig. 5.5A). However, unlike decreasing hematocrit during normal development, gata-2 fish did not experience a period of normal hematocrit level before the decrease in hematocrit initiates. This sets gata-2 4dpf fish apart from wild type fish in a later developmental stage, say 12dpf, and this difference can change the distribution of vessels with RBC flow throughout the trunk. To simulate this effect we explore how the head tail asymmetry depends on two parameters: the initial radius distribution and the scale of shear stress threshold. In later developmental stages the vessel radii have already adapted to the blood flow, while in early stages the vessels have less information from blood flow. The hematocrit also affects the viscosity in aorta, which in turn changes the shear stress experienced by budding Se vessels and can set a different scale of stress threshold in early developmental stages. Therefore while the wild type 12dpf fish have normal stress thresholds and initial radius distribution close to a wild type 4dpf fish, we expect gata-2 fish to have lower stress thresholds and more uniform distribution of vessel radius. This difference leads to different head tail asymmetry in gata-2 4dpf and wild type 12dpf fish in our simulations, with RBC flow focused in the rostral trunk in gata-2 4dpf fish (Fig. 5.5B). This prediction matches our measurements on gata-2 4dpf fish where vessels with RBC flow aggregate in rostral trunk, in sharp contrast with wild type 12dpf fish where those vessels concentrate in the caudal trunk (Fig. 5.5C).

5.3 Acknowledgments

MR and SSC were funded by grants from the NSF (under grant DMS-1351860) and NIGMS (under R01 GM126556). SSC was also supported by the National Institutes of Health, under a Ruth L. Kirschstein National Research Service Award (T32-GM008185). The contents of this chapter are solely the responsibility of the authors and do not necessarily represent the official views of the NIH.

CHAPTER 6

A dynamical bifurcation model of bipolar disorder based on learned expectation and asymmetry in mood sensitivity

This chapter was based on: Shyr-Shea Chang and Tom Chou. "A dynamical bifurcation model of bipolar disorder based on learned expectation and asymmetry in mood sensitivity." *Computational Psychiatry*, 2, 205–222, 2018.

6.1 Introduction

Bipolar disorder is characterized by cycling between manic and depressive episodes [GL97]. Its prevalence is estimated to be $0.3\%-1.5\%$ of the total population [WBC96]. The lifetime cost for a single patient can reach several million US dollars [BAS01], and medication use associated with bipolar disorder comprises about 7% of that used to treat all mental disorders [WDR13]. Bipolar disorder has a serious societal impact, with 65.5 work days lost per year per patient [KAA06] and its early onset a major risk factor for suicide [HSH05]. Despite the significance of bipolar disorder, there is limited structural understanding of the underlying mechanisms [GM13]. Modern techniques such as functional magnetic resonance imaging (fMRI) have located neural circuits including limbic networks and attentional systems, whose dysfunction may be correlated with bipolar disorder [SAH04, CSL11]. However, how the dysfunction of these circuits leads to emotional vulnerability remains unclear.

In order to understand the mechanism of bipolar disorder and accelerate the development of treatment [GM13], many mathematical models have been proposed and fit to ex-

perimental data. An oscillation in mood, either observed or self-reported, is the defining feature of bipolar disorder [GL97]. Thus, early models focus on explaining this oscillation [BGG15, DRU09, Gol11, MLM12]. The models describe mood as being formed from an intrinsically oscillatory brain circuit and explain self-reported mood scores as well as the effects of medication. Following these studies, a natural next step is to clarify the mechanism of the oscillations and distinguish key differences between normal individuals and patients with bipolar disorder (see also [Gol11]). A popular theory states that dysregulation of the Behavioral Approach System (BAS) and the resulting interaction between mood, expectation, and behavior can explain bipolar disorder [UAH08]. Psychological observations provide evidence of malfunction of the BAS, and models have been built to explain bipolar disorder based on this malfunction [SW13]. A key difference between BAS-based models and some earlier models is that BAS models show bistability in mood instead of oscillations and require external input or noise to trigger switching between states of mania and depression [CSM17].

Can a model exhibiting periodic mood oscillations and other observed features be derived by from self-contained and general models that incorporate expectation and behavior? Recent psychological experiments have shown that emotion is affected by the mismatch between expectation and reality instead of the reward value [RSD14]. Theoretically, it has been shown that the interaction between mood and expectation captures the qualitative features of self-reported mood in psychological experiments [EN15] and can indeed lead to bipolar disorder. In reality, there are many factors that can interact with mood and expectation. For example, it was suggested [ERD16, MER17] and reported both clinically and in psychological experiments [GKY04, PB17] that the sensitivities toward positive and negative events can be different.

In this work, we develop and analyze a variant of the models proposed by [EN15, ERD16] and [MER17]. Like these models, our model is based on an interaction between mood and expectation and incorporates experimentally measurable variables (for example, see [PB17]). Following a similar analysis as that in [EN15], we prove that our model exhibits oscillatory mood behavior when a particular psychological parameter, the mood sensitivity, exceeds a

threshold value. Our analysis further quantifies the amplitude and frequency of oscillations in mood and expectation. We also explore the effects of different amplitudes of responses of mood to positive and negative events–or asymmetric mood sensitivity. In our model, we will show that depending on the initial level of asymmetry, changing the response to either positive or negative events may lead to a bipolar state. We introduce a piecewise-linear reality function with random amplitude and time intervals but whose mean does not change over time, and show that it preserves many of the qualitative features predicted under constant reality but produces irregular mood trajectories that qualitatively resemble observations [BGG15]. Finally, we model the effects of pharmaceutical intervention, including those of antidepressants and lithium.

6.2 Mathematical Model

In this work we want to investigate how the interaction between the mood and the expectation models both normal individuals and bipolar disorder patients. The idea of the model is that the mood and expectation are both affected by the difference between perceived reality and the expectation, since the expectation sets a baseline for us to judge the reality, and the current mood can affect how we see the reality. The mood is assumed to be confined by chemical limits, which is reflected by the decay terms in the mood equation. The equations in terms of mood $m(t)$, expectation $v(t)$, and reality $r(t)$ can be written as:

$$\frac{\mathrm{d}m}{\mathrm{d}t} = \eta_m(fm + r - v) - km - k_3m^3 \tag{6.1}$$

$$\frac{\mathrm{d}v}{\mathrm{d}t} = \eta_v(fm + r - v). \tag{6.2}$$

Here, η_m and η_v are learning rates for mood and expectation, respectively; f is a scale factor for how mood contributes to *perceived* reality $fm+r$; and k, k_3 are linear and cubic recovery rates for mood, respectively. The perceived reality $fm+r$ in our model represents, in a linear way, the modification that mood has on reality. Thus, $fm+r-v$ reflects the extent to which an individual is surprised and how strongly she should respond. Unlike for the expectation $v(t)$, the mood equation contains a separate term that drives it to a baseline level, even after

positive reality events such as winning a lottery [BCJ78]. This recovery "force" for the mood is captured by the $-km(t)$ term, with k^{-1} a mood relaxation timescale. We will see that this linear recovery term is essential for explaining the cyclothymic transition from normal to bipolar models. Finally, if mood is viewed as a physiological quantity, its magnitude should be bounded. To prevent the mood from growing indefinitely, we include a higher-order nonlinear cubic term (corresponding to a quartic "potential") in the mood equation. Thus, both linear and cubic recovery terms play key roles in explaining how the bipolar disorder occurs in our model.

The reality $r(t)$ is derived from external events and is not affected by personal mood or expectation. This assumption distinguishes the proposed model from those based on the Behavioral Approach System (BAS) [SW13]. By eliminating the expectation $v(t)$, our model can also be written in terms of a single nonlinear oscillator in mood (assuming that $r(t)$ is differentiable):

$$\frac{\mathrm{d}^2 m}{\mathrm{d}t^2} - (f\eta_m - k - \eta_v - 3k_3 m^2)\frac{\mathrm{d}m}{\mathrm{d}t} + \eta_v k m + \eta_v k_3 m^3 = \eta_m \frac{\mathrm{d}r}{\mathrm{d}t}. \tag{6.3}$$

This is a Liénard equation [Str14] similar to the general Liénard oscillators invoked in previous theories [DRU09, BGG15]. The main new features here are the forcing term $\eta_m(\mathrm{d}r/\mathrm{d}t)$ that depends on *changes* in reality, the higher order term $\eta_v k_3 m^3$, and a possibly non-constant parameter η_m as we will explore later in this section. The main mechanism behind our model is that positive and negative surprises, i.e. the difference between perceived reality and expectation, drive mood in corresponding directions, which in turn adjust the perceived reality and speed up the adaptation of expectation. In this sense, the rate of change of mood is analogous to the momentum of a damped harmonic oscillator [ERD16]. From our daily experience it is apparent that mood changes the way we perceive reality: a minor drawback may have little effect on us when we are happy, but can be a source of depression if we are not in good spirits.

Our model is actually a variant of the one proposed in [ERD16] but differs in three ways. First, the mood affects the perceived reality in the mood dynamics. Second, the linear decay

term $-km$ has an independent parameter k. This is different from the [ERD16] model in which the mood recovery rate is assumed to be the same as the mood learning rate η_m and allows for more mathematical generality, since psychologically the mood recovery rate may be able to vary independently from the mood learning rate. Finally, as noted above, we have added a cubic mood recovery term $-k_3 m^3$. A nonlinear suppression term and the linear decay term are essential for the system to admit limit cycle behavior that captures bipolar disorder.

The model exploits a similar central mechanism as that proposed in [EN15], but with a number of technical differences. In [EN15] the mood is defined through a sigmoidal function tanh of a quantity that reflects recent "prediction-error history." In contrast, the mood in our model directly reflects the prediction-error history, but is susceptible to the effects of a higher order recovery term $-k_3 m^3$, distinguishing it from both [EN15] and [ERD16]. This difference represents two mechanisms for bounding the mood: explicitly specifying the limits of the mood through the tanh function and limiting the mood through a general (allowed by symmetry) cubic "force" term in the dynamics. Our model is also different from [EN15] in that the effect of mood on perceived reality assumes an additive rather than a multiplicative form. In summary, our model has a simpler mathematical form yet generalizes the previous models by [EN15, ERD16] and [MER17] in a way that allows for a clean, self-contained mathematical analysis and a spectrum of qualitative behaviors.

Throughout this chapter we will explore the effects of two forms of the reality function $r(t)$: a constant $r(t) = r_0$, and a random $r(t)$. In the random case, we assume a piecewise constant form for $r(t)$ with normally distributed values and log-normally distributed times between jumps. This functional form reflects the abrupt nature of changes in reality such as salary raises or the death of relatives cause a dramatic change that lasts for certain period of time. We set the mean, standard deviation of $r(t)$ to be $0, \sigma_r$. The time intervals between jumps in $r(t)$ are drawn from a log-normal distributions with mean log time $1/k_r$ and standard deviation of the log time $1/k_r$. The parameters f, k, k_3, η_v are treated as positive constants throughout the chapter. It has also been shown that learning rates η_m can be different for positive and negative events [PB17], which we model using a Heaviside function

of $fm + r - v$:

$$\eta_m = \begin{cases} \eta_m^+, & \text{if } fm + r - v > 0 \\ \eta_m^-, & \text{if } fm + r - v \leq 0 \end{cases}, \tag{6.4}$$

where η_m^+, η_m^- are positive constants. We will show in the Results section how asymmetry in η_m (the case $\eta_m^+ \neq \eta_m^-$) can influence the onset of disorders. The parameters are tuned such that the timescale of mood variation matches the experimental data in [BGG15], except in Fig. 6.3 the timescale is tuned so that the adaptation of mood to positive and negative events fits more to the observed time scale.

To better connect our results with clinical observations, we calculate QIDS-SR16 (Quick Inventory of Depressive Symptomatology) scores [RBT06] from our model. The QIDS-SR16 (QIDS for short) is commonly used for analyzing and testing treatments of bipolar disorder [BWG12, HBH16] and consists of a 16-item self test that measures the level of depression. We calculate this score by taking $-\min(0, m)$ since negative mood corresponds to depression. In principle, our model predicts mood and expectation but does not capture all specific indicators of depression and mania. Here, we adjust the scale of mood to QIDS score to connect our work with clinical observations. The system (6.1,6.2) is solved by explicit 4th to 5th order Runge-Kutta solvers [DP80], carried out by the `ode45` function in MATLAB.

6.3 Results

6.3.1 Mood and expectation become more oscillatory as the mood sensitivity increases

For normal subjects we expect that if the reality $r(t) = r_0$ is constant the expectation should approach r_0 and the mood will relax to zero as there is no additional stimuli; this justifies shifting $r_0 \to 0$ without loss of generality and linearizing Eqs. (6.1-6.2) around the fixed point $(m, v) = (0, 0)$. In this way we can define the parameter regime within which the origin becomes linearly unstable (suggesting the onset of bipolar disorder) and which

parameters are crucial in this process. Before we study more general cases, we first assume symmetry in the mood learning rate η_m, i.e., $\eta_m^+ = \eta_m^-$, to gain insight into the basic model. Upon linearizing Eqs. (6.1-6.2) or Eq. 6.3 about $(m, v) = (0, 0)$ for $r = 0$, we find the two eigenvalues

$$\lambda_\pm = \frac{\eta_m f - \eta_v - k}{2} \pm \frac{\sqrt{\Delta}}{2}, \tag{6.5}$$

where the discriminant

$$\Delta \equiv \left(\eta_m f - \eta_v - k\right)^2 - 4\eta_v k. \tag{6.6}$$

Thus, the origin is linearly stable when $f\eta_m - k - \eta_v < 0$ and $\mathrm{Re}(\lambda_\pm) < 0$, and unstable when $f\eta_m - k - \eta_v > 0$, corresponding to at least one eigenvalue containing a positive real part. This analysis agrees with that of [ERD16] in which bipolar disorder arises either when f is large or $\eta_m \gg \eta_v$. Here, we focus on mood and base our study on the quantity $f\eta_m$, which we call the mood sensitivity parameter. In the linearly stable case, the system can support transiently oscillating behavior in mood and expectation, similar to that of a damped harmonic oscillator [Mar13]. For oscillatory behavior that is underdamped or undamped, there are potentially associated qualitative clinical presentations such as cyclothymic and bipolar personalities [MER17].

Oscillation frequencies are characterized by the imaginary part of the eigenvalues, determined by the sign of Δ. When Δ is positive there will be no oscillation in the solutions, while negative Δ corresponds to oscillatory solutions, with oscillation frequency determined by $\sqrt{|\Delta|}/2$. As a function of the mood sensitivity parameter $f\eta_m$, we see that Δ is a parabola with minimum at $f\eta_m = \eta_v + k$, the critical value for linear stability, with a negative discriminant $-4\eta_v k$. Thus, as $f\eta_m$ increases toward the critical value $\eta_v + k$, the mood and expectation become oscillatory with the frequency in the oscillations increasing. As the mood sensitivity $f\eta_m$ exceeds the critical value, a Hopf bifurcation occurs, the linearized dynamics become unstable, and linear analysis can no longer predict system behavior. This

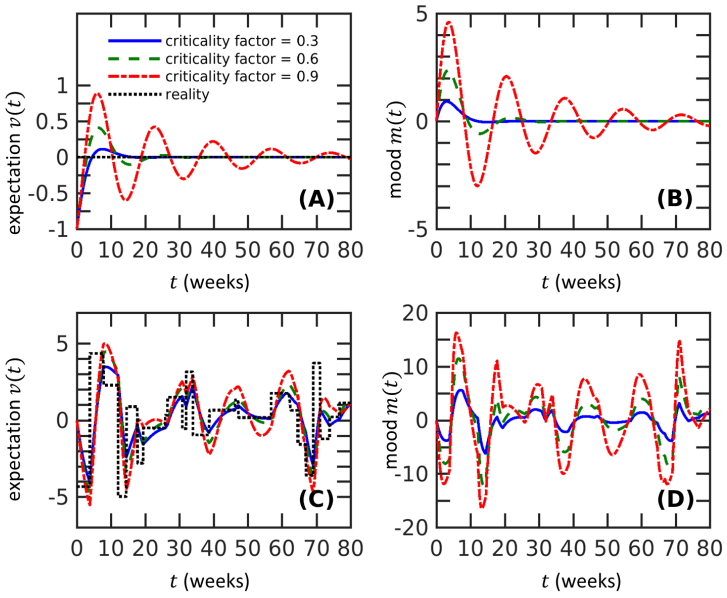

Figure 6.1: The mood and expectation of normal subjects become more oscillatory as the mood sensitivity $f\eta_m$ increases towards the critical value $\eta_v + k$ from below. (A) Oscillations in expectation are highly damped for normal subjects (blue solid, $f\eta_m = 0.3(\eta_v + k)$), but become less damped when the mood sensitivity increases (green dotted, $f\eta_m = 0.6(\eta_v + k)$, and red dash-dot, $f\eta_m = 0.9(\eta_v + k)$). Since we start the solutions at $(m, v) = (0, -1)$, the constant reality $r(t > 0) = 0$ represents a permanent increase in reality from $r(t < 0) = -1$. The numerical values $\eta_v = 0.37, f = 0.3, k = 0.37$, and $k_3 = 2.8 \times 10^{-3}$ are used in all figures. (B) The mood shows similar oscillatory behavior that become less damped with increasing mood sensitivity. (C) When subjected to random reality events, models with large mood sensitivities exhibit larger responses in expectation. (D) Similarly, the fluctuation in mood is greater for in systems with larger mood sensitivity under random reality conditions. Realizations of the random reality function are generated as described in the Mathematical Model section, with $\sigma_r = 2, k_r = 1$. In (C) and (D), mood and expectation are initialized at $(m, v) = (0, 0)$.

argument suggests that mood fluctuations even in normal (subthreshold) systems nonetheless increase as the mood sensitivity increases. We verify these arguments by numerically solving Eqs. (6.1,6.2) using constant $r(t) = 0$ and different mood sensitivities. The numerical

solutions show that the oscillation frequency in mood and expectation increases as the mood sensitivity $f\eta_m$ becomes larger, as predicted by our linear analysis (Fig. 6.4A, B). Notice that when $k = 0$ and there is no linear dissipation of mood, the eigenvalues are strictly real and the system does not support a cyclothymic regime across the stability threshold. The mood dynamics transition from exponentially decaying directly to exponentially growing behavior.

Linear stability analysis does not fully apply when the reality $r(t)$ is time-dependent. However, numerical solutions show that for larger $f\eta_m$, expectation $v(t)$ deviates more from reality $r(t)$ and that mood $m(t)$ experiences higher variations about its baseline (Fig. 6.4C, D). These results suggest that the mood sensitivity controls a spectrum of personality responses, from normal to cyclothymic, and is a key determinant in triggering bipolar disorder as its threshold is exceeded.

6.3.2 A limit cycle occurs as mood sensitivity crosses the critical value, representing a bipolar state

Once the mood sensitivity $f\eta_m$ exceeds the threshold $\eta_v + k$, linear analysis no longer holds since the origin becomes unstable and nonlinearities quickly become important. However, for two dimensional systems, we can rely on the Poincaré–Bendixson theorem to predict the existence of a limit cycle, a periodic solution that attracts solutions starting nearby [Str14]. For this analysis, and in the rest of this subsection, we still assume $\eta_m^+ = \eta_m^-$ and a constant $r(t) = 0$. Since the origin is linearly unstable, we search for a limit cycle by constructing an outer boundary on which the vector fields are pointing inward. One way of finding this boundary is to draw a rectangle whose edges connect two nullclines $v = (f - \frac{k}{\eta_m})m - \frac{k_3}{\eta_m}m^3$ and $v = fm$. Since $\eta_m^+ = \eta_m^-$, both nullclines are rotationally symmetric allowing us to find the distance to the right edge of the boundary by setting $-fm^*$ equal to the m-nullcline:

$$-fm^* = (f - \frac{k}{\eta_m})m^* - \frac{k_3}{\eta_m}m^{*3}, \tag{6.7}$$

which leads to

$$m^* = \sqrt{\frac{2f\eta_m - k}{k_3}}. \tag{6.8}$$

Thus, the rectangle with vertices $(\pm m^*, \pm fm^*)$ serves as an outer boundary confining all trajectories that start inside it, leading to existence of a limit cycle [Str14].

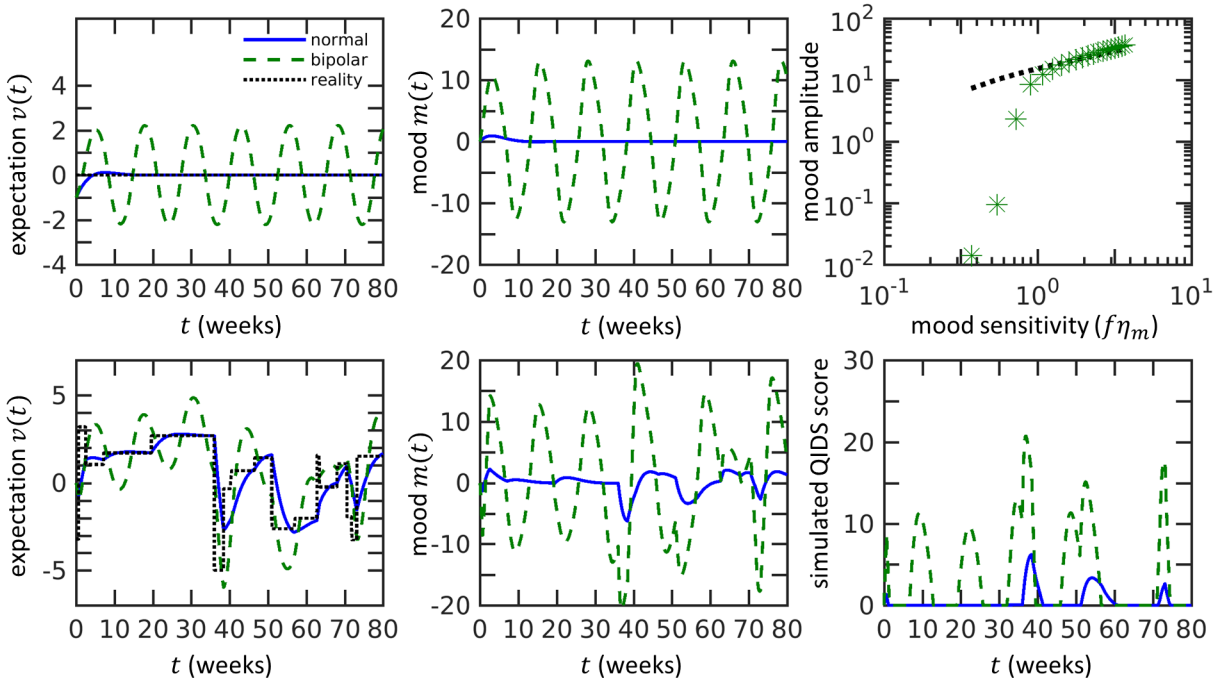

Figure 6.2: Our theory predicts that the onset of bipolar disorder occurs through a supercritical Hopf bifurcation as the mood sensitivity $f\eta_m$ crosses the threshold value $\eta_v + k$ and a limit cycle in mood $m(t)$ is established. (A) In a bipolar state, the expectation $v(t)$ (dotted green) persistently oscillates, in contrast to the normal case (solid blue). We set the reality $r(t > 0) = 0$ and use $(m, v) = (0, -1)$ as the initial condition. The bipolar state is modeled using $f\eta_m = 1.5(\eta_v + k)$, whereas the normal state is computed using $f\eta_m = 0.3(\eta_v + k)$. The numerical values $\eta_v = 0.37, f = 0.3, k = 0.37$, and $k_3 = 2.8 \times 10^{-3}$ are used in all plots. (B) Mood of bipolar subjects also persistently oscillates. (C) The magnitude of mood oscillations increases as the mood sensitivity $f\eta_m$ increases. The amplitude of oscillations obtained from numerical simulations (green stars) compares well to amplitude estimates using Eq. (6.8) (black dots) when $f\eta_m \gg \eta_v + k$.

6.2 *(previous page)*: (D) Expectation $v(t)$ in the bipolar state responds to changes in reality but remains oscillatory (green dashed). This behavior is distinct from the expectation of normal subjects (solid blue curve) that more closely follow the reality function. (E) Under the same reality function as in (D), the mood is much more oscillatory in the bipolar state (green dashed curve) than in the normal state (solid blue curve). (F) The model predicts intermittent spikes in the QIDS score. Realizations of the reality function are generated as described in the Mathematical Model section, with $\sigma_r = 2, k_r = 1$. For (D), (E), and (F), the initial condition is $(m, v) = (0, 0)$.

This result, along with the instability of the $(m, v) = (0, 0)$ state as $f\eta_m$ surpasses $\eta_v + k$, implies a supercritical Hopf bifurcation at $f\eta_m = \eta_v + k$. Psychologically, this means that the expectation and mood persistently oscillate under constant reality conditions, in sharp contrast to the behavior in a normal non-bipolar state (Fig. 6.2A, B). It is difficult to predict how the amplitude of the oscillation scales with the psychological parameters since this requires analytically solving the nonlinear system. However, the formula for outer boundary Eq. (6.8) could give us a prediction. Eq. (6.8) predicts that, after the onset of bipolar disorder, the mood sensitivity $f\eta_m$ still positively correlates with the mood amplitude. This prediction is verified by numerical calculations using large $f\eta_m$ (Fig. 6.2C), suggesting that the mood sensitivity parameter plays an essential role even after the onset of bipolar disorder. How the amplitude of the oscillations depends on the mood sensitivity $f\eta_m \gtrsim \eta_v + k$ can possibly be estimated using weakly nonlinear analysis [BO13] of Eq. 6.3 but will not be treated here.

While the current analysis applies only in the case of constant reality, the qualitative feature of persistent oscillations does not change even if the reality $r(t)$ varies in time. Numerical solutions show that the oscillations are not destroyed by changes in reality but take on an autonomous nature (Fig. 6.2D, E). The QIDS score for the bipolar case shows intermittent peaks that match qualitatively with experimental data [BMG10, BGG15]. Together, our analyses and numerical solutions show the onset of bipolar disorder as the mood sensi-

tivity $f\eta_m$ crosses a critical value, leading to persistent oscillations in mood and expectation qualitatively similar to those observed in mood profiles of bipolar patients.

6.3.3 Asymmetric mood sensitivity to positive and negative events can lead to unipolar depression/mania

Asymmetric response to positive and negative events and its effects on human learning have been widely reported and inferred from psychological experiments [PB17, Lep06]. It has been observed that patients with major depression respond more strongly to negative stimuli than to positive stimuli [GKY04, GKT04]. Patients with mania, on the other hand, show less response to negative stimuli [LJC04]. Interestingly, patients with bipolar disorder, even during euthymic or depressive episodes, show stronger responses to both positive and negative stimuli [LWS04], consistent with our results in the previous subsection where the response was characterized by the mood sensitivity $f\eta_m$.

When the learning rate for mood η_m is asymmetric [as in Eq. (6.4)] and r is constant, the $v-m$ plane is split into two half-planes, separated by the nullcline $\frac{dv}{dt}=0$ ($v=fm$ for $r=0$). The different values $\eta_m^{\pm}$ apply in each of the half-planes, leading to a continuous but non-differentiable vector field. This feature complicates the linear stability analysis (see next subsection), but it is clear that if both $f\eta_m^+ < \eta_v + k$ and $f\eta_m^- < \eta_v + k$, the origin is linearly stable (the non-bipolar state). We show our asymmetric learning model, even in a non-bipolar (stable when r is constant) state, can support unipolar depression/mania when the reality $r(t)$ varies in time about $r=0$. Consider three different systems with different values of $\eta_m^{\pm}$ such that $(f\eta_m^+/(\eta_v+k), f\eta_m^-/(\eta_v+k)) = (0.4, 0.4), (0.8, 0.1)$ and $(0.1, 0.8)$. These sets of learning rates will correspond to "normal," "manic," and "depressive" subjects, respectively.

Figs. 6.3 show simulations started well in the past with $r(t<0)=0$. The reality is then decreased to $r(0\le t<1)=-4$, followed by an increase to $r(t\ge 1)=+4$. We see that the expectation of depressive subjects overreacts to negative reality and fails to fully recover by $t=2$ after the reality switched positive at $t=1$ (Fig. 6.3A). This lag in recovery leads to a prolonged time of depression compared to that of normal and manic subjects,

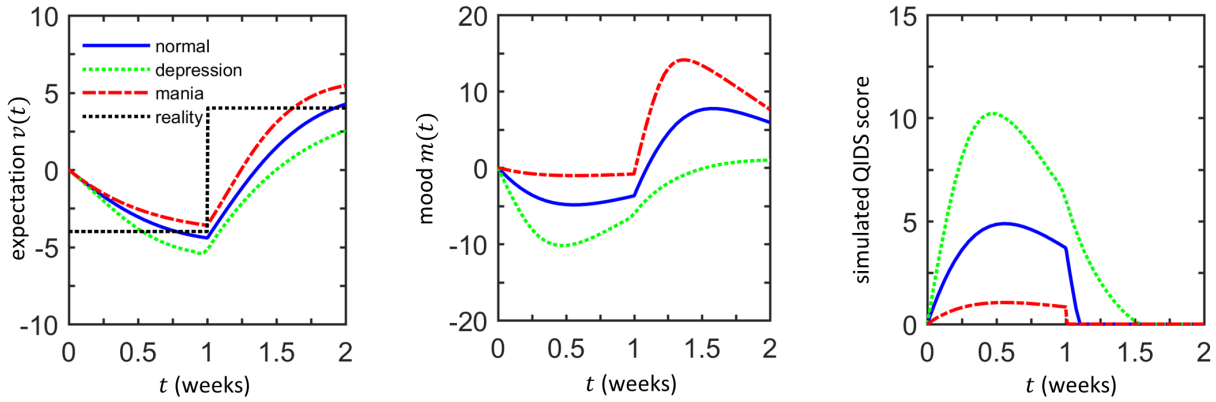

Figure 6.3: Response to jumps in reality with $r(t) = -4$ for $t \in [0, 1)$ and $r(t) = 4$ for $t \in [1, 2]$. Here, normal, manic, and depressive subjects are defined by asymmetric learning rates such that $(f\eta_m^+/(\eta_v + k), f\eta_m^-/(\eta_v + k)) = (0.4, 0.4), (0.8, 0.1)$ and $(0.1, 0.8)$, respectively. Numerical values for other parameters, common to all subjects, are $\eta_v = 1.85, f = 0.3, k = 1.85$, and $k_3 = 0.014$. Initial conditions are set to $(m, v) = (0, 0)$. (A) The predicted expectations v of a normal subject (solid blue), a manic subject (red dash-dot), and a depressive subject (green dotted) all attempt to follow reality (black dotted). In the depressive state, $v(t)$ overshoots decreases in $r(t)$, whereas expectations in the manic state overshoot rises in $r(t)$. (B) Mood levels $m(t)$ exhibit significant systematic differences in the normal, manic, and depressive cases, showing how asymmetric mood sensitivity can lead to unipolar depression/mania when reality $r(t)$ is changing. (C) Prolonged periods of negative mood are reflected by longer periods of large QIDS scores in depressed subjects.

reflected in both mood and QIDS scores (Fig. 6.3B, C). The deviation in mood observed in the model can be explained in terms of psychology. Systems with a higher mood sensitivity for negative events will experience a larger change in mood during negative events, resulting in a lower expectation than reality. Since reality is typically changing, this overshoot in mood and expectation can last until the next event. Since systems in depressive states will always overshoot in response to negative events and undershoot in response to positive ones, their overall mood level remains lower than that of a normal system. A similar reasoning applies to subjects in a manic state, which results in average mood values higher than those in normal subjects. Interestingly, our mechanism for unipolar depression/mania is distinct

from another model based on the interaction of mood and expectation [ERD16], which asserts that asymmetric learning rates lead to expectations higher than reality for people with depression, resulting in constant negative surprise and low mood level. Our simulations show that a different mechanism – the experimentally observed asymmetric mood sensitivity – can possibly underlie unipolar depression/mania when reality fluctuates. A rigorous analysis of the systematic deviation of mood or expectation under more general random reality functions would require more involved stochastic analysis.

6.3.4 Unidirectional changes in asymmetric mood sensitivity can trigger bipolar disorder

Mathematically, bipolar disorder reveals itself in the form of a limit cycle as the origin $(m, v) = (0, 0)$ becomes linearly unstable. When asymmetric mood sensitivity is considered, stability depends on two parameters, $f\eta_m^+$ and $f\eta_m^-$, and its delineation is more involved. Nonetheless, it is easy to show that for $r = 0$, the origin $(m, v) = (0, 0)$ remains stable if both positive and negative mood sensitivities are below the critical value, i.e. $f\eta_m^+, f\eta_m^- < \eta_v + k$. Similarly, the origin is unstable if both mood sensitivities are above the critical value. However, when only one of them is above the critical value, the dynamics will be unstable in one half-plane defined by $\frac{dv}{dt} = 0$ $(v = fm)$, and stable in the other. In such cases, solution trajectories starting in the unstable half-plane may cross into the stable half-plane and eventually arrive at the origin. Alternatively, they may cross back into the unstable half-plane and ultimately move farther from the origin. To obtain heuristic criteria on overall system stability, we can track the trajectories of the linearized system as it traverses the two half-planes.

Consider the linearization of Equations (6.1) and (6.2) about $(m, v) = (0, 0)$ by neglecting the $-k_3 m^3$ term and assume that one half-plane is stable and the other is not, e.g. $f\eta_m^+ > \eta_v + k$ and $f\eta_m^- < \eta_v + k$. Within the positive, unstable half-plane $(fm - v > 0)$, there are two additional parameter regimes corresponding to $\eta_v + k < f\eta_m^+ < \eta_v + k + \sqrt{4\eta_v k}$ where the eigenvalues are complex but with at least one of them having a positive real part, and

$f\eta_m^+ > \eta_v + k + \sqrt{4\eta_v k}$, for which both eigenvalues are real and positive. We do not consider the case at the boundary values as it holds for only a very special parameter relationships. Approaching the origin from the positive half-plane, these two parameter regimes give rise to an unstable spiral and an unstable node, respectively. Similarly, there are two regimes in

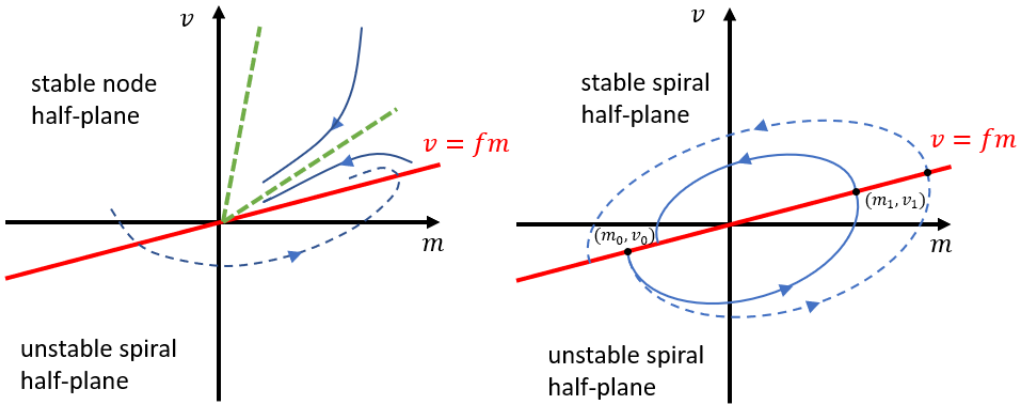

Figure 6.4: Phase plane diagrams depicting possible scenarios of linear stability and instability. (A) Linearized dynamics in the $fm < v$ half-plane show stable node behavior whereas $fm > v$ half-plane supports spiral dynamics. The overall stability is determined by the stability property of the nodal half-plane, whether or not the trajectory crosses into an unstable spiral half-plane. In the illustrated example, the green rays show the stable eigendirections. (B) Both half-planes support spiral dynamics: one stable, one unstable. The overall stability is determined by whether the trajectory starting at (m_0, v_0) increases or decreases in magnitude as it completes a cycle.

the negative plane ($fm - v < 0$): $\eta_v + k > f\eta_m^- > \eta_v + k - \sqrt{4\eta_v k}$ and $f\eta_m^- < \eta_v + k - \sqrt{4\eta_v k}$, corresponding to a stable spiral and a stable node at the origin, respectively. Nodes determine the stability/instability of the origin over spirals since most solutions starting in the node half-plane will stay in that half-plane. The only exceptions are trajectories starting in the wedge between the eigenvector corresponding to an eigenvalue with a larger absolute value and the half-plane boundary $v = fm$. As shown in Fig. 6.4A, if a node and a spiral coexist, solutions starting in the spiral half-plane (or the wedge in the node half-plane) will end up in the part of the node half-plane and follow the stability properties of the node. Hence, the node determines the stability when it coexists with a spiral.

When spiral node behavior arises in both half-planes, the two spiral dynamics alternate along the trajectory and compete in strength. As shown in Fig. 6.4B, solutions starting in one half-plane will enter the other after half a cycle. We can deduce the overall stability by tracking trajectories through a full cycle and returning to the original half-plane. The stability can be inferred from determining the change in magnitude of the trajectory after a full cycle. In the positive half-plane the general form of solutions is

$$m(t) = e^{\frac{f\eta_m^+ - \eta_v - k}{2}t}\Big(A\cos(\frac{\sqrt{4\eta_v k - (f\eta_m^+ - \eta_v - k)^2}}{2}t) + B\sin(\frac{\sqrt{4\eta_v k - (f\eta_m^+ - \eta_v - k)^2}}{2}t)\Big) \tag{6.9}$$

$$v(t) = e^{\frac{f\eta_m^+ - \eta_v - k}{2}t}\Big(C\cos(\frac{\sqrt{4\eta_v k - (f\eta_m^+ - \eta_v - k)^2}}{2}t) + D\sin(\frac{\sqrt{4\eta_v k - (f\eta_m^+ - \eta_v - k)^2}}{2}t)\Big). \tag{6.10}$$

Here the constants A, B, C, D are determined by the initial conditions associated with the linearized equations but do not affect the following stability analysis. Suppose a trajectory starts on the boundary of the two half-planes at (m_0, fm_0). After a time of $\Delta t = \frac{2\pi}{\sqrt{4\eta_v k - (f\eta_m^+ - \eta_v - k)^2}}$, the trajectory reaches the boundary again at point (m_1, fm_1). The distance to origin will change by a multiplicative factor of $\exp\left[\frac{\pi(f\eta_m^+ - \eta_v - k)}{\sqrt{4\eta_v k - (f\eta_m^+ - \eta_v - k)^2}}\right]$. A similar argument applies to the negative half-plane, and the criterion for the solution to move closer to the origin after a full cycle, i.e. linear stability, is

$$\frac{\pi(f\eta_m^+ - \eta_v - k)}{\sqrt{4\eta_v k - (f\eta_m^+ - \eta_v - k)^2}} + \frac{\pi(f\eta_m^- - \eta_v - k)}{\sqrt{4\eta_v k - (f\eta_m^- - \eta_v - k)^2}} < 0. \tag{6.11}$$

This approximate stability analysis is consistent with the results of the numerical simulations shown in Fig. 6.5A. When spirals are induced in both half-planes, the origin is stable when $f(\eta_m^+ + \eta_m^-) < 2(\eta_v + k)$. Since $\sqrt{4\eta_v k} - (f\eta_m^+ - \eta_v - k)^2$ is symmetric for $f\eta_m$ around $\eta_v + k$, it is clear that $f(\eta_m^+ + \eta_m^-) = 2(\eta_v + k)$ (red dashed line) leads to equality in Equation (6.11). This approximate analytic stability boundary (white solid line) closely matches that inferred from numerical solutions. Coexistence of a node and a spiral yields the same stability as that of the node half-plane, predicted by our analysis. However, when a stable node coexists with an unstable node numerical solution show that the origin is always unstable.

The simple linear analysis does not establish the existence of a limit cycle in this case, so the instability may not correspond to bipolar disorder.

Bipolar disorders triggered by asymmetric mood sensitivities show oscillation in mood and expectation that are similar to those predicted in the symmetric case, but they contain systematic biases (Fig. 6.5B, C) which were not observed in the symmetric case. As in unipolar depression/mania, the biases in mood and expectation always have the same sign, i.e., mood and expectations are systematically either both lower or higher. The depression-biased case may describe type II bipolar disorder. The same pattern persists when the reality is treated as random (Fig. 6.5D, E), with the mood and expectation responding to changes in reality as well as exhibiting their intrinsic oscillations. As expected, the predicted QIDS scores for depressive bipolar (or type II) subjects are much higher than those of normal and manic bipolar subjects, but even bipolar manic subjects are predicted to exhibit larger QIDS scores than normal individuals (Fig. 6.5F). Moreover, manic and depressive bipolar subjects could often show high QIDS scores when normal individuals have stable moods. Our numerics suggest that bipolar disorder can be caused by extreme asymmetry in mood sensitivity, which leads to systematically biased mood and expectation patterns. The direction and magnitude of mood sensitivity asymmetry may be an underlying feature of different types of asymmetric bipolar disorders.

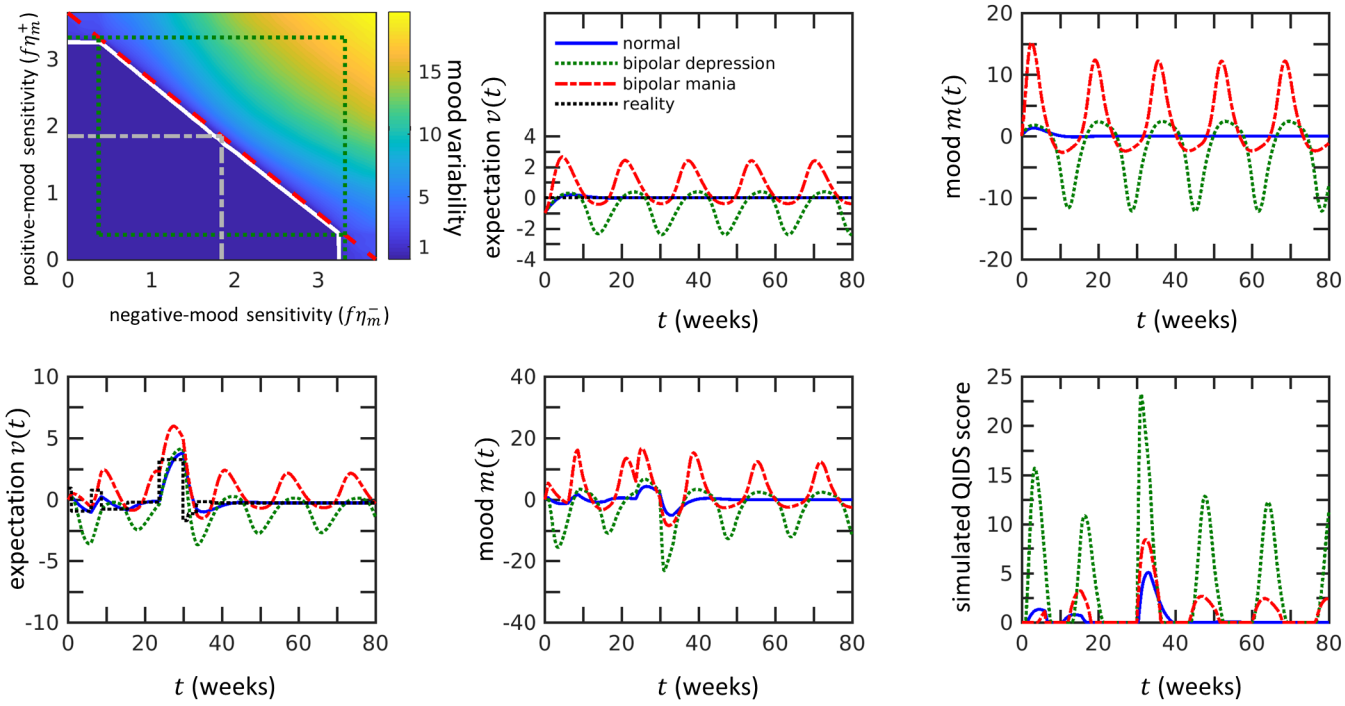

Figure 6.5: Bipolar disorder can be triggered by large unidirectional changes in mood sensitivity, even when one of the mood sensitivities does not cross the stability threshold. (A) Numerical computations were performed within the period $t \in [0, 162.5]$ using $r(t > 0) = 0$. The stability is characterized by the standard deviation of mood when $t \in [81.25, 162.5]$, and the stability boundary (white solid curve) is determined by the contour of mood variability of model with critical mood sensitivities, i.e. $f\eta_m^+ = f\eta_m^- = k + \eta_v$. Other parameter values used in the simulations are $\eta_v = 1.48, f = 0.3, k = 0.37$, and $k_3 = 2.8 \times 10^{-3}$. The curve $f(\eta_m^+ + \eta_m^-) = 2(k + \eta_v)$ (red-dashed line) solves Eq. 6.11 and matches well with the numerically computed stability boundary (white solid curve) when both half-planes support spirals (inside the green-dotted box). When both half-planes are stable (inside the gray-dot-dashed box), the solutions are stable as expected since eigenvalues in both half-planes have negative real parts.

6.5 *(previous page)*: When one half-plane is an unstable spiral and the other is a stable node (upper-left and lower-right rectangles with one gray-dot-dashed and two green-dotted sides), the solutions are stable according to our analysis in Fig. 6.4, consistent with the numerical results. Finally, when an unstable node is present (upper and right to green dotted lines), the system is unstable. We show that the coexistence of stable spiral and unstable node half-planes leads to instability. Stability of the case in which both stable and unstable node half-planes arise depends on initial conditions. (B) Under constant reality, bipolar disorder triggered by mood sensitivity asymmetry in different directions induce different behavior in expectation $v(t)$. Compared to the normal state (solid blue), higher negative mood sensitivity (depressive bipolar state, $f\eta_m^- = 2(\eta_v + k)$ and $f\eta_m^+ = 0.5(\eta_v + k)$) lowers expectations (green-dotted lines) while higher positive mood sensitivity (manic bipolar state, $f\eta_m^- = 0.5(\eta_v + k)$ and $f\eta_m^+ = 2(\eta_v + k)$) leads to higher expectations (red dash-dot). Initial conditions are $(m, v) = (0, -1)$. Parameter values used in this and in the following subfigures are $\eta_v = 0.37, f = 0.3, k = 0.37$, and $k_3 = 2.8 \times 10^{-3}$. (C) Under constant reality, bipolar disorder induced by asymmetry in mood sensitivities in different directions biases the mood $m(t)$ in different directions. (D) The biases in the asymmetry-induced oscillations in the expectation persist under random reality conditions, with depressive/manic bipolar states leading to statistically lower/higher expectations. The realization of reality is drawn as described with $\sigma_r = 2, k_r = 1$. Initial conditions: $(m, v) = (0, 0)$. (E) The mood trajectories $m(t)$ show qualitatively similar biases as in (B). (F) Predictions of QIDS scores of depressive and manic bipolar individuals.

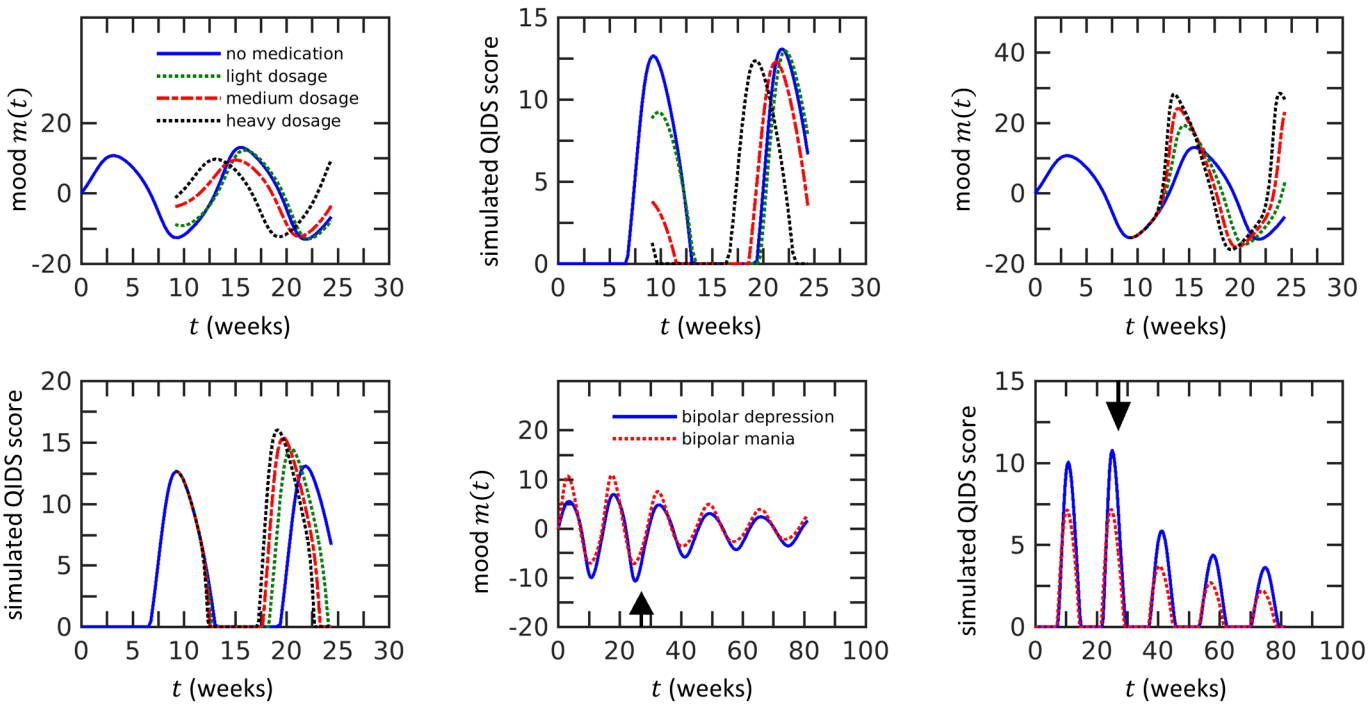

Figure 6.6: Possible effects of antidepressants and lithium on subjects with bipolar disorder, including the mania-inducing effect of antidepressants and the sedative effects of lithium, are assessed in our model. (A) Numerical calculation of the mood of a bipolar subject (solid blue curve) using $f\eta_m = 1.5(\eta_v + k)$. At $t = 9.2$ weeks, within a depressive episode, the patient is treated with antidepressants, modeled by an elevation in mood [Gol11]. Trajectories corresponding to dosages that instantaneously decrease the depression to 70% of its lowest value (green dotted), 30% of its lowest value (red dash-dot), and 10% of its lowest value (black dotted) are shown. Note that higher doses lead to an earlier onset of mania. This antidepressant-induced mania is observed clinically [APL95, GT03]. The numerical values for the simulations are $\eta_v = 0.37, f = 0.3, k = 0.37$, and $k_3 = 2.8 \times 10^{-3}$; the initial conditions are $(m, v) = (0, -1)$. (B) The quick transition to a manic phase results in a depressive episode that occurs sooner than in untreated subjects, as indicated by an earlier peak in QIDS score for subjects treated with a high antidepressant dose.

6.6 *(previous page)*: (C) When the effect of antidepressants is modeled by an increased positive mood sensitivity, an earlier manic episode is observed with larger amplitude. The frequency of mood oscillation also increases as dosage increases. The positive mood sensitivities used in the simulations for low to high dosage are $f\eta_m^+ = 2.25(\eta_v + k), 3(\eta_v + k), 3.75(\eta_v + k)$, respectively, while the negative mood sensitivities are the same as those used in (A). (D) The quick transition to mania also induces an earlier depressive episode, with larger QIDS score as the dosage increases. (E) Simulated mood dynamics for mania-biased mood sensitivity asymmetry (red dotted, $f\eta_m^+ = 1.5(\eta_v + k), f\eta_m^- = (\eta_v + k)$) and depression-biased mood sensitivity asymmetry (blue solid, $f\eta_m^+ = (\eta_v + k), f\eta_m^- = 1.5(\eta_v + k)$). The sedative effects of lithium are modeled via a symmetric 20% reduction in mood sensitivity and are implemented in our numerics at $t = 27.1$ weeks (black arrow). This treatment decreases oscillation amplitudes consistent with clinical observations [PK01]. (F) The reduction in mood oscillation amplitudes yields smaller predicted QIDS scores.

6.3.5 Effects of antidepressants and lithium

In this section, we explore the effects of common medications used to treat bipolar disorder. First we want to see if our model can explain the antidepressant-induced mania seen in bipolar patients. Antidepressants are a category of medicine for treating depression disorder, and their effects on patients with depression are significant [MB74]. For patients with bipolar disorder, it has been reported that $20-40\%$ of their manic episodes are induced by antidepressants [APL95, GT03]. This unanticipated effect was previously studied by [Gol11] using a bistability model of depression and mania. Our model for bipolar disorder is intrinsically oscillatory, and it is not clear whether there is a threshold of dosage above which the manic episodes will be induced, as predicted in [Gol11]. Nevertheless, when the effect of antidepressants is modeled by a shift in mood [Gol11], simulations of our model show that there is, indeed, a threshold of dosage below which a transient alleviation of depression occurs, followed by a usual manic episode. Above this dose threshold, manic episodes are induced earlier (Fig. 6.6A). This result is surprising since small perturbations in mood do

not qualitatively change the subsequent dynamics and our model does not have a built-in mechanism for bistability. Subjects treated with high doses of antidepressants are predicted to show a phase shift in the mood oscillations (Fig. 6.6A). This phase shift would yield an earlier peak in the QIDS score (Fig. 6.6B). Another way to model the effect of antidepressants is to increase the positive mood sensitivity [Har08]. This effect also leads to an earlier manic episode, but with greater strength and a higher frequency (Fig. 6.6C). The QIDS score also shows a sooner and stronger depressive episode (Fig. 6.6D). The observed rapid cycle is consistent with clinical observations [APL95].

The sedative effects of lithium were first discovered in 1949 but its molecular mechanisms of action have not yet been fully elucidated [PK01, CV03]. Nonetheless, lithium is one of the most prescribed treatments for bipolar disorder [PK01]. While our model does not explicitly involve details at the molecular level, it suggests a crucial behavioral property, characterized by the mood sensitivity, that might be regulated by lithium. To see this, we simulate the mood $m(t)$ in the bipolar state and decrease the mood sensitivity parameter after a certain time point (Fig. 6.6E). We observe that after the mood sensitivity is decreased, the amplitudes of oscillations in mood gradually decrease, eventually becoming constant over time. Depression is lessened after treatment, as indicated by a decrease in the QIDS score (Fig. 6.6F); moreover, decreases in mood sensitivity do not induce mania. In contrast to antidepressants, lithium does not trigger manic episodes, which makes it suitable to treat bipolar depression [PK01]. This result suggests that the sedative effect of lithium might be achieved by decreasing the mood sensitivity parameter rather than directly modifying mood.

6.4 Acknowledgments

The authors are grateful for support from the Army Research Office (W911NF-14-1-0472 and W911NF-18-1-0345) and the National Science Foundation (DMS-1516675 and DMS-1814364). SSC was supported in part by the Systems and Integrative Biology predoctoral training grant (T32GM008185).

CHAPTER 7

Conclusion and discussion

In the dissertation I studied the physical principles and dynamics on biological networks, and derived new quantitative tools to analyze them. I started with a particular biological network, the microvascular network in the trunk of embryonic zebrafish, and discovered that the conductances of the fine vessels are carefully tuned to uniformize the red blood cell fluxes in those fine vessels. This finding stands in sharp contrast with the principle of transport efficiency and Murray's law previous proposed for the vascular networks, since I found that there is a trade-off between flow uniformity and transport cost, so a biological network can only optimize one of them or strike a balance between them. To explore the morphologies of networks that follow these principles, I first generalized previous analytical results on transport efficient networks. I showed that the network properties, such as the loopless property and Murray's law, might not hold for transport efficient networks when the pressure boundary conditions are involved, and they are actually properties of networks with minimal complimentary energy, which includes the work done by pressure boundary conditions. Through the introduction of complimentary energy, I expanded the set of boundary conditions under which these properties are true for transport efficient networks. Then I developed a gradient descent algorithm that finds optimal networks for general target functions and constraints. The algorithm used Lagrange multipliers to ensure constraints such as conservation of mass are satisfied during the gradient descent. Through this algorithm I compared the principles of uniform flow and transport efficiency on model microvascular networks, and showed that the principle of uniform flow gives closer morphologies to observed microvascular networks. By exploiting the generality of the algorithm, I also explored the trade-off between these principles, and showed that a bifurcation occurs when the balance between flow uniformity

and transport efficiency changes.

Many biological networks are not static but have features that change with time. To explore that aspect on microvascular networks I took a different look on the microvascular network in the zebrafish trunk. Previously the vessels are assumed to dilate and constrict according to the information given by the blood flow inside, particular the shear stress applied on the endothelial cells. This mechanism has a well-known instability that would prune all but one vessels. By including the particle effect of the red blood cells, I proposed a stable dynamics that generate realistic zebrafish trunk networks that quantitatively describe the observed vasculature. The model correctly predicts the number of fine vessels with flow and the head-tail asymmetry during zebrafish development. Then I looked at a different topic: the dynamics of bipolar disorder. Bipolar disorder is characterized by the alternation of manic and depressive episodes, and mathematical models have been proposed to explain this oscillation in mood. We analyzed a model based on the coupling between mood and expectation, and showed that bipolar disorder can be viewed as an extension from normal to cyclic personalities. We also discussed the effect of asymmetric perception of positive and negative effects, and showed that the model reproduces the clinically observed effects of medicines.

In Chapter 2 we show that feedbacks associated with the occlusion of fine vessels by the red blood cells that pass through may be associated with previously unreported adaptive benefits for control of blood flows within the microvasculature. Although the existence of occlusive feedbacks is well known [SUS80, OWB10, FYS12, SRW15], to our knowledge they have not previously been shown to be associated with adaptive benefits for oxygen perfusion. Although our experimental observations and modeling are focused on zebrafish, which are a model for vascular development, it is likely that similar feedbacks are significant within mammalian microcirculatory systems, where the deformation of cells to pass through capillaries is, if anything, even more extreme than in the zebrafish. Indeed the apparent intrinsic resistance of cells in human blood vessels has a wide range of variability [SSO86, SHP98], and precise tuning of blood flows is already known to be vital e.g. to maintain perfusion-ventilation balance in the lungs [Wes77, WD60, WSW74]. The proposed occlusion

feedback mechanism may be able to explain the variation of capillary blood flow and how it affects the ventilation-perfusion ratio, as well as blood flows in other vascular systems such as brain capillary network.

Capillary networks have been hypothesized to be organized to minimize the cost of blood transport [She81, Mur26b]. Although large vessels seem to conform very closely to this organizing principle [She81, ZSW92], the tuning of occlusive effects to uniformly distribute red blood cell flows takes the zebrafish vascular network far from the configuration that minimizes transport costs. In particular, at the physiological hematocrit, if the same (smallest) occlusive effect, α_c, is assigned to each vessel then the dissipation in the network could be reduced by a factor of 11 (Fig. 2.6B). At the same time, more uniform partitioning of cell fluxes between different SeAs (i.e. a lower value of the Coefficient of Variation of red blood cell flow rates) is possible but altering physiological parameters further decreases the transport efficiency. For example decreasing blood cell concentration, ρ, increases uniformity of flux, but at the cost of increasing dissipation if the total cell supply to all Se vessels is to kept fixed (Fig. 2.6B).

The ability of SeAs to vary the occlusive effect α_c over three orders of magnitude is consistent with previous modeling of red blood cell and microvessel mechanics, and endows the network with tremendous control over red blood cell flow rates. It is natural to ask whether and how uniform red blood cell flux partitioning can be maintained against the numerous sources of perturbation that occur in real cardiovascular networks. Microvascular networks may be disrupted by trauma, micro-anneurysms, or by systemic conditions like diabetes mellitus [FJ05, PRB90, RNR93, BSB06]. As a first step toward answering this question, we considered the effect of well-characterized natural variability in SeA spacing [IHW01], and of the *notch* mutation which alters the trunk network connectivity [LSP01] upon the ability of the network to uniformly distribute red blood cell fluxes. We found that under a wide range of vessel spacing variability, red blood cell fluxes remained uniform across all SeAs (see Appendix A). Indeed vessel spacing variability has no detectable effect on zebrafish growth and maturation. By contrast, in notch mutant zebrafish the cardiovascular network is malformed, with a shunt connection forming between aorta and principal

cardinal vein (Appendix A). Since the diameter of the shunt is much larger than the cell diameter, there is negligible occlusive feedback within the shunt, causing it to irreparably short-circuit the vascular network. Shunt formation is lethal in embryos, and our model shows that it creates conditions under which uniform perfusion of the trunk is impossible. Note however that mechanisms not described in the model can still play significant roles in both developmental process and mutant network phenotypes. For example in the *gridlock* mutant [WSD95] the blood flow to the tail is impeded by a localized vascular defect, but the collateral vessels not present at 4dpf was observed to redirect the flow around the blockade and rescue the embryo. During the development process both the number of vessels and size of zebrafish embryo change dramatically. Therefore we expect an observable change in occlusive feedbacks to maintain uniform cell partition throughout the developmental stages. Extending our analysis to include the topological changes observed as embryonic zebrafish develop [WSD95] is an ongoing effort.

Although we are able to directly demonstrate that occlusive feedbacks vary between different the SeAs, and this variation is consistent with optimization of feedback strengths to ensure uniform distribution of red blood cells across trunk vessels, our model cannot reveal what physical changes within vessels are used with the zebrafish network to modulate the occlusive effect. In our experiments we cannot visualize the glycocalyx lining of the SeAs, and in fact we are aware of no previous works in which glycocalyx was measured in blood vessels simultaneously with flow. However, previous studies have reported large variations in glycocalyx porosity and thickness between different vessels [HCW94, WTD07]. Since cells must squeeze into SeAs, variations in vessel radius below the resolution limit of our microscopy method could also account for the variation in occlusive effect. Finally elastohydrodynamic effects associated e.g. with changes in the speed of cells, [WTD07], may affect feedback models. The analysis is also silent on the mechanisms for coordinating occlusive effects across the network. Recent works have dissected structural adaptations in microvascular networks [PSG98], as well as in biological transport networks generally [HC13, HLM10, RK16]. These works have focused on the question of how a set of vascular elements that have information only about their own flows can alter their resistances in

response to these cues to minimize dissipation within the network. This question is directly relevant to other objective functions i.e. to networks that maximize uniformity rather than maximizing hydraulic efficiency – can vessels adapt their occlusive effects to the their flow to achieve uniform red blood cell transport?

The use of tuned occlusive effects creates uniform distribution of red blood cell fluxes through the zebrafish vascular network, but at the cost of increasing transport costs. Indeed if the network simply used the same value of α_c in every SeA we found that an 11 fold decrease in transport costs would be possible within the zebrafish trunk vasculature (Fig. 2.6B). Physically feedbacks from occlusion represent a form of congestion, and efficient transport networks, both natural [HDF16] and artificial [CJ89, YH98], are often organized to avoid congestion. Previous works have provided algorithms for constructing minimally dissipative networks given a prescribed set of sources and sinks [BM07, KSM10]. Our work suggests that other optimizing principles may govern microvascular network organization. Extending network optimization algorithms to include flow uniformity is likely to further reveal the tradeoffs between uniformity and efficiency.

Murray's law has shaped understanding of biological transport networks including animals and plants [She81, MSA03]. However, the derivation of Murray's law has until now been heuristic, ignoring both the coupling between flows and conductances (i.e. assuming flows remain constant while conductances are optimized), and the potential for different boundary conditions on the network [Mur26b, Dur07]. Chapter 3 establishes Murray's law as a necessary condition for networks globally minimizing a complementary dissipation function (3.24), and for minimal dissipative networks under both Neumann and Dirichlet boundary conditions. As subsidiary steps we reformulated Thomson's principle and Rayleigh's principle for networks with Dirichlet boundary conditions.

Minimally dissipative networks with flow boundary conditions have been studied both theoretically and numerically [BM07, Dur07, KSM10]. However the effect of pressure boundary conditions upon network structure seems to have received little scrutiny. Imposing pressure rather than flow boundary conditions can be convenient when dealing with complex networks in which only a small part of the entire network may be mapped, for example

in high resolution cerebrovascular imaging, which is currently being used to understand the connection between brain function and vascular development or damage [BTK13]. It may be appropriate to apply pressure boundary condition at the vertices making up periphery of the mapped network. Here monotonicity and boundedness results derived from our extension of Rayleigh's theorem can provide useful estimation tools, and insight into the effect, for example, of adding additional pressure vertices to a cardiovascular network.

Our work in Chapter 3 is also among the first to elucidate differences between imposing the total material as a constraint or penalty on minimally dissipative networks. Historically Murray derived his law based on a material penalty formulation [Mur26b], but later work treated material as a constraint [BM07, KSM10, Dur07]. Our results show that for minimally dissipative networks these formulations are equivalent, and so recent results are consistent with Murray's original derivation. However the equivalence of the two formulations hinges on two key results: 1. That flows in physical networks minimize complementary dissipation, which is equivalent in tree-networks to minimizing dissipation. 2. Optimal networks are trees. However, these two results can not be appealed to when optimizing other functions on networks. Indeed for general target functions and constraints the formulation one chooses has fundamental effects on the optimal network; as we demonstrated when we optimize flow uniformity, optimal networks may only exist for one formulation and not for the other. Moreover the optimal network may also vary quantitatively as a function of the total allowed material, and possibly with the coefficient of material penalty. Our work in Chapter 4 on optimizing flow uniformity showed evidence of phase transitions as penalty coefficients varied. For general functions and constraints one needs to analyze the physics and biology carefully to find the appropriate formulation.

Minimal dissipation arguments give theoretical insights in biological networks [Mur26b], but are not universal explanatory tools. It has been shown that the leaf vascular network and slime mold network are adapted for robustness [KSM10, TTS10] whereas some fungal networks are adapted to maximize mixing [RSH13]. Moreover even when we seek to minimize dissipation, our function f may be non-Newtonian. For example the effective viscosity of blood changes with the cell concentration and with vessel radius [PS05], and it is possible

that Murray's law has to be modified in this occasion. The techniques we present in Chapter 3 might be generalized to establish the modified Murray's law as a necessary condition for the minimal dissipative networks. Our work in Chapter 2 on zebrafish embryo showed that the uniformity of blood flow is maintained at the cost of dissipation. While numerical algorithms have been designed for finding optimal networks other than minimal dissipation [KSM10], to our best knowledge there is no theoretical result on the morphology of optimal networks under other functions with either material constraint or penalty. Critically the results presented here draw extensively on monotonicity and boundedness results that cannot be readily generalized to the general case. New methodology is needed to deduce theoretical results for general functions.

Microvascular network mapping tools have until recently lagged far behind our ability to measure the morphology of large vessels using e.g. plasticization. However, recent advances in microscopy have created detailed digitization of microvascular networks [COA03, BTK13, FFS09]. For example Knife-Edge Scanning Microscopy (FESM) and Micro-optical Sectioning Tomography (MOST) have been used to map the blood vessels within rodent brains to micron resolution [MKS11, WHY14]; while mapping the blood vessels in the human brain is one of the central goals of the BRAIN initiative [ILC13]. Meanwhile long working distance two photon microscopes can be used to directly measure blood flows within living rodent brains [COA03, DDD05]. But the revolution in microvascular imaging has not been matched by new theorizing about what are the organizing principles for microvascular networks. For large vessels minimization of dissipation and the concomitant laws for vessel radii have proven to be powerful organizing tools with which to understand both the morphology of healthy and pathological cardiovascular networks [PHL10]. By comparison it is not known whether any optimization principles underly real microvascular networks. In Chapter 4 we explore the principle of uniform flow as a candidate organizing principle for microvascular networks [CTB17] in both an idealized capillary bed geometry and the real embryonic zebrafish trunk. To do so, we devised an algorithm for optimizing general functions on transport networks. On the model capillary bed we showed analytically that the flows in a uniform flow network are identical to a network with constant conductances. In the zebrafish trunk, achieving

uniform flow requires careful tuning of vessel conductances, and implies a distribution of conductances that matches the real zebrafish trunk.

Finally in the chapter we expose a phase transition that occurs if dissipation costs are also modeled, as the relative size of transport and material costs is increased. Surprisingly, networks that are constrained by both material costs and dissipation do not continuously interpolate between optimizing uniformity and optimizing dissipation, but instead are initially invariant under changes in the cost of dissipation, and then undergo a sudden phase transition-like reconfiguration when this cost exceeds a certain threshold. Although further work is needed to show whether such phase transitions occur for other combinations of target functions, it offers two surprising biological insights. First, no two functions will likely shape the network simultaneously, explaining the remarkable power of single target functions to predict the geometry of biological networks. Secondly, the departure of real zebrafish networks from the optimum for creating uniform distributions of fluxes cannot readily be explained as a result of the network needing to balance tradeoffs between multiple target functions. We believe that the non-optimal features of the zebrafish trunk network are more likely due to another cause; for example variability (e.g. due to biological noise) during vessel formation. For example a 10% variation in vessel radius, as has been observed in small arterioles [KDG82], leads to a 40% variation in vessel conductance under the Hagen–Poiseuille model (4.1), and the variation will be even larger when the occlusion of red blood cells is considered [SBM16]. Under even such mild perturbations, variation in red blood cell flux can reach 0.7 $(1/s)$ standard deviation, comparable to the variations measured for real zebrafish in [CTB17].

The principle of uniform flow may be relevant to other biological transport networks as well. Many organisms build networks for transport, such as plants and slime molds [KSM10, AAP13]. Previously the loopy structure of leaf vascular networks was attributed to damage resistance [KSM10]. Yet uniform flow also favors loopy structures, and provides an alternative optimal principle for these networks.

Real blood is a multi-phase fluid containing both plasma and cells. By assuming Hagen–Poiseuille law we omit two of the complexities of real blood flow: non-Newtonian viscosities

and Zweifach–Fung effect [PS05]. Hydraulic conducances depend both on vessel radius (the Fahraeus–Lindqvist effect) and on the concentration of cells due to both the occlusion of red blood cells in narrow capillaries and the disordered flow of cells within large vessels [CTB17, SBM16, SA08]. The Zweifach–Fung effect refers to variation of hematocrit between vessels following uneven partitioning of red blood cells at branching points [ZL77, DPP11]. Our algorithm has the flexibility to incorporate the Fahraeus–Lindqvist effect by changing the constraint term into a non-power law representation of vessel radius. For simplicity we considered the default model (4.1) throughout the chapter, except when comparing uniform flow zebrafish trunk vasculature to experimental data in Section 4.3.3. To incorporate the Zweifach–Fung effect the hematocrit has to be re-calculated each time we calculate blood flows which will affect oxygen perfusion. Although [PLC89] proposed an empirical formula for the Zweifach–Fung effect, the effect of vessel radius and cell geometry upon the Zweifach–Fung effect is still under active research [BAR08, SCK16, CHJ16].

Throughout this work we have used uniformity of flow as a proxy for uniform perfusion. This is defensible if perfusion in limited by the rate of delivery of oxygenated red blood cells to a particular tissue. However it is also affected by the rate at which it subsequently diffuses through the surrounding tissue – which is in turn affected by levels of oxygen saturation and pH in the tissues and blood and may indeed vary in the same tissues due to functional activation of capillaries in response to time varying metabolic demands [ADG04]. Thus although we have previously presented direct evidence of uniform flow across the zebrafish trunk microvasculature, and in Chapter 4 show that this uniformity results from conductances being close to the unique maximum of a constrained optimization problem, the connection between uniform flow and uniform perfusion is not proven.

Although our algorithm easily handles the relatively small number of vessels in the zebrafish trunk or model capillary, the mouse cortex contains about $14,000$ capillaries per mm^3 [BTK13]. Further tool development is needed to determine whether such networks obey the same principles of uniform flow.

There are many other relevant biological functions that have been identified as candidates for optimization in biological transport networks, for example damage resistance [KSM10]

and mixing [RSH13]. Our algorithm has the flexibility to find optimal networks for general biological functions that can be represented by closed-form target functions. Previous numerical work focused on dissipation and functions derived from it [BM07, KSM10], but we hope that our algorithm will help to catalyze systematic study of other target functions.

Our networks are constrained either by material or total transport cost (i.e. material plus dissipation). However, we could equally impose network cost as a penalty function rather than as a constraint. Indeed, in Murray's original paper, optimal vessel geometries were derived by minimizing the total energy formed as a sum of material and transport costs (i.e. by a penalty function approach) [Mur26b, She81]. In contrast, recent works on minimal dissipation networks impose the material cost as a constraint and minimize dissipation under this constraint. The two approaches carry different physical meanings; and under many, but not all conditions, they produce equivalent networks [CR18].

In Chapter 5 We have proposed a physical mechanism for vessel adaptation based on activation by shear stress. Since endothelial cells are stress activated only during the passage of red blood cells, we have considered the new changes in the hematocrit can induce network remodelling, producing predictions that agree quantitatively with the real developmental progression of the zebrafish trunk. Additionally the model is able to stably develop optimally uniform flows in archetypal vascular networks, including branching trees and square grid networks. However the activation of vessels will also be affected by other features of blood's complex rheology – most obviously the Fahraeus effect (which influences wall-cell spacings) and the Zweifach–Fung effect which influences the hematocrit within individual vessels. Our model phenomenologically incorporates both effects, which are incompletely understood, despite a lot of investigation [DPP11, BAR08, SCK16, CHJ16, Poz05, FAB06], so it is surprising that it makes quantitatively accurate predictions.

In its use for the zebrafish trunk, the model requires that different vessels be assigned different shear stress thresholds of activated endothelial cells. Support that different thresholds are possible in different vessels is provided by our data on the networks' changing geometry, where the distal vessels in wild type zebrafish, with the lowest stress threshold for activation, are the last to become too small to allow passage of red blood cells. However the mechanism

by which different scales of the stress threshold can be established remains to be elucidated; in the zebrafish trunk there is a simple monotonic decrease in the threshold from head to tail, which may potentially be induced by a head-tail gradient of morphogens, such as already been observed for retinoic acid, Sdf1 and CXCR7 [SIK13, CM14], or simply by the pressure gradient present in the aorta. However it would be highly interesting to see whether the same precision in shear stress activation tuning is possible or needed in other parts of the zebrafish's circulatory system. In these and other more topologically complex networks, such as the brain [BTK13], physiological demands such as for oxygen or glucose may shape shear stress thresholds [PSG98]. We note that the recovery of uniformly distributed flows across the zebrafish trunk following the decrease of hematocrit charted in this chapter appears to occur after 14 dpf, at which stage the oxygen transport function of blood becomes essential to the zebrafish [WSD95].

Comparison between different isogenic zebrafish individuals shows a high level of variability in vessel radii so that only network adaptation can account for a lack of systematic anisotropy in flows between distal and rostral vessels. Yet our data show that even with adaptation there is a high level of non-uniformity of flow between different vessels. Part of this non-uniformity must result from topological constraints – in some networks a single Se vein may be fed by two different Se arteries – it is unavoidable then for this vein to have a higher flow. At the same time, some of the variability speaks to imprecision in the mechanism of adaptation, and it is a highly interesting next problem for us to study how fluctuations in flows resulting from this variability scales with the size of the circulatory system, or its topological complexification, as during growth, additional fine vessels are added [IHW01] and pruned [CJL12].

Existing models for bipolar disorder are based on one of two basic mechanisms: bistability and biological rhythm. Models invoking bistability assume that there are multiple stable states representing different phenotypes of depression and mania. Here, variations in mood are triggered by random external perturbations arising from life events [CSM17, SW13]. Biological rhythms assume an intrinsic oscillation in the brain. In this case, mood oscillations persist without perturbations [EN15, DRU09, BGG15, Gol11, MER17]. In Chapter 6, we

proposed and analyzed a variant of a model by [ERD16] for bipolar disorder based on the intrinsically oscillating interaction between mood and expectation. Our model exhibits oscillatory mood behavior when the mood sensitivity exceeds a threshold. Previous models have explained such oscillations via the dynamics of intrinsic brain circuits or mutual inhibition of depression and mania [BGG15, DRU09, Gol11]. Our model proposes that mood oscillations arise from a psychological mechanism in which high expectation induces high mood until it reaches a physiological limit. The mood then decreases, followed by a concomitant decrease in expectation. This mechanism is similar to that proposed by [EN15], [ERD16], and [MER17], but we identified a key psychological property, defined by the mood sensitivity $f\eta_m^{\pm}$, that may control a whole spectrum of states, from normal to cyclothymic personality to type I and type II bipolar disorders. Measuring mood sensitivity may result in a more refined method to diagnose, classify, and describe such disorders.

The perturbations from life events in biological rhythm models are usually treated as a noise term in oscillator models. We have modeled life events explicitly by a known time-dependent reality function $r(t)$ to explore the response of our model to specific changes in reality. This also enables a direct comparison of the two mechanisms since different forms of $r(t)$ can be used to investigate which mechanism better explains the observations. For example, when an individual experiences a prolonged negative life event, biological rhythm models would predict a persistence in mood oscillation, while bistability models would likely predict a prolonged state of depression. By directly incorporating reality $r(t)$ into models with different central mechanisms and then comparing their predictions with observations, we may be able to decide which model better describes bipolar disorder. This may also reveal a need for combination of different mechanisms.

We also explored in detail the effects of asymmetric mood sensitivity on unipolar depression/mania and bipolar disorder. Humans are known to react differently toward positive and negative events [PB17], and patients with major depression and bipolar disorder have a stronger bias toward these events [Lep06]. It was suggested by [ERD16] that this asymmetry can lead to unrealistic expectation and low mood in depressive patients. Our analysis shows that depression can result from a higher mood sensitivity toward negative events, which leads

to a reasonable expectation but negative mood. Our model also predicts that depression is a dynamical phenomenon, i.e. when no strong environmental stimulus is present, depressive patients may appear normal, but they react more negatively than normal subjects once reality fluctuates. Our prediction is supported by clinically observed processing bias [FWC04], but additional psychological experiments should be performed to test our model hypotheses. Our model also shows that unidirectional changes in mood sensitivity can trigger a full bipolar state.

Our mathematical framework can explain the paradoxical observation that while depressive patients react more strongly to negative events, bipolar patients in the depressive phase can react more strongly to positive events [Lep06, LWS04]. Asymmetry in the mood sensitivity introduces an interesting mathematical question on stability. Conventionally, the local stability of an equilibrium is determined by the stability of the system linearized around the equilibrium point [Str14]. To analyze our model with an asymmetric parameter, we concatenated the linear solutions in the two half-planes. Our conclusions accurately match those derived from numerical simulations of our full nonlinear model.

Our work focused on the effect of mood sensitivities on unipolar depression/mania and bipolar disorder. Similar analyses can be carried out with an emphasis on e.g. the expectation learning rate η_v or linear decay rate of mood k, but clarification of the main parameter that triggers bipolar disorder would require experimental input such as quantification of those parameters from both normal and bipolar subjects. The characterization of mania can include complex, multi-dimensional traits such as irritability, rapidity of thoughts, inability to concentrate, increased goal-directed behavior, etc. [BCB91]. Despite this, models for bipolar disorder, including ours, simplify mania to a one-dimensional variable in order to focus on the bipolar behavior of mood [EN15, BGG15, Gol11]. Development and analysis of multi-dimensional models may highlight the role of more specific traits in triggering bipolar disorder, e.g., goal-directed behavior through a BAS-type model [UAH08].

Due to a lack of understanding of the underlying physiological mechanisms of bipolar disorder, the parameters in models, including ours, for bipolar disorder are often phenomenological and treated as fitting parameters to the experimental data. However, we have identified

parameters that can be expressed in psychological terms, such as learning rate for expectation, recovery rate for mood, etc., that can be measured by psychological experiments instead of fitting to data. For example, reaction toward events can be measured by fMRI or pupilometry [LWS04, FWC04, PB17], which can then be used to estimate the learning rates and the mood sensitivity parameter. In fact, the measurements of [LWS04] showing that bipolar patients react more strongly to both positive and negative events agree with our model predictions.

Finally, our model parameters have been assumed to be constant in time. In reality, higher-order nonlinearities may arise if these physiological parameters themselves depend mood and expectation. At the cellular level, neural synapses can be modified by the synaptic current [Fai99], which suggests that recurrence of negative events might strengthen reactions to them. It has been observed that depression is correlated to chronic pain [GRT00] and that an initial depression might become long-term because of prolonged negative realities such as environmental difficulties and lack of social support, the so-called cognitive vulnerability [PM92]. This evidence suggests a possibility that the psychological parameters in our model are dynamical and affected by the environment instead of heredity, so the depression persists even if the reality returns to normal level. Therefore, a natural next step in our work is to the incorporate the dynamics of mood sensitivity as well as other parameters – that incidentally may lead to bistability – to explore how recurrences of external events can trigger depression/mania or bipolar disorder.

APPENDIX A

Measurements and additional calculations on zebrafish blood flow

A.1 Lengths and radii of trunk vessels

In Table. A.1, we record the measurements of lengths and radii of aorta segments and intersegmental arteries.

i	l_i (μm)	r_i (μm)	i	l_i (μm)
1	150	5.9	2	151
3	183	7.6	4	141
5	178	6.1	6	156
7	174	6.6	8	160
9	155	6.0	10	172
11	175	6.4	12	166
13	169	5.9	14	163
15	166	6.1	16	156
17	174	5.4	18	146
19	168	6.0	20	138
21	168	4.8	22	123
23	169	3.5	24	113

Table A.1: The lengths of all 24 vessels and radii of all 12 aorta segments in a 4dpf zebrafish embryo. The radius of capillaries is set to be the mean value 2.9 μm in Fig. 1C and Fig. S1. Vessels are numbered as in Fig. 1B (i.e. odd numbered vessels correspond to sections of dorsal aorta, even numbered vessels to intersegmental arteries).

A.2 Modeling oxygen perfusion

In the early stages of embryogenesis, diffusion of oxygen through the zebrafish's skin is generally sufficient to supply zebrafish tissues with oxygen[RD09]. However, circulatory system looping defects are typically lethal by 17.5 d.p.f.[WSD95], suggesting oxygen transport by the circulatory system contributes to oxygen supply relatively early in embryonic development. To determine whether diffusion of oxygen through tissues might compensate for unequal partitioning of oxygen supply between micro-vessels, we directly model the diffusive transport of oxygen through the zebrafish torso using a reaction-diffusion model[KBL03]. Within the zebrafish trunk the oxygen partial pressure, P, obeys a reaction diffusion equation:

$$D\alpha\nabla^2 P = -C + S \tag{A.1}$$

where S represents the distribution of oxygen supply from the blood, and C the rate of oxygen consumption per volume of tissue, α is the solubility of oxygen and D is the diffusivity of dissolved oxygen. We solved this Partial Differential Equation by creating a Finite Element Model with first order tetrahedral elements implemented in Comsol Multiphysics (Comsol, Los Angeles). We extracted the geometry of the trunk muscles from the Zebrafish Anatomy Portal [SMC12], and the distribution of intersegmental vessels within the trunk from the Zebrafish Vascular Atlas [IHW01]. The parameter $D\alpha$, sometimes called the oxygen permeability, was measured by [KBL03] to be: $D\alpha = 8 \times 10^{-14}$ m^2/(s mmHg). We modified the oxygen consumption rate found by [KBL03] to: $C = 5.1 \times 10^{-4} P/40$ ml oxygen/(ml tissue mmHg). This formula agrees with the rate measured by [KBL03] when $P = 40$ mmHg, but is smaller at lower oxygen partial pressures, representing the regulation of tissue oxygen consumption with oxygen availability. The source term represents the rate of oxygen release from blood, and is compactly supported on the intersegmental vessels. We used the following conversion factors: assuming that when a red blood cell enters a vessel with all of its hemoglobin molecules bound to oxygen, and that all of this oxygen is released, the total oxygen release from each intersegmental vessel can be computed from:

$$\text{rate of oxygen release (ml/s)} = 1.39 \times 10^{-10} \times \text{flow rate (in cells/s)} \tag{A.2}$$

we distribute this flux uniformly across the length of each segmental artery. We apply no-flux boundary conditions on the boundaries of the trunk. By applying this boundary condition, our model represents only the contribution of oxygen transport in the circulatory system to tissue oxygen levels. Oxygen diffusing through the skin of the fish will increase the oxygen partial pressure everywhere by a constant amount and will ensure that all tissues are sufficiently oxygenated, but does not affect the absolute differences in partial pressure that our model is designed to measure. The results of this calculation are shown in Figure 1D in the main text.

A.3 Incorporating phase separation in the zebrafish trunk network model

In our models for red blood cell transport within the trunk vasculature, we assume that red blood cells divide at branching points in the same ratio as whole blood. In fact, red blood cells are more likely to enter the larger of the two daughter vessels at a branching point than would be expected based on the ratio of fluxes [PS05] an effect known as phase separation. We use the mathematical model developed in [PS05], to see whether phase separation can lead to uniform distribution of red blood cells between SeAs.

Incorporating the phase separation model of [PS05] significantly alters hematocrits between different SeAs. However the overall change in fluxes is much smaller than the predicted 11-fold decrease in flux between the first and last SeA. The ratio of SeA diameters to DA diameters ranges from 0.39 for the first SeA to 0.85 for the last SeA (Table A.1) and velocities are similar over the entire length of the DA. Due to the increasing in the ratio of SeA to DA radius with distance from the heart the red blood cells are more likely to enter SeAs further from the heart than those closer. This leads to a 2-fold increase of SeA hematocrit (Fig. A.1B) from $Hct = 0.35$ in the first SeA to $Hct = 0.65$ in the twelfth SeA. However the increase in Hct is not enough to compensate for the 11-fold change in whole blood fluxes between first and last SeA: when phase separation was incorporated into the model we still saw a 5 fold decrease in red blood cell fluxes between first and last SeAs (Fig. A.1A).

The phase separation model of [PS05] parameterizes observations blood flows in the rat mesentery. The difference between the sizes, shapes and mechanical properties of zebrafish red blood cells and rat red blood cells may mean the the model is not quantitatively accurate for the zebrafish microvasculature. It is therefore worth asking whether any model for phase separation could account for the experimental observations. Recall that the model predicts an 11-fold difference between the red blood cell fluxes in the first and last of the SeAs. To compensate for this difference the hematocrit in the last SeA would need to be 11 times larger than the hematocrit in the first SeA. Such a large difference in hematocrit would be easy to detect, and is not supported by our observations, nor are such large differences

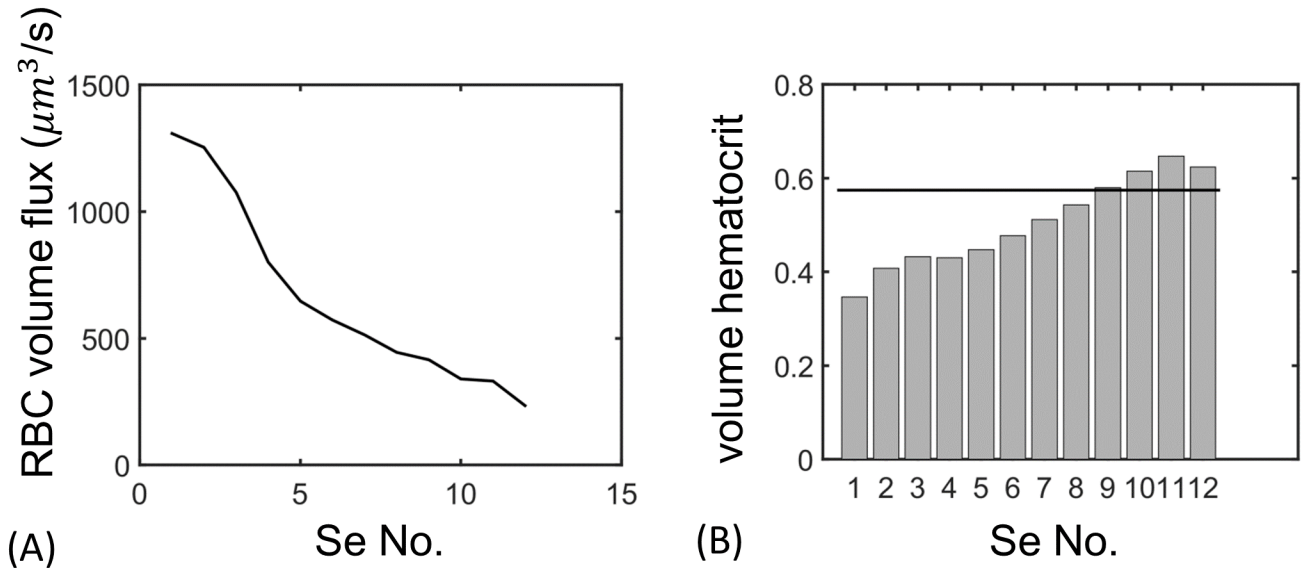

Figure A.1: Incorporating phase separation into the model does not produce uniform red blood cell fluxes between the SeAs. (A) Predicted red blood cell fluxes in the SeAs continue to decay with distance from the heart, when the model from [PS05] is used to parameterize phase separation. Se vessels with smaller numberings are closer to the heart. (B) Hematocrit is predicted to increase with the distance from the heart but Hematocrit changes are not enough to compensate for the decrease in flow predicted by the hydraulic resistor network model. Bars show the hematocrits in the different SeAs, while the black reference line shows the mean hematocrit in the DA.

observed in any of the mammalian vessels measured by [PS05].

A.4 Mean-field model for a two-vessel network

To understand the role of variations in the occlusive effect between SeA-vessels, we develop a continuum model on a reduced network that included only the DA and the first and last of the SeAs. The results of this analysis are summarized in the main text. Here, we describe in more detail the equations that are set up within the model, as well as their solution. The reduced network consists of 4 blood vessels indexed 1 (the segment of DA between the two Se), 3 (the segment of DA after the last Se, which connects directly to the PCV) and $2, 4$ being the two Se-vessels (Fig. 5A in Chapter 2). We define variables n_i, l_i, S_i, V_i, Q_i, R_{i0}, R_i $i = 1, 2, 3, 4$ to be the number of cells contained in vessel i, its length, cross-section area, volume, total flow rate, resistance when no red blood cells are present within the vessel, and resistance modified by the presence of cells following Equation (1) in the main text. Since our analyses from Section A.3 suggest that phase separation effects are slight in these trunk microvasculature, we neglect them altogether, assuming constant hematocrit in each vessel. In the mean-field formulation, the effect of this is to take $\frac{n_i}{V_i} = \rho, i = 1, 2, 3, 4$, where ρ is the constant concentration (# per volume) of red blood cells. ρ is related to the hematocrit (or volume fraction of red blood cells) by Hct$= \rho V_c$ where V_c is the volume of a cell. Thus the flux of red blood cells in vessel i is equal to ρQ_i. Finally we define $p_j, j = 1, 2$ to be the unknown pressures at the two branching points within the network (as in the model without feedbacks, the symmetry of the network allows us to assign the same pressure value, $p = 0$ at the points where the SeAs meet the DLAV and where the DA terminates at the tail of the fish). We make a continuum or mean-field approximation for the effect of the red blood cells contained in each vessel. Specifically, we assume that red blood cells in each vessel are uniformly dispersed through that vessel. Then, in steady state we can balance the flux of cells into each vessel with the flux of cells out of each vessel. For example, for vessel 1, the flux of cells (number/time) out of the vessel is equal to the volume of blood leaving the vessel in unit time Q_1 multiplied by the density (number/volume) of cells: n_1/V_1. Similarly the flux of cells into the vessel is given by the total flux of cells entering the network through node 1, in unit time multiplied by the ratio in which flow is

divided between vessels 1 and 2 ($\frac{Q_1}{Q_1+Q_2}$). Since the total number of red blood cells in the network is constant in the continuum approximation, the number of red blood cells entering the network in unit time must be equal to the number leaving, i.e. $\frac{n_2Q_2}{V_2}+\frac{n_3Q_3}{V_3}+\frac{n_4Q_4}{V_4}$. Thus in steady state:

$$\left(\frac{n_2Q_2}{V_2}+\frac{n_3Q_3}{V_3}+\frac{n_4Q_4}{V_4}\right)\frac{Q_1}{Q_1+Q_2}=\frac{n_1Q_1}{V_1}. \tag{A.3}$$

Similar conservation statements for each of the other 3 vessels in the network give:

$$\begin{aligned}\left(\frac{n_2Q_2}{V_2}+\frac{n_3Q_3}{V_3}+\frac{n_4Q_4}{V_4}\right)\frac{Q_2}{Q_1+Q_2} &= \frac{n_2Q_2}{V_2}\\ \frac{n_1Q_1}{V_1}\frac{Q_3}{Q_3+Q_4} &= \frac{n_3Q_3}{V_3}\\ \frac{n_1Q_1}{V_1}\frac{Q_4}{Q_3+Q_4} &= \frac{n_4Q_4}{V_4}\end{aligned} \tag{A.4}$$

Flux conservation at each node, plus the resistance-to-cell number relationship in Eqn. (1) from the main text then allows us to compute the fluxes Q_i. Specifically, suppose the fluid inflow is F into the first node. Then since flow rate is proportional to the pressure difference across a vessel:

$$Q_1=\frac{p_1-p_2}{R_1}, Q_2=\frac{p_1}{R_2}, Q_3=\frac{p_2}{R_3}, Q_4=\frac{p_2}{R_4}. \tag{A.5}$$

while conserving fluxes at the two nodes gives:

$$\begin{aligned}F &= \frac{p_1-p_2}{R_1}+\frac{p_1}{R_2}\\ \frac{p_1-p_2}{R_1} &= \frac{p_2}{R_3}+\frac{p_2}{R_4}\end{aligned} \tag{A.6}$$

We can solve for the nodal pressures p_1, p_2 by linear algebra. Define a matrix determinant:

$$\Delta=\begin{vmatrix}\frac{1}{R_1}+\frac{1}{R_2} & -\frac{1}{R_1}\\ \frac{1}{R_1} & -(\frac{1}{R_1}+\frac{1}{R_3}+\frac{1}{R_4})\end{vmatrix}=-\left(\frac{1}{R_1}+\frac{1}{R_2}\right)\left(\frac{1}{R_1}+\frac{1}{R_3}+\frac{1}{R_4}\right)+\frac{1}{R_1^2}. \tag{A.7}$$

Then Cramer's rule gives:

$$\begin{aligned}p_1 &= \frac{1}{\Delta}\begin{vmatrix}F & -\frac{1}{R_1}\\ 0 & -(\frac{1}{R_1}+\frac{1}{R_3}+\frac{1}{R_4})\end{vmatrix}=\frac{-F(\frac{1}{R_1}+\frac{1}{R_3}+\frac{1}{R_4})}{\Delta}\\ p_2 &= \frac{1}{\Delta}\begin{vmatrix}\frac{1}{R_1}+\frac{1}{R_2} & F\\ \frac{1}{R_1} & 0\end{vmatrix}=\frac{-\frac{F}{R_1}}{\Delta}.\end{aligned} \tag{A.8}$$

From the formulas for the nodal pressures p_i we can use Eqn. (A.5) to calculate the fluxes in each vessel, Q_i:

$$Q_1 = \frac{-F}{\Delta R_1}\left(\frac{1}{R_3}+\frac{1}{R_4}\right),\ Q_2 = -\frac{F}{\Delta R_2}(\frac{1}{R_1}+\frac{1}{R_3}+\frac{1}{R_4}),\ Q_3 = \frac{-F}{\Delta R_3 R_1},\ Q_4 = \frac{-F}{\Delta R_4 R_1} \quad \text{(A.9)}$$

Although these represent volume fluxes (volume/time), the cell flux in each vessel can then be computed by multiplying by the cell concentration, ρ. Using Equation (1) from the main text, we may rewrite $R_2 = R_{20} + \alpha_2 \rho V_2$, and so on.

To analyze flows within the network we focused on two measures of efficiency, (i) One is the ratio of the cells fluxes in the two SeAs:

$$\begin{aligned} \text{flux ratio} &= \frac{\rho Q_2}{\rho Q_4} = \frac{Q_2}{Q_4} = \frac{R_1 R_4}{R_2}\left(\frac{1}{R_1}+\frac{1}{R_3}+\frac{1}{R_4}\right) \\ &= \frac{\bar{R}_4 + V_4\rho\alpha_4}{\bar{R}_2 + V_2\rho\alpha_2}\left(1+\frac{R_1}{R_3}+\frac{R_1}{R_4+V_4\rho\alpha_4}\right) . \end{aligned} \quad \text{(A.10)}$$

(ii) We also compute the viscous dissipation within the network when the flux through all SeAs, i.e. $\rho(Q_2+Q_4)$, is fixed. The dissipation for a single vessel is given by $D = Q^2 R$ where Q is the flow rate of the vessel, R is the resistance of the vessel. Thus the dissipation of the entire network is

$$D_{\text{network}} = \sum_{i=1}^{4} Q_i^2 R_i. \quad \text{(A.11)}$$

For the aorta segments, we assume constant resistance (not strongly affected by the number of red blood cells) so

$$D_{\text{aorta}} = \frac{8\mu_{wb}}{\pi r_a^4}\sum_{i=1}^{2} l_{2i-1} Q_{2i-1}^2. \quad \text{(A.12)}$$

In contrast the dissipation within SeAs depends on the number of cells traveling through them:

$$D_{\text{Se}} = \sum_{i=1}^{2} Q_{2i}^2 R_{2i} = \sum_{i=1}^{2} Q_{2i}^2 R_{2i0} + \sum_{i=1}^{2} Q_{2i}^2 n_{2i}\alpha_{2i} \quad \text{(A.13)}$$

Substituting $n_i = \rho V_i$, we obtain:

$$D_{\text{Se}} = \frac{8\mu_{pl}}{\pi r_c^4}\sum_{i=1}^{2} l_{2i} Q_{2i}^2 + \rho\sum_{i=1}^{2} V_{2i}\alpha_{2i} Q_{2i}^2 \quad \text{(A.14)}$$

and

$$D_{\text{network}} = D_{\text{aorta}} + D_{\text{Se}} = \frac{8\mu_{wb}}{\pi r_a^4} \sum_{i=1}^{2} l_{2i-1} Q_{2i-1}^2 + \frac{8\mu_{pl}}{\pi r_c^4} \sum_{i=1}^{2} l_{2i} Q_{2i}^2 + \rho \sum_{i=1}^{2} V_{2i} \alpha_{2i} Q_{2i}^2 \quad \text{(A.15)}$$

which is Equation (6) in the main text.

A.5 Estimation of occlusive effects in a 4 dpf zebrafish

To analyze the effect of occlusive feedbacks upon the distribution of red blood cell fluxes within the trunk vessels, we directly measured the occlusive feedback parameter α_c from Equation (1). Namely, for each vessel, we fit an equation for the resistance of the vessel as a function of the number, n of cells that it contains:

$$R = R_0 + n\alpha_c \tag{A.16}$$

where R is the resistance of Se, R_0 is the resistance of the SeA when it contains no cells, which is given by Hagen–Poiseuille law calculated with plasma viscosity $\mu_{pl} \approx 1cP$, and α_c is the occlusive effect per cell. We directly measure the coefficient α_c by tracking red blood cells in a real zebrafish embryo. To do this me must convert Eqn. (A.16) into an equation for velocity in the vessel. Here we expand our discussion of how this model was fit to the real data, and show the fits for each of the SeAs.

Since the resistance R is the ratio between the pressure drop Δp over the Se vessel and the flow rate Q in the vessel we have

$$QR = \Delta p. \tag{A.17}$$

Plugging Eqn. (A.16) into Eqn. (A.17) we obtain:

$$R_0 + n\alpha_c = \frac{\Delta p}{Q} = \frac{\Delta p}{u\pi r^2}, \tag{A.18}$$

where u is the mean plasma velocity and r is the radius of the vessel. Hence in the vessel $\frac{1}{u}$ is linearly related to n:

$$\frac{1}{u} = \frac{\pi r^2}{\Delta p}(R_0 + n\alpha_c), \tag{A.19}$$

assuming that Δp is constant. Since in the theory developed in [SHP98], red blood cells travel at the mean velocity of the plasma, we calculated $\frac{1}{u}$ by tracking by hand the cells traveling through the Se arterial network. If we regress $\frac{1}{u}$ against n then the slope a and the intercept b of the line satisfies

$$a = \frac{\pi r^2 \alpha_c}{\Delta p}, \quad b = \frac{\bar{R}\pi r^2}{\Delta p}, \tag{A.20}$$

which allows us to calculate the resistance per cell α_c:

$$\frac{a\bar{R}}{b} = \alpha_c. \tag{A.21}$$

Fig. A.2 shows the experimental measurements and the regression. The maximum number of cells in a vessel is quite low due to the occlusive effect, which greatly decreases flow when a vessel contains multiple cells. Therefore we decided to use the theoretical prediction of plasma velocity with no cells from Figure 1C in the main text to fit $1/v$ when $n = 0$, and thereby the pressure drop Δp. In applying the cell-free model we ascribed all Se vessels the same radius and also fixed the radii of all aorta segments. This reduces the noise caused by variation of radius but preserves the key feature of exponential decay. The resulting apparent intrinsic viscosities α_c are shown in Fig. 2.4B in the dissertation. Note that there is considerable scatter in the mean velocity data shown in Fig. A.2 (a single panel of this figure is displayed in the main text as Fig. 2A). This scatter is probably dominated by the complex stick-slip dynamics of red blood cells even when propelled by steady pressure gradients[SHP98], and by the variation in the pressure drop Δp across each Se vessel over each cardiac cycle. Previous measurements have shown that flow rates in the aorta vary by a factor of 6 over a single heart beat[MSS07]. By lumping together velocimetric measurements from different phases of the cardiac cycle, our data include unavoidable velocity variation, distinct from measurement error. However, our theory and fits extract the average values of Δp over a full cardiac cycle.

A.6 Effect of network perturbation upon red blood cell partitioning

Real zebrafish vascular networks, and microvascular networks generally vary from individual to individual[IHW01, ZL77]. Some forms of anatomical variation lead to embryo death, while others do not affect embryo viability at all. We used the model of feedbacks due to vessel occlusion to determine whether uniform red blood cell fluxes could be achieved in two previously studied forms of vascular network variability.

A.6.1 Variation in spacing between intersegmental vessels

In real vascular networks the SeAs are not evenly spaced. In our model (and supported by visualization of the dsRed-tagged cell movements), we assume that the Se vessels alternate artery-vein-artery-... etc.. Real trunk vasculature does not always follow this pattern of strict alternation; in fact arteries and veins can be ordered in many different ways, and the particular ordering of vessels seems to have little impact on embryo growth[IHW01], we therefore infer that it does not affect oxygen perfusion through the trunk. To investigate whether the feedback mechanism robustly uniformizes cell fluxes, independently of the ordering of arteries and veins, we simulated cell partitioning between SeA in zebrafish with large variations in SeA spacing. Specifically, we define a vector $\{Pa(i) \ : \ i = 1, ...11\}$ of normalized intersegmental distances. The entries of Pa are normalized such that $\sum_{i=1}^{11} Pa(i) = 11$. The lengths $l_{2i-1}, i = 1, ..., 11$ of the DA segments are then given by

$$l_{2i-1} = l_{\text{aorta}} Pa(i), \tag{A.22}$$

where $l_{\text{aorta}} = 169$ μm is the mean Se spacing in a 4 dpf zebrafish. Fix the length of the last DA segment (between the final Se and the direct connection to the PCV) to be $l_{23} = 169$ μm. We create a network with high variation in the Se spacing by setting $Pa(2i-1) = 1.69, i = 1, \ldots, 6$ and $Pa(2i) = 0.169, i = 1, \ldots, 5$, so that successive spacings differ by a factor of 10. Just as in Fig. 4, we assume a linearly decreasing feedback strength (i.e. a linear form for the resistance per cell α_i), in which the resistance per cell in the i-th SeA is given by a formula:

$$\alpha_i = \frac{(\alpha_{\min} - \alpha_{\max})i}{n-1} + \alpha_{\max} - \frac{\alpha_{\min} - \alpha_{\max}}{n-1}, \quad i = 1, \ldots, n \tag{A.23}$$

where $\alpha_{\max} = 2.334 \times 10^{-5}$ g/μm^{4}s is the feedback strength within the first Se from the data and $\alpha_{\min} = 1.01 \times 10^{-6}$ g/μm^{4}s is that of the last Se. $\alpha_{\max}$ and $\alpha_{\min}$ are obtained from linear regression on the measured feedback strengths (see main-text, Fig. 2C). We then used a direct numerical simulation of the cell dynamics in this network (see Materials and Methods in the main text) to calculate the partitioning of cells in the modified network. We estimate the uniformity of flows for each set of network parameters by computing the Coefficient of Variation (CV) of the cell flux. The CV is 0.2538 in the uneven spacing case, which indicates

a lower uniformity compared to a network with the empirically determined Se spacings (with CV value 0.1815, see Fig. A.3). However, if the feedback strength varies with distance along the DA, (i.e. with vessel distance from the heart, rather than simply being a function of vessel index), namely:

$$\alpha_i = (\alpha_{\max} - \alpha_{\min}) \frac{\sum_{j=i}^{n-1} Pa(j)}{\sum_{j=1}^{n-1} Pa(j)} + \alpha_{\min} \tag{A.24}$$

then the CV of cell fluxes under the same simulation conditions as were used to create Fig. 2, is 0.1827, which is almost identical to the unperturbed network.

A.6.2 DA-PCV shunt

Genetically modified mib^{ta52b} mutant zebrafish have altered differentiation of vessels into arteries or veins. In particular the mutant trunk vasculature includes a circulatory loop (shunt) between DA and PCV in the middle of the trunk [LSP01]. mib^{ta52b} mutants die before two weeks post fertilization [LSP01]. To simulate the effect of mib^{ta52b} upon the partitioning of cells through the zebrafish trunk vasculature we created a model of the network, by starting with the same wild type network geometry as in Fig. 1B in the main text but with the 6th SeA being assigned a radius 7 μm (identical to the aorta) and a length 17 μm, based on vessel measurements from [LSP01]. The length of the DA vessel segments on either side of the shunt connection were set to be one half of the mean DA vessel segment length, mimicking the DA malformation seen around the shunt in real zebrafish [LSP01]. The cell flux in the shunt, 39 s^{-1}, is much greater than the mean cell flux in all the SeAs, 0.3 s^{-1}. Because cells have smaller radii than the shunt connection, cells do not occlude this vessel, there is no negative feedback and cells are not redistributed to SeAs beyond the shunk (Fig. A.4). We expect the low cell fluxes in the other vessels to be associated with low oxygen transport to the rest of the trunk, which may contribute to the lethality of the mib^{ta52b} mutation.

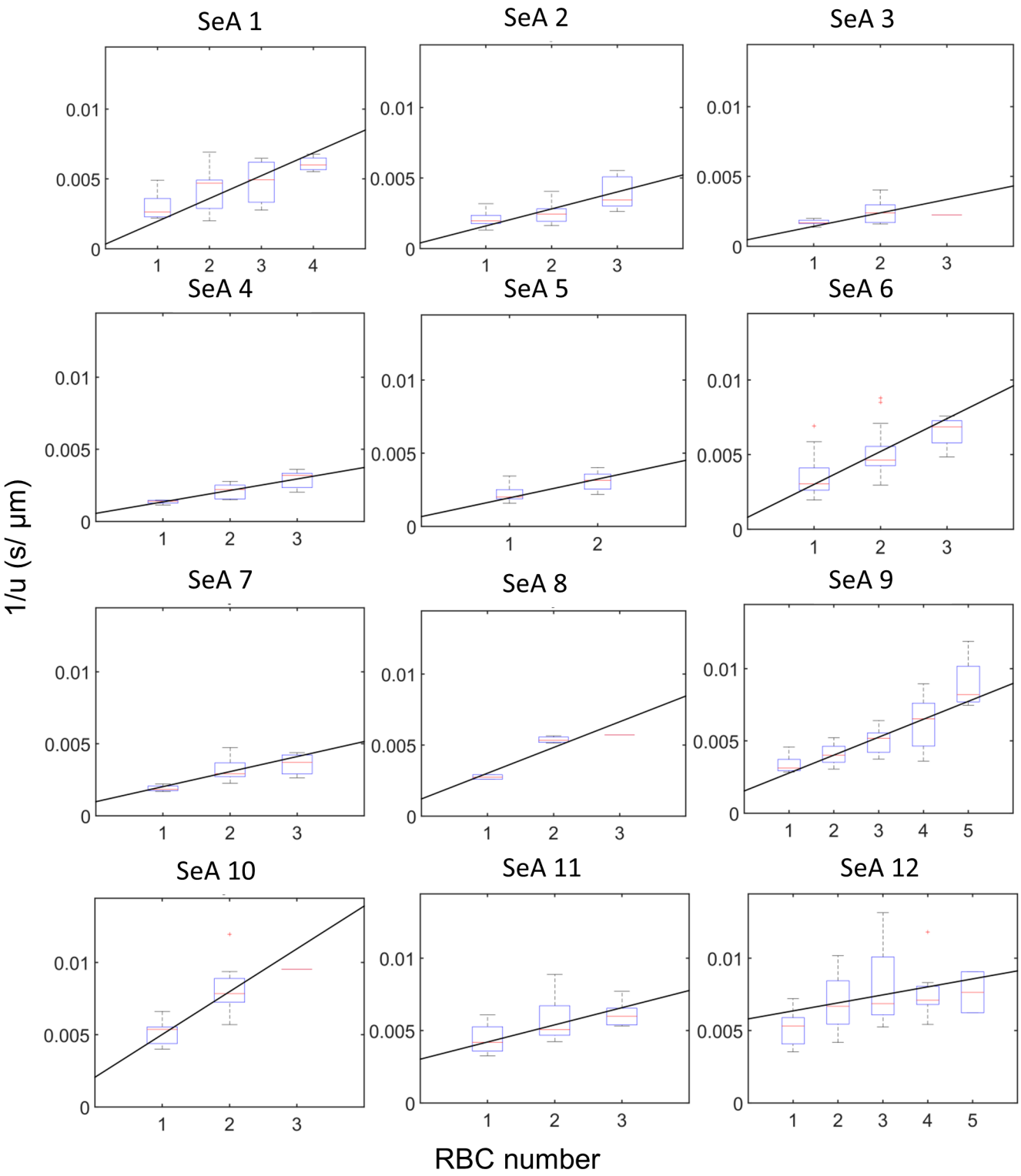

Figure A.2: Occlusive effects are measured in all 12 Se arteries in a 4 dpf zebrafish; we regress the reciprocal of the average velocity $\frac{1}{u}$ against the cell number n. Line: linear regression with intercept determined by the numerical solution with no cells.

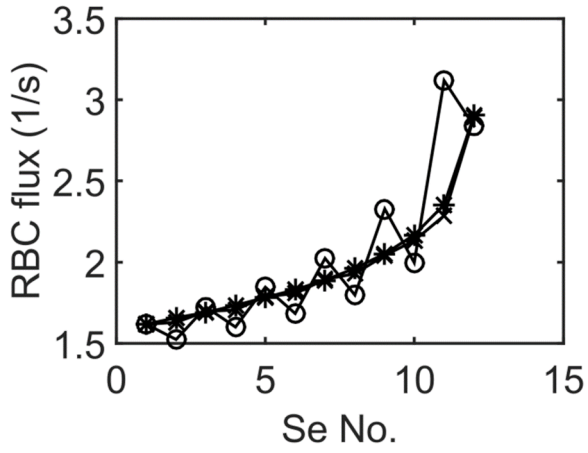

Figure A.3: Predicted cell fluxes in wildtype zebrafish due to variability in Se spacing variant. The wildtype cell fluxes (star) becomes oscillatory under variant spacing (circle), but shows similar overall uniformity. If the feedback variation is adjusted then uniform partitioning of cell fluxes is restored (cross, overlapped with the stars. Se vessels with smaller numberings are closer to the heart.).

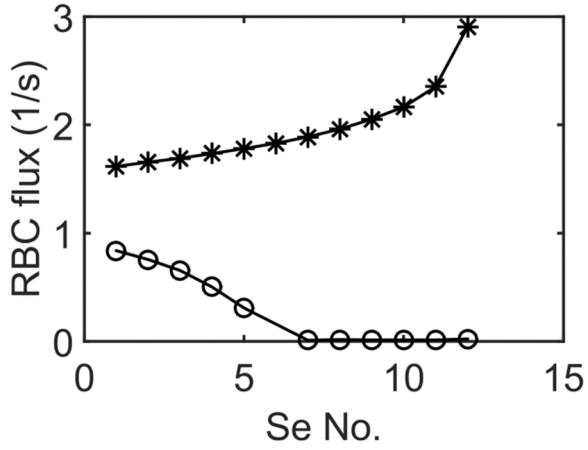

Figure A.4: Predicted cell fluxes in mib^{ta52b} mutant zebrafish. In this mutant, the DA and PCV are directly connected by a shunt, which creates a short-circuit in the network. A shunt introduced at the location of the 6th Se leads to lower and less uniform fluxes (circle) compared to wild type embryos (star), and there is almost no cell flux posterior to the shunt location. Se vessels with smaller numberings are closer to the heart.

APPENDIX B

Well-posedness of Kirchhoff's Laws

For completeness we give a proof on well-posedness of Kirchhoff's laws. If the network has several connected components we can prove that each component has a unique Kirchhoff flow so without loss of generality we can consider a connected network G, i.e. $\forall k, l \in G\ \exists k_1, ..., k_n$ s.t. $\langle k_i, k_{i+1}\rangle = 1, \kappa_{k_i k_{i+1}} > 0$ for all $i = 1, ..., n-1$ and $k_1 = k, k_n = l$, where κ_{kl} denotes the conductance of the link kl. Now we write down the Kirchhoff system

$$Dp = b \tag{B.1}$$

where

$$D_{kl} \doteq \begin{cases} \sum_{l,\langle k,l\rangle=1} \kappa_{kl}\,, & k = l, k \notin \mathcal{P} \\ -\kappa_{kl}\,, & \langle k, l\rangle = 1, k \notin \mathcal{P} \\ 1\,, & k = l, k \in \mathcal{P} \\ 0\,, & \text{otherwise} \end{cases} \tag{B.2}$$

and

$$b_k = \begin{cases} q_k\,, & k \in \mathcal{F} \\ \bar{p}_k\,, & k \in \mathcal{P} \\ 0\,, & \text{otherwise} \end{cases} . \tag{B.3}$$

Here the notations follow those in Section 3.3. First we show that if $\mathcal{P} \neq \phi$ then D is invertible, which is equivalent to showing that

$$Dp = 0 \Rightarrow p = 0\,. \tag{B.4}$$

The solution p for Equation (C.1) corresponds to a network where we do not have any flows into the system except possibly at vertices with pressure boundary conditions prescribed zero pressures, denoted by $\mathcal{P}$. The goal is to show that $p_k = 0\ \forall k$. Suppose for contradiction that $\exists i \notin \mathcal{P}$ s.t. $p_i \neq 0$ (since we already have $p_j = 0\ \forall j \in \mathcal{P}$). Then we would have $Q_{kl} \neq 0$ for some $\langle k, l\rangle = 1$ since the network is connected, and without loss of generality let $Q_{kl} > 0$. Now we can trace this flow throughout the network in the following procedure:

1. Given that $Q_{k_{n-1}k_n} > 0$ first check if $k_n \in \mathcal{P}$, and stop if this is the case.

2. Consider all vertices l s.t. $\langle k_n, l\rangle = 1$. According to Kirchhoff's first law there must be an l s.t. $Q_{k_n l} > 0$. Since the network is finite we can pick e.g. the smallest l satisfying these conditions and let $k_{n+1} = l$.

3. Repeat the procedure until $k_N \in \mathcal{P}$ for some N and stop.

If we start with $k_1 = k, k_2 = l$ we can initiate the process since the first condition is satisfied. This procedure has to stop eventually because the network is finite and that $k_1, ..., k_n$ are all distinct for any given $n > 1$. To see this suppose $k_n = k_m$ with $m > n$. Then we would have $p_n > p_{n+1} > \cdots > p_m = p_n$, a contradiction. Thus we would end up with a chain of distinct vertices $k_1, k_2, ..., k_N$ with $\langle k_n, k_{n+1}\rangle = 1, Q_{k_n k_{n+1}} > 0\ \forall n = 1, ..., N-1$, and $N \in \mathcal{P}$. Now we repeat the same procedure just with $k'_1 = l, k'_2 = k$ to trace the flows upstream, and we would end up with another chain $k'_1, k'_2, ..., k'_{N'}$ with $\langle k'_n, k'_{n+1}\rangle = 1, Q_{k'_n k'_{n+1}} < 0\ \forall n = 1, ..., N'-1$, and $N' \in \mathcal{P}$. Notice that there is no repetition in the set $\{k_1, ..., k_N, k'_1, ..., k'_{N'}\}$ since $k_n = k'_m$ would lead to the same contradiction due to loop flow. Now we have a loop flow starting and ending at vertices in $\mathcal{P}$, a contradiction since all vertices in $\mathcal{P}$ have pressure zero. Therefore we have $p_k = 0\ \forall 1 \leq k \leq M$ and D is invertible. Now suppose $\mathcal{P} = \phi$ but $\sum_{k\in\mathcal{F}} q_k = 0$. We want to show that solutions p exist and are determined up to an additive constant, so the flows Q_{kl} are uniquely determined. Notice that if we replace say the last row of D by e_V then D is invertible by the previous argument, so $\text{rank}(D) \geq V - 1$. Also notice that $\sum_k D_{kl} = 0\ \forall 1 \leq l \leq V$, so $\text{rank}(D) = V - 1$. Now without loss of generality let vertex $1 \in \mathcal{F}$ and we want to find a solution (if $\mathcal{F} = \phi$ then

$p = (0, ..., 0)^T$ is a solution). If we change the first row of D to e_1 it is equivalent to setting $1 \in \mathcal{P}$ with $\bar{p}_1 = q_1$, which admits a unique solution p'_k by our previous argument. Now calculate

$$0 = \sum_{\langle k,l\rangle=1} (p'_k - p'_l)\kappa_{kl} = \sum_k \sum_{l\,:\,\langle k,l\rangle=1} Q'_{kl} = \sum_{l\,:\,\langle 1,l\rangle=1} Q'_{1l} + \sum_{k\in\mathcal{F}, k\neq 1} q_k \tag{B.5}$$

$$\Rightarrow \sum_{l\,:\,\langle 1,l\rangle=1} Q'_{1l} = q_1 \tag{B.6}$$

so p'_k is a solution to the original linear system. By $\sum_k D_{kl} = 0\ \forall 1 \leq l \leq V$ and $\text{rand}(D) = V - 1$ we know that the null space of D is $\{(a, ..., a)^T | a \in \mathbb{R}\}$, so the general solution is

$$p_k = p'_k + a \quad \forall 1 \leq k \leq V \tag{B.7}$$

for every $a \in \mathbb{R}$. Thus p is determined up to a constant and the flow is uniquely determined.

Finally we show that there is no solution of p when $\sum_{k\in\mathcal{F}} q_k \neq 0$. This is straight-forward since suppose for contradiction that $\exists p \in \mathbb{R}^V$ s.t.

$$Dp = b. \tag{B.8}$$

Then if we multiply both side from the left by $(1, ..., 1)$ then since $(1, ..., 1)D = 0$ we gent

$$0 = \sum_{k\in\mathcal{F}} q_k, \tag{B.9}$$

a contradiction.

APPENDIX C

Solvability of $\{\mu_k\}$

Here we prove that $\{\mu_k\}$ in Equation (4.7) are uniquely solvable under a general configuration of flow (i.e. Neumann) and pressure (i.e. Dirichlet) boundary conditions (BCs). We assume that $\kappa_{kl} > 0 \ \forall \langle k, l \rangle = 1$ (since $\kappa_{kl} = 0$ is the same as $\langle k, l \rangle = 0$) and that the network is connected. It suffices to show that the matrix D is invertible. This is the same matrix in the linear system for solving $\{p_k\}$ with the specified boundary conditions, so we only have to show that there exists a unique flow given any flow and pressure boundary conditions, which is a well-known [LP16]. Since our derivation makes use of multiple invertibility results for different matrices $D, D^{(2)}$ and so on, we provide a proof in order to highlight under what conditions invertibility is allowed. The problem is equivalent to showing that

$$Dp = 0 \Rightarrow p = 0. \tag{C.1}$$

The solution p for Eqn. (C.1) corresponds to a network where we do not have any flows into the system except possibly at vertices with pressure boundary conditions, denoted by $\mathcal{V}_D$. The goal is to show that $p_k = 0 \ \forall k$. Suppose for contradiction that $\exists i \notin \mathcal{V}_D$ s.t. $p_i \neq 0$ (since we already have $p_j = 0 \ \forall j \in \mathcal{V}_D$). Then we would have $Q_{kl} \neq 0$ for some $\langle k, l \rangle = 1$ since the network is connected, and without loss of generality let $Q_{kl} > 0$. Now we can trace this flow throughout the network in the following procedure:

1. Given that $Q_{k_{n-1}k_n} > 0$ first check if $k_n \in \mathcal{V}_D$, and stop if this is the case.

2. Consider all vertices l s.t. $\langle k_n, l \rangle = 1$. According to Kirchhoff's first law there must be an l s.t. $Q_{k_n l} > 0$. Since the network is finite we can pick e.g. the smallest l satisfying these conditions and let $k_{n+1} = l$.

3. Repeat the procedure until $k_N \in \mathcal{V}_D$ for some N and stop.

If we start with $k_1 = k, k_2 = l$ we can initiate the process since the first condition is satisfied. This procedure has to stop eventually because the network is finite and that $k_1, ..., k_n$ are all distinct for any given $n > 1$. To see this suppose $k_n = k_m$ with $m > n$. Then we would have $p_n > p_{n+1} > \cdots > p_m = p_n$, a contradiction. Thus we would end up with a chain of distinct vertices $k_1, k_2, ..., k_N$ with $\langle k_n, k_{n+1} \rangle = 1, Q_{k_n k_{n+1}} > 0 \ \forall n = 1, ..., N-1$, and $N \in \mathcal{V}_D$. Now we repeat the same procedure just with $k'_1 = l, k'_2 = k$ to trace the flows upstream, and we would end up with another chain $k'_1, k'_2, ..., k'_{N'}$ with $\langle k'_n, k'_{n+1} \rangle = 1, Q_{k'_n k'_{n+1}} < 0 \ \forall n = 1, ..., N'-1$, and $N' \in \mathcal{V}_D$. Notice that there is no repetition in the set $\{k_1, ..., k_N, k'_1, ..., k'_{N'}\}$ since $k_n = k'_m$ would lead to the same contradiction since pressures must be ordered.

REFERENCES

[AAP13] Karen Alim, Gabriel Amselem, François Peaudecerf, Michael P Brenner, and Anne Pringle. "Random network peristalsis in Physarum polycephalum organizes fluid flows across an individual." *Proceedings of the National Academy of Sciences*, **110**(33):13306–13311, 2013.

[Ach90] David J Acheson. *Elementary Fluid Dynamics*. Oxford University Press, 1990.

[ADG04] Cenk Ayata, Andrew K Dunn, Yasemin Gursoy-Özdemir, Zhihong Huang, David A Boas, and Michael A Moskowitz. "Laser speckle flowmetry for the study of cerebrovascular physiology in normal and ischemic mouse cortex." *Journal of Cerebral Blood Flow & Metabolism*, **24**(7):744–755, 2004.

[AGP79] KH Albrecht, P Gaehtgens, A Pries, and M Heuser. "The Fahraeus effect in narrow capillaries (id 3.3 to 11.0 μm)." *Microvascular Research*, **18**(1):33–47, 1979.

[APL95] Lori L Altshuler, Robert M Post, Gabriele S Leverich, Kirstin Mikalauskas, Ann Rosoff, and Laura Ackerman. "Antidepressant-induced mania and cycle acceleration: a controversy revisited." *American Journal of Psychiatry*, **152**(8):1130–1138, 1995.

[AST12] Yoshifumi Abe, Masaki Sekino, Yasushi Terazono, Hiroyuki Ohsaki, Yugo Fukazawa, Seiichiro Sakai, Hiromu Yawo, and Tatsuhiro Hisatsune. "Opto-fMRI analysis for exploring the neuronal connectivity of the hippocampal formation in rats." *Neuroscience Research*, **74**(3):248–255, 2012.

[BAR08] Jared O Barber, Jonathan P Alberding, Juan M Restrepo, and Timothy W Secomb. "Simulated two-dimensional red blood cell motion, deformation, and partitioning in microvessel bifurcations." *Annals of Biomedical Engineering*, **36**(10):1690–1698, 2008.

[BAS01] Charles E Begley, John F Annegers, Alan C Swann, Christopher Lewis, Sharon Coan, William B Schnapp, and Lynda Bryant-Comstock. "The lifetime cost of bipolar disorder in the US." *Pharmacoeconomics*, **19**(5):483–495, 2001.

[BB06] Danielle S Bassett and Edward Bullmore. "Small-world brain networks." *The Neuroscientist*, **12**(6):512–523, 2006.

[BBW06] Peter E Bayliss, Kimberly L Bellavance, Geoffrey G Whitehead, Joshua M Abrams, Sandrine Aegerter, Heather S Robbins, Douglas B Cowan, Mark T Keating, Terence O'Reilly, Jeanette M Wood, et al. "Chemical modulation of receptor signaling inhibits regenerative angiogenesis in adult zebrafish." *Nature Chemical Biology*, **2**(5):265–273, 2006.

[BCB91] Mark S Bauer, Paul Crits-Christoph, William A Ball, Edward Dewees, Thomas McAllister, Peter Alahi, John Cacciola, and Peter C Whybrow. "Independent assessment of manic and depressive symptoms by self-rating: Scale characteristics and implications for the study of mania." *Archives of General Psychiatry*, **48**(9):807–812, 1991.

[BCF00] Jayanth R Banavar, Francesca Colaiori, Alessandro Flammini, Amos Maritan, and Andrea Rinaldo. "Topology of the fittest transportation network." *Physical Review Letters*, **84**(20):4745, 2000.

[BCJ78] Philip Brickman, Dan Coates, and Ronnie Janoff-Bulman. "Lottery winners and accident victims: Is happiness relative?" *Journal of Personality and Social Psychology*, **36**(8):917, 1978.

[BF10] Richard L Burden and J Douglas Faires. "Numerical analysis." *Cengage Learning*, **9**, 2010.

[BFB92] John L Barron, David J Fleet, Steven S Beauchemin, and TA Burkitt. "Performance of optical flow techniques." In *Proceedings 1992 IEEE Computer Society Conference on Computer Vision and Pattern Recognition*, pp. 236–242. IEEE, 1992.

[BGG15] Michael B Bonsall, John R Geddes, Guy M Goodwin, and Emily A Holmes. "Bipolar disorder dynamics: affective instabilities, relaxation oscillations and noise." *Journal of the Royal Society Interface*, **12**(112):20150670, 2015.

[BLB17] Kyung In Baek, Rongsong Li, Tyler Beebe, Howard Choi, Nelson Jen, Amir Kaboodrangi, Peipei Ping, David Liem, and Tzung K Hsiai. "Flow-responsive Vegfr-pkcε Signaling Mediates Glycolytic Metabolites for Vascular Repair." *Circulation*, **136**(Suppl_1):A14822, 2017.

[BLJ09] Timo Betz, Martin Lenz, Jean-François Joanny, and Cécile Sykes. "ATP-dependent mechanics of red blood cells." *Proceedings of the National Academy of Sciences*, **106**(36):15320–15325, 2009.

[BM07] Steffen Bohn and Marcelo O Magnasco. "Structure, scaling, and phase transition in the optimal transport network." *Physical Review Letters*, **98**(8):088702, 2007.

[BMG10] Jedediah M Bopp, David J Miklowitz, Guy M Goodwin, Will Stevens, Jennifer M Rendell, and John R Geddes. "The longitudinal course of bipolar disorder as revealed through weekly text messaging: a feasibility study." *Bipolar Disorders*, **12**(3):327–334, 2010.

[BO13] Carl M Bender and Steven A Orszag. *Advanced mathematical methods for scientists and engineers I: Asymptotic methods and perturbation theory*. Springer Science & Business Media, 2013.

[BSB06] Geert Jan Biessels, Salka Staekenborg, Eric Brunner, Carol Brayne, and Philip Scheltens. "Risk of dementia in diabetes mellitus: a systematic review." *The Lancet Neurology*, **5**(1):64–74, 2006.

[BTK13] Pablo Blinder, Philbert S Tsai, John P Kaufhold, Per M Knutsen, Harry Suhl, and David Kleinfeld. "The cortical angiome: an interconnected vascular network with noncolumnar patterns of blood flow." *Nature Neuroscience*, **16**(7):889–897, 2013.

[BWG12] Michael B Bonsall, Sophie M A Wallace-Hadrill, John R Geddes, Guy M Goodwin, and Emily A Holmes. "Non-linear time series approaches in characterising mood stability and mood instability in bipolar disorder." *Proceedings of the Royal Society Series B*, **279**:916–924, 2012.

[CFJ18] Changsi Cai, Jonas C Fordsmann, Sofie H Jensen, Bodil Gesslein, Micael Lønstrup, Bjørn O Hald, Stefan A Zambach, Birger Brodin, and Martin J Lauritzen. "Stimulation-induced increases in cerebral blood flow and local capillary vasoconstriction depend on conducted vascular responses." *Proceedings of the National Academy of Sciences*, **115**(25):E5796–E5804, 2018.

[CHJ16] Francesco Clavica, Alexandra Homsy, Laure Jeandupeux, and Dominik Obrist. "Red blood cell phase separation in symmetric and asymmetric microchannel networks: effect of capillary dilation and inflow velocity." *Scientific Reports*, **6**:36763, 2016.

[CIC08] Timothy J A Chico, Philip W Ingham, and David C Crossman. "Modeling cardiovascular disease in the zebrafish." *Trends in Cardiovascular Medicine*, **18**(4):150–155, 2008.

[CJ89] Dah-Ming Chiu and Raj Jain. "Analysis of the increase and decrease algorithms for congestion avoidance in computer networks." *Computer Networks and ISDN Systems*, **17**(1):1–14, 1989.

[CJL12] Qi Chen, Luan Jiang, Chun Li, Dan Hu, Ji-wen Bu, David Cai, and Jiu-lin Du. "Haemodynamics-driven developmental pruning of brain vasculature in zebrafish." *PLoS Biology*, **10**(8):e1001374, 2012.

[CM14] Danfeng Cai and Denise J Montell. "Diverse and dynamic sources and sinks in gradient formation and directed migration." *Current Opinion in Cell Biology*, **30**:91–98, 2014.

[COA03] Emmanuelle Chaigneau, Martin Oheim, Etienne Audinat, and Serge Charpak. "Two-photon imaging of capillary blood flow in olfactory bulb glomeruli." *Proceedings of the National Academy of Sciences*, **100**(22):13081–13086, 2003.

[Cor10] Francis Corson. "Fluctuations and redundancy in optimal transport networks." *Physical Review Letters*, **104**(4):048703, 2010.

[CR18] Shyr-Shea Chang and Marcus Roper. "Minimal transport networks with general boundary conditions." *SIAM Journal on Applied Mathematics*, **78**(3):1511–1535, 2018.

[CR19] Shyr-Shea Chang and Marcus Roper. "Microvscular networks with uniform flow." *Journal of Theoretical Biology*, **462**:48–64, 2019.

[CSL11] Chi-Hua Chen, John Suckling, Belinda R Lennox, Cinly Ooi, and Ed T Bullmore. "A quantitative meta-analysis of fMRI studies in bipolar disorder." *Bipolar Disorders*, **13**(1):1–15, 2011.

[CSM17] Amy L Cochran, André Schultz, Melvin G McInnis, and Daniel B Forger. "A comparison of mathematical models of mood in bipolar disorder." In *Computational Neurology and Psychiatry*, pp. 315–341. Springer, 2017.

[CTB17] Shyr-Shea Chang, Shenyinying Tu, Kyung In Baek, Andrew Pietersen, Yu-Hsiu Liu, Van M Savage, Sheng-Ping L Hwang, Tzung K Hsiai, and Marcus Roper. "Optimal occlusion uniformly partitions red blood cells fluxes within a microvascular network." *PLoS Computational Biology*, **13**(12):e1005892, 2017.

[CV03] B Corbella and E Vieta. "Molecular targets of lithium action." *Acta Neuropsychiatrica*, **15**(6):316–340, 2003.

[CZ13] Edwin KP Chong and Stanislaw H Zak. *An introduction to optimization*. John Wiley & Sons, 2013.

[DDD05] Andrew K Dunn, Anna Devor, Anders M Dale, and David A Boas. "Spatial extent of oxygen metabolism and hemodynamic changes during functional activation of the rat somatosensory cortex." *Neuroimage*, **27**(2):279–290, 2005.

[DH17] Yvonne L Dorland and Stephan Huveneers. "Cell–cell junctional mechanotransduction in endothelial remodeling." *Cellular and Molecular Life Sciences*, **74**(2):279–292, 2017.

[DP80] John R Dormand and Peter J Prince. "A family of embedded Runge-Kutta formulae." *Journal of Computational and Applied Mathematics*, **6**(1):19–26, 1980.

[DPP11] Vincent Doyeux, Thomas Podgorski, Sarah Peponas, Mourad Ismail, and Gwennou Coupier. "Spheres in the vicinity of a bifurcation: elucidating the Zweifach–Fung effect." *Journal of Fluid Mechanics*, **674**:359–388, 2011.

[DRU09] Darryl Daugherty, Tairi Roque-Urrea, John Urrea-Roque, Jessica Troyer, Stephen Wirkus, and Mason A Porter. "Mathematical models of bipolar disorder." *Communications in Nonlinear Science and Numerical Simulation*, **14**(7):2897–2908, 2009.

[Dur06] Marc Durand. "Architecture of optimal transport networks." *Physical Review E*, **73**(1):016116, 2006.

[Dur07] Marc Durand. "Structure of optimal transport networks subject to a global constraint." *Physical Review Letters*, **98**(8):088701, 2007.

[EN15] Eran Eldar and Yael Niv. "Interaction between emotional state and learning underlies mood instability." *Nature Communications*, **6**:6149, 2015.

[ERD16] Eran Eldar, Robb B Rutledge, Raymond J Dolan, and Yael Niv. "Mood as representation of momentum." *Trends in Cognitive Sciences*, **20**(1):15–24, 2016.

[FAB06] Magalie Faivre, Manouk Abkarian, Kimberly Bickraj, and Howard A Stone. "Geometrical focusing of cells in a microfluidic device: an approach to separate blood plasma." *Biorheology*, **43**(2):147–159, 2006.

[Fai99] Gordon L Fain. *Molecular and cellular physiology of neurons*. Harvard University Press, 1999.

[FFS09] Cassot Francis, Lauwers Frederic, Lorthois Sylvie, Puwanarajah Prasanna, and Duvernoy Henri. "Scaling laws for branching vessels of human cerebral cortex." *Microcirculation*, **16**(4):331–344, 2009.

[FJ05] Vivian Fonseca and Ali Jawa. "Endothelial and erectile dysfunction, diabetes mellitus, and the metabolic syndrome: common pathways and treatments?" *The American Journal of Cardiology*, **96**(12):13–18, 2005.

[FO85] MB Furman and WL Olbricht. "Unsteady cell distributions in capillary networks." *Biotechnology Progress*, **1**(1):26–32, 1985.

[FTC17] Yuan-cheng Fung, Pin Tong, and Xiaohong Chen. *Classical and computational solid mechanics*. World Scientific Publishing Company, 2017.

[Fun73] Yuan-Cheng Fung. "Stochastic flow in capillary blood vessels." *Microvascular Research*, **5**(1):34–48, 1973.

[FWC04] Cynthia HY Fu, Steven CR Williams, Anthony J Cleare, Michael J Brammer, Nicholas D Walsh, Jieun Kim, Chris M Andrew, Emilio Merlo Pich, Pauline M Williams, Laurence J Reed, M T Mitterschiffthaler, J Suckling, and E T Bullmore. "Attenuation of the neural response to sad faces in major depressionby antidepressant treatment: a prospective, event-related functional magnetic resonance imaging study." *Archives of General Psychiatry*, **61**(9):877–889, 2004.

[FYS12] Omid Forouzan, Xiaoxi Yang, Jose M Sosa, Jennie M Burns, and Sergey S Shevkoplyas. "Spontaneous oscillations of capillary blood flow in artificial microvascular networks." *Microvascular Research*, **84**(2):123–132, 2012.

[GBW01] James F Gillooly, James H Brown, Geoffrey B West, Van M Savage, and Eric L Charnov. "Effects of size and temperature on metabolic rate." *Science*, **293**(5538):2248–2251, 2001.

[GKT04] Ian H Gotlib, Karen L Kasch, Saskia Traill, Jutta Joormann, Bruce A Arnow, and Sheri L Johnson. "Coherence and specificity of information-processing biases in depression and social phobia." *Journal of Abnormal Psychology*, **113**(3):386, 2004.

[GKY04] Ian H Gotlib, Elena Krasnoperova, Dana Neubauer Yue, and Jutta Joormann. "Attentional biases for negative interpersonal stimuli in clinical depression." *Journal of Abnormal Psychology*, **113**(1):127, 2004.

[GL97] Barbara Geller and Joan Luby. "Child and adolescent bipolar disorder: a review of the past 10 years." *Journal of the American Academy of Child & Adolescent Psychiatry*, **36**(9):1168–1176, 1997.

[GM13] John R Geddes and David J Miklowitz. "Treatment of bipolar disorder." *The Lancet*, **381**(9878):1672–1682, 2013.

[Gol11] Albert Goldbeter. "A model for the dynamics of bipolar disorders." *Progress in Biophysics and Molecular Biology*, **105**(1-2):119–127, 2011.

[GRT00] Michael E Geisser, Randy S Roth, Mary E Theisen, Michael E Robinson, and Joseph L Riley III. "Negative affect, self-report of depressive symptoms, and clinical depression: relation to the experience of chronic pain." *The Clinical Journal of Pain*, **16**(2):110–120, 2000.

[GT03] Joseph F Goldberg and Christine J Truman. "Antidepressant-induced mania: an overview of current controversies." *Bipolar Disorders*, **5**(6):407–420, 2003.

[GWS81] P Gaehtgens, G Will, and F Schmidt. "Comparative rheology of nucleated and non-nucleated red blood cells. II. Rheological properties of avian red cells suspensions in narrow capillaries." *Pflugers Archiv*, **390**(3):283–287, 1981.

[Hal15] John E Hall. *Guyton and Hall textbook of medical physiology*. Elsevier Health Sciences, 2015.

[Har08] Catherine J Harmer. "Serotonin and emotional processing: does it help explain antidepressant drug action?" *Neuropharmacology*, **55**(6):1023–1028, 2008.

[HBG91] CM Hawkey, PM Bennett, SC Gascoyne, MG Hart, and JK Kirkwood. "Erythrocyte size, number and haemoglobin content in vertebrates." *British Journal of Haematology*, **77**(3):392–397, 1991.

[HBH16] EA Holmes, MB Bonsall, SA Hales, H Mitchell, F Renner, SE Blackwell, P Watson, GM Goodwin, and M Di Simplicio. "Applications of time-series analysis to mood fluctuations in bipolar disorder to promote treatment innovation: a case series." *Translational Psychiatry*, **6**(1):e720, 2016.

[HC13] Dan Hu and David Cai. "Adaptation and optimization of biological transport networks." *Physical Review Letters*, **111**(13):138701, 2013.

[HCR12] Dan Hu, David Cai, and Aaditya V Rangan. "Blood Vessel Adaptation with Fluctuations in Capillary Flow Distribution." *PloS One*, **7**(9):e45444, 2012.

[HCW94] KA Haldenby, DC Chappell, CP Winlove, KH Parker, and JA Firth. "Focal and regional variations in the composition of the glycocalyx of large vessel endothelium." *Journal of Vascular Research*, **31**(1):2–9, 1994.

[HDF16] Patrick C Hickey, Haoxuan Dou, Sierra Foshe, and Marcus Roper. "Anti-jamming in a fungal transport network." *arXiv preprint arXiv:1601.06097*, 2016.

[HEB05] Sui Huang, Gabriel Eichler, Yaneer Bar-Yam, and Donald E Ingber. "Cell fates as high-dimensional attractor states of a complex gene regulatory network." *Physical Review Letters*, **94**(12):128701, 2005.

[HKF03] Jay R Hove, Reinhard W Köster, Arian S Forouhar, Gabriel Acevedo-Bolton, Scott E Fraser, and Morteza Gharib. "Intracardiac fluid forces are an essential epigenetic factor for embryonic cardiogenesis." *Nature*, **421**(6919):172, 2003.

[HLM10] Luke LM Heaton, Eduardo López, Philip K Maini, Mark D Fricker, and Nick S Jones. "Growth-induced mass flows in fungal networks." *Proceedings of the Royal Society of London B: Biological Sciences*, **277**(1698):3265–3274, 2010.

[Hov04] Jay R Hove. "In vivo biofluid dynamic imaging in the developing zebrafish." *Birth Defects Research Part C: Embryo Today: Reviews*, **72**(3):277–289, 2004.

[HSH05] Keith Hawton, Lesley Sutton, Camilla Haw, Julia Sinclair, and Louise Harriss. "Suicide and attempted suicide in bipolar disorder: a systematic review of risk factors." *The Journal of Clinical Psychiatry*, 2005.

[HST98] Clifford M Hurvich, Jeffrey S Simonoff, and Chih-Ling Tsai. "Smoothing parameter selection in nonparametric regression using an improved Akaike information criterion." *Journal of the Royal Statistical Society: Series B (Statistical Methodology)*, **60**(2):271–293, 1998.

[HVS96] WJ Hacking, E VanBavel, and JA Spaan. "Shear stress is not sufficient to control growth of vascular networks: a model study." *American Journal of Physiology-Heart and Circulatory Physiology*, **270**(1):H364–H375, 1996.

[IHW01] Sumio Isogai, Masaharu Horiguchi, and Brant M Weinstein. "The vascular anatomy of the developing zebrafish: an atlas of embryonic and early larval development." *Developmental Biology*, **230**(2):278–301, 2001.

[ILC13] Thomas R Insel, Story C Landis, and Francis S Collins. "The NIH brain initiative." *Science*, **340**(6133):687–688, 2013.

[JNE06] Elizabeth AV Jones, Ferdinand le Noble, and Anne Eichmann. "What determines blood vessel structure? Genetic prespecification vs. hemodynamics." *Physiology*, **21**(6):388–395, 2006.

[KAA06] Ronald C Kessler, Hagop S Akiskal, Minnie Ames, Howard Birnbaum, Paul Greenberg, Robert M Hirschfeld, Robert Jin, Kathleen R Merikangas, Gregory E Simon, and Philip S Wang. "Prevalence and effects of mood disorders on work performance in a nationally representative sample of US workers." *American Journal of Psychiatry*, **163**(9):1561–1568, 2006.

[KBL03] Sander Kranenbarg, Jos GM van den Boogaart, and Johan L van Leeuwen. "Oxygen profile in zebra fish embryo (Danio rerio) elucidated by theory and experiment." *Animal Biology*, **53**(4):339–346, 2003.

[KBS15] Inken D Kelch, Gib Bogle, Gregory B Sands, Anthony RJ Phillips, Ian J LeGrice, and P Rod Dunbar. "Organ-wide 3D-imaging and topological analysis of the continuous microvascular network in a murine lymph node." *Scientific Reports*, **5**:16534, 2015.

[KDG82] Bruce Klitzman, David N Damon, Richard J Gorczynski, and Brian R Duling. "Augmented tissue oxygen supply during striated muscle contraction in the hamster. Relative contributions of capillary recruitment, functional dilation, and reduced tissue PO2." *Circulation Research*, **51**(6):711–721, 1982.

[KMH98] David Kleinfeld, Partha P Mitra, Fritjof Helmchen, and Winfried Denk. "Fluctuations and stimulus-induced changes in blood flow observed in individual capillaries in layers 2 through 4 of rat neocortex." *Proceedings of the National Academy of Sciences*, **95**(26):15741–15746, 1998.

[Kro22] August Krogh. *The anatomy and physiology of capillaries*. Yale University Press, 1922.

[KSK93] Akos Koller, Dong Sun, and Gabor Kaley. "Role of shear stress and endothelial prostaglandins in flow-and viscosity-induced dilation of arterioles in vitro." *Circulation Research*, **72**(6):1276–1284, 1993.

[KSM10] Eleni Katifori, Gergely J Szöllősi, and Marcelo O Magnasco. "Damage and fluctuations induce loops in optimal transport networks." *Physical Review Letters*, **104**(4):048704, 2010.

[KT80] AKIRA Kamiya and TATSUO Togawa. "Adaptive regulation of wall shear stress to flow change in the canine carotid artery." *American Journal of Physiology-Heart and Circulatory Physiology*, **239**(1):H14–H21, 1980.

[Lep06] Jukka M Leppänen. "Emotional information processing in mood disorders: a review of behavioral and neuroimaging findings." *Current Opinion in Psychiatry*, **19**(1):34–39, 2006.

[Lig75] James Lighthill. *Mathematical biofluiddynamics*. Siam, 1975.

[LJC04] BR Lennox, R Jacob, AJ Calder, V Lupson, and ET Bullmore. "Behavioural and neurocognitive responses to sad facial affect are attenuated in patients with mania." *Psychological Medicine*, **34**(5):795–802, 2004.

[Lov13] Augustus Edward Hough Love. *A treatise on the mathematical theory of elasticity*. Cambridge university press, 2013.

[LP16] Russell Lyons and Yuval Peres. *Probability on trees and networks*. Cambridge University Press, New York, 2016. Available at `http://pages.iu.edu/~rdlyons/`.

[LPS01] Howard A Levine, Serdal Pamuk, Brian D Sleeman, and Marit Nilsen-Hamilton. "Mathematical modeling of capillary formation and development in tumor angiogenesis: penetration into the stroma." *Bulletin of Mathematical Biology*, **63**(5):801–863, 2001.

[LSP01] Nathan D Lawson, Nico Scheer, Van N Pham, Cheol-Hee Kim, Ajay B Chitnis, Jose A Campos-Ortega, and Brant M Weinstein. "Notch signaling is required for arterial-venous differentiation during embryonic vascular development." *Development*, **128**(19):3675–3683, 2001.

[LWS04] Natalia S Lawrence, Andrew M Williams, Simon Surguladze, Vincent Giampietro, Michael J Brammer, Christopher Andrew, Sophia Frangou, Christine Ecker, and Mary L Phillips. "Subcortical and ventral prefrontal cortical neural responses to facial expressions distinguish patients with bipolar disorder and major depression." *Biological Psychiatry*, **55**(6):578–587, 2004.

[MA18] Felix J Meigel and Karen Alim. "Flow rate of transport network controls uniform metabolite supply to tissue." *Journal of The Royal Society Interface*, **15**(142):20180075, 2018.

[Mar13] Jerry B Marion. *Classical dynamics of particles and systems*. Academic Press, 2013.

[MB74] Jeffery B Morris and Aaron T Beck. "The efficacy of antidepressant drugs: A review of research (1958 to 1972)." *Archives of General Psychiatry*, **30**(5):667–674, 1974.

[MBR09] Alison L Marsden, Adam J Bernstein, V Mohan Reddy, Shawn C Shadden, Ryan L Spilker, Frandics P Chan, Charles A Taylor, and Jeffrey A Feinstein. "Evaluation of a novel Y-shaped extracardiac Fontan baffle using computational fluid dynamics." *The Journal of Thoracic and Cardiovascular Surgery*, **137**(2):394–403, 2009.

[MD09] Andrew N Makanya and Valentin Djonov. "Parabronchial angioarchitecture in developing and adult chickens." *Journal of Applied Physiology*, **106**(6):1959–1969, 2009.

[MER17] Liam Mason, Eran Eldar, and Robb B Rutledge. "Mood Instability and Reward Dysregulation—A Neurocomputational Model of Bipolar Disorder." *JAMA Psychiatry*, 2017.

[MJ79] A Miodoński and A Jasiński. "Scanning electron microscopy of microcorrosion casts of the vascular bed in the skin of the spotted salamander, Salamandra salamandra L." *Cell and Tissue Research*, **196**(1):153–162, 1979.

[MKS11] David Mayerich, Jaerock Kwon, Chul Sung, Louise Abbott, John Keyser, and Yoonsuck Choe. "Fast macro-scale transmission imaging of microvascular networks using KESM." *Biomedical Optics Express*, **2**(10):2888–2896, 2011.

[MLM12] Paul J Moore, Max A Little, Patrick E McSharry, John R Geddes, and Guy M Goodwin. "Forecasting depression in bipolar disorder." *IEEE Transactions on Biomedical Engineering*, **59**(10):2801–2807, 2012.

[MM07] Andrew N Makanya and Jacopo P Mortola. "The structural design of the bat wing web and its possible role in gas exchange." *Journal of Anatomy*, **211**(6):687–697, 2007.

[MQK03] Jill M Murtha, Weici Qi, and Evan T Keller. "Hematologic and serum biochemical values for zebrafish (Danio rerio)." *Comparative Medicine*, **53**(1):37–41, 2003.

[MSA03] Katherine A McCulloh, John S Sperry, and Frederick R Adler. "Water transport in plants obeys Murray's law." *Nature*, **421**(6926):939–942, 2003.

[MSS07] Michael H Malone, Noah Sciaky, Lisa Stalheim, Klaus M Hahn, Elwood Linney, and Gary L Johnson. "Laser-scanning velocimetry: a confocal microscopy method for quantitative measurement of cardiovascular performance in zebrafish embryos and larvae." *BMC Biotechnology*, **7**(1):1, 2007.

[Mur26a] Cecil D Murray. "The physiological principle of minimum work applied to the angle of branching of arteries." *The Journal of General Physiology*, **9**(6):835–841, 1926.

[Mur26b] Cecil D Murray. "The physiological principle of minimum work: I. The vascular system and the cost of blood volume." *Proceedings of the National Academy of Sciences*, **12**(3):207, 1926.

[NEL06] Thi-Hanh Nguyen, Anne Eichmann, Ferdinand Le Noble, and Vincent Fleury. "Dynamics of vascular branching morphogenesis: the effect of blood and tissue flow." *Physical Review E*, **73**(6):061907, 2006.

[NR18] Claudia Neuhauser and Marcus L Roper. *Calculus for biology and medicine*. Pearson, 2018.

[OWB10] Dominik Obrist, Bruno Weber, Alfred Buck, and Patrick Jenny. "Red blood cell distribution in simplified capillary networks." *Philosophical Transactions of the Royal Society of London A: Mathematical, Physical and Engineering Sciences*, **368**(1921):2897–2918, 2010.

[PB96] Bernd Pelster and Warren W Burggren. "Disruption of hemoglobin oxygen transport does not impact oxygen-dependent physiological processes in developing embryos of zebra fish (Danio rerio)." *Circulation Research*, **79**(2):358–362, 1996.

[PB17] Erdem Pulcu and Michael Browning. "Affective bias as a rational response to the statistics of rewards and punishments." *eLife*, **6**, 2017.

[PBA10] YongKeun Park, Catherine A Best, Thorsten Auth, Nir S Gov, Samuel A Safran, Gabriel Popescu, Subra Suresh, and Michael S Feld. "Metabolic remodeling of the human red blood cell membrane." *Proceedings of the National Academy of Sciences*, **107**(4):1289–1294, 2010.

[Ped03] Timothy J Pedley. "Mathematical modelling of arterial fluid dynamics." *Journal of Engineering Mathematics*, **47**(3-4):419–444, 2003.

[PEM09] David M Parichy, Michael R Elizondo, Margaret G Mills, Tiffany N Gordon, and Raymond E Engeszer. "Normal table of postembryonic zebrafish development: staging by externally visible anatomy of the living fish." *Developmental Dynamics*, **238**(12):2975–3015, 2009.

[PHL10] Axel R Pries, Michael Höpfner, Ferdinand Le Noble, Mark W Dewhirst, and Timothy W Secomb. "The shunt problem: control of functional shunting in normal and tumour vasculature." *Nature Reviews Cancer*, **10**(8):587, 2010.

[PK01] Christopher J Phiel and Peter S Klein. "Molecular targets of lithium action." *Annual Review of Pharmacology and Toxicology*, **41**(1):789–813, 2001.

[PLC89] AR Pries, K Ley, M Claassen, and P Gaehtgens. "Red cell distribution at microvascular bifurcations." *Microvascular Research*, **38**(1):81–101, 1989.

[PM92] Jacqueline B Persons and Jeanne Miranda. "Cognitive theories of vulnerability to depression: Reconciling negative evidence." *Cognitive Therapy and Research*, **16**(4):485–502, 1992.

[Poz05] C Pozrikidis. "Axisymmetric motion of a file of red blood cells through capillaries." *Physics of Fluids*, **17**(3):031503, 2005.

[PRB90] Roger E Pecoraro, Gayle E Reiber, and Ernest M Burgess. "Pathways to diabetic limb amputation: basis for prevention." *Diabetes Care*, **13**(5):513–521, 1990.

[PS05] AR Pries and TW Secomb. "Microvascular blood viscosity in vivo and the endothelial surface layer." *American Journal of Physiology-Heart and Circulatory Physiology*, **289**(6):H2657–H2664, 2005.

[PSG90] AR Pries, TW Secomb, P Gaehtgens, and JF Gross. "Blood flow in microvascular networks. Experiments and simulation." *Circulation Research*, **67**(4):826–834, 1990.

[PSG95] AR Pries, TW Secomb, and P Gaehtgens. "Structure and hemodynamics of microvascular networks: heterogeneity and correlations." *American Journal of Physiology-Heart and Circulatory Physiology*, **269**(5):H1713–H1722, 1995.

[PSG98] AR Pries, TW Secomb, and P Gaehtgens. "Structural adaptation and stability of microvascular networks: theory and simulations." *American Journal of Physiology-Heart and Circulatory Physiology*, **275**(2):H349–H360, 1998.

[RBC09] Satish Rao, Štefan Bálint, Benjamin Cossins, Victor Guallar, and Dmitri Petrov. "Raman study of mechanically induced oxygenation state transition of red blood cells using optical tweezers." *Biophysical Journal*, **96**(1):209–216, 2009.

[RBT06] A John Rush, Ira H Bernstein, Madhukar H Trivedi, Thomas J Carmody, Stephen Wisniewski, James C Mundt, Kathy Shores-Wilson, Melanie M Biggs, Ada Woo, Andrew A Nierenberg, and Maurizio Fava. "An evaluation of the quick inventory of depressive symptomatology and the Hamilton rating scale for depression: A sequenced treatment alternatives to relieve depression trial report." *Biological Psychiatry*, **59**(6):493–501, 2006.

[RD09] Peter Rombough and Holly Drader. "Hemoglobin enhances oxygen uptake in larval zebrafish (Danio rerio) but only under conditions of extreme hypoxia." *Journal of Experimental Biology*, **212**(6):778–784, 2009.

[RK06] Thorsten Reffelmann and Robert A Kloner. "The no-reflow phenomenon: a basic mechanism of myocardial ischemia and reperfusion." *Basic Research in Cardiology*, **101**(5):359–372, 2006.

[RK16] Henrik Ronellenfitsch and Eleni Katifori. "Global optimization, local adaptation, and the role of growth in distribution networks." *Physical Review Letters*, **117**(13):138301, 2016.

[RNR93] Per Reichard, Bengt-Yngve Nilsson, and Urban Rosenqvist. "The effect of long-term intensified insulin treatment on the development of microvascular complications of diabetes mellitus." *New England Journal of Medicine*, **329**(5):304–309, 1993.

[RSD14] Robb B Rutledge, Nikolina Skandali, Peter Dayan, and Raymond J Dolan. "A computational and neural model of momentary subjective well-being." *Proceedings of the National Academy of Sciences*, **111**(33):12252–12257, 2014.

[RSH13] Marcus Roper, Anna Simonin, Patrick C Hickey, Abby Leeder, and N Louise Glass. "Nuclear dynamics in a fungal chimera." *Proceedings of the National Academy of Sciences*, **110**(32):12875–12880, 2013.

[RUM11] Jane Reece, Lisa A Urry, Noel Meyers, Michael L Cain, Steven A Wasserman, Peter V Minorsky, Robert B Jackson, and Bernard N Cooke. *Campbell biology*. Pearson Higher Education AU, 2011.

[SA08] Michael Schindler and Armand Ajdari. "Droplet traffic in microfluidic networks: a simple model for understanding and designing." *Physical Review Letters*, **100**(4):044501, 2008.

[SAF12] Johannes Schindelin, Ignacio Arganda-Carreras, Erwin Frise, Verena Kaynig, Mark Longair, Tobias Pietzsch, Stephan Preibisch, Curtis Rueden, Stephan Saalfeld, Benjamin Schmid, et al. "Fiji: an open-source platform for biological-image analysis." *Nature Methods*, **9**(7):676–682, 2012.

[SAH04] Stephen M Strakowski, Caleb M Adler, Scott K Holland, Neil Mills, and Melissa P DelBello. "A preliminary fMRI study of sustained attention in euthymic, unmedicated bipolar disorder." *Neuropsychopharmacology*, **29**(9):1734, 2004.

[SBM16] T Savin, MM Bandi, and L Mahadevan. "Pressure-driven occlusive flow of a confined red blood cell." *Soft Matter*, **12**(2):562–573, 2016.

[SCK16] Zaiyi Shen, Gwennou Coupier, Badr Kaoui, Benoît Polack, Jens Harting, Chaouqi Misbah, and Thomas Podgorski. "Inversion of hematocrit partition at microfluidic bifurcations." *Microvascular Research*, **105**:40–46, 2016.

[SH96] TW Secomb and R Hsu. "Analysis of red blood cell motion through cylindrical micropores: effects of cell properties." *Biophysical Journal*, **71**(2):1095, 1996.

[She81] Thomas F Sherman. "On connecting large vessels to small. The meaning of Murray's law." *The Journal of General Physiology*, **78**(4):431–453, 1981.

[SHL10] Lothar Schermelleh, Rainer Heintzmann, and Heinrich Leonhardt. "A guide to super-resolution fluorescence microscopy." *The Journal of Cell Biology*, **190**(2):165–175, 2010.

[SHP98] TW Secomb, R Hsu, and AR Pries. "A model for red blood cell motion in glycocalyx-lined capillaries." *American Journal of Physiology-Heart and Circulatory Physiology*, **274**(3):H1016–H1022, 1998.

[SHP01] TW Secomb, R Hsu, and AR Pries. "Motion of red blood cells in a capillary with an endothelial surface layer: effect of flow velocity." *American Journal of Physiology-Heart and Circulatory Physiology*, **281**(2):H629–H636, 2001.

[SIK13] Satoshi Shimozono, Tadahiro Iimura, Tetsuya Kitaguchi, Shin-ichi Higashijima, and Atsushi Miyawaki. "Visualization of an endogenous retinoic acid gradient across embryonic development." *Nature*, **496**(7445):363, 2013.

[SMC12] David Salgado, Christophe Marcelle, Peter D Currie, and Robert J Bryson-Richardson. "The Zebrafish Anatomy Portal: A novel integrated resource to facilitate zebrafish research." *Developmental Biology*, **372**(1):1–4, 2012.

[SRB15] Andy Y Shih, Charlotta Rühlmann, Pablo Blinder, Anna Devor, Patrick J Drew, Beth Friedman, Per M Knutsen, Patrick D Lyden, Celine Mateo, Lisa Mellander, et al. "Robust and fragile aspects of cortical blood flow in relation to the underlying angioarchitecture." *Microcirculation*, **22**(3):204–218, 2015.

[SRW15] Franca Schmid, Johannes Reichold, Bruno Weber, and Patrick Jenny. "The impact of capillary dilation on the distribution of red blood cells in artificial networks." *American Journal of Physiology-Heart and Circulatory Physiology*, **308**(7):H733–H742, 2015.

[SS88] Jefferson A Singer and Peter Salovey. "Mood and memory: Evaluating the network theory of affect." *Clinical Psychology Review*, **8**(2):211–251, 1988.

[SSO86] TW Secomb, R Skalak, N Özkaya, and JF Gross. "Flow of axisymmetric red blood cells in narrow capillaries." *Journal of Fluid Mechanics*, **163**:405–423, 1986.

[Str14] Steven H Strogatz. *Nonlinear dynamics and chaos: with applications to physics, biology, chemistry, and engineering.* Westview Press, 2014.

[SUP03] Thorsten Schwerte, Dietmar Überbacher, and Bernd Pelster. "Non-invasive imaging of blood cell concentration and blood distribution in zebrafish Danio rerio incubated in hypoxic conditions in vivo." *Journal of Experimental Biology*, **206**(8):1299–1307, 2003.

[SUS80] Geert W Schmid-Schönbein, Shunichi Usami, Richard Skalak, and Shu Chien. "The interaction of leukocytes and erythrocytes in capillary and postcapillary vessels." *Microvascular Research*, **19**(1):45–70, 1980.

[SW13] Arno Steinacher and Kim A Wright. "Relating the bipolar spectrum to dysregulation of behavioural activation: a perspective from dynamical modelling." *PloS One*, **8**(5):e63345, 2013.

[TG99] James N Topper and Michael A Gimbrone Jr. "Blood flow and vascular gene expression: fluid shear stress as a modulator of endothelial phenotype." *Molecular Medicine Today*, **5**(1):40–46, 1999.

[TH03] Pamela L Tuma and Ann L Hubbard. "Transcytosis: crossing cellular barriers." *Physiological Reviews*, **83**(3):871–932, 2003.

[TNQ01] Larry A Taber, Stella Ng, Alicia M Quesnel, Jennifer Whatman, and Craig J Carmen. "Investigating Murray's law in the chick embryo." *Journal of Biomechanics*, **34**(1):121–124, 2001.

[Tom14] Giovanna Tomaiuolo. "Biomechanical properties of red blood cells in health and disease towards microfluidics." *Biomicrofluidics*, **8**(5):051501, 2014.

[TTS10] Atsushi Tero, Seiji Takagi, Tetsu Saigusa, Kentaro Ito, Dan P Bebber, Mark D Fricker, Kenji Yumiki, Ryo Kobayashi, and Toshiyuki Nakagaki. "Rules for biologically inspired adaptive network design." *Science*, **327**(5964):439–442, 2010.

[UAH08] Snežana Urošević, Lyn Y Abramson, Eddie Harmon-Jones, and Lauren B Alloy. "Dysregulation of the behavioral approach system (BAS) in bipolar spectrum disorders: review of theory and evidence." *Clinical Psychology Review*, **28**(7):1188–1205, 2008.

[VFL09] Julien Vermot, Arian S Forouhar, Michael Liebling, David Wu, Diane Plummer, Morteza Gharib, and Scott E Fraser. "Reversing blood flows act through klf2a to ensure normal valvulogenesis in the developing heart." *PLoS Biology*, **7**(11):e1000246, 2009.

[WBC96] Myrna M Weissman, Roger C Bland, Glorisa J Canino, Carlo Faravelli, Steven Greenwald, Hai-Gwo Hwu, Peter R Joyce, Eile G Karam, Chung-Kyoon Lee, Joseph Lellouch, Jean-Pierre Lépine, Stephen C Newman, Maritza Rubio-Stipec, J Elizabeth Wells, Priya J Wickramaratne, Hans-Ulrich Wittchen, and Eng-Kung Yeh. "Cross-national epidemiology of major depression and bipolar disorder." *JAMA*, **276**(4):293–299, 1996.

[WBE97] Geoffrey B West, James H Brown, and Brian J Enquist. "A general model for the origin of allometric scaling laws in biology." *Science*, **276**(5309):122–126, 1997.

[WBP03] U Windberger, A Bartholovitsch, R Plasenzotti, KJ Korak, and G Heinze. "Whole blood viscosity, plasma viscosity and erythrocyte aggregation in nine mammalian species: reference values and comparison of data." *Experimental Physiology*, **88**(3):431–440, 2003.

[WD60] JB West and CT Dollery. "Distribution of blood flow and ventilation-perfusion ratio in the lung, measured with radioactive CO 2." *Journal of Applied Physiology*, **15**(3):405–410, 1960.

[WDR13] Harvey A Whiteford, Louisa Degenhardt, Jürgen Rehm, Amanda J Baxter, Alize J Ferrari, Holly E Erskine, Fiona J Charlson, Rosana E Norman, Abraham D Flaxman, Nicole Johns, Roy Burstein, Christopher J L Murray, and Theo Vos. "Global burden of disease attributable to mental and substance use disorders: findings from the Global Burden of Disease Study 2010." *The Lancet*, **382**(9904):1575–1586, 2013.

[Wes77] JB West. "Ventilation-Perfusion Relationships 1, 2." *American Review of Respiratory Disease*, **116**(5):919–943, 1977.

[WHY14] Jingpeng Wu, Yong He, Zhongqin Yang, Congdi Guo, Qingming Luo, Wei Zhou, Shangbin Chen, Anan Li, Benyi Xiong, Tao Jiang, et al. "3D BrainCV: simultaneous visualization and analysis of cells and capillaries in a whole mouse brain with one-micron voxel resolution." *Neuroimage*, **87**:199–208, 2014.

[WP93] Chi-Hwa Wang and Aleksander S Popel. "Effect of red blood cell shape on oxygen transport in capillaries." *Mathematical Biosciences*, **116**(1):89–110, 1993.

[WRS08] Jiandi Wan, William D Ristenpart, and Howard A Stone. "Dynamics of shear-induced ATP release from red blood cells." *Proceedings of the National Academy of Sciences*, **105**(43):16432–16437, 2008.

[WSA96] Brant M Weinstein, Alexander F Schier, Salim Abdelilah, Jarema Malicki, Lilliana Solnica-Krezel, Derek L Stemple, DY Stainier, Fried Zwartkruis, Wolfgang Driever, and Mark C Fishman. "Hematopoietic mutations in the zebrafish." *Development*, **123**(1):303–309, 1996.

[WSD95] Brant M Weinstein, Derek L Stemple, Wolfgang Driever, and Mark C Fishman. "Gridlock, a localized heritable vascular patterning defect in the zebrafish." *Nature Medicine*, **1**(11):1143, 1995.

[WSW74] PD Wagner, HA Saltzman, and JB West. "Measurement of continuous distributions of ventilation-perfusion ratios: theory." *Journal of Applied Physiology*, **36**(5):588–599, 1974.

[WTD07] Sheldon Weinbaum, John M Tarbell, and Edward R Damiano. "The structure and function of the endothelial glycocalyx layer." *Annual Review of Biomedical Engineering*, **9**:121–167, 2007.

[YH98] Hai Yang and Michael G H Bell. "Models and algorithms for road network design: a review and some new developments." *Transport Reviews*, **18**(3):257–278, 1998.

[ZL77] Benjamin W Zweifach and Herbert H Lipowsky. "Quantitative studies of microcirculatory structure and function. III. Microvascular hemodynamics of cat mesentery and rabbit omentum." *Circulation Research*, **41**(3):380–390, 1977.

[ZSW92] Mair Zamir, Paula Sinclair, and Thomas H Wonnacott. "Relation between diameter and flow in major branches of the arch of the aorta." *Journal of Biomechanics*, **25**(11):1303–1310, 1992.